Firmware, Detector Performance and First Data of the AMIGA Muon Counters for the Pierre Auger Observatory

Dissertation
zur Erlangung des akademischen Grades eines
Doktors der Naturwissenschaften

vorgelegt von
M. Sc. Uwe Fröhlich

eingereicht bei der Naturwissenschaftlich-Technischen Fakultät
der Universität Siegen

Siegen 2013

Gutachter der Dissertation:	Prof. Dr. Peter Buchholz Prof. Dr. Markus Risse
Datum der Disputation:	30. Oktober 2013

Gedruckt auf alterungsbeständigem, holz- und säurefreiem Papier.

Abstract

With the Pierre Auger Observatory, being the largest air shower detector setup in the world, ultra-high-energy cosmic rays are studied with full trigger efficiency above $E = 3 \times 10^{18}\,\mathrm{eV}$. In order to achieve a more detailed understanding of cosmic ray physics at lower energies down to $E \approx 10^{17}\,\mathrm{eV}$, e.g. the transition from galactic to extragalactic sources and a possible change in the composition of the primary cosmic rays, the observatory is currently upgraded by the AMIGA enhancement (Auger Muons and Infill for the Ground Array). The muon counters of AMIGA, buried underground, will allow for dedicated measurements of the number of muons in air showers, thus increasing the precision in determining the type of the primary particle.
Until middle of 2012, eight prototype muon counters of the AMIGA enhancement were installed at the experimental site of the Pierre Auger Observatory at Malargüe, Argentina, forming one detector hexagon referred to as the pre-unitary cell (PUC). Each muon counter comprises a highly modular electronics readout system. Following the production of these systems, tests of single components as well as of the full readout electronics were carried out.

In the framework of this thesis dedicated firmware, allowing for the commissioning and first data taking with the PUC, has been developed and tested. Among other features, this firmware includes a self-trigger of the muon counters as well as algorithms for the synchronization of the muon detector (MD) with the existing surface detector (SD) array. The functionality and performance of the electronics readout system with regard to this firmware has been investigated. In addition, first analyses of combined MD and SD data have been performed.

Zusammenfassung

Mit dem Pierre Auger Observatorium, dem weltweit größten Luftschauer-Experiment, wird ultrahochenergetische kosmische Strahlung mit voller Triggereffizienz oberhalb von $E = 3 \times 10^{18}\,\mathrm{eV}$ untersucht. Um ein detaillierteres Verständnis der Astroteilchenphysik bei niedrigeren Energien bis $E \approx 10^{17}\,\mathrm{eV}$ zu erlangen, z.B. vom Übergang von galaktischen zu extragalaktischen Quellen und einer möglichen Änderung in der Zusammensetzung der primären kosmischen Strahlung, wird das Observatorium gegenwärtig durch die AMIGA-Erweiterung (Auger Muons and Infill for the Ground Array) weiter ausgebaut. Die unterirdisch installierten AMIGA-Myonzähler erlauben eine dedizierte Messung der Anzahl der Myonen in Luftschauern und erhöhen somit die Präzision der Bestimmung des primären Teilchens.
Bis Mitte des Jahres 2012 wurden acht Prototypen der Myonzähler der AMIGA-Erweiterung am Standort des Pierre Auger Observatoriums bei Malargüe, Argentinien, installiert. Diese sind in einem ersten Hexagon angeordnet, welches als „pre-unitary cell“ (PUC) bezeichnet wird. Jeder Myonzähler beinhaltet ein hochmodulares, elektronisches Auslesesystem. Nach der Produktion dieser Systeme wurden Tests der einzelnen Komponenten sowie der gesamten Ausleseelektronik durchgeführt.

Im Rahmen der vorliegenden Arbeit wurde Firmware entwickelt und getested, welche die Inbetriebnahme der PUC sowie erste Datennahmen ermöglicht. Neben anderen Funktionen beinhaltet diese Firmware einen Selbst-Trigger der Myonzähler sowie Algorithmen zur Synchronisation des Myondetektors (MD) mit dem bestehenden Oberflächen-Detektor-Feld (SD). Die Funktionalität und das Betriebsverhalten der elektronischen Auslesesysteme wurde hinsichtlich dieser Firmware untersucht. Zusätzlich wurden erste Analysen von kombinierten MD- und SD-Daten durchgeführt.

Contents

1 Introduction **1**

2 Ultra-High-Energy Cosmic Radiation **3**
2.1 History of Cosmic Ray Physics . . . 3
2.2 High-Energy Primary Cosmic Radiation . . . 4
2.2.1 Elemental Composition of Cosmic Radiation . . . 4
2.2.2 Acceleration of Cosmic Ray Particles . . . 5
2.2.3 Sources of Cosmic Ray Particles . . . 7
2.2.4 Anisotropy of Primary Cosmic Rays . . . 10
2.2.5 The Energy Spectrum of Cosmic Rays . . . 11
2.3 Cosmic Ray Air Showers . . . 17
2.3.1 The Electromagnetic Component . . . 18
2.3.2 The Hadronic and Muonic Components . . . 21

3 The Pierre Auger Observatory **25**
3.1 The Surface Detector . . . 26
3.1.1 The Surface Detector Station . . . 27
3.1.2 Surface Detector Calibration . . . 28
3.1.3 The Trigger System of the Surface Detector . . . 30
3.2 The Fluorescence Detector . . . 33
3.2.1 The Trigger System of the Fluorescence Detector . . . 34
3.3 Enhancements of the Hybrid Detector . . . 35
3.3.1 AMIGA . . . 36
3.3.2 HEAT . . . 36
3.3.3 Radio Detection of Air Showers - AERA . . . 38
3.3.4 Microwave Detection of Air Showers . . . 40

4 The Muon Detector of the AMIGA Enhancement **43**
4.1 Comparison of Composition Sensitive Air Shower Observables . . . 44
4.2 Determination of the Number of Muons with the AMIGA Muon Detector . . . 46
4.3 The Pre-Unitary Cell . . . 48
4.4 The Muon Counter Modules . . . 48
4.4.1 The Scintillator Module . . . 48
4.4.2 The Photomultiplier . . . 50
4.5 The Muon Detector Electronics . . . 50
4.5.1 The Underground Electronics of a Muon Counter Module . . . 51

4.5.2 The Surface Electronics of a Muon Counter 54

5 Firmware Features of the AMIGA Digital Board **57**
5.1 Structure of the FPGA Firmware 58
5.2 Buffer Structure 60
5.3 Input and Output Registers 62
5.4 Sampling/Downsampling of Input Pulses 63
5.4.1 Dependence of the Downsampling Algorithm on the Trigger Mode . . 66
5.4.2 Comparison of Monte Carlo Data with Measurements 66
5.5 The Occupancy-N Trigger 75
5.5.1 Test of the Occupancy-N Trigger 77
5.6 The Prescaler Algorithm 80
5.6.1 Implementation of the Prescaler Algorithm 81
5.6.2 Dependence of the Prescaling on the Trigger Rate 82
5.7 The T1/T3 Trigger Chain 88
5.7.1 Algorithm for Decoding the T1 Timestamp 88
5.7.2 Requesting Event Data by Timestamp 89
5.7.3 Efficiency of the T1/T3 Trigger Chain 90
5.8 End-of-Event Information 96
5.8.1 Check of T3 Requested Events 96
5.8.2 Verification of Correct Event Handling 97
5.8.3 Reconstruction of the Trigger Rate 99
5.9 Upgrade to 320 MHz Data Acquisition 100

6 Analysis of First Prototype Data **105**
6.1 Event Structure of the AMIGA MD Data 106
6.2 Data Taking Periods 107
6.3 System Debugging Using Occupancy- and T1/T3-triggered Data 111
6.3.1 Trash Events in T1/T3-triggered Data 113
6.3.2 Magic Word Information in T1/T3-triggered Data 116
6.3.3 Repeated Events in T1/T3-triggered Data 117
6.4 Selection of Combined MD/SD Events 118
6.4.1 Properties of Combined MD/SD Events 119
6.5 Occupancy-based Analyses of T1/T3-triggered Data 120
6.5.1 Definition of N_{Occ} and N_{Trig} 122
6.5.2 Dataset for Occupancy-based Analyses 122
6.6 Correlation of N_{Occ} with SD-related Shower Observables 124
6.6.1 Occurrence of Signal Multiplicities in T1/T3-triggered Data 127
6.6.2 Correlation of N_{Occ} with Distance to the Shower Axis or SD Energy . 128
6.6.3 Correlation of N_{Occ} with SD Energy for Different Distances to the Shower Axis 134

7 Summary and Outlook **141**

A The Pattern Board 145

List of Figures 147

List of Tables 149

List of Abbreviations and Acronyms 151

List of Components and Devices 155

List of Software 157

Bibliography 159

Acknowledgements 173

1 Introduction

> *"From a consideration of the immense volume of newly discovered facts in the field of physics, especially atomic physics, in recent years it might well appear to the layman that the main problems were already solved and that only more detailed work was necessary."*
>
> Victor Hess

Cosmic rays have been discovered more than one century ago by Victor Hess in 1912, but still remain of considerable interest for physicists as messenger particles of very powerful astrophysical processes. Answering fundamental questions about the origin, the underlying propagation mechanisms, the energy spectrum and the composition of cosmic rays is subject of ongoing research.

The Pierre Auger Observatory, being the largest earthbound cosmic ray experiment, has been installed to provide answers to these questions. It is reliably taking data since January 2004 and its construction was completed in 2008. By now it has accumulated a large amount of data regarding extensive air showers in the EeV (10^{18} eV) regime, aiming for the understanding of the physics of ultra-high-energy cosmic rays (UHECRs). In order to extend the energy range accessible to the Pierre Auger Observatory towards lower energies, the detector enhancements AMIGA (Auger Muons and Infill for the Ground Array) and HEAT (High Elevation Auger Telescopes) were installed. These additional detectors not only allow for a comparison of analysis results with other experiments operating at lower energies, such as KASCADE-Grande (Karlsruhe Shower Core and Array Detector Grande), but also for a precise determination of the composition of primary cosmic rays at these energies.
The muon detector (MD) of the AMIGA enhancement will permit measuring the muon content of extensive air showers on an event-by-event basis. This observable is suitable for the identification of the primary particle. During the last years, a prototype array of seven MD modules, referred to as the pre-unitary cell (PUC), has been installed at the experimental site in Argentina. Within the framework of this thesis, the FPGA (field programmable gate array) firmware of the readout electronics, that has been used for commissioning and debugging of the prototype detectors, has been developed and tested. In addition, first analyses of the data taken with these systems will be presented.

The thesis is structured as follows. In Chapter 2, an overview of the history and theory of ultra-high-energy cosmic rays and extensive air showers is given. The Pierre Auger Observatory is introduced in Chapter 3, focusing on the properties of its surface detector (SD) and the

corresponding data acquisition system. Other detectors, such as the fluorescence detector or the enhancements of the Pierre Auger Observatory, are outlined. Chapter 4 concentrates on the description of the AMIGA MD. The MD array as well as the design of the single muon counter modules are presented in detail. The individual parts of the firmware of the muon counter readout electronics, that has been developed, are described in Chapter 5. Multiple laboratory measurements, investigating the functionality and the performance of this firmware, are discussed. In Chapter 6, first analyses of the data, that has been acquired with the muon counters of the PUC synchronously to the SD, are presented. Special focus is put on correlations between the multiplicity of signals measured with the muon counter modules and air shower related SD observables. Finally, the results of the work presented in this thesis are summarized in Chapter 7.

2 Ultra-High-Energy Cosmic Radiation

Contents

2.1 History of Cosmic Ray Physics . . . 3
2.2 High-Energy Primary Cosmic Radiation . . . 4
2.2.1 Elemental Composition of Cosmic Radiation . . . 4
2.2.2 Acceleration of Cosmic Ray Particles . . . 5
2.2.3 Sources of Cosmic Ray Particles . . . 7
2.2.4 Anisotropy of Primary Cosmic Rays . . . 10
2.2.5 The Energy Spectrum of Cosmic Rays . . . 11
2.3 Cosmic Ray Air Showers . . . 17
2.3.1 The Electromagnetic Component . . . 18
2.3.2 The Hadronic and Muonic Components . . . 21

The terms cosmic radiation and cosmic rays usually refer to charged nuclei originating from outside the solar system. Cosmic radiation with energies above 10^{18} eV is then referred to as ultra-high-energy cosmic rays (UHECRs). Whereas within the past century mankind gained a lot of knowledge about the properties of radiation in the vicinity of the Earth, relatively little is known about the properties of cosmic radiation. Especially at the highest energies, our knowledge decreases due to the diminishing intensity of incoming cosmic rays and the increasing difficulties of measuring the properties of these particles.

2.1 History of Cosmic Ray Physics

Astroparticle physics in today's form is a comparatively young discipline that started to develop since the late 1980s, but its real hour of birth goes back to more than 100 years ago. The exploration of cosmic radiation began as a consequence of the discovery of radioactivity. In 1900, the British physicist Charles T.R. Wilson, among others like Julius Elster and Hans Geitel, studied the ionization of air. He observed a discharge of his electroscopes, although air was supposed to be an isolating material, and concluded that this effect must be due to the natural radioactivity of the Earth. In order to prove this hypothesis, the ionization rate was measured at different altitudes. In 1910, Theodor Wulf performed measurements on the Eiffel tower but found the discharge of his self-made electroscope to be much smaller than expected [Wul10]. A few years later, in 1912, Victor Hess measured the ionization rate flying a balloon up to altitudes of around 5 km [Hes12]. By observing an increase of ionization, rather than the expected decrease, he found the first evidence of the existence of cosmic rays, for which he later, in 1936, received the Nobel Prize in physics. In the 1930s, the more detailed exploration

of cosmic radiation, using e.g. cloud chambers, lead to the discovery of many new particles like the positron, the muon and the pion.
In 1938, at the Jungfraujoch in Switzerland (3,500 m a.s.l.), Pierre Auger performed several measurements using multiple Geiger-Müller counters at large distances from each other [Aug39]. By measuring time-coincident signals, he concluded the existence of air showers made up of secondary cosmic ray particles. The knowledge scientists gained from the numerous experiments performed in the 1930s lead to the development of an overall theory of cosmic radiation and of cosmic ray air showers [Ros41]. The measurement of cosmic ray air showers also allowed for a first estimation of the energy of the primary particles. Auger estimated that the showers were initiated by primary cosmic rays with energies up to 10^{15} eV, but with improving techniques for measuring air showers and the installation of new detectors over the last 70 years, this limit didn't hold. In 1994, the Fly's Eye experiment detected the highest-energy air shower ever measured with a reconstructed energy of the primary cosmic ray particle of 3.2×10^{20} eV [Elb95].

2.2 High-Energy Primary Cosmic Radiation

Since cosmic rays with energies up to some 10^{14} eV can be measured directly, e.g. using satellite-borne experiments, their properties are well known. Although huge efforts have been made to measure high-energy cosmic rays with primary energies in the 10^{18} eV range, predictions concerning the properties of these particles are often strongly dependent on underlying models of e.g. particle propagation or hadronic interactions. In collider experiments man-made particle accelerators are currently limited to a maximum center-of-mass energy in the order of $E_{\mathrm{CMS}} \approx 1.4 \times 10^{13}$ eV (LHC, [Brü04]), corresponding to an equivalent energy of a cosmic ray impinging on a fixed proton (nucleon) target of $E_{\mathrm{CR}} \approx 10^{17}$ eV [Tay08]. Therefore, the physics processes taking place at high and the highest energies can only be estimated through extrapolations. This gives rise to uncertainties in the description of the properties of high-energy cosmic rays.

2.2.1 Elemental Composition of Cosmic Radiation

98% of the charged particles penetrating the Earth's atmosphere from outer space are fully ionized atomic nuclei, only 2% are electrons. The fraction of nuclei is dominated by protons (approx. 85%) whereas α particles and particles with a nuclear charge $Z \geq 3$ contribute approximately 12% and 3%, respectively [Gru05]. With different occurrences, all elements of the periodic table have been found in cosmic rays.

Taking current experimental results into account, the elemental composition of primary cosmic rays in comparison to the relative abundance of elements in the solar system is shown in Figure 2.1. Overall, both distributions are in good agreement. However, for some values of the charge number Z, the elemental composition clearly differs from the measured abundance of elements in the solar system, in some cases by several orders of magnitude. The suppression of elemental groups reveals information about the acceleration mechanisms of cosmic rays or

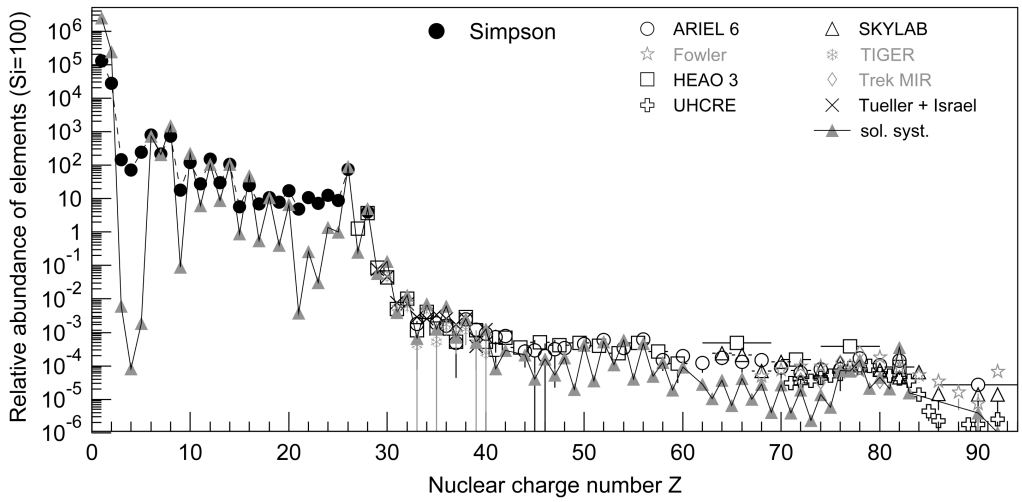

Figure 2.1: *Elemental composition of cosmic radiation [Blü09]. The abundance of elements is shown as a function of their nuclear charge number Z at energies of around 10^9 eV per nucleon. The data points are normalized to the abundance of silicon ($Z = 14$). In comparison, the abundance of elements in the solar system is shown (taken from [Lod03]). The data points for $Z \leq 18$ are taken from [Sim83], for a complete list of references see [Blü09].*

about processes cosmic rays are undergoing when propagating through space.

The suppression of the abundance of hydrogen and helium in cosmic rays can be accounted for by the relatively high ionization energies of both elements and the fact that most acceleration mechanisms only affect charged particles. The light elements lithium, beryllium and boron are more abundant in cosmic rays than in the solar system. Since these elements are destroyed in hot environments, only a small fraction could have been produced by the Big Bang nucleosynthesis or be a product of the stellar nucleosynthesis. This is reflected in the relatively low abundance of these nuclei within the solar system. Instead, the elements of the $LiBeB$ group as well as the elements below iron (Mn, Cr, V, Ti and Sc) are produced in spallation processes caused by collisions of galactic cosmic rays (protons, α-particles) with the interstellar matter, i.e. nuclei of the CNO group and the iron group, respectively. As a consequence, the solar system as well as cosmic rays, at a larger extent, get enriched with the elements mentioned above.

2.2.2 Acceleration of Cosmic Ray Particles

Nowadays there exists a wide variety of theories trying to explain both the origin of cosmic ray particles as well as their acceleration up to the highest energies. Unfortunately, none of these theories is capable of explaining all the measured features of cosmic rays. This becomes even more difficult when taking the propagation of particles through the interstellar medium into account. In general, all acceleration theories can be categorized into two scenarios: 'top-down' (decay) and 'bottom-up' (acceleration) scenarios.

Top-down scenarios

In top-down theories, UHECRs originate from some yet unknown mechanisms, which are capable of providing an enormous amount of energy without the need for any further acceleration of the particles. One possible solution could be the decay of super-massive 'X'-particles with masses close to the GUT scale ($m_X \gg 10^{20}\,\mathrm{eV}$), which could have been produced in the early Universe and which have a very long lifetime comparable to the age of the Universe. Other theories assume the 'X'-particles to have a very short lifetime, therefore they have to be continuously produced, e.g. in emissions from cosmological defects like magnetic monopoles [Sig03].
However, top-down scenarios are heavily constrained by recent measurements of several cosmic ray experiments. Since these models often imply the existence of ultra-high-energy photons or neutrinos, recent upper limits on the particle fluxes already allow for an exclusion of individual scenarios (Figure 2.2).

Bottom-up scenarios

In bottom-up scenarios, the charged particles gain energy by being accelerated in special astrophysical environments. The details of the acceleration as well as the maximum energy, the particles can gain, strongly depend on the individual scenario. The acceleration can be achieved either by strong electric fields accelerating the particles in a direct way or by statistical acceleration in e.g. a magnetized plasma. The jets of active galactic nuclei [Rac93] as well as rapidly rotating neutron stars (pulsars) [Che86] are possible sites for direct acceleration.

The idea of statistical acceleration was first mentioned in 1949 [Fer49]. It is supposed that charged particles interact with randomly moving inhomogeneities of turbulent magnetic fields. Although individual particles can gain or lose energy due to these interactions, there can be an overall macroscopic increase of the particle's energy. Because the average fractional gain in energy is proportional to the square of the relative velocity of the magnetized plasma $(u/c)^2$, this mechanism is often called second-order Fermi acceleration. The resulting energy spectrum is of the form of a power-law spectrum, but since the power-law index depends on the velocity of the individual acceleration site, the superposed spectrum of many different sources would, in general, not be a power-law spectrum. In addition, the second-order Fermi mechanism is not very efficient due to the dependence on the square of the velocity and $u/c < 1$.

The most promising concept of statistical acceleration is the diffusive shock acceleration mechanism (DSAM). It is based on the idea that low-energy particles can gain energy by repeated collisionless scatterings with plane relativistic shock fronts. The compression of the interstellar medium at the shock causes differences in the magnetic field topologies, which allow for multiple diffusive scattering processes between the particle and the shock. In each acceleration cycle, the average increase of energy is proportional to the speed of the shock (first-order Fermi acceleration). The maximum energy of the DSAM is only limited by the number of acceleration cycles, which only depends on the lifetime of the shock and the typical time of energy losses of the particle, as well as on the size of the shock, since its radius has to be larger than the gyroradius of the particle. One intrinsic feature of this mechanism is

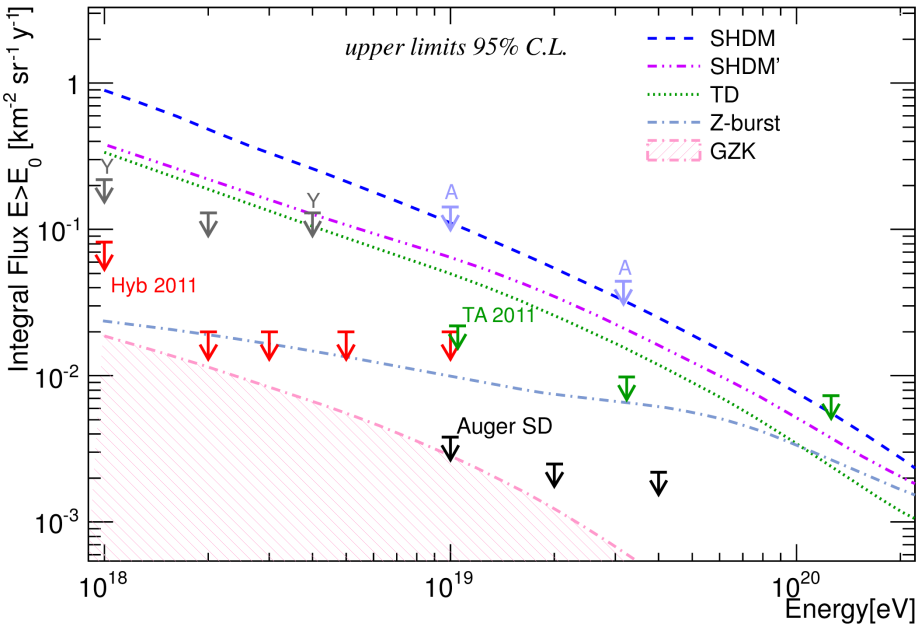

Figure 2.2: *Upper limits on the photon flux [Set11b] measured by Auger (Hybrid, SD), AGASA (A, [Shi02]) and Yakutsk (Y, [Glu10]). The shaded region and the lines give the predictions for the GZK photon flux [Gel08] and for various top-down models. For a complete list of references see [Set11b].*

that particles leave the acceleration site with a characteristic power-law spectrum, where the power-law index only depends on the shock compression ratio rather than the velocity. A more detailed discussion of the theory of diffusive shock acceleration can be found in [Dru83].

Shocks are omnipresent in astrophysical situations. Promising candidates allowing for a diffusive acceleration at relativistic shocks are supernova remnants (SNRs). Provided that approximately 10 % of the estimated total power output in a supernova explosion are in the form of kinetic energy of the ejected material [Bha00] and that the maximum achievable cosmic ray energy is in the order of 10^{12} eV up to 10^{17} eV, first-order Fermi acceleration is assumed to be the predominant source for cosmic rays with energies at least up to around some 10^{15} eV. Recent results can even explain the acceleration of iron primaries in Type IIb SNRs up to an energy of 5×10^{18} eV [Ptu10].

2.2.3 Sources of Cosmic Ray Particles

Identifying the sources of UHECRs is one of the problems in astroparticle physics which has not yet been solved. Nevertheless, there are only a few astronomical sites which fulfill the requirements for being able to accelerate particles to the highest energies, irrespective of the precise acceleration mechanisms. In any case, large magnetic field strengths or extensive

acceleration regions are necessary to keep the particles confined within the acceleration region, i.e. the size L of the acceleration region has to be larger than the diameter of the particle's orbit defined by its gyroradius. This relation can be written as [Hil84]

$$\left(\frac{B}{\mu\mathrm{G}}\right)\left(\frac{L}{\mathrm{kpc}}\right) > 2\left(\frac{E}{10^{18}\,\mathrm{eV}}\right)\frac{1}{Z\beta} \tag{2.1}$$

with B being the magnetic field strength of the acceleration region, E the maximum energy of the accelerated particle, Z the nuclear charge number of the particle and β the characteristic velocity of the magnetic scattering centers in units of the speed of light c. A graphical representation of this expression is shown in Figure 2.3. In the following, the major characteristics of possible source candidates are briefly summarized.

Active Galactic Nuclei

Active galactic nuclei (AGNs) are nowadays agreed to be source candidates for UHECRs. Typical estimates for their magnetic field strengths and their sizes are in the order of $L \approx 0.02\,\mathrm{pc}$ and $B \approx 5\,\mathrm{G}$, respectively [Hal97], allowing for a maximum particle energy of $E_{\max} \approx 10^{19}\,\mathrm{eV}$ for protons. Although it is therefore unlikely for cosmic rays with extremely high energies ($E \gtrsim 10^{20}\,\mathrm{eV}$) to originate from AGNs, they could well be the source of some part of cosmic rays with energies up to a few $10^{19}\,\mathrm{eV}$. However, taking into account that the highly accelerated protons will lose energy due to synchrotron and Compton processes and that they can interact with the dense radiation field around AGNs in photo-pion production, their maximum energy will be limited to some $10^{16}\,\mathrm{eV}$ [Nor95].

Photo-pion production will contribute to the production of highly energetic neutrons, which could escape from the central region of the active galactic nucleus and which could later decay to protons through β-decay [Pro92]. However, due to the fact that these neutrons themselves will lose energy through photo-pion production, neither protons nor neutrons with energies above some $10^{16}\,\mathrm{eV}$ are supposed to be able to escape from the central region of AGNs.

Hot Spots of Radio Galaxies

Fanaroff-Riley class II radio galaxies (FR-II radio galaxies) [Fan74] are one of the most promising source candidates for UHECRs. These radio objects are located at the endpoints of powerful, relativistic jets ejected by active galactic nuclei. Confirmed by calculations of the synchrotron spectra of FR-II galaxies in the radio-to-optical regime [Bie87], they are believed to form very large and powerful shocks, which could accelerate cosmic rays to energies above $10^{18}\,\mathrm{eV}$ [Rac93]. Since the regions of intense synchrotron radiation within the jets, referred to as hot spots, are located at the edges of the extended radio lobes, high-energy particles could immediately leave the acceleration region without being subject to any further energy losses. Due to the low density of soft photons at the hot spots, the energy loss due to photo-pion production is not significant [Bha00]. Depending on the assumption of the magnetic field strengths within the hot spots, a maximum energy even above $10^{21}\,\mathrm{eV}$ could be possible.

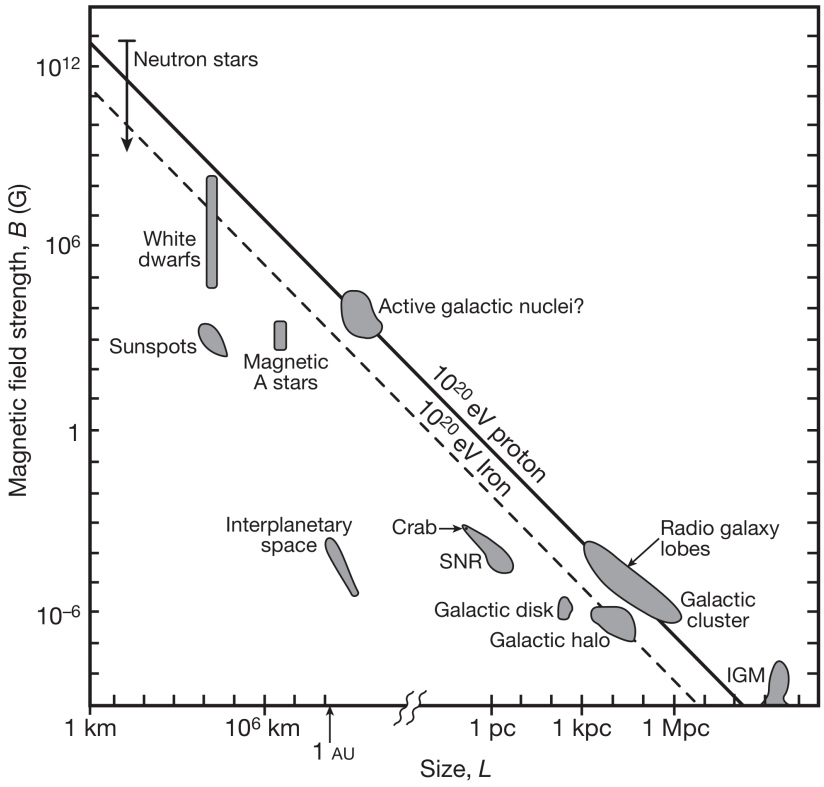

Figure 2.3: *Hillas diagram (taken from [Bau09]), a visualization of Equation 2.1. Data for possible source candidates are shown, arranged according to their typical magnetic field strengths B and sizes L. The site requirements for a maximum energy ($E_{max} \approx \beta ZBL$) of 10^{20} eV proton and iron primaries are indicated with the solid and dashed lines, respectively. Only source candidates above the diagonal lines are capable of accelerating the primary cosmic rays to the corresponding maximum energy.*

Due to the fact that FR-II galaxies are very bright radio objects, their distribution up to high redshifts, i.e. large distances, is well known from measurements [Pea85]. It turns out that radio galaxies, which correlate with the arrival directions of observed UHECR events, can only be found at large distances (above 100 Mpc) from the Earth [Elb95]. This, as a consequence, would lead to energy losses of the cosmic rays due to the GZK effect (Section 2.2.5). Thus, although the hot spots of radio galaxies seem to be sufficiently powerful source candidates for cosmic rays in the energy range up to some 10^{18} eV, it is difficult to consider them contributing to the ultra-high-energy part of the cosmic ray spectrum.

Pulsars

As can be seen from Figure 2.3, fast rotating neutron stars (pulsars) are potential accelerators for cosmic rays. Here, most theories are based on the assumption of a direct acceleration of the particle in the strong drop of the electrostatic potential which is induced at the surface of

the rotating neutron star due to its axially symmetric rotating magnetic field. For a typical pulsar with an angular velocity of $\Omega \approx 10^{-4}\,\mathrm{Hz}$, a radius of $R \approx 10^{4}\,\mathrm{m}$ and a magnetic field of strength $B \approx 10^{13}\,\mathrm{G}$ the maximum potential drop is in the order of $10^{21}\,\mathrm{V}$ [Ven97]. Thus, pulsars could be assumed to be accelerators for cosmic rays in the UHECR regime.

However, the basic problem is that if the acceleration takes place along the magnetic field lines with finite radii of curvature, a seed electron will produce electron-positron pairs due to the emission of curvature radiation [Lon11]. Therefore, the strong potential drop will be significantly short-circuited by cascades formed of electrons and positrons moving in opposite directions along the magnetic field lines. Overall, the maximum energy achievable due to direct acceleration by pulsars lies most likely in the order of $10^{15}\,\mathrm{eV}$ [Bha00].

In another class of models, cosmic ray particles gain energy by statistical acceleration in accretion shocks, which envelope the neutron stars. But also here it seems difficult to raise the maximum possible energy above $10^{15}\,\mathrm{eV}$ [She95].

Gamma-Ray Bursts

Gamma-ray bursts (GRBs) are flashes of gamma-rays due to extremely high energetic explosions or astrophysical processes. Most of the GRBs, which have been observed, are believed to occur during supernova explosions forming a neutron star or a black hole, whereas others might be connected to the merger of neutron stars in binary systems. Assuming an average energy release of typical GRBs in the order of $5 \times 10^{43}\,\mathrm{J}$ [Fra01] within a few seconds, sequential acceleration processes might allow for an energy gain of light nuclei or electrons of a few $10^{18}\,\mathrm{eV}$. Taking an acceleration in forward shocks of long GRBs into account, these processes can even be considered to be possible sources for cosmic ray particles in the energy range around the ankle (Section 2.2.5) [Eic11]. In fact, there are attempts to associate cosmic ray events in the ultra-high-energy regime with strong GRBs [Mil95]. However, since the rate of GRBs is very low (approximately 10^{-6} to $10^{-5}\,\mathrm{yr}^{-1}$ per galaxy) [Pod04] and since most of them are far apart, it is unlikely that GRBs significantly contribute to the cosmic rays detected at Earth.

2.2.4 Anisotropy of Primary Cosmic Rays

The search for anisotropies in the arrival directions of primary cosmic rays on different angular scales and thus, identifying source regions or even individual sources, can lead to a more profound understanding of particle acceleration processes in the Universe. Whereas large-scale anisotropies are connected to propagation processes in the Galaxy, small-scale anisotropies can provide information about the cosmic-ray sources.

Because of the relative motion of the Earth with respect to the rest frame of cosmic rays, a dipole structure in the arrival directions of primary particles is expected (Compton-Getting effect) [Com35]. This large-scale structure has been observed for galactic cosmic rays at low energies [Cut86], at which the isotropic flux is modulated at the solar frequency by the motion of the Earth relative to the frame in which the galactic cosmic rays have no bulk motion.

At higher energies, also other experiments like e.g. EAS-TOP [Agl96] or Akeno [Kif86] have found large-scale anisotropies. However, the derived results do not agree between the different experiments. Apart from that, measurements taken with the KASCADE detector in the energy range between 0.7×10^{15} eV and 6×10^{15} eV yield no hint for anisotropy in the right ascension distribution of extensive air showers [Ant04].
In measurements at even higher energies above the second knee (Section 2.2.5) and up to above the ankle (Section 2.2.5) performed by various experiments like Yakutsk, AGASA or the Pierre Auger Observatory, no significant large-scale anisotropy and, in particular, no dipole structure in the distribution of the arrival directions of cosmic rays could be found [Blü09].

With increasing rigidity of the primary particles, searches for small-scale anisotropies and individual sources become possible. Recent analyses of air shower data taken with the Pierre Auger Observatory at the highest energies [Abr08a] resulted in a significant correlation between the arrival directions of primary cosmic ray particles with energies $E > 5.7 \times 10^{19}$ eV and the known positions of AGNs up to a distance of 75 Mpc from the Véron-Cetty & Véron catalog [Vcv06] (Figure 2.4). However, a repetition of the analysis performed by the HiRes collaboration could not confirm the correlation [Abb08b]. Although this discrepancy is not yet understood, possible explanations could be found in the incompleteness of the catalog in use or in a difference in the overall energy scale of the two experiments.

2.2.5 The Energy Spectrum of Cosmic Rays

Cosmic rays enter the outer layer of the atmosphere with a rather high integrated rate of approximately $1000\,\mathrm{s^{-1}sr^{-1}m^{-2}}$ in total [Gai91]. Overall, the differential spectrum of incoming cosmic rays (Figure 2.5) covers about twelve orders of magnitude in energy, whereas the flux ranges over about 30 orders of magnitude resulting in integrated rates of approximately $1\,\mathrm{s^{-1}m^{-2}}$ at an energy of a few 10^{11} eV down to around $1\,\mathrm{yr^{-1}km^{-2}}$ in the 10^{18} eV regime. At energies below about 10^{10} eV, i.e. the part which is not shown in Figure 2.5, the flux of particles is strongly affected by solar modulations and the geomagnetic field. The magnetic fields connected to the plasma winds, which are continuously emitted from the Sun and which vary in eleven-year cycles, deflect the low-energy particles and thus make measurements of cosmic rays highly dependent on location and time. In the energy range above the region of significant solar modulation (about 10^9 eV/nucleon, [Buc03]) the primary cosmic ray spectrum can be approximated by a power-law function of the form

$$\frac{dN}{dE} \propto E^{-\gamma} \quad . \tag{2.2}$$

Despite the large range covered, the differential spectral index γ is piecewise approximately constant and lies in the range of $\gamma \approx 2.5 \ldots 3.2$.

Although the all-particle spectrum appears to be rather structureless, it shows several distinctive features connected to changes of the spectral index. At an energy of $E_{\mathrm{knee}} \approx 3 \times 10^{15}$ eV, a steepening of the spectrum occurs, which is usually referred to as the knee. Here, the spectral index changes from $\gamma \approx 2.7$ below E_{knee} to $\gamma \approx 3.1$ above E_{knee}. A further rise of γ

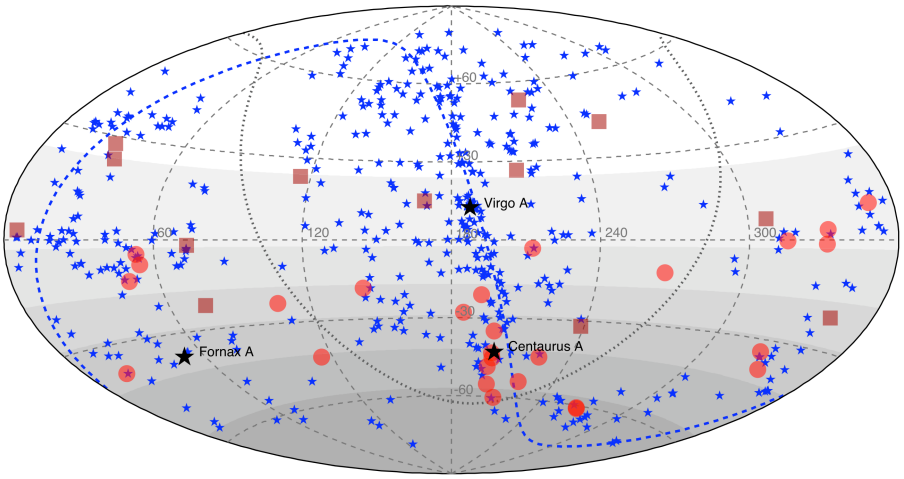

Figure 2.4: *Arrival directions of the highest-energy cosmic rays in equatorial coordinates (taken from [Blü09]). Data points of the Pierre Auger Observatory [Abr08a] are plotted as red circles and red squares indicate the data of the HiRes collaboration [Abb08b]. The positions of active galactic nuclei up to a distance of 75 Mpc from the Véron-Cetty & Véron catalog [Vcv06] are represented by the blue asterisks. The relative exposure of the Pierre Auger Observatory is indicated by the gray shaded area, the galactic disk and the super-galactic plane are shown by the black dotted line and the blue dashed curve, respectively.*

by a value of approximately 0.2 seems to occur at the second knee at an energy of around $E_{\mathrm{2kn}} \approx 4 \times 10^{17}\,\mathrm{eV}$. At an energy of $E_{\mathrm{ankle}} \approx 4 \times 10^{18}\,\mathrm{eV}$, the spectrum flattens again and the spectral index returns to a value of $\gamma \approx 2.7$. This feature is often called the ankle of the energy spectrum of cosmic radiation. Finally, a suppression of the primary particle flux due to the GZK effect is expected to occur for energies above $E_{\mathrm{GZK}} \approx 6 \times 10^{19}\,\mathrm{eV}$. In the following sections, the main features of the energy spectrum mentioned above will be briefly summarized.

The Knee of the Cosmic Ray Spectrum

The knee appears as a kink in the all-particle spectrum around $E_{\mathrm{knee}} \approx 3 \times 10^{15}\,\mathrm{eV}$. Identifying the origin of this feature is still subject to further scientific investigations. Based on the four most developed models explaining the origin of the knee, it could be caused by

- a change of the propagation of galactic cosmic ray particles related to a more rapid particle escape from our Galaxy,
- a limited confinement in the acceleration region,
- the presence of only one or a few sources within our Galaxy or
- a yet unknown change of the hadronic interactions of the cosmic ray particles either during the propagation through the interstellar medium or inside our atmosphere.

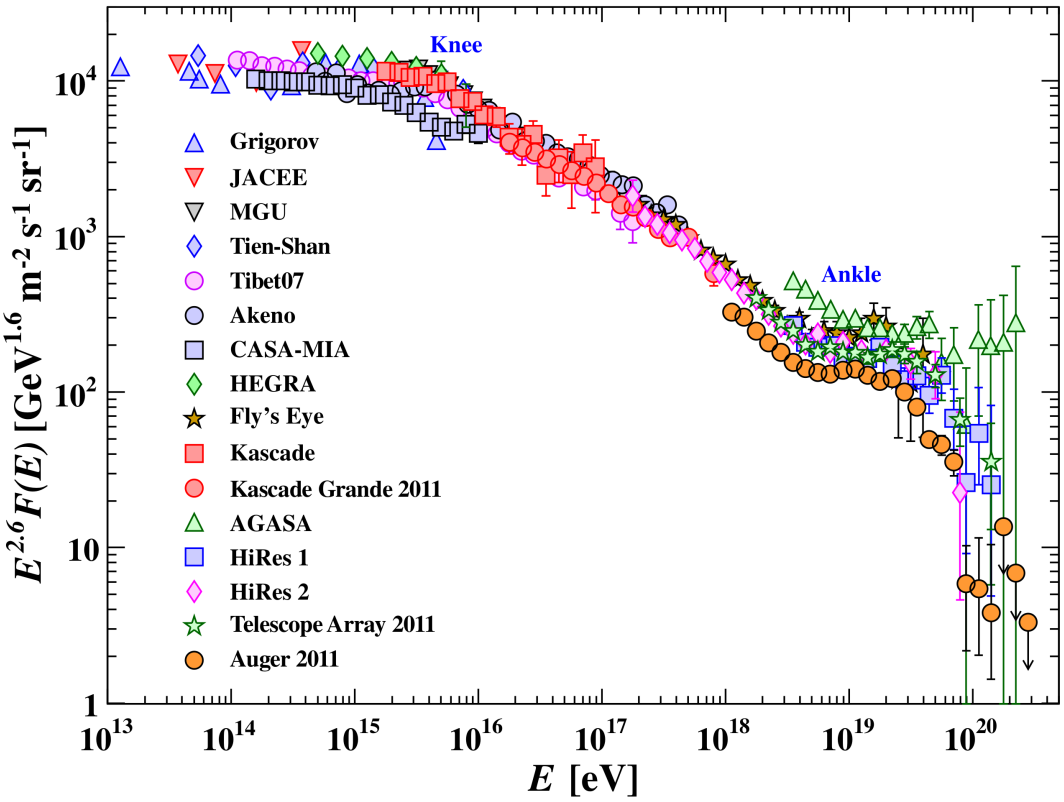

Figure 2.5: *The all-particle spectrum of cosmic rays [Beh12]. The flux $F(E) = dN/dE$ is multiplied by a factor $E^{2.6}$ to emphasize the features of the power-law spectrum, i.e. the knee and the ankle. The data points are taken from direct or air shower measurements of various experiments: PROTON [Gri70], JACEE [Asa93], MSU [Fom91], Tien-Shan [Dan77], Tibet [Ame96], Akeno [Nag84], CASA-MIA [Gla99], HEGRA [Arq00], Fly's Eye [Bir94], KASCADE [Ant05], KASCADE-Grande [Ape11], AGASA [Tak03], HiRes [Abb08a], Telescope Array [Tsu11] and Auger [Abr08b]. For a complete list of references see [Beh12].*

Following the first three models, the knee would have its origin in astrophysical processes and would therefore be an intrinsic feature of the all-particle spectrum. For the last model, new particle physics processes are considered, which modify a featureless primordial spectrum. The models listed above will be treated briefly in the following sections, a more complete and detailed review can be found in [Hör04].

In the first scenario, the flux of particles arriving at Earth decreases above E_{knee} due to the rigidity cut-off of the particles propagating through the Galaxy. The propagation of cosmic rays is usually described as a diffusive process with the particles interacting with the galactic magnetic field. The galactic magnetic field is a superposition of a regular field, which retains the particles within the Galaxy, and an irregular, turbulent component, which causes a drift of the cosmic ray particles and which therefore affects the confinement of the particles within our Galaxy [Can03]. Since the drift of a primary particle is proportional

to its energy E and to the reciprocal of its nuclear charge Z, also the probability that the particle will escape from the Galaxy will increase with E/Z, leading to a depletion of light elements [Ptu93]. Therefore, the observed flux of particles will start to drop above a maximum energy, which is dependent on the nuclear charge number, i.e. $E_{\mathrm{max}} \approx Z \times E_{\mathrm{knee}}$, thus leading to the prediction that the primary cosmic ray composition becomes heavier above the knee.

Another possible scenario refers the reduction of the flux at energies above the knee to the limited confinement of the particles at the source. The maximum energy a particle can gain in processes based on shock acceleration mechanisms is inseparably connected to the size and the magnetic field strength of the acceleration region. The gyroradius r_{g} of a particle being accelerated increases with the reciprocal of the nuclear charge number and of the magnetic field strength of the particular acceleration site, i.e. $r_{\mathrm{g}} \propto (Z \times B)^{-1}$. Since the gain in energy depends on the number of crossings between the particle and the relativistic shock front, the maximum achievable energy for a given magnetic field strength B is limited by the nuclear charge Z of the particle to be accelerated, hence again leading to a depletion of light particles with small Z [Ber99]. Therefore, also this theoretical model predicts a dependence of the position of the knee in the all-particle spectrum on the charge of the primary cosmic ray particle. Recently published results of the KASCADE-Grande experiment, in which different positions of the knee in the energy spectra of light and heavy primaries have been reported, support this prediction [Ape13].

The knee in the cosmic ray spectrum could also be due to only a very limited number of nearby sources. One possible scenario assumes a featureless background spectrum of cosmic ray particles, which is superimposed by the spectrum of only one relatively young SNR in the Galaxy [Erl97]. Here, the knee can be identified as the maximum achievable energy that can be transfered from the shock front of the SNR to particles of the CNO group. A change in the spectral index of heavier elements can then be found at higher energies. But whereas the acceleration of particles in the context of SNRs has been elaborated in detail, it is difficult to identify appropriate sources for the background part of the spectrum. One possible solution that would lead to the required form of the spectrum could be found in the combination of a pulsar-related particle acceleration with a modified propagation model. Some of the consequences, which are implied by having only one local source, are developed in [Erl98].

According to the fourth class of models, the knee is supposed to be a result of the air shower development in the Earth's atmosphere. Here, new physics processes transfer energy to a shower component which cannot yet be detected by air shower experiments, the consequence being that the reconstructed energy is systematically underestimated. One candidate for New Physics, which could match the requirements, could be supersymmetry with the lightest supersymmetric particle carrying away the missing energy [Kaz01]. However, these scenarios are purely based on theoretical considerations since the threshold for the interactions in the knee region is above the center-of-mass energy of today's collider experiments (LHC: $E_{\mathrm{CMS}} \lesssim 1.4 \times 10^{13}\,\mathrm{eV}$, [Brü04]) and therefore cannot be substantiated by measurements.

The Second Knee Feature

Most scenarios for the origin of the knee lead to a dependence of the drop-off energy E_{knee} on the nuclear charge Z. With a phenomenological model, the poly gonato-model[1], the all-particle spectrum can be described by superimposing the flux components for different groups of elements. In this picture, the knee is supposed to be the end of the galactic cosmic ray spectrum with all elements of the periodic table which have been found in primary cosmic rays (i.e. $Z \leq 92$) being expected to contribute to the overall particle flux [Hör03, Hör06]. The poly-gonato model describes the knee in the primary cosmic ray spectrum as a result of a series of subsequent cut-offs for individual elements. Following this idea, the second knee at $E_{\text{2kn}} \approx 4 \times 10^{17}\,\text{eV}$ can be explained by the cut-off of the heaviest stable nuclei whereas the knee at $E_{\text{knee}} \approx 3 \times 10^{15}\,\text{eV}$ corresponds to the end of the galactic proton component. Overall, the poly gonato model is able to give a satisfying description of the development of the spectral index in the energy range around the first and second knee, i.e. $E_{\text{2kn}} \approx 92 \times E_{\text{knee}}$, but since the chemical composition of primary cosmic rays at the highest energies is not yet well known from measurements, this model is still missing a profound confirmation based on experimental results.

A different approach to explain the first and second knee feature relies on the consideration of exotic particle interactions between the cosmic ray particles and e.g. relic Big Bang neutrinos [Wig00]. Primary cosmic ray protons could interact via the inverse β-decay according to

$$p + \bar{\nu}_e \longrightarrow n + e^+ \tag{2.3}$$

and thus be converted into neutrons. The threshold energy of the proton for this process depends on the mass of the electron antineutrino. Provided that the rest mass of the antineutrinos is in the order $m(\bar{\nu}_e) \approx 0.4\,\text{eV}/c^2$, the change of the spectral index at the knee of the all-particle spectrum around $E_{\text{knee}} \approx 3 \times 10^{15}\,\text{eV}$ could be caused by the onset of the reaction mentioned above.
In a similar way, also α-particles may interact with relic background neutrinos according to the following reactions

$$\begin{aligned} \alpha + \nu_e &\longrightarrow 3p + n + e^- \\ \alpha + \bar{\nu}_e &\longrightarrow p + 3n + e^+ \quad , \end{aligned} \tag{2.4}$$

which become energetically possible at energies which are larger than the threshold energy of Equation 2.3 by factors of 61 and 66, respectively. Thus, due to the fact that the α-particles will gradually disappear from the spectrum above the threshold energy, the model predicts another kink in the spectrum at an energy of around $E \approx 3 \times 10^{17}\,\text{eV}$, which is in good agreement with the position of the second knee feature.

The Ankle of the Cosmic Ray Spectrum

As for the knee, also the origin of the ankle feature in the all-particle spectrum at an energy of $E_{\text{ankle}} \approx 4 \times 10^{18}\,\text{eV}$ has not yet been unequivocally identified, but there are two prominent

1 Greek for 'many knees'.

theories attempting to explain the ankle itself and an accompanying dip in the cosmic ray spectrum at $E_{\mathrm{dip}} \approx 1 \times 10^{19}\,\mathrm{eV}$.

The ankle model assumes, in conflict with some theories explaining the origin of the knee, the transition from galactic to extragalactic sources to appear at energies from the second knee to the ankle. Although this model takes galactic sources, capable of accelerating particles to energies above the knee, into account, considerations about the confinement of particles in the Galaxy imply that particles at the highest energies must have en extragalactic origin. It is proposed that the hardening of the spectrum is caused by a harder, extragalactic component, dominated by protons, taking over a soft, galactic component with a mixed source composition similar to that of the low-energy cosmic rays [All07].

Another possible explanation of the ankle is given by the dip model, having the advantage of a lower transition energy and therefore being more compatible to individual knee models. Here, e^+e^- pair production by extragalactic protons interacting with photons from the cosmic microwave background (CMB) according to

$$p + \gamma_{\mathrm{CMB}} \longrightarrow p + e^+ + e^- \tag{2.5}$$

leads to the dip in the all-particle spectrum. In particular calculations, the transition energy coincides with the position of the second knee as it has been observed in air shower measurements. Overall, the shape of the dip, as it results from the simulations for a power-law generation spectrum with a spectral index of $\gamma_{\mathrm{g}} = 2.7$, could be well confirmed by measurements of the AGASA, HiRes, Yakutsk or Fly's Eye experiments [Ber06a]. However, since the dip model is based on a strongly proton-dominated primary flux, it seems to be in contradiction with recent measurements of the Pierre Auger Collaboration [Fac11], in which the composition of primary particles at high energies shows a tendency towards heavier nuclei [Alo12].

A detailed description of both scenarios as well as a comparison between the two models and their implications on the understanding of astrophysical analyses can be found in [All07, Don09, Alo12].

The GZK Suppression

Soon after the discovery of the 2.7 K CMB radiation in 1965 [Pen65] and its interpretation as a relic signature of the Big Bang in the same year [Dic65], a suppression of the primary cosmic ray flux at the highest energies due to interactions of high-energy protons (or other nuclei) with the relic CMB was predicted [Gre66, Zat66]. The GZK (Greisen-Zatsepin-Kuz'min) suppression (or GZK cutoff) caused by photo-pion production via an intermediate resonance ($\Delta(1232)^+$) according to

$$\begin{aligned} p + \gamma_{2.7\,\mathrm{K}} &\longrightarrow \Delta(1232)^+ \longrightarrow p + \pi^0 \\ p + \gamma_{2.7\,\mathrm{K}} &\longrightarrow \Delta(1232)^+ \longrightarrow n + \pi^+ \end{aligned} \tag{2.6}$$

is energetically possible above a threshold energy in the center-of-mass system of the primary proton and the CMB photon of $E_{\mathrm{GZK}} \approx 6 \times 10^{19}\,\mathrm{eV}$. The pions produced in these interactions will further decay via the standard pion channels ending up in high-energy photons, e^+e^--pairs and neutrinos. High-energy protons will continue to interact in pion production until their energy drops below the threshold energy for the processes mentioned. Given the mean interaction length for photo-pion production [Pro96] in the order of $\lambda_{p\pi} \approx 10\,\mathrm{pc}$ and assuming that the sources of the particles in question are extragalactic, the flux of primary cosmic rays at the highest energies above E_{GZK} is supposed to be highly suppressed.

In the last years a cut-off of the energy spectrum around the GZK energy has been confirmed through measurements by the Pierre Auger Observatory [Abr08b] as well as by the HiRes [Abb08a] and Fly's Eye [Bir94] experiments. However, the origin of this feature in the spectrum could not yet be properly identified, i.e. no high-energy GZK photons resulting from the decay of neutral pions (Equation 2.6) [Gel08] have been observed. Contrary to these results, the data taken by the AGASA collaboration show a significant number of air shower events with reconstructed primary energies above E_{GZK}, thus not being compatible with the theory of a flux suppression according to the GZK mechanism [Tak03]. However, the systematic uncertainties in the energy reconstruction of AGASA and the overall energy shift of the AGASA spectrum with respect to measurements of other experiments suggest that this could be predominantly due to experimental effects rather than to intrinsic features of the spectrum.

2.3 Cosmic Ray Air Showers

Primary cosmic rays that enter the atmosphere of the Earth can interact with air nuclei and produce secondary particles. Subsequent interactions of these secondary particles with other nuclei will initiate a cascade of particles. For primary energies above $E \gtrsim 10^{14}\,\mathrm{eV}$ [Gru12] the cascade forms an extensive air shower (EAS) and contains so many particles that they reach the surface of the Earth. Here the shower can be detected by ground-based experiments. Whereas a direct detection of the primary cosmic ray particles is still feasible at low energies up to $E \approx 10^{15}\,\mathrm{eV}$, an indirect measurement of the properties of the primary particle by detecting the corresponding air shower is the only practicable method resulting in sufficiently high statistics, since the flux of the incoming particles is heavily limited at extreme energies.

When a primary cosmic ray particle enters the atmosphere, the first interaction with a nucleus of the air will take place at high altitudes in the range of 15 km to 35 km above sea level [Gru12], depending on the inelastic cross section of the particular interaction process and thus, depending on energy, on the species of the primary particle and on the angle of incidence. The particles of the resulting air shower form a disc with a lateral spread of up to some kilometers which propagates through the atmosphere at approximately the speed of light c. Usually, the thickness of this shower front is in the order of a few meters close to the shower axis and increasing to $\approx 100\,\mathrm{m}$ towards its edge (Figure 2.6). However, the extent of the lateral and the longitudinal development of the air shower depends on the energy as well

as on the type of the primary particle.

The development of an air shower is determined by the processes of particle production as well as by the decays of secondary particles. Although the air shower comprises many different types of particles, its evolution can be subsumed in three basic categories (Figure 2.6), which will be discussed in the following.

2.3.1 The Electromagnetic Component

A primary cosmic ray photon may interact with an air nucleus and by this produce pairs of electrons and positrons (pair production) through

$$\gamma + N_{\text{air}} \longrightarrow e^+ + e^- + N_{\text{air}} \quad . \tag{2.7}$$

The electrons and positrons produced in these interactions may, in turn, emit photons in bremsstrahlung processes in the vicinity of the Coulomb field of another air nucleus through

$$e^\pm + N_{\text{air}} \longrightarrow e^\pm + \gamma + N_{\text{air}} \quad . \tag{2.8}$$

Alternating repetitions of both processes lead to the formation of an electromagnetic cascade. For the evolution of the cascade other electromagnetic interactions like photo-electric effect, Compton effect or ionization are of minor importance only. Since these processes only contribute at a later stage of the shower development, at atmospheric depths beyond the shower maximum, they are often disregarded when dealing with high energy phenomena [Gri10]. The electromagnetic cascade can also be initiated by a primary electron or by the decay of neutral pions, themselves produced in e.g. kaon decays or other hadronic interaction processes. Since a multitude of neutral pions is produced in the hadronic shower component (Section 2.3.2) at all stages of the shower development, the electromagnetic component rapidly becomes the most predominant one with respect to the overall number of air shower particles (Figure 2.7).

The basic properties of a photon-induced electromagnetic shower can be derived from a simple analytical model [Bha37], usually referred to as the Heitler model. The development of the electromagnetic cascade can be modeled in steps of particle splittings according to the processes given in Equations 2.7 and 2.8. The radiation length of electrons, defined as the characteristic amount of matter that a high-energy electron traverses until its energy is reduced by a factor of e due to bremsstrahlung processes, is $X_{\text{brems}} = 36.62\,\text{g/cm}^2$ [Beh12], independent of the type of the material. If, for reasons of simplicity, the radiation length of photons is set to $X_{\text{pair}} = X_{\text{brems}} = X_0$, splittings in which new particle generations will be produced occur in distinct intervals of $d = X_0 \ln 2$. Consequently the electromagnetic cascade will grow and after n splittings, corresponding to a distance of $x = nd$ traveled by the particles, the number of particles in the shower amounts to $N = 2^n = e^{x/X_0}$. The multiplication of particles abruptly ends as soon as the individual $e^\pm$ energy drops below a critical energy E_{crit} ($\approx 85\,\text{MeV}$ in air), for which collision energy losses (Compton scattering for γs and ionization for $e^\pm$) begin to dominate radiative losses. The shower reaches its maximum size N_{max} after k splitting lengths, when all particles have an energy of E_{crit}. In particular for a primary

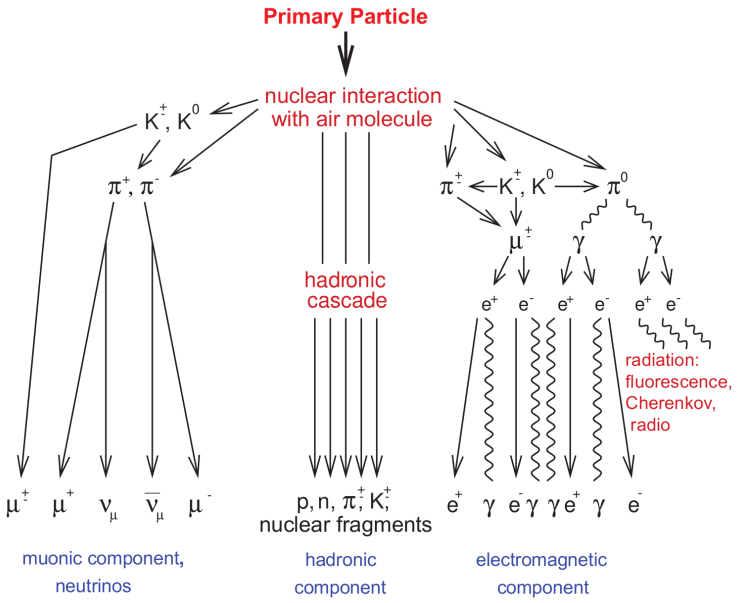

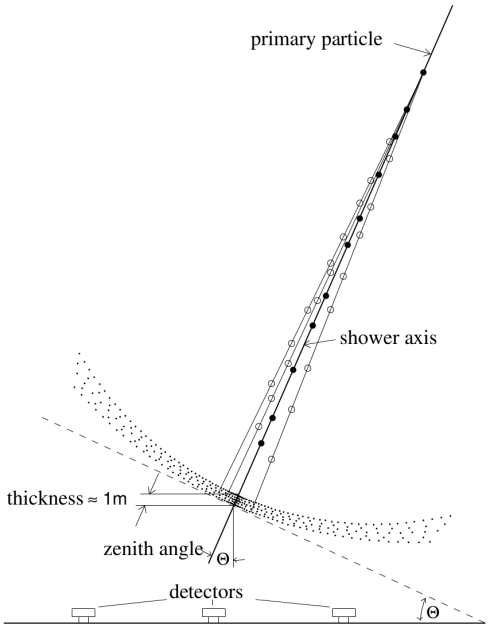

Figure 2.6: *Schematic view of an extensive air shower. In the upper panel, the particle interactions and decays contributing to the development of an air shower are depicted [Sch12]. Specifically, the muonic, the hadronic and the electromagnetic shower component are shown. The lower panel indicates the geometric properties of an air shower including the shower axis and the shower front [Alk75]. The dimensions are not to scale in both figures.*

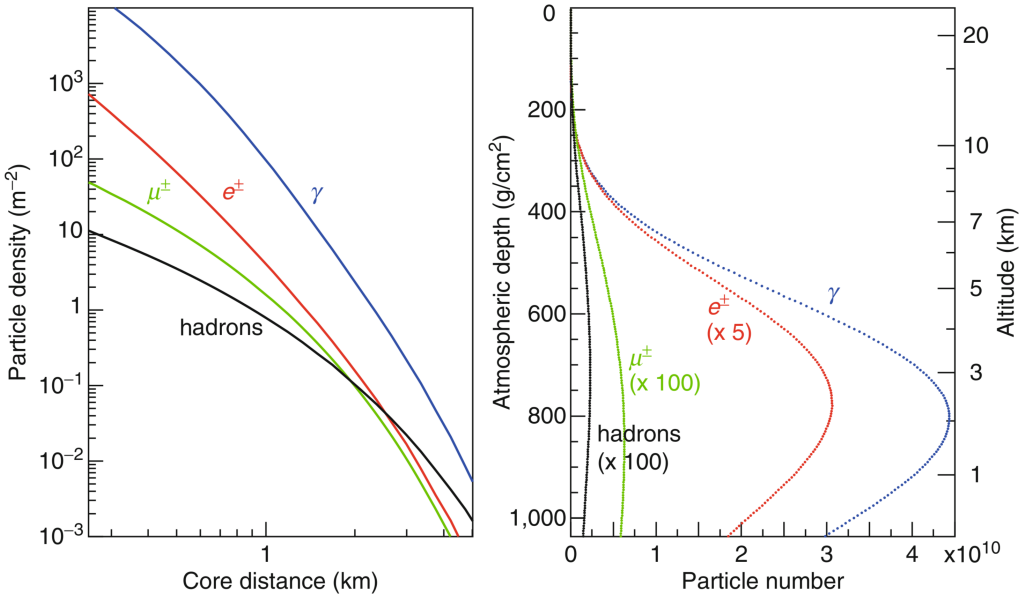

Figure 2.7: *Lateral (left) and longitudinal (right) shower profiles for vertical, proton-initiated showers with a primary energy of $E_0 = 10^{19}$ eV simulated with CORSIKA [Eng11]. The lateral distribution of the particles at ground is calculated for the depth of the Pierre Auger Observatory (870 g/cm^2). For the simulation, only photons and electrons/positrons as well as muons and hadrons with energies above 0.25 MeV and 0.1 GeV, respectively, have been taken into account.*

energy E_0 it is

$$N_{\max} = \frac{E_0}{E_{\text{crit}}} = 2^k \quad . \tag{2.9}$$

From this, the penetration depth $X_{\max}$ of the shower maximum can be calculated through

$$X_{\max} = kX_0 \ln 2 = X_0 \ln\left(\frac{E_0}{E_{\text{crit}}}\right) \quad . \tag{2.10}$$

This simple model quite well describes the properties of electromagnetic showers when compared to air shower simulations [Mat05]. It reproduces two important features, namely the maximum shower size $N_{\max}$ to be proportional to the primary energy E_0 and the depth of the shower maximum $X_{\max}$ to be proportional to $\ln E_0$. However, it appears to be incomplete in the sense that it does not account for second order effects like e.g. the reduction of the cross sections of pair production and bremsstrahlung due to the LPM effect (Landau–Pomeranchuk–Migdal) [Lan53, Mig56] at high energies. In addition, it overestimates the actual ratio of electrons to photons since it does not account for multiple photon generation in bremsstrahlung processes and, in turn, neglects the quick absorption of electrons.

The Heitler model only describes the shower development up to the shower maximum. A more complete approximation of the number of particles in electromagnetic showers covering

the full longitudinal development is given through [Gre56]:

$$N_{\mathrm{em}}\left(E_0,t\right) = \sqrt{\frac{1}{10\beta_0}} \times e^{(2-3\ln s)\frac{t}{2}} \quad , \tag{2.11}$$

with

$$t = \frac{x}{X_0} \quad , \quad \beta_0 = \ln\frac{E_0}{E_{\mathrm{crit}}} \quad \text{and} \quad s = \frac{3t}{t+2\beta_0} \quad . \tag{2.12}$$

The age parameter s describes the longitudinal shower development. A value of $s = 0$ represents the initiation of the shower, for $s = 1$ the cascade reaches its maximum size and for $s > 1$ the shower dies out, implying a decrease of the number of particles.

The lateral spread of the electromagnetic component, resulting from multiple Coulomb scattering, can be described with a lateral distribution function (LDF) which is commonly based on the Nishimura-Kamata-Greisen (NKG) approach [Kam58, Gre56]:

$$\rho_e(r,t) = N_e(t)\frac{C(s)}{r r_{\mathrm{M}}}\left(\frac{r}{r_{\mathrm{M}}}\right)^{s-1}\left(1+\frac{r}{r_{\mathrm{M}}}\right)^{s-4.5} \quad . \tag{2.13}$$

Here, ρ_e, which is the area density of charged particles, is given as a function of the distance r from the shower axis, the penetration depth $t = x/X_0$, the total number of charged particles at this depth $N_e(t)$ and the shower age parameter s. $C(s)$ is constant for a fixed shower age. The Molière radius r_{M} is a measure of the transverse dimension of the electromagnetic shower. It is related to the radiation length by $r_{\mathrm{M}} \approx 0.0265 X_0(Z+1.2)$, with Z being the atomic number of the material penetrated. The NKG approach only provides a valid description of the lateral spread for photon/electron-induced showers. Without an appropriate adjustment of its parameters it can only be used as an estimator of the lateral spread of hadron-initiated showers, in which the electromagnetic component is given by a superposition of multiple air showers resulting from neutral pion decays.

2.3.2 The Hadronic and Muonic Components

The description of interactions of protons or nuclei with atoms in the atmosphere is more complicated than the one discussed in the previous section. The first generation of secondary particles, produced in strong interactions between the primary cosmic ray and a nucleus of the air, mainly consists of hadrons, i.e. pions, kaons and nucleons. Provided that the interaction lengths of these secondary hadrons are shorter than the corresponding decay lengths and that their energies are sufficiently high, they will themselves interact again, thus forming the hadronic shower component. For a vertical particle incidence, the height of the Earth's atmosphere is approximately eleven times larger than the average interaction length of hadrons, therefore it is more than unlikely that the primary hadron itself will reach ground level. On average, high-energetic hadrons only carry rather low transverse momenta compared to their overall momentum. Thus, they are concentrated within a radius of a few tens of meters around the shower axis (Figure 2.7). Although hadrons only contribute a small fraction of the total number of particles in an air shower (approximately 1 %, cf. Figure 2.7), their impact on the overall shower development is essential since they can feed all other shower components.

The Heitler model for electromagnetic cascades can be adapted to describe the evolution of hadron induced showers [Mat05]. Again, the atmosphere is imagined to be divided into splitting lengths of fixed thickness $d = \lambda_\mathrm{I} \ln 2$, where λ_I is the interaction length of strongly interacting particles. For high-energy interactions in the order of 10-100 GeV λ_I can be approximated to be constant. For pions in air it is $\lambda_\mathrm{I} = 120\,\mathrm{g/cm^2}$ [Gai91]. Under the assumption that the interactions exclusively result in pions, which are the lightest mesons, hadrons will produce N_ch charged pions and $\frac{1}{2}N_\mathrm{ch}$ neutral pions. Due to the short lifetime of neutral pions ($\tau(\pi^0) \approx 8.5 \times 10^{-17}\,\mathrm{s}$, [Beh12]) compared to charged pions ($\tau(\pi^\pm) \approx 2.6 \times 10^{-8}\,\mathrm{s}$, [Beh12]), the π^0 will immediately decay to photons via

$$\pi^0 \longrightarrow \gamma\gamma \tag{2.14}$$

whereas the latter continue through another layer and interact again. These interactions are possible until the energy per particle of the $\pi^\pm$ falls below a critical energy E^π_crit where the pions have equal probability to interact or to decay via

$$\pi^+ \longrightarrow \mu^+ + \nu_\mu \qquad \text{and} \qquad \pi^- \longrightarrow \mu^- + \bar{\nu}_\mu \quad . \tag{2.15}$$

Through the processes given in Equations 2.14 and 2.15 the hadronic cascade feeds the electromagnetic and the muonic shower components, respectively. Since the lifetime of low energy muons ($\tau(\mu) \approx 2.2\,\mu\mathrm{s}$, [Beh12]) is almost unaffected by relativistic time dilatation, decays via

$$\mu^+ \longrightarrow e^+ + \bar{\nu}_\mu + \nu_e \qquad \text{and} \qquad \mu^- \longrightarrow e^- + \nu_\mu + \bar{\nu}_e \tag{2.16}$$

become probable. Therefore, also these muons will end up feeding the electromagnetic air shower component.

When considering a proton with an energy E_0 as primary particle, the number of charged pions produced after n splittings can be calculated through $N_\pi = (N_\mathrm{ch})^n$. Here, N_ch denotes the average multiplicity of charged pions produced in hadron interactions. Although the multiplicity changes as the shower develops, a constant value $N_\mathrm{ch} = 10$ for the pion energies considered is in good agreement with multiplicity measurements [Beh12]. For the energy being equally distributed between all particles, the charged pions carry an overall energy of $E_\mathrm{ch} = (2/3)^n\, E_0$. The energy of each charged pion after n splitting lengths is then given through

$$E_\pi = \frac{E_0}{\left(\frac{3}{2}N_\mathrm{ch}\right)^n} \quad . \tag{2.17}$$

The number of splittings n_c, after which E_π equals the critical energy E^π_crit, is

$$n_\mathrm{c} = \frac{\ln\left(\frac{E_0}{E^\pi_\mathrm{crit}}\right)}{\ln\left(\frac{3}{2}N_\mathrm{ch}\right)} \approx 0.85 \log_{10}\left(\frac{E_0}{E^\pi_\mathrm{crit}}\right) \quad . \tag{2.18}$$

Since the critical energy slowly decreases with increasing primary energy, e.g. for $N_\mathrm{ch} = 10$ it is $E^\pi_\mathrm{crit} \approx 30\,\mathrm{GeV}$ at $E_0 = 10^{14}\,\mathrm{eV}$ and $E^\pi_\mathrm{crit} \approx 10\,\mathrm{GeV}$ at $E_0 = 10^{17}\,\mathrm{eV}$ [Mat05], a critical

energy of pions in air of $E^{\pi}_{\mathrm{crit}} = 20\,\mathrm{GeV}$ is taken. Under the assumption that all pions decay into muons, the number of muons N_μ in the shower is given through $N_\mu = N_\pi = (N_{\mathrm{ch}})^{n_{\mathrm{c}}}$. Applying Equation 2.18 allows for a calculation of N_μ as a function of the energy of the primary particle:

$$N_\mu = (N_{\mathrm{ch}})^{n_{\mathrm{c}}} = \left(\frac{E_0}{E^{\pi}_{\mathrm{crit}}}\right)^{\beta} \quad \text{with} \quad \beta = \frac{\ln N_{\mathrm{ch}}}{\ln\left(\frac{3}{2}N_{\mathrm{ch}}\right)} \approx 0.85 \quad . \tag{2.19}$$

The principle of superposition allows for extending the derived model from protons to heavier nuclei. Here, the shower induced by a primary particle of mass A is considered to be constituted of A independent proton initiated showers, each with a primary energy of E_0/A. The resulting air shower can then be treated as the sum of these showers. Applying this method to Equation 2.19 yields for the number of muons in an air shower initiated by a nucleus of mass A

$$N_\mu = A \times \left(\frac{E_0}{A E^{\pi}_{\mathrm{crit}}}\right)^{\beta} = A^{1-\beta} \times \left(\frac{E_0}{E^{\pi}_{\mathrm{crit}}}\right)^{\beta} \quad . \tag{2.20}$$

This equation reveals two features of the number of muons in cosmic ray air showers:

1. N_μ increases with the primary energy slightly less than exactly linear and
2. N_μ increases with the mass of the primary particle $\propto A^{0.15}$ for $\beta = 0.85$.

The latter implies that the number of muons in an air shower induced by an iron primary ($A = 56$) amounts to about 1.8 times the number of muons of a proton initiated shower. Therefore, measuring the number of muons in an air shower is suitable to determine the type of the primary cosmic ray. This measurement will be performed by the AMIGA (Auger Muons and Infill for the Ground Array) enhancement of the Pierre Auger Observatory. A detailed description of the AMIGA enhancement as well as a comparison of different composition-sensitive air shower observables will be given in Chapter 4.

This basic model of hadronic cascades results in several predictions of air shower properties, which are in good agreement with air shower simulations [Mat05]. However, it neglects some of the fundamental aspects of hadronic processes like e.g. the inelasticity κ of the interactions. Whereas the model assumes the energy E in each interaction to be equally distributed between the resulting particles, usually an energy of $(1-\kappa)E$ is transferred to one leading particle and only a fraction κE of the energy is available for the production of new particles. Implications of this effect as well as a more detailed discussion of the model itself is given in [Hör07].

3 The Pierre Auger Observatory

Contents

3.1 The Surface Detector . . . 26
3.1.1 The Surface Detector Station . . . 27
3.1.2 Surface Detector Calibration . . . 28
3.1.3 The Trigger System of the Surface Detector . . . 30
3.2 The Fluorescence Detector . . . 33
3.2.1 The Trigger System of the Fluorescence Detector . . . 34
3.3 Enhancements of the Hybrid Detector . . . 35
3.3.1 AMIGA . . . 36
3.3.2 HEAT . . . 36
3.3.3 Radio Detection of Air Showers - AERA . . . 38
3.3.4 Microwave Detection of Air Showers . . . 40

The most apparent obstacle in studying the nature of ultra-high-energy cosmic rays is the very low flux of primary particles arriving at Earth. In lower energy regimes a direct measurement of primary cosmic rays is still possible and medium-sized detector arrays at ground level, which cover areas of few square kilometers, are suitable for measuring air showers up to primary energies of some 10^{17} eV. Acquiring a considerable amount of data from measurements in the 10^{18} eV regime and beyond, where the flux of primary cosmic rays drops to values in the order of a few particles per square kilometer and century, only becomes feasible when the low event rates are compensated by substantially extending the active detection area.

The Pierre Auger Observatory was planned to consist of two independent detector sites at the northern and southern hemisphere covering an overall area for the joint operation of more than 20,000 km^2. This would have allowed for achieving an almost uniform acceptance for cosmic rays from all parts of the sky [Pac97]. The southern observatory site has been completely deployed whereas the construction of the northern part has been ceased due to funding reasons. Therefore, the term 'Pierre Auger Observatory' in the following will only refer to the southern detector site, unless otherwise stated.

The Pierre Auger Observatory (Figure 3.1) is located in the Pampa Amarilla, close to the city of Malargüe in the province of Mendoza, Argentina (35 ° S, 69 ° W). It combines two complementary detectors for the observation of extended air showers (EAS), namely the surface detector and the fluorescence detector, to a hybrid approach. Whereas the surface detector mainly records the lateral distribution of an EAS on ground, the fluorescence detector

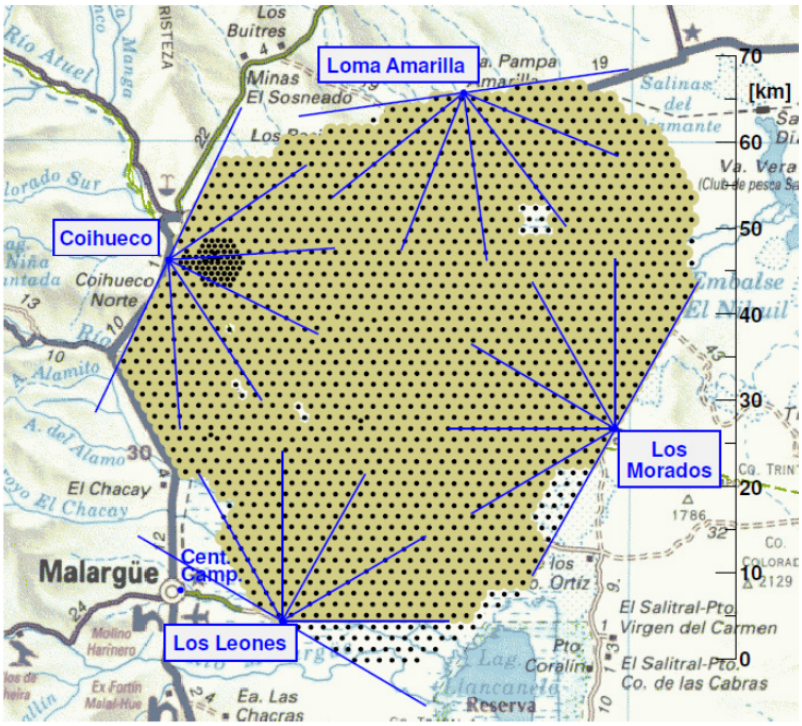

Figure 3.1: *Schematic view of the Pierre Auger Observatory [Oeh13]. The geographical map shows the positions of the individual detector stations of the surface detector (SD) as black dots against a yellow shaded background. The other black dots represent empty positions. The positions of the four buildings of the fluorescence detector (FD) 'Coihueco', 'Loma Amarilla', 'Los Morados' and 'Los Leones', each one located at the borders of the array, are given by the blue dots. Their field of view is indicated with blue lines. The infill array (Section 3.3.1), defined by an increase of the density of SD stations, is found in the western part of the standard array close to the FD station 'Coihueco'.*

is capable of measuring the energy deposit in the atmosphere.
In the following, both detectors will be presented in more detail. The main focus lies on the surface detector, which will be the source of data used in the analyses presented in Chapter 6. As a last point, further detectors designed to enhance and/or complement the existing hybrid detector will be briefly described.

3.1 The Surface Detector

The lateral extent of air showers can be in the order of several kilometers, mainly depending on the energy of the primary particle. The surface detector (SD) measures the footprint of the shower at ground level. By sampling the shower front at several discrete positions it records a snapshot of the amount of particles reaching ground and of their arrival times.

The SD consists of about 1,600 independent detector stations aligned in a hexagonal grid with a spacing of 1.5 km, covering an overall area of 3,000 km^2 (Figure 3.1). The altitudes of

the stations range from 1,300 m up to 1,500 m [Blü10]. Since the SD allows for measurements with a duty cycle of almost 100 % [Abr10b], it records the largest fraction of data acquired by the Pierre Auger Observatory. The SD reaches full trigger efficiency for energies of the primary particles above 3×10^{18} eV for the full range of zenith angles. For lower energies between 0.7×10^{18} eV through 1×10^{18} eV, the trigger efficiency drops to about 50 %, depending on the type of the primary particle and the zenith angle of its incidence [Blü10]. Close to the fluorescence detector station 'Coihueco' 85 SD stations were additionally deployed, forming a denser array with station distances of 750 m and 433 m. These stations constitute the infill array of the AMIGA enhancement (Auger Muons and Infill for the Ground Array) [Etc10], which will be described in more detail in Section 3.3.

3.1.1 The Surface Detector Station

Each of the 1,600 SD stations (Figure 3.2) consists of a polyethylene tank containing 12 m^3 of purified water. The water is used as the detection medium for relativistically moving charged air shower particles exploiting the Cherenkov effect [Che34]. Three photomultiplier tubes (PMTs), each one with a diameter of 9 inch [All08], are installed on the top cover of the tank, facing downwards. They are optically coupled to the water to detect the photons emitted during the passage of the charged particles. Since mainly downgoing particles are expected, the Cherenkov photons need to be reflected from the bottom and the walls of the tank before they can be detected by the PMTs. Therefore, the water is filled into a reflecting liner, which provides uniform reflectivity at wavelengths in the ultraviolet (UV) regime. The PMTs reach an amplification of the signals in the order of 10^5. In addition to the anode signals, the PMTs provide the signals of the last dynode. This allows for measurements with two different amplifications, thus enabling saturated signals at the anode to be recovered. The three high-gain and the three low-gain signals are processed by the data acquisition (DAQ) system of the local station electronics, which consists of the Front-End Board (FEB) [Sza09] and the Unified Board (UB). Using FADCs (flash analog-to-digital converters), the signals are digitized at a frequency of 40 MHz resulting in a timing resolution of 25 ns per FADC bin. Each bin contains 1,024 channels for resolving the digitized amplitude of the signals. A pedestal of 50 channels is added to the signal to measure possible fluctuation of the baseline. The FPGA-based (field programmable gate array) readout electronics includes the first triggers on local station level (Section 3.1.3). In case of a trigger generation, the data of all six FADC traces covering a time window of 19.2 µs is locally stored together with the timestamp of the trigger. The system allows for storing the event data for about ten seconds. During this time, the event information is sent to the central data acquisition system (CDAS) on request.

Each SD station is an autonomous system, i.e. it is battery-powered, with the batteries being charged by a solar panel system, that is mounted on top of the SD station. The total power consumption of all systems of an SD station, including the PMTs and the electronics package, does not exceed 10 W on average [All08]. Recorded event data is transferred to CDAS via a wireless communication network. The timing information gained by the individual stations as well as the synchronization between the stations and CDAS are based on the Global Positioning System (GPS). Each station automatically records monitoring data of e.g.

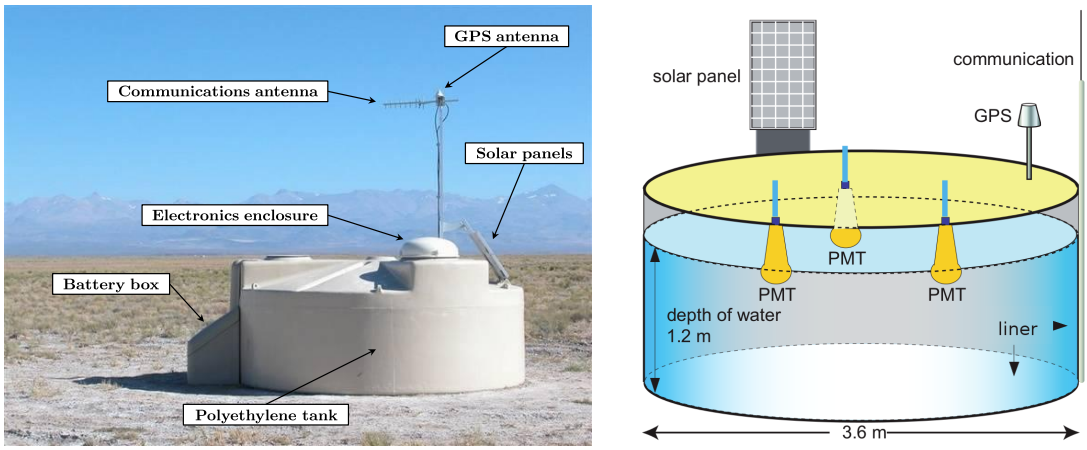

(a) Image of a surface detector station.

(b) Schematic layout of a surface detector station.

Figure 3.2: *One station of the surface detector (SD). The left panel shows an image with explanatory labels applied (adapted from [All08]). In the right panel, the schematic layout of a water Cherenkov station of the SD is depicted (adapted from [Dem09]). A detailed description is given in the text.*

the battery, PMT and supply voltages and the water temperature, which are sent to CDAS every six minutes [Ber03].

3.1.2 Surface Detector Calibration

Both, the amplitudes of the recorded FADC traces I as well as their integrals over time Q are proportional to the amount of Cherenkov light, that is detected by the PMTs. Whereas Q is equivalent to the collected charge at the anode of a single PMT, I is proportional to the peak current at the anode. However, the strengths of these signals do not only depend on the properties of the particles traversing the water volume but also on the characteristics of the individual stations. This involves e.g. the reflectivity of the liner, the gain of the PMTs or their optical coupling to the water. Therefore, the average values of Q and I resulting from identical particles varies from station to station and from one PMT to another. Since the trigger probability of the individual SD stations and the recorded data should not depend on these characteristics, each detector is constantly calibrated in two ways. The online calibration is continuously performed by the single SD station itself. The offline calibration is more precise but computationally too expensive to be performed by the local station electronics and is therefore carried out by CDAS. Both methods are described in detail in [Ber06b] and will briefly be summarized in the following.

The strengths of signals measured with a station of the SD is expressed in terms of a physical measure, referred to as a vertical equivalent muon (VEM). One VEM corresponds to the average charge measured by the station for a vertical and centrally through-going muon. The online calibration exploits the fact, that above a certain threshold the signal

rate in each PMT of the SD station is dominated by signals originating from the background muon flux over other sources of noise. The calibration is accomplished by stabilizing the trigger rate due to atmospheric low-energy muons to about 100 Hz. By adjusting the threshold of a calibration trigger accordingly every minute [Ber06b], an estimate for the VEM signal $I^{\text{est}}_{\text{VEM}}$ ($Q^{\text{est}}_{\text{VEM}}$) can be derived and a uniform performance of the SD trigger is achieved. The actual calibration procedure is more complex but follows this principle. In addition, an online calibration is performed once during the startup procedure of the individual SD station to set up the supply voltages for each of the three PMTs in the SD station.

For the offline calibration the amplitude I and the pulse charge Q of each signal trace recorded during the operation of the SD station are calculated and the information is filled into histograms. Since the track length of a vertically through-going muon does not depend on the impact point on the surface of the water tank, the VEM signal appears more frequent than other signals. This results in a pronounced peak in both histograms, which is closely related to the signal strength of one VEM (Figure 3.3). After applying a correction factor, that has been determined from hodoscope measurements for one station [Ber06b], to each of the two distributions, the average values $Q^{\text{peak}}_{\text{VEM}}$ and $I^{\text{peak}}_{\text{VEM}}$ are derived. The precision of the offline resolution is in the order of 2 % [Abr10b], which is much better than the typical statistical resolution of the measured signals.

The signal strength S used in the SD event reconstruction is finally calculated using the calibrated pulse charge, i.e. $S = Q_{\text{meas}}/Q^{\text{peak}}_{\text{VEM}}$.

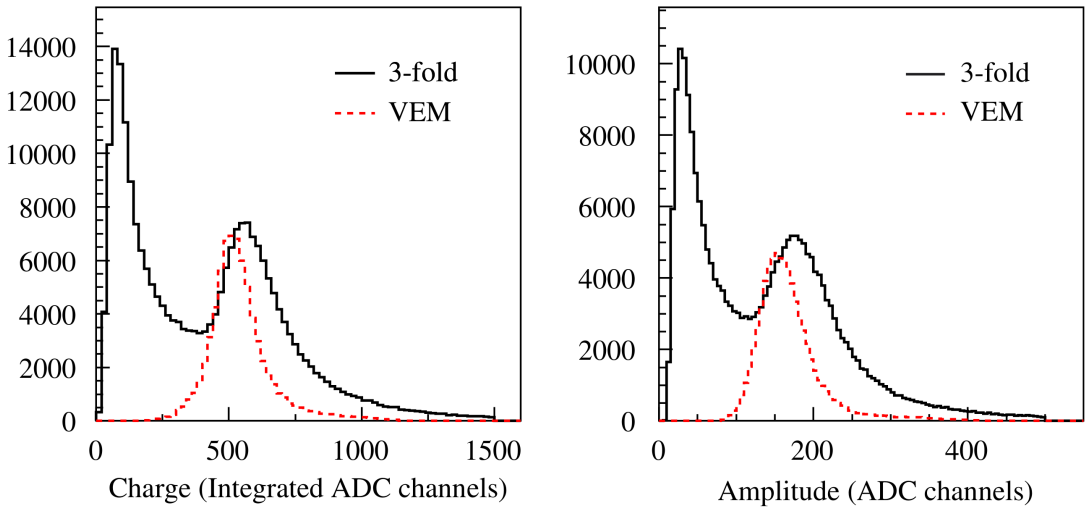

Figure 3.3: *Charge (left panel) and pulse height (right panel) histograms from an SD station [Ber06b], triggered by a three-fold coincidence of all three PMTs of the station. The signals of the three PMTs are summed up. The first peak in each of the two black histograms is caused by low energy particles, the second peak is due to vertically through-going muons. The red dashed histograms result from reference measurements with an external muon hodoscope connected.*

3.1.3 The Trigger System of the Surface Detector

The hierarchy of the SD trigger system can be subdivided into two parts: the local trigger system on station level (Figure 3.4a) and the trigger decisions that are taken on array level (Figure 3.4b). Both systems will be discussed in the following, a detailed description is given in [Abr10b].

SD Trigger on Local Station Level

The first two trigger levels (T1 and T2) are formed at each individual SD station. Based on the T1 trigger signal, the DAQ is started and the recorded data is stored in the local memory. The T1 actually comprises two different, but complementary, trigger modes. The first mode is a pure threshold trigger (T1-TH), which requires the coincidence of all three PMTs of the local station and each of them measuring a signal amplitude above $1.75\, I_{\mathrm{VEM}}^{\mathrm{peak}}$. The T1-TH is mainly sensitive to large signals that are not necessarily spread in time. Therefore, it is particularly efficient for detecting very inclined air showers, for which the electromagnetic component has mainly died out while propagating through the atmosphere, whereas the muonic component still reaches ground level. This trigger mode reduces the trigger rate to approximately 100 Hz, corresponding to about 3 % of the total rate of atmospheric muons. The second T1 mode is adopted to be sensitive to air showers that are less inclined or to showers with the shower core falling close to the local station. In these cases, the dispersion of the electromagnetic air shower component causes the signals recorded by the SD station to be spread in time [Lin62]. Since these signals do not necessarily exhibit a pronounced peak value, this variant of the T1 is designed as a time-over-threshold trigger (T1-ToT). It requires at least 13 bins (i.e. > 325 ns) in a sliding window of 120 FADC bins (i.e. 3 µs) to show a signal above $0.2\, I_{\mathrm{VEM}}^{\mathrm{peak}}$ in coincidence in at least two out of the three PMTs of the local station. The trigger rate of the T1-ToT is in the order of 2 Hz. Since the signal length of a single muon recorded with the SD station is in the order of 150 ns, this trigger is extremely efficient at eliminating the random muonic background.

In order to further reduce the number of events that have to be transmitted via the wireless communication system, another trigger level (T2) refines the trigger conditions of the T1. Whereas events fulfilling the T1-ToT condition are always promoted to the T2 level (T2-ToT), events triggered by the T1-TH have to pass another, higher, threshold trigger. The T2-TH requires the recorded data to exhibit a three-fold coincidence among the three PMTs with each of the signals exceeding a threshold of $3.2\, I_{\mathrm{VEM}}^{\mathrm{peak}}$. Overall, the rate of T2 triggers is around 20 Hz. Events that fulfill any of the T2 trigger conditions are automatically reported to CDAS, together with the local station identifier (LSID) and the timestamp of the trigger.

SD Trigger on Array Level

CDAS continuously monitors the incoming T2 messages searching for compact spatial and temporal patterns. Once this third level trigger (T3), also often referred to as event level trigger, is formed, all FADC traces of the SD stations, that passed the T2 level, are requested and sent to CDAS. In addition, data recorded by stations, that fulfilled the T1 but not the T2 criteria, are read out, provided that the timestamp information of the trigger matches the

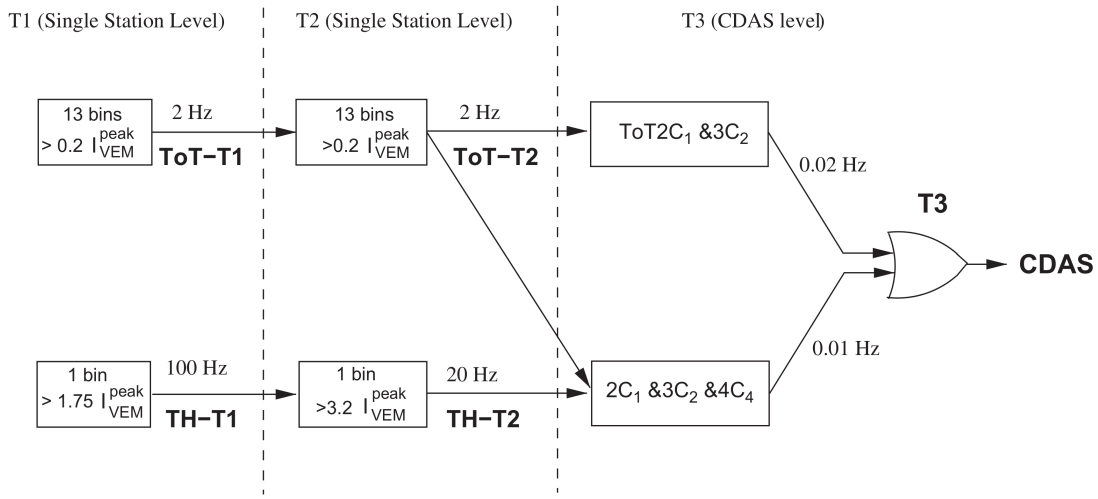

(a) Trigger system hierarchy of the SD.

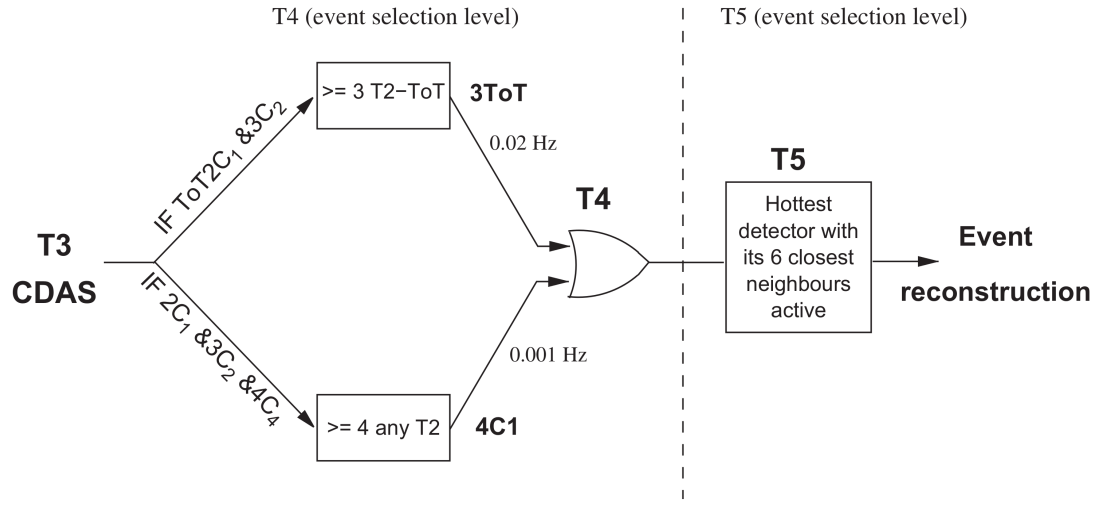

(b) Event selection hierarchy of the SD.

Figure 3.4: *Schematic view of the hierarchy of the SD trigger and event selection system [Abr10b]. The upper panel depicts the trigger conditions of the T1 and T2 trigger, that are formed on local station level, as well as of the T3 trigger, that is formed on array level. The lower panel shows the event selection based on decisions taken on array level (T4 and T5 trigger).*

T3 timestamp within a time interval of 30 µs.

Two different trigger modes are realized on the T3 level, both illustrated in Figure 3.5. The first mode requires at least three SD stations fulfilling the T2-ToT condition in a compact spatial configuration, i.e. one of the detectors must have one triggered station among its closest neighbors (first crown, C_1) and one in the second crown (C_2). With C_n indicating the n-th set of neighboring stations, this trigger is referred to as ToT2C_1&3C_2 (left panel of Figure 3.5). Once the spatial pattern is verified, additional timing criteria are applied: with respect to the first station, all other stations must be triggered within $(6 + 5C_n)$ µs. Since this T3 mode is purely based on the ToT conditions of lower trigger levels, it results in a very efficient background suppression: about 90 % of all triggered events are real showers. It is mostly efficient for showers with zenith angles below 60 °. With the full regular array in operation, the rate of events triggered in this T3 mode is around 1,600 per day.

The second, more permissive, T3 mode requires a four-fold coincidence of SD stations in a less compact spatial configuration, triggered by any of the two T2 trigger modes. Here, one of the detectors must be among the closest neighbors of a selected station (C_1), one must be in the second crown (C_2) and the third one can be as far as in the fourth crown (C_4). Finally, identical timing criteria as for the ToT2C_1&3C_2 are applied. This trigger is referred to as 2C_1&3C_2&4C_4 (right panel of Figure 3.5). It is mainly effective for the detection of horizontal, dominantly muonic air showers, which exhibit narrow time spreads in the PMT signals but that come with a large footprint on ground. Taking the full array into account, the rate of events selected in this trigger mode is about 1,200 per day, out of which approximately 10 % are real air showers.

SD Event Selection on Array Level

All events passing the T3 trigger level are written into a data storage system. Therefore, the third level trigger is the last real trigger stage of the SD. However, event candidates are further processed offline and have to pass two more selection levels, which are often referred to as the physics trigger (T4) and the quality trigger (or fiducial trigger, T5), even though they are only applied to data that has already been recorded.

The T4 level is needed to select real showers from the set of recorded T3 data. Again, two different criteria are defined. The first T4 criterion, referred to as 3ToT, requires three T2-ToT triggered detectors in a triangular pattern of neighboring stations. The trigger times of the signals recorded by these stations have to fit a model of a plane shower front moving at the speed of light c. This way, events with zenith angles below 60 ° are selected with an efficiency of more than 98 %, the number of chance coincidences passing this trigger level is smaller than one event per day.
The second T4 criterion, referred to as 4C1, requires 4 nearby stations fulfilling any of the two T2 conditions. Again, the timing of these stations has to fit a plane shower front moving at the speed of light. This trigger aims at selecting inclined showers with zenith angles above 60 °, its efficiency reaches a level of almost 100 %.

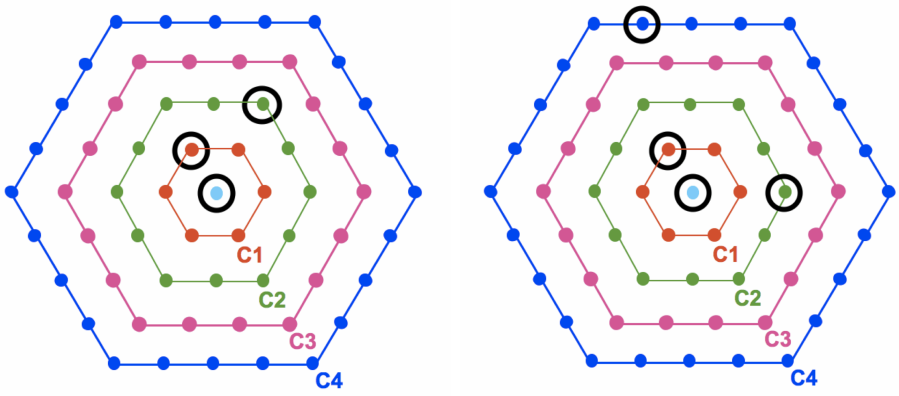

Figure 3.5: *T3 trigger configurations [Abr10b]. The right panel depicts the three-fold trigger mode (ToT2C_1&3C_2), the four-fold mode (2C_1&3C_2&4C_4) is shown in the right panel. C_n denotes the n-th set of neighbors.*

In addition, the T4 level is designed not only to reject accidental events but also to identify accidental SD stations in real air shower events and to reject them from any further event reconstruction. To this end, an initial triangle of non-aligned stations is chosen as a seed to estimate the arrival direction of the air shower. Subsequently, all other stations are examined by comparing their timing information with a model of a plane shower front moving at the speed of light. SD stations, which do not fit the expected timing within an interval of $[-2\,\mu s; +1\,\mu s]$, are marked as 'out of time'. In addition, stations that have no triggered neighbor within a distance of 3 km are marked as 'lonely stations'. Both classes of detector stations are not taken into account for the event reconstruction. After the T4 level, 99.9 % of the selected events also pass the full reconstruction procedure.

The T5 criterion is fulfilled if the station with the highest signal is surrounded by six active stations, i.e. it must be surrounded by a working hexagon of SD stations. This ensures that only events which are well contained inside the array are reconstructed. The processing of events in which parts of the air shower data may be missing can lead to a wrong reconstruction of the shower core and by this to an incorrect estimate of the primary energy. The T5 level mainly affects events with the shower core falling close to the borders of the SD array or close to a non-working detector station. By applying the T5 condition, the maximum statistical uncertainty of the energy estimator $S(1000)$ (Section 6.6.2) can be reduced to approximately 3 % [Ghi05].

3.2 The Fluorescence Detector

As described in Section 2.3, a primary cosmic ray can interact with nuclei of the air in the uppermost layers of the Earth's atmosphere and, thus, initiate a cascade of secondary particles. The arising electromagnetic air shower component (Section 2.3.1) is capable of exciting the nitrogen molecules of the air. The deexcitation of these excited states, which occurs after approximately 10 ns, leads to the isotropic emission of fluorescence light in the

UV regime. The number of photons emitted in these interactions is proportional to the energy loss of the shower particles. However, the amount of photons produced per unit of deposited energy, usually referred to as fluorescence yield, depends on the properties of the atmosphere, i.e. on the pressure, the temperature and the humidity of the air [Ave07a, Ave08]. Under standard conditions (20 °C, 1,013 hPa, dry air), approximately five photons with wavelengths between 300 nm and 400 nm are emitted per MeV of deposited energy [Nag04]. Since the electromagnetic component carries about 90 % of the energy of the primary cosmic ray, the detection of the fluorescence light allows for a calorimetric energy measurement and for the reconstruction of the longitudinal shower profile dE/dX. Here, X denotes the atmospheric depth.

The fluorescence detector (FD) of the Pierre Auger Observatory consists of four separate telescope buildings ('Coihueco', 'Loma Amarilla', 'Los Morados' and 'Los Leones', Figure 3.6a) arranged at the perimeter of the SD array (Figure 3.1), each hosting six Schmidt telescopes [Sch38]. These telescopes cover a field of view of approximately $30\,^\circ \times 30\,^\circ$ each, adding up to about $180\,^\circ$ in azimuth and $30\,^\circ$ in elevation, starting at the horizon, for a single FD building. In this way, the four FD sites allow for the observation of air showers in the atmosphere above the SD array.

The experimental setup of one telescope is shown in Figure 3.6b. The optical system consists of a diaphragm with an aperture of 3.8 m^2 and a spherical mirror with a radius of curvature of 3.4 m and a size of approximately 13 m^2. 440 hexagonal PMTs [17] arranged in a matrix of 22 rows and 20 columns, each one covering a field of view of 1.5 °, constitute the camera, which is installed in the focal plane of the mirror. In order to improve the signal-to-noise ratio an UV transmitting filter is included into the aperture, which is transparent for photons with wavelength between 290 nm and 410 nm, covering almost all of the nitrogen fluorescence spectrum. An additional ring of corrector lenses is used to reduce aberrations in the optical system and increases the collection area by almost a factor of two. The signals of each PMT, after being filtered and amplified, are digitized using analog-to-digital converter (ADCs) with a frequency of 10 MHz and a dynamic range of 12 bits. The resulting signal traces are stored in a circular buffer, taking into account a time window of a length of 100 µs. A more detailed description of the FD system is given in [Abr10a].

The FD is in operation if the illuminated fraction of the moon drops below 60 %, which is, on average, the case in 16 nights per month. Data taking starts with the onset of the astronomical dust and it ends with the onset of the astronomical dawn, yielding an average time of ten hours of operation per night. Individual telescopes become inactive, i.e. the corresponding telescope bays are closed, if the data taking is affected by e.g. direct moon light or by too much reflected moon light from clouds. Overall, the FD reaches a duty cycle of about 13 %.

3.2.1 The Trigger System of the Fluorescence Detector

A detailed description of the full trigger system is given in [Abr10a], it will briefly be summarized in the following.

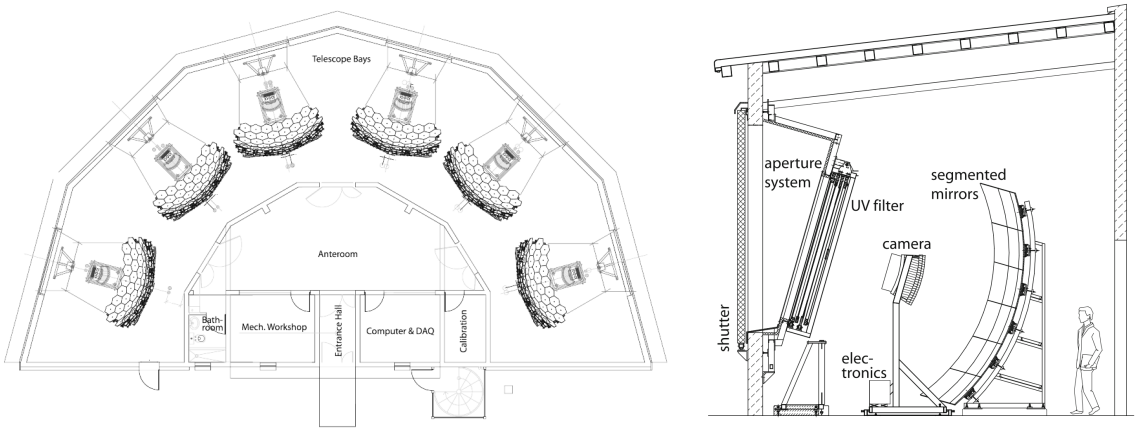

(a) *FD building.* ***(b)*** *FD telescope bay.*

Figure 3.6: *Schematic view of a fluorescence telescope [Abr10a]. The left panel shows an FD building hosting the six telescope bays. One of the telescopes is depicted in the right panel with explanatory labels attached. Each telescope covers a field of view of approximately* $30\,^\circ \times 30\,^\circ$*, adding up to about* $180\,^\circ \times 30\,^\circ$ *in total.*

The hierarchy of the FD trigger system consists of three levels. The first level trigger (FLT) operates on individual camera pixels of each telescope and is realized as a simple threshold trigger. It is implemented into the firmware of an FPGA of the readout electronics. For the trigger generation the integrated PMT signals of a sliding window with a length of 1.6 µs are compared to a given threshold value. The threshold itself is not fixed but constantly adjusted to retain a constant trigger rate of 100 Hz in each pixel. The second level trigger (SLT), also implemented into the logic of an FPGA, searches for spatial patterns of FLT-triggered pixels and in particular for five adjacent pixels that roughly form a line on the camera. Based on the SLT the event is considered a real shower and a GPS timestamp is attached to the event. The third level trigger (TLT) is implemented in software. Here, the time structures in the events are taken into account. The TLT is supposed to suppress events resulting from muon impacts on the camera or lightning events. The latter can cause hundreds of pixels to be triggered in bursts of about 100 Hz, causing a significant dead time of the detector. The TLT algorithms are capable of rejecting 99 % of the lightning events while removing less than 1 % of real air shower events [Sch09].
A readout of the SD array can also be initiated upon the acquisition of FD event data. In these cases, a TLT reported to CDAS will act as a T3 trigger on the SD array.

3.3 Enhancements of the Hybrid Detector

The Pierre Auger Observatory has been designed to measure EAS in the energy range from 10^{18} eV to 10^{20} eV. With decreasing energy of the primary particles, the resulting air showers develop higher in the atmosphere and exhibit a smaller lateral spread. In order to be capable of covering the energy regime down to 10^{17} eV, two low-energy enhancements of the existing

hybrid detector, namely HEAT (High Elevation Auger Telescopes) and AMIGA (Auger Muons and Infill for the Ground Array), have been built. Both enhancements aim at an improvement of the data quality with respect to energy and compositions sensitive analyses at low energies. Various theoretical models predict the transition from galactic to extragalactic cosmic ray sources to occur at energies between 10^{17} eV and 4×10^{18} eV (Section 2.2.5). Thus, these enhancements should enable a discrimination between the different scenarios or might even allow for exclusions of distinct models. In addition, by expanding the energy range below 10^{18} eV a direct comparison of the experimental results with other experiments, e.g. KASCADE-Grande (Karlsruhe Shower Core and Array Detector Grande), becomes feasible.

The area covered by these enhancements, close to the FD station 'Coihueco', is an ideal test bed for new air shower detectors exploiting other detection techniques, which complement the existing detectors. Whereas the AERA detector (Auger Engineering Radio Array) is designed to study the coherent radio emission of air showers, four other experiments, namely AMBER (Air-shower Microwave Bremsstrahlung Experimental Radiometer), EASIER (Extensive Air Shower Identification using Electron Radiometer), FDWave and MIDAS (Microwave Detection of Air Showers), aim at air shower measurements in the microwave regime.
In the following, these enhancements will be outlined.

3.3.1 AMIGA

The AMIGA experiment comprises two enhancements of the Pierre Auger Observatory, the infill array and the muon detector (MD). The infill array consists of 85 additional SD stations on dense, triangular grids with spacings of 750 m and 433 m [Pla09]. The stations are bound by two hexagons covering areas of 32.5 km^2 and 5.9 km^2 corresponding to the 750 m and 433 m array, respectively [Sup08]. The installation of the infill was started in 2008 after the completion of the original detectors. As of September 2011, the 61 infill stations belonging to the 750 m grid have been deployed. The installation of the 24 detector stations of the smaller grid has not yet been started (Figure 3.7).

The trigger system of the infill array is adopted from the one of the regular SD array [Mar11]. The efficiency of the T3-ToT trigger (Section 3.1.3) for both, the infill and the regular array, is shown in Figure 3.8a for comparison. For this type of trigger, the full efficiency of the 750 m infill has been determined to be approximately 3×10^{17} eV for showers with $\theta < 55\,^\circ$, almost independent of the type of the primary particle. Thus, the 750 m infill lowers the threshold for full efficiency by one decade when compared to the regular 1,500 m array. The angular resolution of the infill reconstruction is found to be in the order of $1\,^\circ$, depending on the number of SD stations participating in the air shower event (Figure 3.8b).

In Chapter 4, the MD of the AMIGA enhancement will be described in detail.

3.3.2 HEAT

Air showers with primary energies below 10^{18} eV emit less fluorescence light compared to showers of higher energies. Therefore, only air showers, that evolve close to the FD sites,

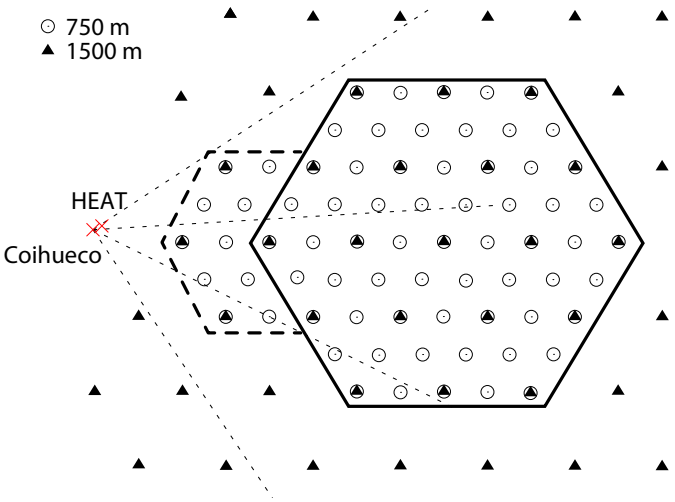

Figure 3.7: *Layout of the infill array (adapted from [Rav13]). SD stations of the 750 m infill are drawn as circles, stations of the regular array are represented by filled triangles. Some of the detector stations belong to both arrays. The hexagon of the infill array is surrounded by the bold solid line, the HEATLet sub-array (Section 3.3.2) is indicated by the bold dashed line. The azimuthal field of view of three FD telescopes, overlooking the infill area, is shown by the dashed lines.*

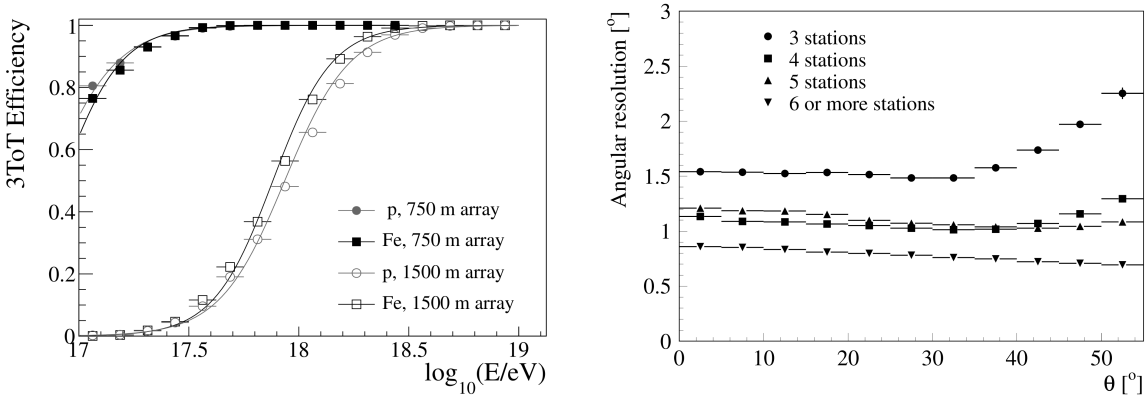

(a) *Infill trigger efficiency.* ***(b)*** *Infill angular resolution.*

Figure 3.8: *Properties of the infill array. The simulated T3-ToT trigger efficiency of the 750 m infill is shown in the left panel for proton and iron primaries in comparison to the regular SD array [Rav13]. For this trigger, the infill array reaches full trigger efficiency at approximately 3×10^{17} eV. The left panel depicts the angular resolution of the infill array, dependent on the number of triggered stations and the zenith angle [Mar11].*

can be observed by the telescopes. In addition, low energy air showers develop earlier in the atmosphere. In particular, the position of the shower maximum $X_{\max}$ may be outside the field of view of the standard FD. In this case, $X_{\max}$ can only be determined with lower accuracy from the fit of the longitudinal shower profile. As a consequence, showers detected by the FD will only be taken into account for physics analyses if the reconstructed $X_{\max}$ is within the field of view of the telescopes. In order to be able to detect low energy showers close to the FD, the telescopes must provide a field of view which extends towards higher altitudes.

In 2009, three telescopes of the HEAT enhancement were added to the FD at the 'Coihueco' site, overlooking the SD stations of the infill array. These telescopes are constructed similar to the original FD design, except that they are installed in individual shelters, which can be tilted upwards by an angle of 30 °. Each telescope shelter is made out of lightweight insulated walls coupled to a steel structure. It rests on a strong steel frame filled with concrete [Kle09]. In tilted mode HEAT provides a field of view ranging from 30 ° to 60 ° in elevation. For installation and calibration, the telescopes can also be operated in untilted mode. Inclination and distance sensors inside the telescope shelters allow for a monitoring of the camera position in the optical aperture, guaranteeing the mechanical stability of the system. Showers that develop close to the telescopes will appear in the field of view of HEAT for a shorter time. Therefore, the DAQ electronics of HEAT uses an increased sampling rate of 20 MHz compared to 10 MHz of the standard FD. A detailed description of the HEAT enhancement is given in [Kle09].

A combined DAQ allows for the stereo detection of air showers with the standard cameras of 'Coihueco' and those of HEAT. In Figure 3.9a, a schematic illustration of a shower detection with two HEAT telescopes in combination with one standard FD telescope is depicted. A recorded air shower event with a similar geometry is shown in Figure 3.9b. The position of the shower maximum $X_{\max}$ is in the field of view of one HEAT telescope. Without the HEAT measurement, this shower would be rejected from physics analyses.

In order to complement the HEAT measurement with information from the infill array for showers that evolve very close to the telescopes, the infill has been extended towards the 'Coihueco' site with the deployment of additional SD stations. The sub-array consisting of these stations is referred to as the HEATLet (Figure 3.7).

3.3.3 Radio Detection of Air Showers - AERA

Air showers, propagating through the atmosphere of the Earth, emit radiation at radio frequencies. Commonly, this is interpreted as geosynchrotron radiation of relativistic secondary electrons and positrons deflected in the geomagnetic field [Fal03]. For a physical thickness of the shower front in the order of a few meters, this radiation turns out to be coherent in a frequency range from approximately 1 MHz through 150 MHz, leading to strong radio pulses with pulse lengths in the order of some tens of nanoseconds [Hue05]. A second approach explaining the radio emission of air showers is based on the Askaryan effect [Ask65], which considers a coherent superposition of radio waves from a negative charge excess of the air shower. This net charge then leads to an emission of Cherenkov radiation at radio frequencies.

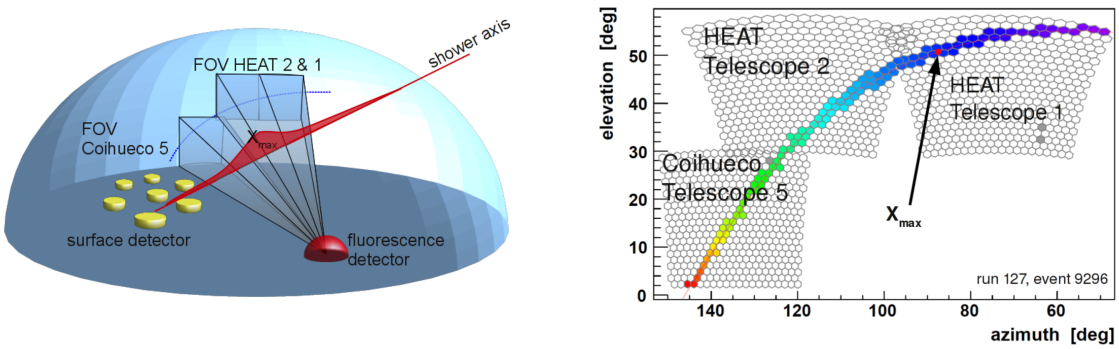

(a) Schematic illustration of a shower detection.

(b) Event display of an combined FD event.

Figure 3.9: *Air shower measurement with the HEAT telescopes [Meu11]. The left panel shows a schematic illustration of the shower detection with a standard FD telescope in combination with the HEAT enhancement. The field of view (FOV) of three telescopes are depicted. The event display of two HEAT cameras and one 'Coihueco' camera is shown in the right panel. The color code represents the timing information of the individual pixels of the cameras from early (blue) to late (red).*

AERA [Fuc12] will consist of about 150 radio detection stations (RDSs) distributed over an area of approximately 20 km^2 (Figure 3.10). AERA is located at the experimental site of the infill array and within the field of view of the HEAT telescopes. It will have an inner core of 24 detector stations deployed on a triangular grid with a spacing of 150 m. Around this core a second triangular grid consisting of 60 stations with a pitch size of 250 m will be installed. Additional 72 detectors will constitute the outer region of the AERA site with a spacing of 375 m [Ber09]. The installation of AERA is planned to develop in three stages. As of October 2010, 21 radio stations of the inner array were deployed [Fuc12]. Stable data taking is established since March 2011.

Each RDS of the currently operated stage 1 consists of a logarithmic periodic dipole antenna (LPDA), the electronics, a solar panel, a GPS receiver and a fence around the station. The antenna is orientated such that the electric field strength of the signal in the east-west and in the north-south polarization is measured. It is sensitive in a relatively radio-quiet region with frequencies ranging from 27 MHz to 84 MHz, between the shortwave and and the frequency modulated (FM) bands. The measured signals are amplified with two low-noise amplifiers, which incorporate a bandpass filter from 23 MHz to 79 MHz to eliminate any inter-modulation from the FM bands. After another amplification stage and a bandpass filter for frequencies between 30 MHz to 78 MHz the signals of the analog output channels are digitized with a sampling rate of 200 MHz and a dynamical range of 12 bit. An FPGA processes the digitized signals by filter and trigger logics using the time-domain radio signals. Once a trigger signal is formed, the recorded data, covering a time window of 10.2 µs, and the GPS timestamp of the trigger are transferred to the central radio station (CRS). The CRS contains the DAQ

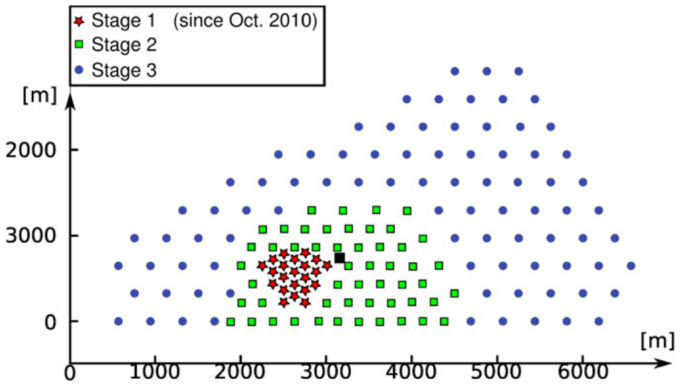

Figure 3.10: *Layout of the AERA array [Fuc12]. Radio detection stations (RDSs) associated to installation stage 1 are plotted as red asterisks, the stations of stage 2 and stage 3 are represented by green squares and blue circles, respectively. The position of the central radio station (CRS) is designated with a black square marker.*

hardware for the full radio array. All detector stations are connected via optical fibers. A replacement of these fibers by a high-speed, low-power wireless communication system is planned for the next installation stages. The CRS is powered by its own photo-voltaic array. Since thunderstorms influence the measurement in the radio regime, it is equipped with a weather station to monitor the local electric field.

The CRS analyzes the timestamps of all received single-station events. A multi-station trigger is formed whenever the trigger times of neighboring radio stations are consistent with a signal moving across the array at the speed of light c [Kel11]. Once such a coincidence is detected, the recorded signals of all detector stations are read out and stored for further analyses. On average, the trigger rate of a single RDS is in the order of 100 Hz, while the multi-station trigger is one decade below. The sources of the radio sources can be localized using the RDS data. The reconstruction of the arrival directions of self-triggered events shows several excesses close to the horizon, i.e. for zenith angles between 85 ° and 90 °. From this, the majority of acquired events can be associated to man-made sources. These events have to be rejected from further physics analyses. Events in coincidence with the SD are measured at a rate of 0.3 to 0.9 events per day, depending on the trigger settings and the number of stations required in coincidence [Kel11].

3.3.4 Microwave Detection of Air Showers

The development of the electromagnetic component in an EAS of ultra-high energy leads to the emission of radiation in the microwave regime [Gor08], which may allow for a novel detection technique. Due to the minimal atmospheric attenuation of microwaves, their detection combines the advantages of measurements with the FD and the SD since it enables the observation of the longitudinal shower development at a 100 % duty cycle of the detector. On top, the measurement can be performed by using low-cost commercial equipment. Currently, four prototype detectors at the Pierre Auger Observatory exploit the microwave detection of

air showers. A detailed overview over these enhancements is presented in [All11].

The AMBER detector (Air-shower Microwave Bremsstrahlung Experimental Radiometer) consists of a single parabolic dish located at the FD station 'Coihueco' alongside the HEAT telescopes and overlooking the infill array. It aims at the observation of air showers in coincidence with the SD array without self-triggering.
The aim of the EASIER enhancement (Extensive Air Shower Identification using Electron Radiometer) is to observe air showers in the GHz as well as in the MHz regime. Its antennas are supposed to be installed on each SD station covering a field of view of 6° around the zenith. After being processed by the EASIER electronics, the radio signals measured by the antenna are fed into the regular local station electronics of the SD station, thus replacing signals of one of the three PMTs. By this, EASIER benefits from the existing power distribution and the communication system of the SD, allowing for a good and fast integration into the SD data taking. Up to now, EASIER prototype antennas have been successfully installed at two hexagons of the SD array, one hexagon equipped with MHz antennas, the other one with GHz antennas. A first evidence for signals in the radio band between 3.4 GHz to 4.2 GHz resulting from air showers have been found [Aub11].
The FDWave detector is made up of 264 GHz antennas that are installed in empty pixels of the FD telescopes at the 'Los Leones' site. The spherical mirrors of these telescopes are made of aluminum and therefore conveniently reflecting [All11]. Detector simulations predict the detector to be capable of recording the microwave emission of air showers for primary energies above 3×10^{18} eV. The microwave signal will be acquired in coincidence with an air shower event recorded by the FD.
The MIDAS detector (Microwave Detection of Air Showers) is designed as a stand-alone, self-triggered system [Wil10]. It consists of a parabolic reflector with a diameter of 4.5 m. Microwave signals emitted by air showers in the 10^{18} eV regime are detected with a 53-pixel camera and processed by standard commercial satellite television electronics. FADCs digitize the 53 analog channels with a sampling frequency of 20 MHz and a dynamical range of 14 bit. Further signal processing and triggering is performed by an FPGA-based readout electronics. An absolute calibration of the MIDAS prototype was performed using several astronomical sources, the relative calibration was done using a calibrated source at the center of the reflector dish. The MIDAS prototype has been in stable operation for six months at the University of Chicago and will be relocated to the 'Los Leones' FD site [All11].

First analyses of the data acquired with these prototype detectors will soon determine the capabilities of microwave detection of cosmic ray air showers.

4 The Muon Detector of the AMIGA Enhancement

Contents

4.1 Comparison of Composition Sensitive Air Shower Observables 44
4.2 Determination of the Number of Muons with the AMIGA Muon Detector 46
4.3 The Pre-Unitary Cell 48
4.4 The Muon Counter Modules 48
4.4.1 The Scintillator Module 48
4.4.2 The Photomultiplier 50
4.5 The Muon Detector Electronics 50
4.5.1 The Underground Electronics of a Muon Counter Module 51
4.5.2 The Surface Electronics of a Muon Counter 54

The AMIGA enhancement (Auger Muons and Infill for the Ground Array) comprises two upgrades of the Pierre Auger Observatory, the infill array and the muon detector (MD). Whereas the infill array will lower the energy threshold for full trigger efficiency of the surface detector (SD) array by about one decade (Section 3.3.1), the MD will improve the identification of the mass of the primary cosmic ray particles by providing an independent measurement of the muon contents of the air showers. Therefore, muon counters shall be buried alongside the SD stations in the infill array.

The baseline design of the AMIGA MD foresees the installation of an underground muon counter with each of the SD stations of the infill array. Thus, the MD consists of 85 muon counters in total. Each muon counter is subdivided into up to four modules, overall covering an active detection area of $30\,\mathrm{m}^2$ with underground scintillators (Figure 4.1). Whereas the first prototype detectors consist of two modules with $10\,\mathrm{m}^2$ and another two modules with $5\,\mathrm{m}^2$ of detection area, a segmentation into three $10\,\mathrm{m}^2$ modules is favored for the final design. The MD modules are located approximately 2.25 m under ground and about 5 m away from the associated SD station. This distance was found to be sufficient to reduce any angular dependence of the measurement due to a shading of the muon counter by the SD station. The shadow of the SD station denotes the region in which the measurement of the number of muons is affected by a possible absorption of the muons inside the water volume of the detector.
The optimum depth, at which the MD modules are installed, has been derived from air shower simulations [Pac06]. The depth of the atmosphere above the Pierre Auger Observatory (approximately 1,400 m a.s.l.) corresponds to a slant depth of about $874\,\mathrm{g/cm}^2$. Vertical air showers with primary energies of $10^{18}\,\mathrm{eV}$ at this depth are mainly composed of γ, $\mathrm{e}^{\pm}$

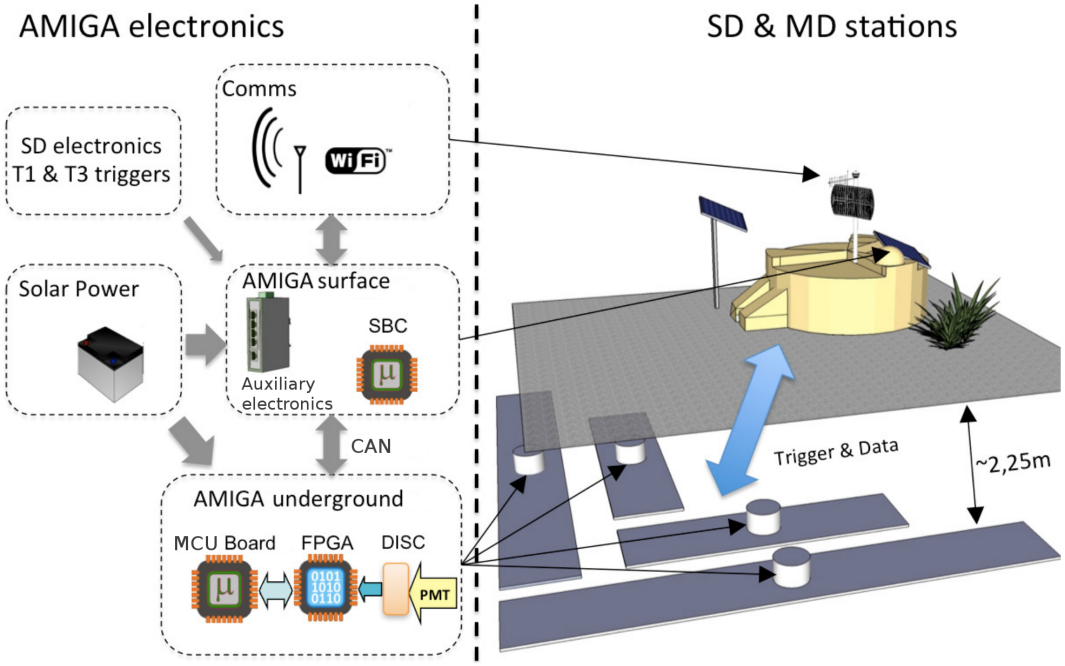

Figure 4.1: *Schematic view of an AMIGA detector pair consisting of the SD station and four underground muon counter modules (adapted from [Sua13]). The flow diagram on the left depicts the communication between the different detector components as it is realized for the detectors of the PUC. The individual processes will be described in the following sections.*

and $\mu^{\pm}$. At a distance of 200 m from the shower core, the average energy of particles of the electromagnetic component is below 100 MeV, whereas it is close to 10 GeV for the muons. Detailed simulations of muons propagating result in an energy threshold for muons to pass 2.25 m of the soil, corresponding to a slant depth of 540 g/cm^2, of 1 GeV at ground level [Nie11]. Thus, although scintillators are sensitive to charged particles in general, the particles detected by the muon counters at the given depth are mainly muons. High energy muons traversing the soil may initiate local electromagnetic sub-showers, which may contaminate the muon measurements. The contribution of this effect, usually referred to as punch-through, on the measurement has been determined to be in the order of 13 % and 5 % for an installation depth of the muon counters of 1.5 m and 2.5 m, respectively [Pac06].

4.1 Comparison of Composition Sensitive Air Shower Observables

One of the key objectives of the Pierre Auger Observatory is to study the composition of primary cosmic rays at the highest energies. In order to investigate composition trends as a function of energy, multiple observables of the SD as well as the fluorescence detector (FD) can be chosen to distinguish between light primaries (protons) and heavy primaries (iron). The most prominent composition-sensitive observable is the depth of the shower maximum

$X_{\max}$, since it is closely connected to the primary mass A through [Mat05]

$$X^{\mathrm{A}}_{\max} \approx X^{\mathrm{p}}_{\max} - \lambda_r \ln A \tag{4.1}$$

(λ_r: radiation length in air) and can directly be measured by the FD. Other observables, that can be accessed by the SD, are linked to $X_{\max}$ or the number of muons N_μ contained in the air shower. Such observables are e.g. the rise time $t_{1/2}$ of the signals in the SD, the slope β of the lateral distribution function (LDF), the radius of curvature R of the shower front or the signal strength S at a given distance from the shower axis.

The rise time $t_{1/2}$ of the SD signals is typically defined between 10 % and 50 % of the maximum amplitude. It is related to the muon content of the shower and only to a lesser degree to $X_{\max}$. Once the muons are created in an air shower they essentially propagate on straight trajectories whereas the electromagnetic particles are subject to multiple scattering processes. As a consequence, the bulk of particles arriving early at the SD station will be muons. Light primaries penetrate deeper in the atmosphere than heavy primaries of the same energy. In addition, the energy per nucleon is higher for light primaries. Therefore, the muons produced in showers of light primaries are longitudinally more separated in space. Due to the different path lengths of these muons to travel to an SD station, their signals will spread out in time. Thus, light primaries will have a longer rise time of the signal in the SD station compared to heavy primaries. This effect is even strengthened due to the fact, that heavy primaries in general produce more muons compared to light primaries, thus resulting in faster rise times [Hea06].
In first order, the front of an air shower can be described as a hemisphere expanding from the point of the first interaction of the primary cosmic ray. Since heavy primaries interact early in the atmosphere, their shower front will have a larger radius of curvature R compared to the one of light primaries [Hea06].
At a given distance from the shower core, the electromagnetic and the muonic shower component contribute to the measured SD signal at different extents. Therefore, the analysis of SD observables like e.g. the time-integrated signal strength S or the slope β of the LDF allow for an estimation of the muon density. Due to the large abundance of electromagnetic particles near the shower core, it is easier to estimate the muon density far from the axis. Contrary, shower-to-shower fluctuations become dominant for large distances. Air shower simulations reveal a significant muon density for distances between 400 m and 1,000 m from the shower core for showers at 10^{19} eV [Mau03]. For showers in the energy range addressed by AMIGA, S_{600}, being the SD signal at a distance of 600 m from the shower axis, is chosen [Sup08].

The capabilities of the AMIGA MD allow for a direct measurement of the muon content in an air shower. Simulations have been performed in order to study a new composition sensitive observable, which is the reconstructed muon density at a distance of 600 m from the shower axis $N_\mu(600)$ [Sup08]. The calculation of a merit factor

$$\eta(q) = \frac{|\langle q_{\mathrm{p}}\rangle - \langle q_{\mathrm{Fe}}\rangle|}{\sqrt{\sigma^2\left(q_{\mathrm{p}}\right) + \sigma^2\left(q_{\mathrm{Fe}}\right)}} \tag{4.2}$$

allows for a comparison of the mass discrimination power of the different observables ($q = N_\mu(600)$, $X_{\max}$, $t_{1/2}$, β, R, S_{600}). Here, q_A denotes the observable for a primary of mass A. $\langle q_A \rangle$ is the mean value and $\sigma(q_A)$ the standard deviation of the distribution of q_A. In Figure 4.2a, the linear fits of η are shown as a function of the primary energy for zenith angles of $\theta = 30\,^\circ$ and $\theta = 45\,^\circ$ and for the different observables considered. It is found, that $N_\mu(600)$ best separates protons from iron primaries, followed by $X_{\max}$. For all observables, that are based on SD measurements, the discrimination power η increases with energy, since an increase in the number of triggered stations leads to smaller uncertainties in the event reconstruction. Although the reconstruction error of $X_{\max}$ decreases with primary energy, a slow decrease of η is observed. This effect results from a convergence of the average values of $X_{\max}$ for proton and iron primaries with increasing energy, which is an artifact of the hadronic interaction model considered [Sup08].
If the uncertainty of the energy reconstruction is negligible, $N_\mu(600)$ is found to be the best observable for composition analyses. However, the number of muons in an air shower is almost proportional to the primary energy (Section 2.3.2), whereas the other observables depend on the energy logarithmically. Assuming an energy uncertainty of 20 %, which is a realistic estimate for the energy reconstruction with the infill array [Rav13], the discrimination power of $N_\mu(600)$ becomes comparable to the one of $X_{\max}$ [Sup08] (Figure 4.2b).

4.2 Determination of the Number of Muons with the AMIGA Muon Detector

The reconstruction procedure for determining the composition sensitive parameter $N_\mu(600)$ from the measurements performed by the single muon counters has been derived from simulations [Pac06]. This study comprises 50 simulated showers initiated by either proton or iron with a primary energy of 10^{18} eV and an incidence angle of $\theta = 45\,^\circ$. Each shower was reused 20 times by randomly changing its core position within the simulated array.
An estimate for the true number of muons N_μ^{est} is derived by applying a correction of the form

$$N_\mu^{\text{est}} = \frac{\ln\left(1 - \frac{N_\mu^{\text{C}}}{N_{\text{seg}}}\right)}{\ln\left(1 - \frac{1}{N_{\text{seg}}}\right)} \approx -N_{\text{seg}} \ln\left(1 - \frac{N_\mu^{\text{C}}}{N_{\text{seg}}}\right) \tag{4.3}$$

to the number of muons N_μ^{C}, that has been measured with a single muon counter. This correction compensates an underestimation of the true number of muons due to the limited amount of channels N_{seg} of each muon counter, referred to as pile-up. For muon counters consisting of three 10 m^2 modules it is $N_{\text{seg}} = 192$. The efficiency of the muon counter modules is assumed to be 100 %. The measurements of multiple MD stations are combined by fitting the data with a muon lateral density function (MLDF) of the form

$$N_\mu(r) = P_0 \left(\frac{r}{r_0}\right)^{-\alpha} \left(1 + \frac{r}{r_0}\right)^{-\beta} \left(1 + \left(\frac{r}{10 r_0}\right)^2\right)^{-\gamma} \quad . \tag{4.4}$$

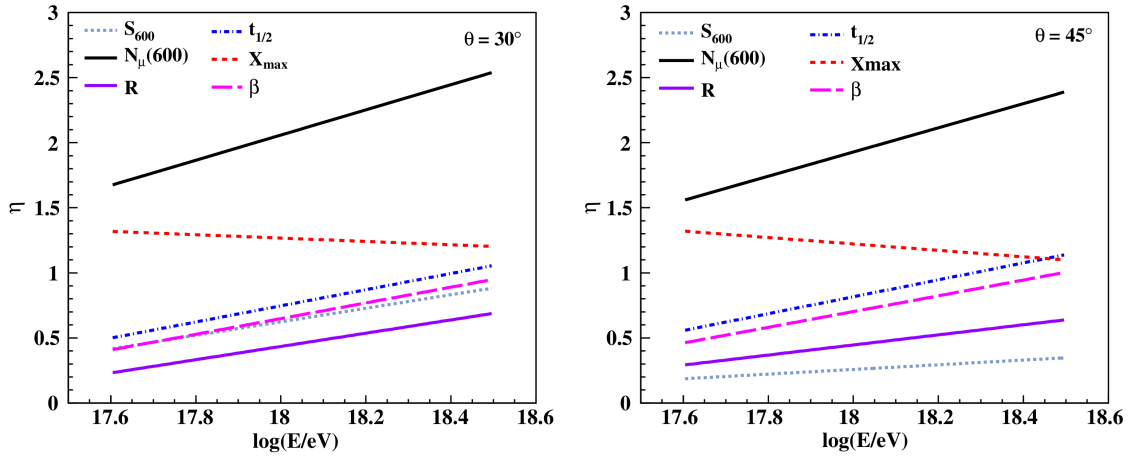

(a) Linear fits of η.

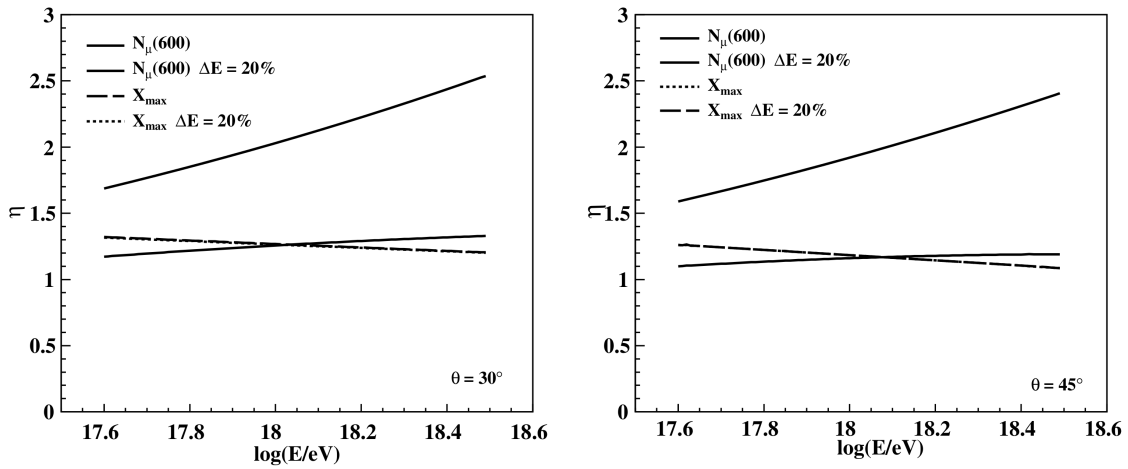

(b) Comparison of $N_\mu(600)$ and X_{max}.

Figure 4.2: *Mass discrimination power of different air shower observables [Sup08]. Figure 4.2a depicts the the linear fits of η as a function of the primary energy for the different observables considered and for incidence angles of $\theta = 30\,^\circ$ and $\theta = 45\,^\circ$. Figure 4.2b shows the evolution of η for $N_\mu(600)$ and X_{max} with and without an energy uncertainty of 20 %. The difference between the two lines corresponding to X_{max} is too small to be visible in both plots.*

Here, the parameters $r_0 = 320\,\mathrm{m}$, $\alpha = 0.75$ and $\gamma = 2.93$ are fixed, whereas P_0 and β are used as free fit parameters. The MLDF is an adaption of a function proposed by the KASCADE-Grande collaboration (Karlsruhe Shower Core and Array Detector Grande) [Bur05]. The parameter $N_\mu(600)$ is then derived from the result of the fit. The resolution of $N_\mu(600)$ for a $30\,\mathrm{m}^2$ detector is determined to be 13 % and 17 % for iron and proton primaries, respectively [Pac06].

4.3 The Pre-Unitary Cell

The deployment of the AMIGA muon counters is organized in different stages. In a first step, a $5\,\mathrm{m}^2$ module was installed connected to the SD station 'Corrientes' in November 2009. This first installation was not only thought of as a test of the infrastructure necessary for a successful deployment, it also enabled the first data taking with a muon counter module at the experimental site. In August 2010, a second module with a size of $10\,\mathrm{m}^2$ was installed at the same SD station. The next stage of the MD deployment included the installation of $10\,\mathrm{m}^2$ modules connected to the SD stations 'Heisenberg' and 'Phil Collins' in April 2011. Finally, another four technically identical modules were commissioned in February 2012 at the SD stations 'Kathy Turner', 'Los Piojos', 'Toune' and 'Yeka'. By this, the installation of the first hexagon of muon counters, each one consisting of at least one $10\,\mathrm{m}^2$ muon counter module, was completed. This hexagon is referred to as the pre-unitary cell (PUC).

4.4 The Muon Counter Modules

An underground muon counter consists of up to four independent units, commonly referred to as muon counter modules. Each of these modules consists of a scintillator, a multi-pixel photomultiplier (PMT) and the detector electronics. The MD electronics itself is subdivided into two parts. The readout electronics is directly connected to the muon counter and, thus, installed underground. Contrary, the surface electronics is installed inside the electronics dome of the water Cherenkov tank. It is needed for the synchronization between the muon counter modules and the associated SD station. In the following, all constituents of the MD modules will be described in detail.

4.4.1 The Scintillator Module

Each scintillator module is segmented in 64 scintillator strips with a rectangular cross section of $41 \times 10\,\mathrm{mm}^2$. For the $10\,\mathrm{m}^2$ modules the length of the individual strips is 4 m, while it is half that size for the $5\,\mathrm{m}^2$ modules. The design of the scintillator strips (Figure 4.3a) is based on the design of the MINOS experiment (Main Injector Neutrino Oscillation Search) [Ada98]. Each strip is made of polystyrene as the base material, doped with fluorescent chemicals [12]. It is coated with a reflective layer of titanium dioxide to improve the collection of scintillation light. The attenuation length of the extruded scintillator bars is in the order of 55 mm [Pla11]. Therefore, a wavelength shifting (WLS) fiber [20] with a diameter of 1.2 mm and an attenuation length of about 6 m [Pac06] is glued [19] into a groove along the scintillator, enabling the transport of the scintillation light to the connected PMT. The process of gluing

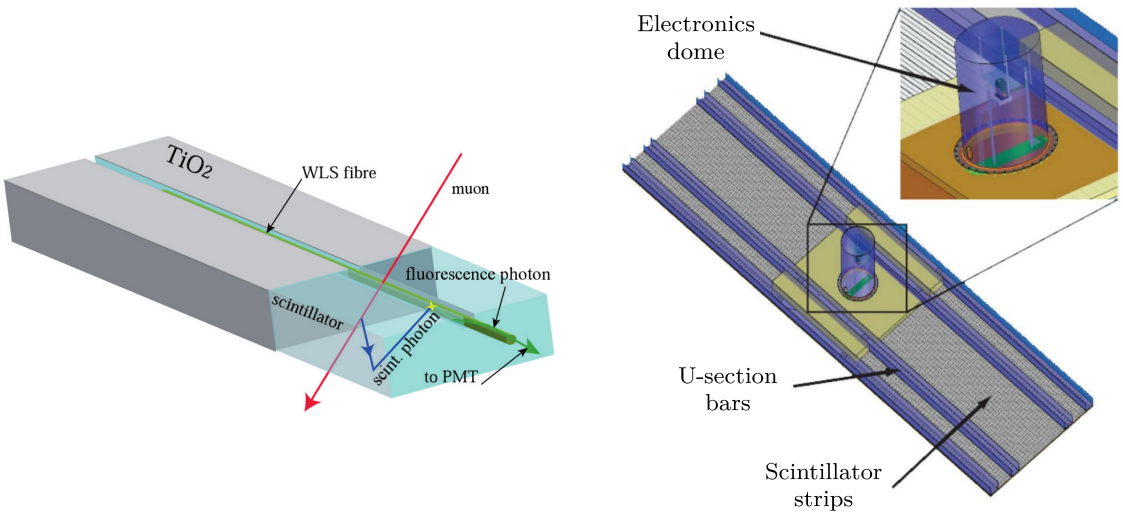

(a) Scintillator strip. *(b) AMIGA scintillator module.*

Figure 4.3: *Schematic view of a scintillator strip and a scintillator module. The left panel depicts the principle of particle detection in a scintillator strip (adapted from [Ada07]). The impinging muon (red arrow) generates a scintillation photon with a wavelength in the blue region. By the excitation and deexcitation of molecules inside the wavelength shifting (WLS) fiber a fluorescence photon in the green region is emitted. The right panel shows a scintillator module with explanatory labels attached (adapted from [Pla09]).*

the fibers into the scintillator bars is critical, since variations in the refractive index of the coupling due to inhomogeneities of the material may lead to reflections of the scintillation light and by this may influence the measurement [Pla11]. The open end of each fiber is blackened to prevent a reflection of light, which might lead to an overcounting of the signals, whereas the end connected to the PMT is polished with a diamond-bit on a fly cutter [Pac06].
The energy deposition needed to produce a single photo-electron (SPE) has been measured to be at least 100 keV. For a particle hitting the scintillator bar at a distance of 4 m from the PMT an average number of six photo-electrons has been determined [Pac06]. The scintillators emit light at wavelength of about 400 nm, thus matching the characteristics of the WLS fiber, that have maximum light absorption and emission at 410 nm and 485 nm, respectively.
Two groups of 32 scintillator bars are mounted at opposite sides of a central dome, which houses the PMT and the underground part of the muon counter electronics. The module casing is built from polyvinyl chloride (PVC) panels onto which the scintillator bars are glued. Structural stability is provided by four PVC U-section bars placed at both sides of the central dome all along the module (Figure 4.3b) [Pla09].

A more detailed description of the production and testing of the scintillator bars as well as of the module assembly is given in [Pla11].

4.4.2 The Photomultiplier

The 64 fibers of the scintillator module are optically coupled to a multi-anode PMT [15] with 64 pixel, which is used to convert the optical into electrical signals. The pixels are arranged in a matrix of 8×8 pixels, each covering an active area of $2 \times 2\,\mathrm{mm}^2$. The PMT is based on an existing type [14] but has been modified to fit the needs of the AMIGA muon counter. This change mainly affects the casing of the PMT, which was modified such that it can be coupled to a plastic optical connector guiding the fibers onto the individual PMT pixels [Pla11]. The alignment procedure is adapted from the one performed for the target tracker of the OPERA experiment (Oscillation Project with Emulsion-Tracking Apparatus) [Ada07]. The optical coupling between the fibers and the entrance window of the PMT is improved and reflections are minimized by applying optical grease [18] to the contact surface.
The PMT contains a $18.1 \times 18.1\,\mathrm{mm}^2$ ultra-bialkali photo cathode with a quantum efficiency of typically 43 % peaking at 350 nm with a still significant efficiency at around 485 nm [Sua08], thus fitting the wavelength of the WLS fiber. Among other features, the PMT has a high speed response with typical rise times of the anode signals of 1 ns, a typical gain of 3×10^5 for a supply voltage of -1 kV, a low dark current of less than 2 nA per channel [Ham11] and low cross-talk at a level of 2 % [Ham03]. The cross-talk either results from light, that enters a specific pixel but originates from a neighboring fiber (optical cross-talk), or from electrons, that enter a neighboring dynode on their way through the PMT (internal cross-talk). Since the electrons resulting from optical cross-talk will undergo all the amplification stages of the PMT, the amplitudes of these signals will be in the order of the SPE. Contrary, signals of internal cross-talk will not be affected by all dynodes and, thus, they will widen or shift the noise peak of the channel.
The PMTs have a considerable maximum gain uniformity of about 1:3. In order to be able to develop a suitable method for an offline calibration of each muon counter module, laboratory tests are performed to determine each pixel gain with reasonable precision. In addition, the test routine includes the characterization of each PMT pixel with respect to its dark rate, cross-talk, quantum efficiency and mean amplitude of the SPEs [Sua08]. Similar tests have already been performed for the PMTs used for the OPERA experiment [Bor04].

4.5 The Muon Detector Electronics

The electronics of each muon counter can be subdivided into two parts. Only the combination of both, the surface and the underground electronics, allows for a synchronization in the data streams between the individual muon counter modules and the associated SD station. A direct requirement for the synchronization of both detector systems is the need of a possibility to trigger the muon counter modules with a trigger signal generated by the SD station. Reacting to this external trigger signal, the underground electronics will acquire the output signals of the PMT. This information is locally stored as a muon counter event. A potential event request performed by the central data acquisition system (CDAS) of the Pierre Auger Observatory will initiate the readout of the event and the corresponding data will be transmitted. Whereas the surface electronics is used for extracting the trigger signal from the SD station, the event handling is performed by the underground electronics. Both parts will be described in the following.

4.5.1 The Underground Electronics of a Muon Counter Module

In order to process the output signals of the PMT, a modular readout system of five different electronic boards, namely the Power Distributor Board, the Mother Board, the Analog Board, the Digital Board and the Microcontroller Board, has been developed. Tests of the individual boards [Buc12] as well as full system tests [Pon12] have been performed in order to ensure the correct functionality of the electronics. The modularity of the system allows for a development or reworking of different parts of the electronics in different places. Independent of the SD station, the muon counters are powered by two batteries, that are charged by a photovoltaic system. It is therefore essential, that the overall power consumption of the electronics system is kept to a minimum in order to allow for the operation of up to four MD modules with one SD station. In Figure 4.4, a completely assembled underground electronics system in the laboratory is shown. Brief descriptions of the individual boards will be given next. More detailed information can be found in [Frö09].

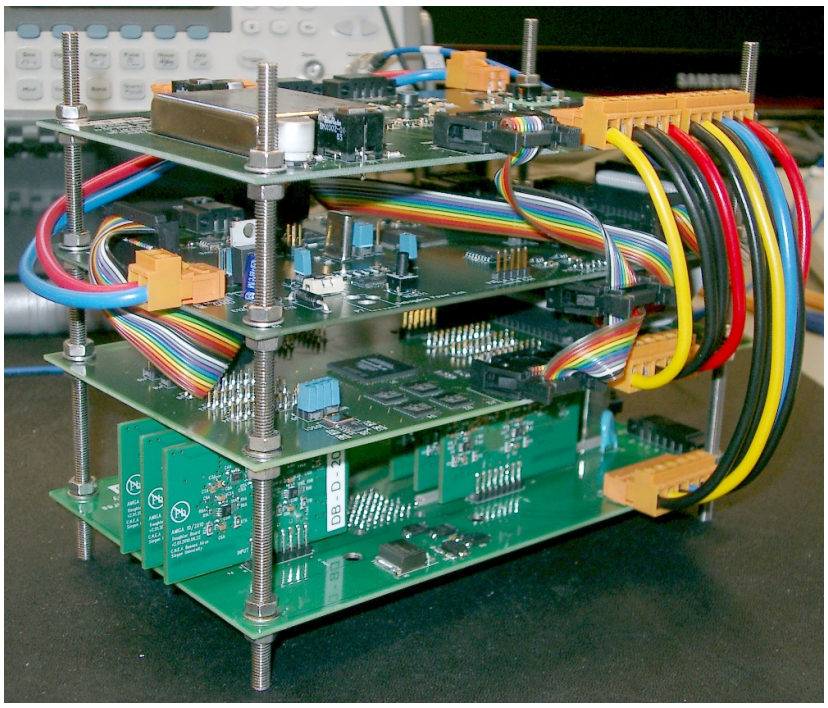

Figure 4.4: *A completely assembled system of the underground muon counter electronics. From top to bottom: the Power Distributor Board, the Microcontroller Board, the Digital Board, the vertically mounted Analog Boards and the Mother Board.*

The Power Distributor Board

For each AMIGA muon counter, the Power Distributor Board is the interface between the SD station and the underground electronics and serves two purposes: the distribution of all supply voltages for the other components of the electronics setup and the galvanic isolation of the ground levels of the SD electronics and the underground system. The latter is required to avoid ground loops, and hence minimizes the electronics noise level. The electrical power for the underground muon counter is provided by two batteries of +24 V. In a first step, this basic supply voltage is transformed into a voltage of +12 V and the galvanic isolation of the two different ground levels is performed. In separate circuits this voltage is then converted into voltages of +3.9 V for the Mother Board, the Analog Boards and the Microcontroller Board. In addition, voltages of +1.8 V for the Digital Board as well as -3.9 V and +12 V for the Mother Board are provided. In order to retain the separation of the ground levels of the two systems, also all signal lines between surface and underground electronics are electrically isolated. This concerns the differential trigger line as well as the communication link, realized through a bidirectional CAN bus (controller area network).

The Mother Board

The Mother Board is the connecting link between the readout electronics and the multi-anode PMT. It provides the socket for the PMT, its high voltage supply [13] as well as a monitoring circuit for the high voltage applied. The high voltage is generated from the input voltage of +12 V, its exact value can be adjusted with a control voltage provided by the Microcontroller Board. The monitoring is realized by the usage of a high precision voltage divider [10] with a division factor of 1,000, that allows for a direct measurement of the monitoring signal using the Microcontroller Board. An operational amplifier, used as an impedance converter, protects the Mother Board from overload. An additional protection circuit limits the high voltage to a maximum of -1 kV in order to prevent the PMT from being damaged. The 64 anode outputs of the PMT are distributed to the eight Analog Boards, which are soldered to the Mother Board in a vertical alignment. The operating voltages for the Analog Boards of ±3.3 V are generated from the input voltages of ±3.9 V on the Mother Board.

The Analog Boards

The eight Analog Boards are the only signal forming components of the electronics chain of the muon counter modules. An Analog Board comprises eight individual channels, each channel including an amplifier and a discriminator circuit, which process the signals of eight anode outputs of the PMT by converting them into digital signals according to the TTL standard (transistor-transistor logic). The negative PMT signals are amplified using an operational amplifier [09] with a nominal gain of $G = 3.1$, inverted and, afterwards, compared to a threshold voltage with the discriminator [25]. In case the amplitude of the amplified PMT signal exceeds the threshold voltage, the voltage at the discriminator output drops from +3.3 V to 0 V, corresponding to a change from logic 0 to logic 1, respectively. A digital-to-analog converter (DAC) [26] with eight programmable outputs allows for setting an individual threshold voltage for each channel of the Analog Board. By this, the different characteristics of each channel, largely determined by the gain of the single PMT pixel and the gain of the

corresponding operational amplifier on the Analog Board, can be accounted for. The linearity of the DAC has already been measured in [Frö09], more detailed measurements are presented in [Pon12].
Operational amplifiers in general have limited bandwidth. The frequency response of the amplification circuit of the Analog Board has been measured in [Frö09]. The -3 dB bandwidth of the operational amplifier has been determined as $f_{\text{-3dB}} = (134 \pm 5)\,\text{MHz}$ for the nominal amplification factor of $G = 3.1$. Thus, for typical pulse widths of SPE pulses in the order of $t_{\text{SPE}} = (3.0 \pm 0.4)\,\text{ns}$, the amplifier is operating at its limit. It was measured that the SPE pulses are prolonged by about 25 % to $t'_{\text{SPE}} = (3.8 \pm 0.5)\,\text{ns}$, good signal integrity is achieved for pulse widths $\gtrsim 6\,\text{ns}$.

The Digital Board

The Digital Board (Figure 4.5) represents the main unit of the data acquisition (DAQ) system in each muon counter module. The 64 outputs of the eight Analog Boards, providing the digitized information of the PMT signals, are directly connected to 64 input pins of an FPGA (field programmable gate array) [07]. The signals are sampled at a frequency of 320 MHz, which is sufficient for resolving SPE pulses but which is still below the specification limit of the device of 400 MHz. A detailed description of the signal processing performed by the FPGA, including the sampling of the input signals, possible trigger forming and the event handling, will be given in Chapter 5.
The FPGA is driven by an external 40 MHz oscillator [16]. For the Digital Board, the Power Distributor Board provides supply voltages of +3.9 V and +1.8 V. The FPGA places severe demands on the stability of its operating voltages of +1.2 V, +2.5 V and +3.3 V. Therefore, these voltages are directly generated on the Digital Board. An LVDS receiver chip (low voltage differential signaling) [27] is used for the processing of incoming trigger signals, that were sent by the SD station electronics and that have already been electrically isolated by the Power Distributor Board. For the communication with the Microcontroller Board, the Digital Board comprises a 16-bit wide parallel data bus, an 8-bit wide address bus and three additional control lines. Four control lines are fed to each Analog Board. These are used to adjust the individual threshold voltages. The configuration of the FPGA can be performed by either directly using the JTAG protocol (Joint Test Action Group, IEEE-Standard 1149.1) or by sending the firmware via the Microcontroller Board, which applies a PS (passive serial) configuration scheme.
At any time, the last 2,048 muon counter module events, which are stored in four external 2×16 Mbit static memory blocks [11], are available for readout. For an average trigger rate of approximately 100 Hz (Section 3.1.3), this memory depth suffices for the event handling of about 20 s of recording time.

The Microcontroller Board

The Microcontroller Board, also referred to as the Interface Board, provides the bidirectional communication between the surface electronics and the underground system. A CAN bus allows for the data transfer between the Microcontroller Board and a single board computer (SBC) [21] at the surface. Control commands, e.g. the programming of the DACs on the

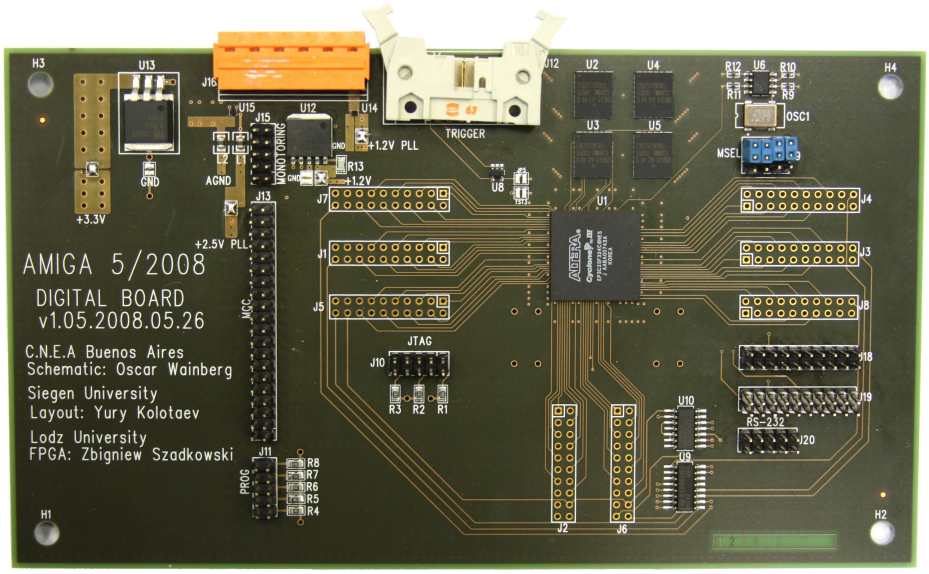

Figure 4.5: *The AMIGA Digital Board. The power connector (orange), the trigger input (gray connector), the FPGA, the four RAM chips as well as the eight sockets for to the Analog Boards are clearly visible.*

Analog Boards or commands for setting the operational mode of the FPGA, are sent by the SBC via the CAN bus and received by the the microcontroller (MCU) [24]. The commands are then forwarded through the data and address busses between the Microcontroller Board and the Digital Board, and the data is written into dedicated input registers of the FPGA (Section 5.3). In opposite direction, data acquired by the muon counter modules can be requested by the SBC at the surface, which can then be transmitted to CDAS.
The Microcontroller Board contains a DAC [08] with a precision of 12 bit to adjust the control voltage for the high voltage supply on the Mother Board. Twelve ADCs (analog-to-digital converter) with a resolution of 10 bit each are included into the MCU, which allow for a monitoring of the most crucial parameters of the electronics system. This, in particular, concerns the monitoring of all supply voltages of the electronics and of the high voltage as well as the readout of two temperature sensors. More information on the monitoring is presented in [Pon12]. A detailed description of the board including laboratory measurements determining its performance is given in [Vid12].

4.5.2 The Surface Electronics of a Muon Counter

In order to synchronize the underground muon counter modules with the associated SD station, additional hardware connected to the DAQ electronics of the local station (LS) is required. Two auxiliary boards, referred to as Local Station Auxiliary Board (AuxLS) and SBC Auxiliary Board (AuxSBC), are installed inside the electronics dome of the SD tank.
The AuxLS is directly connected to the front-end board (FEB) [Sza09] of the LS and receives a modified T1 trigger signal, consisting of the actual trigger pulse and a 24 bit long local timestamp (LTS). This TTL signal is converted into a differential LVDS signal, which is

sent to the AuxSBC and further on distributed to up to two muon counter modules. The operating voltage of the LVDS driver is drawn from the FEB. After receiving the GPS (Global Positioning System) timestamp (GTS) of the trigger, the AuxLS provides the pairwise information of LTS and GTS for the AuxSBC. A CPLD (complex programmable logic device) [05] on the AuxSBC receives this data via an SPI bus (serial peripheral interface) and stores it into a 48-bit wide shift register. The AuxSBC is connected to the SBC through a PC/104 bus communicating using an interrupt protocol. Applying an 8-bit ISA protocol (industry standard architecture), the SBC reads both timestamps and stores them into a local look-up table, which contains the information of the last 2,048 trigger signals. Following a T3 event request (Section 3.1.3) performed by CDAS, this table will then later be used for the identification of the correct event data that has to be transmitted.
In addition, the AuxSBC provides a voltage converter circuit that is used for transforming the battery voltage of +24 V into a operating voltage of +5 V for the SBC.

5 Firmware Features of the AMIGA Digital Board

Contents

5.1 Structure of the FPGA Firmware . . . 58
5.2 Buffer Structure . . . 60
5.3 Input and Output Registers . . . 62
5.4 Sampling/Downsampling of Input Pulses . . . 63
5.4.1 Dependence of the Downsampling Algorithm on the Trigger Mode . . . 66
5.4.2 Comparison of Monte Carlo Data with Measurements . . . 66
5.5 The Occupancy-N Trigger . . . 75
5.5.1 Test of the Occupancy-N Trigger . . . 77
5.6 The Prescaler Algorithm . . . 80
5.6.1 Implementation of the Prescaler Algorithm . . . 81
5.6.2 Dependence of the Prescaling on the Trigger Rate . . . 82
5.7 The T1/T3 Trigger Chain . . . 88
5.7.1 Algorithm for Decoding the T1 Timestamp . . . 88
5.7.2 Requesting Event Data by Timestamp . . . 89
5.7.3 Efficiency of the T1/T3 Trigger Chain . . . 90
5.8 End-of-Event Information . . . 96
5.8.1 Check of T3 Requested Events . . . 96
5.8.2 Verification of Correct Event Handling . . . 97
5.8.3 Reconstruction of the Trigger Rate . . . 99
5.9 Upgrade to 320 MHz Data Acquisition . . . 100

The Digital Board (Section 4.5.1) of each AMIGA (Auger Muons and Infill for the Ground Array) muon counter electronics system incorporates a field programmable gate array (FPGA) [07] that allows for an advanced processing of the incoming signals resulting from muons traversing the scintillator modules. Among other features, this data processing includes a multifunctional trigger system, the acquisition and the storage of the data as well as the communication with the local station (LS) electronics of the surface detector (SD), which makes the recorded data to be available for the central data acquisition system (CDAS) of the Pierre Auger Observatory. The advantage of using programmable logic devices such as FPGAs as compared to the usage of e.g. application-specific integrated circuits (ASICs) lies in the possibility of implementing complex algorithms, which can be modified at a later stage due to experiences gained from experimental results. The basic structure of the AMIGA Digital Board FPGA firmware, written in Altera hardware description language (AHDL), is based on

already existing code [S5], which has been used to operate the front-end (FE) electronics of the individual detector stations of the SD for several years. A detailed description of the LS FPGA firmware can be found in [Sza05]. The process of further adopting the first AMIGA FPGA firmware [S1], as it is described in [Sza11], to the needs of the AMIGA detector, as well as the implementation of new features into the code, have lead to multiple versions of the firmware. The descriptions of the code and the corresponding measurements presented in this chapter refer to the version [S2] of the firmware, which is used for data taking with the AMIGA pre-unitary cell (PUC). Unless otherwise stated, it is this version of the firmware which will be referred to as the AMIGA FPGA firmware. The following sections 5.1 to 5.3 summarize the overall structure of the firmware. In Section 5.4 through Section 5.9 new or modified features of the code are described in detail and results of connected measurements are discussed.

5.1 Structure of the FPGA Firmware

In contrast to computer based systems, programming the firmware of an FPGA does not primarily refer to the concept of defining the temporal operational sequence of the program, but rather to the definition of the functional structures of the device. During the runtime of the program, the operation of the FPGA is driven by an external master clock so that each logic circuit, which the code uses, is executed synchronously to the rising edges of this master clock. This allows to divide the firmware into logic blocks, in the following referred to as bins, which can be characterized by their time consumption in measures of clock cycles. In the following, the eight different logic blocks (A-bin ... H-bin), which define the structure of the AMIGA FPGA firmware and which contain the algorithms used for the processing of the incoming data, are described in more detail.

A-bin

Inside the A-bin routine the 64 digital signals, which are formed by the discriminator circuits of the AMIGA Analog Boards and which contain the information of the photomultiplier (PMT) signals, are latched with a 320 MHz sampling clock. Since the discriminator outputs provide negative TTL (transistor-transistor logic) signals, the incoming data pulses are inverted so that a PMT signal, that is above the given discriminator threshold, is represented by a logical high state for any further data processing. The combination of both steps is realized through the usage of 64 flip-flops.

B-bin

The B-bin routine contains the downsampling algorithm, which is implemented into the firmware to be able to reduce the frequency of the data processing to 80 MHz. This downsampling procedure can be disabled by setting the value of the 14th bit of the control register (`0x48`, Section 5.3) to a logical 1. A detailed description of this algorithm is given in Section 5.4. To allow for a debugging of not only the FPGA code but also of the data processing by externally connected devices such as the Microcontroller Board of the AMIGA muon counter electronics or the single board computer (SBC), an event generator is included into

the B-bin routine, which can be set up to produce either pattern data or noise like data. By implementing the event generator at a very early stage of the signal chain, the test data will be subject to any data processing procedures that also real data would be affected by with the exception of the input part (A-bin) and the downsampling algorithm. The event generator can be enabled and controlled by adjusting the contents of bits four through seven of the control register. It was already implemented into the first version of the firmware [S1] and therefore has been used in multiple stages of the detector development.

C-bin

The C-bin contains routines which are intended to be used for an online calibration of the thresholds applied to the discriminators of the Analog Boards. However, the development of this part of the code has been stopped. Instead, the detector calibration of the muon detectors contributing to the AMIGA PUC is done through dedicated calibration measurements as described in [Pon12]. These routines have no influence at all on the data acquired by the system. The signals of the 64 data streams are only pipelined by one clock cycle of the internal 80 MHz clock in order to preserve the full synchronicity of the data flow.

D-bin and E-bin

In order to be able to take data without the need for an external trigger source, the internal Occupancy-N trigger has been invented. This algorithm forms a trigger signal depending on the number of channels which simultaneously show a signal. The implementation of this algorithm extends to the D- and the E-bin routines. A detailed description of the implementation and the functionality of the Occupancy-N trigger is given in Section 5.5. In addition, the E-bin routine is used to latch the external trigger signals, which can be fed into the system by using one of the two trigger inputs that the Digital Board is equipped with, to the internal 80 MHz clock of the firmware. Here, the first trigger input is connected to the trigger circuit of the Digital Board (Section 4.5.1) enabling the system to react on the T1 trigger signal sent by the local station electronics of the SD, whereas the second trigger input uses the RS-232 connector of the Digital Board. Since any trigger source can be connected to this port, it is possible to e.g. operate the AMIGA system to take data in connection with a muon hodoscope as it is described in [Lau12].

F-bin

The structures implemented into the F-bin routine serve several purposes. They include a method that allows the user to declare one of the possible trigger sources as the definitive trigger signal, which starts the recording of the incoming data, by evaluating the content of the control register (`0x48`, Section 5.3). For the version of the firmware which is designed to be used with the AMIGA PUC, four different trigger modes are available: (1) the Occupancy-N trigger, which can be activated by setting the third bit of the control register to a logical high state (`Ctrl[3]`=1), (2) the T1 trigger including the timestamp information sent by the LS (`Ctrl[1]`=1), (3) a hodoscope trigger which makes use of simultaneously receiving trigger signals from the Occupancy-N trigger and both external trigger inputs (`Ctrl[11]`=1) and (4) a dedicated trigger mode which has been implemented for testing purposes only and which

can be easily adapted to the individual test under consideration (`Ctrl[0]`=1).
Apart from that, the F-bin routine contains the prescaler algorithm, which sets up the system to only react on one out of n incoming trigger signals, where the prescaling factor n can be chosen by the user. The functionality of the prescaler as well as its implementation are discussed in Section 5.6. In addition, the F-bin routine includes all algorithms which are used to isolate the local timestamp (LTS) from the train of pulses which form a T1 trigger signal. Decoding this timestamp makes it available for the subsequent processes that manage the event handling, as well as for the readout of the event data if an appropriate T3 request is received by the system. A detailed description of the T1/T3 trigger chain is given in Section 5.7.

G-bin and H-bin

These bins comprise the implementation of the input buffers, which are used to record the incoming event data as soon as a trigger signal is detected. The structure of the input buffers as well as the overall event storage mechanism are described in Section 5.2.

In addition to the structures that are implemented into these logic blocks, some functions of the code are not assigned to the routines mentioned above. This mainly concerns algorithms which handle the communication of the FPGA with external devices, i.e. the input and output registers (Section 5.3) of the FPGA used for controlling the firmware by e.g. sending the appropriate commands from the SBC to the FPGA, the event buffer, that is used to make the recorded event data available to be read by the Microcontroller Board (Section 5.2), the connection to the external RAM (random access memory) and the algorithm for programming the digital-to-analog converters (DACs) of the Analog Boards.

5.2 Buffer Structure

The data recording and the subsequent event handling carried out by the FPGA firmware of an AMIGA muon counter, as it is implemented for the use with the AMIGA PUC, has to fulfill different requirements. The exact shape of the data, which is to be acquired by the detector, is a priori only known to a certain extent. Therefore and also to allow for a wide range of different methods to analyze the data, the system is designed to not only record the incoming data after but also, in a given time window, before a trigger signal is detected. The data then has to be stored so that it is available to be requested by the central data acquisition system for around 10 s. Based on such a request, the data has to be transmitted via the Microcontroller Board to an externally connected system, e.g. to the SBC. On top, the implementation of the respective algorithms has to be optimized with respect to a minimization of dead time effects, which originate from the read and write processes within the buffer structure. A schematic overview of the buffer structure implemented into the firmware is drawn in Figure 5.1.

After being processed by the downsampling algorithm, the incoming data of the 64 discriminator channels of the Analog Boards are continuously written into a ring buffer (AC-buffer) with a depth of 256 words of 64 bits each. Since the data is processed synchronously to the internal 80 MHz clock, this buffer size corresponds to a time window of $\tau_C = 3.2\,\mu s$. Once a

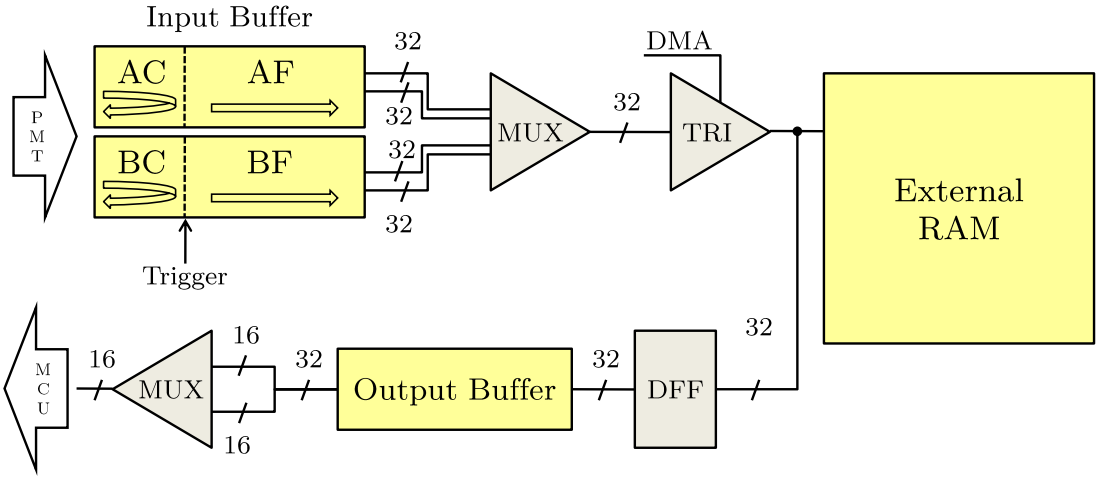

Figure 5.1: *Schematic overview of the buffer structure as it is implemented into the AMIGA FPGA firmware [S2]. The numbers indicate the bus widths of the individual processes.*

trigger signal is detected, the system will write the following incoming data into a second buffer (AF-buffer), in the following also referred to as fast buffer, with a depth of 512 words. Since this buffer can store the event data of a time window of $\tau_{\mathrm{F}} = 6.4\,\mu\mathrm{s}$, the total length of an AMIGA muon counter event amounts to $\tau_{\mathrm{event}} = \tau_{\mathrm{C}} + \tau_{\mathrm{F}} = 9.6\,\mu\mathrm{s}$ with the position of the trigger dividing the event at the ratio of 1:2. The acquired event is then rewritten into the external RAM modules of the Digital Board, which can hold a total number of 2048 events. Since these RAMs only support a bus width of the data connection of 32 bit, the data inside the input buffers, which is going to be rewritten, has to be selected by a 2-to-1 multiplexer (MUX) which allows for choosing between the 32 most or least significant bits of the data. By operating the external memory with a frequency of $f_{\mathrm{RAM}} = 10\,\mathrm{MHz}$ and due to its limited bus width, the time consumption of rewriting the data of one event, in the way it is realized for this firmware version, amounts to $\tau_{\mathrm{rw}} = 154.1\,\mu\mathrm{s}$. So as to reduce the dead time of the detector, which arises from not being able to write to the buffer while rewriting the data to the RAM, the structure of the input buffers is doubled (BC- and BF-buffer), so that ideally one buffer always remains in an idle state awaiting new data to be recorded. By in parallel writing the data which goes to the last third of a buffer to the respective other ring buffer, it can be avoided to record events that are contaminated with old and unrelated data. However, at very high trigger rates of $f_{\mathrm{trig}} \gtrsim 6.489\,\mathrm{kHz}$ even this realization of the input buffer circuit is no longer capable of totally preventing a dead time of the detector. A more detailed discussion of the different dead time effects is presented in Section 5.6.2.

When an event is requested by the SD electronics, either by sending a T3 request in combination with an appropriate timestamp or by transmitting the corresponding memory address of the event under consideration, the data is read from the external RAM and rewritten into a dedicated output buffer. Again, the time consumption of this process is given by the operating frequency of the RAM of 10 MHz. Since the bus width of the data connection between the Digital Board and the Microcontroller Board, which is used as an

interface between the muon counter and the surface electronics, is limited to 16 bit, the content of this buffer that is going to be read out by the Microcontroller Board has to be selected by using a multiplexer circuit before it can be transmitted with a frequency of the transmission of 20 MHz.

5.3 Input and Output Registers

The AMIGA muon counter electronics can be controlled from the SBC of the SD electronics by sending dedicated control commands to adjust multiple parameters inside the firmware of the FPGA. For this purpose, the FPGA provides several input and output registers with a depth of 16 bit, which are used for interchanging data between the surface and the underground electronics. The most important registers, that can be addressed with the firmware version [S2] and especially the ones which are related to the descriptions given in the following sections, are listed in Table 5.1.

MCU Address		***Writing***	***Reading***
Decimal	***Hexadecimal***		
63 - 0	3F - 00	Initial thresholds for DACs (12 bit)	Initial thresholds for DACs (12 bit)
64	40	Reset signals (12 bit)	Firmware version (16 bit)
65	41	—	Event counter (10 bit)
66	42	—	Rate counter (11 bit)
67	43	—	Local timestamp ([15..0])
68	44	Requested T3 timestamp ([15..0])	Requested T3 timestamp ([15..0])
69	45	Requested T3 timestamp ([31..16])	Requested T3 timestamp ([31..16])
70	46	—	T3 comparator result ([15..0])
71	47	—	T3 comparator result ([31..16])
72	48	Control register (16 bit)	Control register (16 bit)
73	49	—	Local timestamp ([23..16])
74	4A	Occupancy value (6 bit) + Event address (10 bit)	Occupancy value (6 bit) + Event address (10 bit)
76	4C	PMT enable ([15..0])	PMT enable ([15..0])
77	4D	PMT enable ([31..16])	PMT enable ([31..16])
78	4E	PMT enable ([47..32])	PMT enable ([47..32])
79	4F	PMT enable ([63..48])	PMT enable ([63..48])
80	50	DAC channel selector ([5..0])	DAC channel selector ([5..0])
82	52	enable/set prescaler (16 bit)	—

Table 5.1: *Important input and output registers of the FPGA firmware [S2]. The particular implementation may be different in other versions of the code.*

While most of the registers are intended to contain parameters like e.g. the initial thresholds for the DACs of the Analog Boards or the LTS for being able to read out data as a reaction on a T3 request, register `0x48` is designed as the control register of the FPGA firmware. Each one of the 16 bits of the register is interpreted as a switch with regard to individual processes executed by the FPGA. Setting individual bits of the control register to either a logical high state or a logical low state allows the user to control the detector's operational behavior ranging from the choice of the trigger mode of the muon counter through to the selection of the mode of how to read out the acquired event data. A complete list of the individual bits of the control register together with their effects on the functions implemented into the FPGA firmware is given in Table 5.2.

Bit	*Value*	*Function*	*Bit*	*Value*	*Function*
0	1	Test trigger enabled	8	1	T3 request high
	0	Test trigger disabled		0	T3 request low
1	1	T1 trigger enabled	9	1	MCU reads data[31..16]
	0	T1 trigger disabled		0	MCU reads data[15..0]
2	1	Read T3 event	10	1	MCU reads data from external RAM
	0	Read event at RAM address		0	MCU reads data from output buffer
3	1	Occupancy-N trigger enabled	11	1	Hodoscope trigger enabled
	0	Occupancy-N trigger disabled		0	Hodoscope trigger disabled
4	1	Event generator (EG) enabled	12	1	—
	0	EG disabled		0	—
5	1	EG: fixed number of packages	13	1	DAC auto calibration enabled
	0	EG: continuous run		0	DAC auto calibration disabled
6	1	EG: noise generation	14	1	Downsampling disabled
	0	EG: pattern generation		0	Downsampling enabled
7	1	EG: interruptions enabled	15	1	Status T3 mode high
	0	EG: interruptions disabled		0	Status T3 mode low

Table 5.2: *Structure of the control register (`0x48`) of the FPGA firmware [S2]. The particular implementation may be different in other versions of the code.*

5.4 Sampling/Downsampling of Input Pulses

The 64 output lines of the discriminators of the Analog Boards are directly connected to input pins of the Digital Board's FPGA. These TTL signals are then sampled with a frequency of 320 MHz synchronously to the rising edges of the sampling clock. In order to reduce the amount of data, which has to be stored, and also to be able to reduce the internal frequency at which the FPGA will process the data to 80 MHz, the input data is downsampled by a factor of four. Therefore an incoming signal is first stored into a 4-bit shift register. Synchronously to the next rising edge of the 80 MHz clock, the output of this downsampling procedure is calculated from the four bits of the shift register by means of a logic OR-function, thus defining the logic state of the output for a time window of 12.5 ns (in the following referred to as "1 time bin"), which will be processed further on. By concatenating the input of the

shift register and its three least significant bits with a NAND-operation, at all times only one logical 1 is stored in the shift register. This algorithm prevents a short pulse with a pulse length of less than $\Delta t_\mathrm{p} = 12.5\,\mathrm{ns}$ to be stored on more than one consecutive time bins.

Putting both steps of the downsampling procedure together ends up in disabling the sampling of input signals for three clock cycles as soon as an input signal is detected. According to this, for a given input signal the number of consecutive time bins of the output showing a signal is dependent on the length of the input signal itself as well as on the position of the input signal with respect to the sampling clock. Two possible cases illustrate this behavior, they are shown in Figure 5.2.

In order to get a more thorough understanding of the output dependency on the overall timing, a Monte Carlo simulation of the downsampling procedure has been done. In this simulation, the starting point of a pulse of length Δt_p is randomly chosen from a uniform distribution in the interval $[0\,\mathrm{ns}; 12.5\,\mathrm{ns})$. Comparing each resulting pulse with a fixed grid of equidistant sample points at intervals of $\Delta t_\mathrm{s} = 3.125\,\mathrm{ns}$ starting at $t_0 = 0\,\mathrm{ns}$ allows for counting the total number of sampling hits n_hits for the given pulse. The number of time bins, which show a signal at the output of the downsampling procedure n_tb, can be calculated from that number by

$$n_\mathrm{tb} = (n_\mathrm{hits} - 1) \div 4 + 1 \tag{5.1}$$

with the $\div$-operator being the logical integer number division without remainder.
Figure 5.3 shows the probability of having n_tb time bins filled at the output as a function of the input pulse width Δt_p. For the simulation, Δt_p has been increased in steps of 0.02 ns within the interval $[0\,\mathrm{ns}; 30.1\,\mathrm{ns})$ with $N = 1{,}000{,}000$ simulations for each pulse length, thus summing up to a total number of $N_\mathrm{tot} = 1.505 \times 10^9$ simulated pulses.

In general, the number of time bins, which show a signal at the output, can also be calculated from geometrical considerations. Therefore a reduced pulse width $\Delta t_\mathrm{r} = \Delta t_\mathrm{p} - n \times 12.5\,\mathrm{ns}$ can be defined with Δt_p being the pulse width of the input pulse and n being a non-negative integer, which has to be chosen in such a way that Δt_r is in the range of $[0\,\mathrm{ns}; 12.5\,\mathrm{ns}]$. In case the reduced pulse width ends up in the interval $[3.125\,\mathrm{ns}; 12.5\,\mathrm{ns}]$, the input signal will always end up in $n + 1$ time bins at the output:

$$\mathcal{P}(n+1) = 1 \quad \text{for} \quad \Delta t_\mathrm{r} \in [3.125\,\mathrm{ns}; 12.5\,\mathrm{ns}] \quad . \tag{5.2}$$

For the transition regions where the sampling procedure results in n or $n + 1$ time bins ($\Delta t_\mathrm{r} \in [0\,\mathrm{ns}; 3.125\,\mathrm{ns}]$) the probability $\mathcal{P}(n + 1)$ of having $n + 1$ time bins filled is given by the overlap of the reduced pulse width and the width of one clock cycle of the sampling clock $\Delta t_{320\,\mathrm{MHz}} = 3.125\,\mathrm{ns}$ by

$$\mathcal{P}(n+1) = \frac{\Delta t_\mathrm{r}}{3.125\,\mathrm{ns}} = \frac{\Delta t_\mathrm{p} - n \times 12.5\,\mathrm{ns}}{3.125\,\mathrm{ns}} \quad \text{for} \quad \Delta t_\mathrm{r} \in [0\,\mathrm{ns}; 3.125\,\mathrm{ns}] \quad . \tag{5.3}$$

Respectively, the probability of having n time bins filled at the output can be calculated by $\mathcal{P}(n) = 1 - \mathcal{P}(n + 1)$.

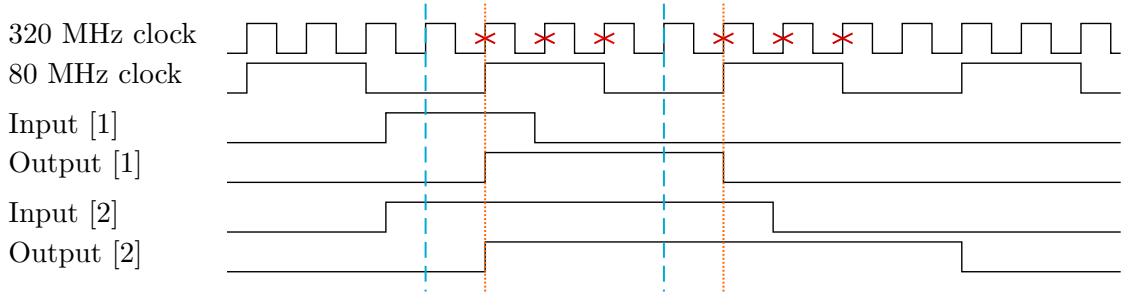

Figure 5.2: *Examples of 320 MHz sampling and downsampling to 80 MHz as it is realized with the AMIGA FPGA firmware [S2]. Input [1] will be sampled once (first blue dashed line), which results in one 12.5 ns wide output pulse starting synchronously to the next rising edge of the 80 MHz clock (Output [1], first orange dotted line). Accordingly, a longer input signal (Input [2]) will be sampled twice (both blue dashed lines) and thus will be processed further on as one 25 ns wide output pulse corresponding to two time bins (Output [2], both orange dotted lines). The red crosses indicate the disabling of the sampling procedure.*

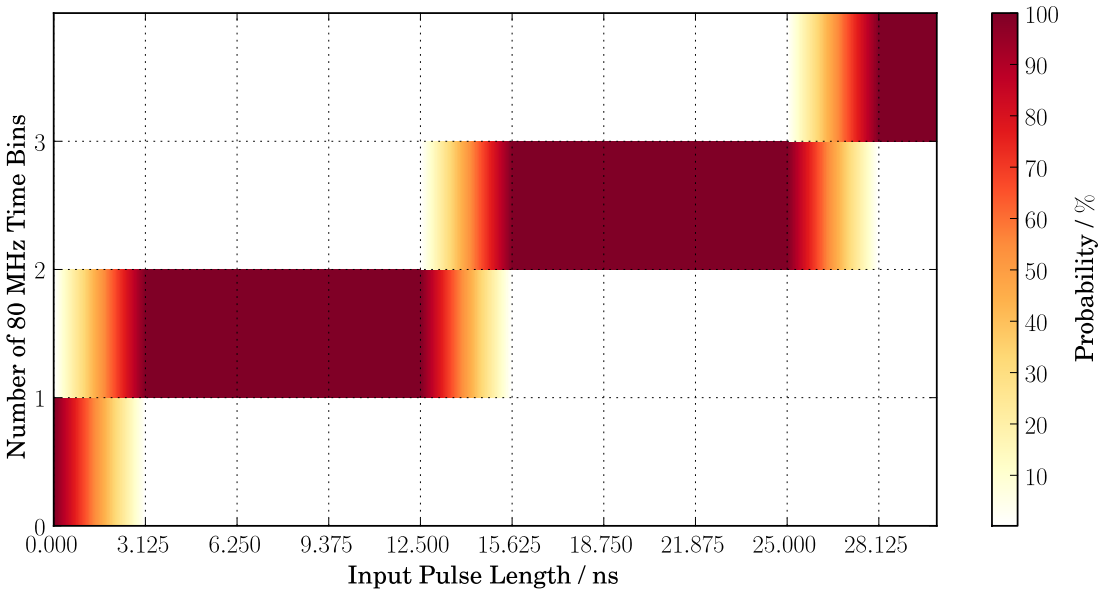

Figure 5.3: *Simulated output pulse length distribution for the downsampling algorithm as implemented in firmware [S2] as a function of the pulse width of input signals according to Equations 5.2 and 5.3. Overall, a total number of* $N = 1.505 \times 10^9$ *events (1,505 bins,* 10^6 *events each) have been simulated.*

5.4.1 Dependence of the Downsampling Algorithm on the Trigger Mode

When using the FPGA's internal self-trigger mode (occupancy mode, Section 5.5), for which the trigger is formed out of the incoming discriminated PMT signals, the output of the downsampling algorithm only depends on the width of the input signal and its position with respect to the 320 MHz sampling clock (Section 5.4). In contrast, when triggering the detector with external trigger signals, additional effects have to be taken into account. Even if both, the trigger signal and the data signals, arrive at the FPGA at the same time, the definitive criterion for the timing is now no more the relative position of both the signals relative to the sampling clock but to the internal 80 MHz clock, since the external trigger signal is only sampled synchronously to this clock. In addition, whenever the detector is connected to an external trigger source, an a priori arbitrary time delay between the data and the trigger signal has to be taken into account. Since all the data acquisition procedures of the FPGA work periodically in terms of the 80 MHz clock cycles, corresponding to a shift of the data by an integer multiple of $\Delta t_{80\,\mathrm{MHz}} = 12.5\,\mathrm{ns}$, this external delay can be considered to be positive or negative (for an example see Figure 5.4).

Depending on both effects, i.e. the sampling of the data and of the trigger signals with different frequencies as well as having an additional external delay between these signals, multiple different scenarios for the output of the downsampling procedure are possible. These scenarios are solely defined by the relative timing of the position of the first sample point of the input data stream and the sampling of the trigger signal.

5.4.2 Comparison of Monte Carlo Data with Measurements

The correct operation and performance of the downsampling procedure implemented is crucial for the integrity and the structure of the recorded data. Therefore, the functionality of this procedure is verified by comparing measurements with theoretical predictions derived from Monte Carlo simulations. In order to also account for the delay, that is due to the usage of an external trigger source, the Monte Carlo code described in the previous section has to be modified. In addition to the 320 MHz sampling clock another clock with a frequency of 80 MHz is implemented, which is used for the detection of the external trigger signal. The delay between this trigger signal and the starting time of the data pulse ΔT can be set as an input parameter of the Monte Carlo simulation.

The measurement is done using the Pattern Board (Section A), that generates an analog output pulse of a given length $\Delta t_{\mathrm{p}}^{\mathrm{pb}}$ on one of its 64 outputs, followed by a T1 trigger signal, which is delayed by a fixed time of $\Delta T^{\mathrm{pb}} = 300\,\mathrm{ns}$ and routed to the dedicated trigger output of the board. The 24-bit T1 timestamp, which follows the T1 trigger signal, is purposely overlooked in the following since it has no effect on the measurement. Whereas the LVDS (low voltage differential signaling) trigger line is directly connected to the AMIGA Digital Board, the signal pulse is fed into the AMIGA Analog Board, where it is processed by the amplifier and discriminator circuit. By this, the relative timing between the signal and the T1 trigger will be modified in two ways. On the one hand, the different routings of both signals will lead to differences in the propagation times and thus will influence the measured

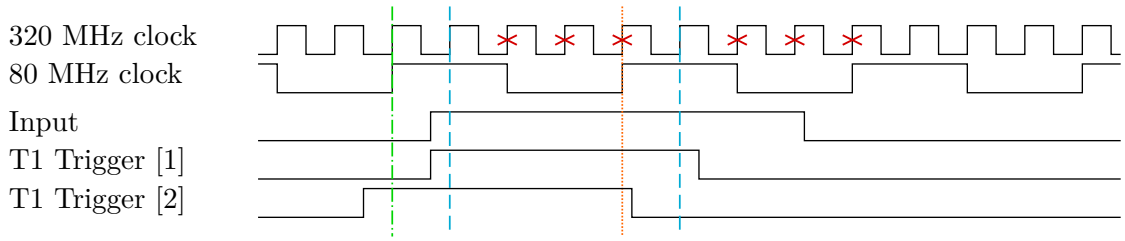

Figure 5.4: *Examples of the processing of T1 triggered data with the FPGA firmware [S2]. The sampling of the input signal (both blue dashed lines) will result in a 25 ns wide output signal. Compared to the data, T1 Trigger [1] will be sampled at a later (orange dotted line) and T1 Trigger [2] at an earlier (green dot-dashed line) time causing the data to be stored on and after the trigger time bin, respectively. The red crosses indicate the disabling of the sampling procedure.*

delay between the two signals, i.e. it is $\Delta T^{\text{meas}} \neq \Delta T^{\text{pb}}$. On the other hand, the measured pulse width $\Delta t_{\text{p}}^{\text{meas}}$ of the data pulse depends on the threshold setting of the Analog Board of the channel under consideration resulting in a decrease of the measured pulse width (i.e. $\Delta t_{\text{p}}^{\text{meas}} < \Delta t_{\text{p}}^{\text{pb}}$). In order to be able to compare the measurement with an independent simulation, it is indispensable to measure the overall timing of the experimental setup as close as possible to the FPGA, since the results will be subject to effects which are in the order of few tens of picoseconds. Therefore, the FPGA's inputs for data and trigger are internally routed to two dedicated output pins where the signals can be tapped with active probes and can then be measured with an oscilloscope. This loop-back causes constant timing offsets on each of both signals due to the signal propagation. These offsets can be estimated to be in the order of a few tens of picoseconds for the given signal routing. The effect of the loop-back on the relative delay between the trigger signals and the data pulses, that will be of particular importance in the following, may therefore total a maximum of a few picoseconds only and will be neglected in the following analysis. By performing the measurement of the timing in the described way, it is avoided to tap the signals between the Pattern Board and the FPGA, which in turn could influence the measurement itself by e.g. adding parasitic capacities. As an example, one measurement and the comparison with the corresponding simulation will be discussed in the following.

Comparison of the Pulse Length Distribution in Self-triggered Mode

For this measurement, the Pattern Board is configured to generate a data pulse with a width of $\Delta t_{\text{p}}^{\text{pb}} = 15.625\,\text{ns}$ corresponding to 5 clock cycles of the internal 320 MHz clock on one of the 64 outputs. On the Analog Boards a global threshold voltage for all channels is set by programming the DACs with a decimal value of $U_{\text{thr}}^{\text{code}} = 950$. By first setting up the AMIGA electronics in the self-triggered mode by using the Occupancy-1 trigger, it is possible to solely measure the pulse length distribution of the downsampling procedure without taking the external trigger delay into account. This limits the Monte Carlo simulation to only one free parameter (compare Section 5.4), namely the measured pulse width $\Delta t_{\text{p}}^{\text{meas}}$ itself. By scanning the simulated input pulse width in an appropriate range with a resolution of 10 ps, the simulation can be tuned to fit the measurement, i.e. the simulation reproduces the

fraction of having one or two time bins filled after the downsampling procedure. For the example discussed here, the pulse width is determined to be $\Delta t_{\mathrm{p}}^{\mathrm{sim}} = 15.14\,\mathrm{ns}$ (Figure 5.5). The results of this simulation are shown in Table 5.3, the errors are derived from binomial statistics.

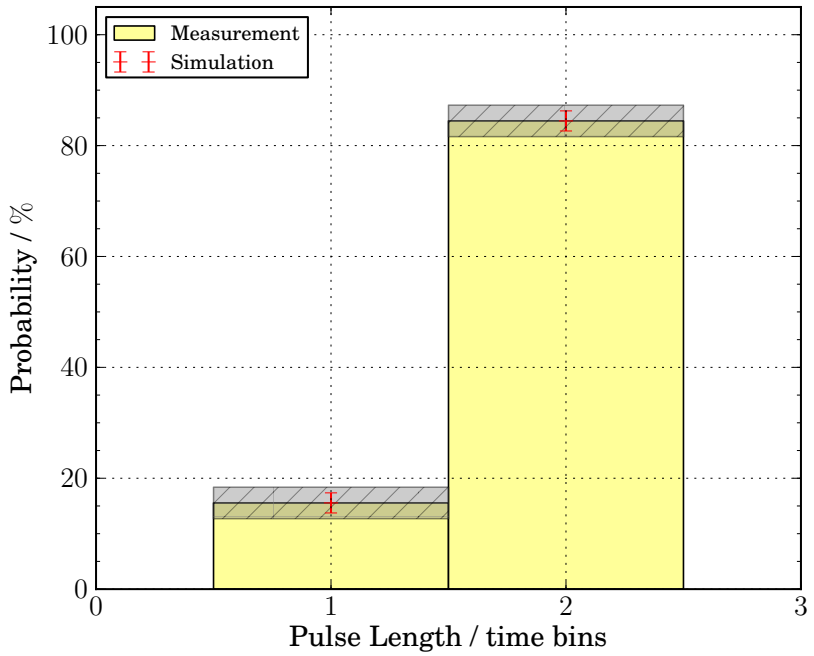

Figure 5.5: *Comparison of a measured pulse length distribution with Monte Carlo simulations. The yellow histogram shows the result of the measurement, the simulated result is represented by the red data points. The statistical errors (gray shaded boxes for the measurement, red error bars for the simulation) are derived from binomial statistics and scaled by a factor of 50 for reasons of visibility. Overall, 405,760 pulses have been measured and a total number of 1,000,000 pulses have been simulated.*

	one time bin	***two time bins***
measurement	$(15.55 \pm 0.06)\,\%$	$(84.45 \pm 0.06)\,\%$
simulation	$(15.56 \pm 0.04)\,\%$	$(84.44 \pm 0.04)\,\%$

Table 5.3: *Comparison of a measured pulse length distribution with Monte Carlo simulations for a simulated input pulse width of $\Delta t_p^{sim} = 15.14\,\mathrm{ns}$. The errors are calculated from binomial statistics.*

A measurement of the real pulse width distribution with an oscilloscope [04] in combination with an active probe [02] after the internal loop-back of the FPGA is shown in Figure 5.6. For an overall number of 559,335 pulses, the width of each individual pulse has been measured at the 50 %-levels of the rising and the falling edges. The 50 %-levels are determined by calculating the average of the high and low level of the pulse using an internal algorithm of the oscilloscope. The resulting pulse widths are stored into a histogram, which is shown in Figure 5.7.

In order to compare the measured pulse width with the result of the Monte Carlo simulation, the mean of the distribution is calculated to $\Delta t_{\mathrm{p}}^{\mathrm{meas}} = (15.15817 \pm 0.00006)\,\mathrm{ns}$. Due to geometrical considerations, the width of a symmetrical distribution centered around the mean has no effect on the overall probability of the downsampling procedure to result in a given number of filled time bins. In order to quantify the deviation of the measured from a symmetrical distribution, which is indicated by a Gaussian fit to the measured distribution ($\chi^2/\mathrm{NDF} = 1639.28/369 = 4.442$) and which is solely shown for illustrative purposes, the skewness γ_1 of the measured distribution, given by its third standardized moment, can be calculated through

$$\gamma_1(X) = \mathcal{E}\left[\left(\frac{X-\mu}{\sigma}\right)^3\right] = \frac{1}{N}\sum_{i=1}^{N}\left(\frac{x_i-\mu}{\sigma}\right)^3 \quad , \tag{5.4}$$

and its error can be estimated to be $\sigma(\gamma_1) = \sqrt{6/N}$ [Ken77]. The x_i are the single measured data points and μ, σ and N are the mean, the standard deviation and the total number of entries of the distribution, respectively. By this, the skewness of the measured distribution is calculated to $\gamma_1(\Delta t_{\mathrm{p}}^{\mathrm{meas}}) = 0.011 \pm 0.003$, which can be interpreted as a small asymmetric accumulation of data points on the left side of the distribution. However, this asymmetry will not be accounted for in the analysis presented here since its influence on the results can be neglected compared to other sources of statistical and especially systematic uncertainties.

In addition to the statistical uncertainty gained from the pulse width measurement described above, a systematic overestimation of the pulse width has to be taken into account. Contrary to the measurement with the oscilloscope, the FPGA does not detect the level of a digital input signal, and thus switches its logical state, at a level of 50 % of the rising or the falling edge. Following the specifications of both AC (alternating current) and DC (direct current) input signals established by the JEDEC (Joint Electron Device Engineering Council) standard for low-voltage TTL input/output signals [Jed07], the detection characteristics of a receiver for a digital input signal is defined by four threshold voltages ($V_{\mathrm{IL(AC)}}$, $V_{\mathrm{IH(AC)}}$, $V_{\mathrm{IL(DC)}}$ and $V_{\mathrm{IH(DC)}}$). After the input signal crosses the AC value ($V_{\mathrm{IL(AC)}}$ for a logic low and $V_{\mathrm{IH(AC)}}$ for a logic high), the receiver changes to the new logic state. The DC values $V_{\mathrm{IL(DC)}}$ and $V_{\mathrm{IH(DC)}}$ indicate the voltage levels at which the final logic state of the receiver is unambiguously defined to be logic low or high [Alt12] (Figure 5.8). In general, this behavior can be accounted for by considering the minimum positive voltage applied to the input which is accepted by the receiver as a logic high V_{IH} and the maximum voltage which is accepted as a logic low V_{IL}. For the FPGA in use, the values of these two voltages are given by the data sheet [Alt12]:

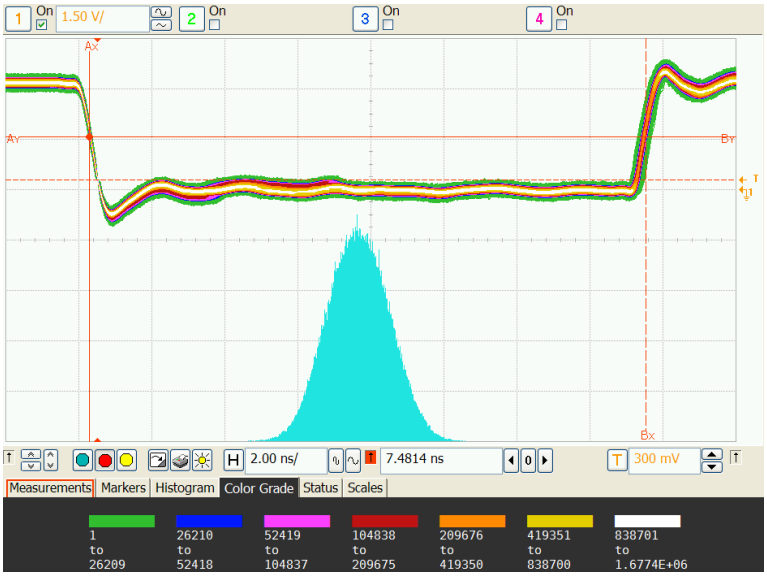

Figure 5.6: *Measurement of the input pulse width of a total number of 559,335 pulses using an oscilloscope [04]. The color coded graphics shows the persistent overlay of all measured pulses divided into seven bins according to the occurrence of the individual data points. The number of entries in each bin is given on the very bottom of the figure. The distribution of the measured pulse lengths is shown by the light blue histogram. The orange markers indicate the pulse width of the last measurement.*

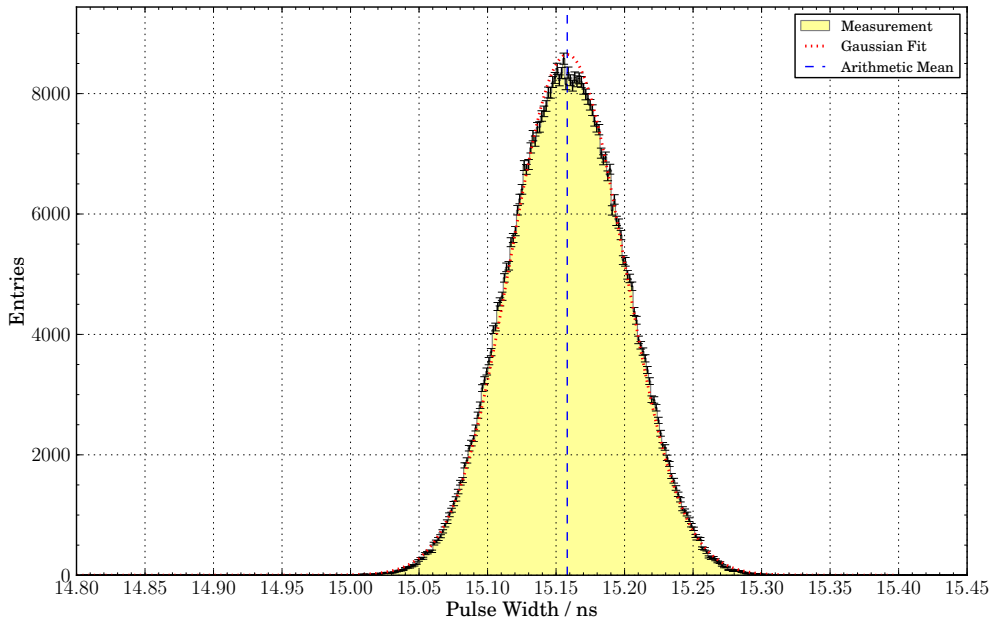

Figure 5.7: *Measurement of the input pulse width for the comparison with Monte Carlo simulations. The measured data is represented by the yellow shaded histogram, the corresponding Poissonian errors are indicated with black error bars. The red dotted curve shows a Gaussian fit to the data ($\chi^2/NDF = 4.442$), the arithmetic mean of the measured distribution is given by the blue dashed line. In total, the pulse widths of 559,335 pulses have been measured.*

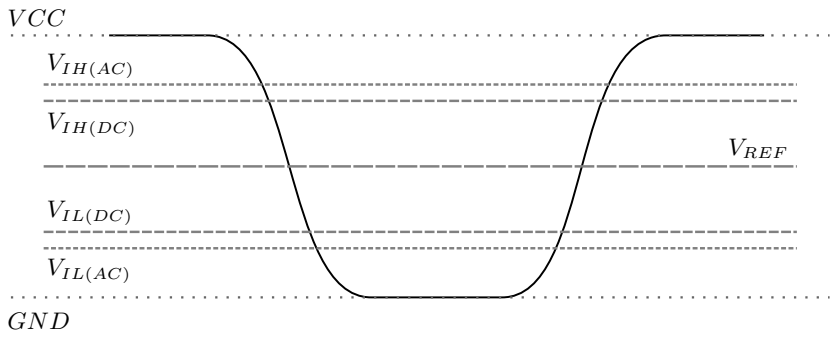

Figure 5.8: *Detection of the logic states of digital input signals. After the input signal crosses the AC value ($V_{IL(AC)}$ for a logic low and $V_{IH(AC)}$ for a logic high), the receiver changes to the new logic state. The DC values $V_{IL(DC)}$ and $V_{IH(DC)}$ indicate the voltage levels at which the final logic state of the receiver is unambiguously defined to be logic low or high [Alt12]. V_{REF} denotes the reference voltage for the HSTL (High-speed transceiver logic) input/output standard, VCC and GND indicate the voltage levels of logic high and low, respectively.*

$V_{\mathrm{IH}} = 1.7\,\mathrm{V}$ and $V_{\mathrm{IL}} = 0.8\,\mathrm{V}$.

The assumption that the final pulse width, which is detected by the FPGA, is determined by the crossings of the signal with the threshold voltages V_{IH} and V_{IL} is equivalent to a measurement of the pulse width between the point where the falling edge crosses 24.24 % and the point where the rising edge crosses 51.52 % of the amplitude. Further on assuming that the slopes of the rising and the falling edges of the input pulses are constant on an interval between 10 % and 90 % of the high level allows for a calculation of the systematic overestimation of the input pulse width. The rise times as well as the fall times of the input signals were measured and the average values were found to be in the order of $t_{\mathrm{r}} \approx t_{\mathrm{f}} \approx 350\,\mathrm{ps}$ (Figure 5.6). A conservative calculation leads to a systematic uncertainty of the measured pulse width of

$$\sigma_{\mathrm{sys}}(\Delta t_{\mathrm{p}}) = -\frac{24.24\,\%}{80\,\%} \times 350\,\mathrm{ps} \approx -110\,\mathrm{ps} \quad . \tag{5.5}$$

This uncertainty dominates the statistical error by about four orders of magnitude since the extent of the effect is independent of the statistics of the measurement whereas the statistical error diminishes when the statistics is increased. Overall, the measured pulse width is found to be

$$\Delta t_{\mathrm{p}}^{\mathrm{meas}} = \left(15.15817 \pm 0.00006\,(\mathrm{stat.})\,{}^{+0}_{-0.11}\,(\mathrm{sys.})\right)\,\mathrm{ns} \quad . \tag{5.6}$$

For the given uncertainties, the result of the measurement is in agreement with the simulated pulse width of $\Delta t_{\mathrm{p}}^{\mathrm{sim}} = 15.14\,\mathrm{ns}$ within an error interval of

$$\frac{\Delta t_{\mathrm{p}}^{\mathrm{meas}} - \Delta t_{\mathrm{p}}^{\mathrm{sim}}}{\sigma(\Delta t_{\mathrm{p}}^{\mathrm{meas}})} = 0.17 \tag{5.7}$$

when quadratically summing up the errors given in Equation 5.6.

Comparison of the Time Distribution of Externally Triggered Events

When using the external T1 trigger, the additional delay due to the different routings of the trigger and the data signals has to be taken into account. This delay will cause the digitized pulses, when stored on the Digital Board, to be spread out over several time bins since the trigger and the data are sampled with different frequencies. Therefore, the trigger signal will be randomly detected before or after the sampling of the input data, dependent on the overall timing for the individual events (cf. Figure 5.9 for the settings considered in this analysis). Although this random process will affect the structure of single events, the final distribution of all recorded events will depend on the average timing only and can again be explained by geometrical considerations.

Since the average width of the input pulses has already been determined in the previous section and will be kept untouched in the following, the delay between trigger and data is the only free parameter left and can now be used to tune the simulation in such a way that it matches the laboratory measurement. By scanning the parameter range in steps of 10 ps it is found that simulation and measurement are in agreement within the statistical uncertainties when applying an external delay of $\Delta T^{\mathrm{sim}} = -8.03\,\mathrm{ns}$. The results of the comparison are shown in Figure 5.10, the exact numbers are given in Table 5.4. As it is apparent from Figure 5.9, all events can be subdivided into six different classes, only distinguished by the timing of the data and trigger signals with respect to the sampling clocks. In particular, the probability of having data in the trigger time bin (time bin 0) as well as in time bin 2 depends on the input timing of the event under consideration whereas time bin 1 will be filled at all times independent of the overall timing.

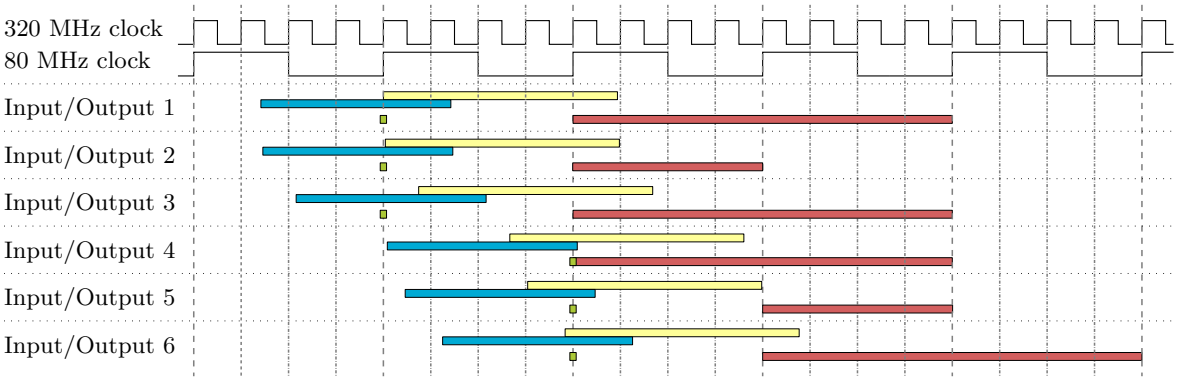

Figure 5.9: *Possible timing scenarios of pulse and trigger detection. The blue bars represent the trigger signals. The data pulses with a width of $\Delta t_p = 15.14\,\mathrm{ns}$ are indicated by the yellow bars, they are delayed by $\Delta T = 8.03\,\mathrm{ns}$ with respect to the corresponding trigger signals. Filled time bins at the output of the downsampling algorithm are represented by the red bars, the sampling points where the trigger signal is formed synchronously to the rising edge of the 80 MHz clock are indicated by the green markers. The dashed and the dash-dotted lines mark the rising edges of the 320 MHz clock and the 80 MHz clock, respectively.*

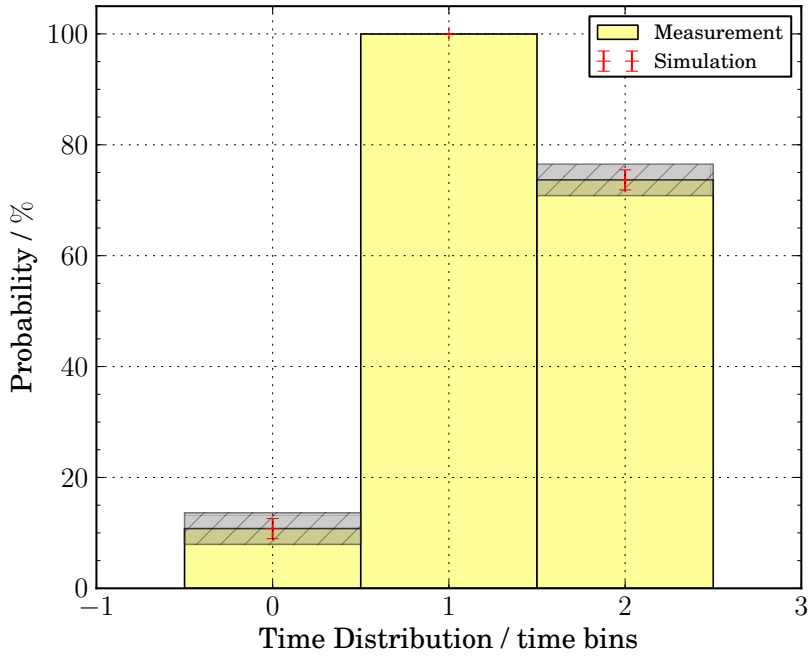

Figure 5.10: *Comparison of the measured time distribution with Monte Carlo simulations for externally triggered data. The yellow histogram shows the result of the measurement, the simulated result is represented by the red data points. The statistical errors (gray shaded boxes for the measurement, red error bars for the simulation) are derived from binomial statistics and scaled by a factor of 50. The trigger time bin is defined as time bin 0. Overall, 405,760 pulses have been measured and a total number of 1,000,000 pulses have been simulated.*

	time bin		
	0	***1***	***2***
measurement	$(10.78 \pm 0.06)\,\%$	$(100.00 \pm 0.00)\,\%$	$(73.67 \pm 0.06)\,\%$
simulation	$(10.78 \pm 0.04)\,\%$	$(100.00 \pm 0.00)\,\%$	$(73.67 \pm 0.04)\,\%$

Table 5.4: *Comparison of the measured time distribution with Monte Carlo simulations for externally triggered data for a simulated input pulse width of $\Delta t_p^{sim} = 15.14\,\mathrm{ns}$ and an additional delay of the trigger signal of $\Delta T^{sim} = -8.03\,\mathrm{ns}$. The errors are calculated from binomial statistics.*

With the laboratory setup already described in the previous section, the delay between the falling edge of the data pulse (negative TTL signal) and the rising edge of the T1 trigger signal (positive TTL signal) is measured with a digital oscilloscope [23] by tapping the signals at the loop-back outputs of the Digital Board with two active probes [22] (Figure 5.11). For an overall number of 21,493 events, the average delay measured between the 50 % levels of both signals is found to be $\Delta T^{\text{scope}} = (292.135 \pm 0.003)\,\text{ns}$, where the statistical error is given by the timing resolution of the oscilloscope $\sigma_{\text{t}} = 400\,\text{ps/pt}$ divided by the square root of the number of recorded events. Since the firmware of the FPGA works periodically in intervals of 12.5 ns, implying in particular that the output of the downsampling algorithm is invariant under shifting both clocks (320 MHz and 80 MHz) by integral multiples of 12.5 ns, the measured delay can be translated into $\Delta T^{\text{scope}} = (-7.865 \pm 0.003)\,\text{ns}$. By this, the delay is in the predefined interval $[-12.5\,\text{ns}; 0\,\text{ns})$ and can therefore directly be compared with the Monte Carlo simulation.

On top of the statistical error mentioned above, further systematic uncertainties have to be accounted for. On the one hand, since the delay is measured between a falling and a rising edge of the signals, the considerations concerning the signal detection of the FPGA as discussed above apply equally to this measurement and the resulting systematic uncertainty of $\sigma_{\text{sys}} = ^{+0}_{-0.11}$ ns has to be taken into account here as well. On the other hand, another systematic uncertainty arises due to the jitter of the rising edge of the T1 trigger signal with respect to the falling edge of the data pulse. In order to account for this effect, a more

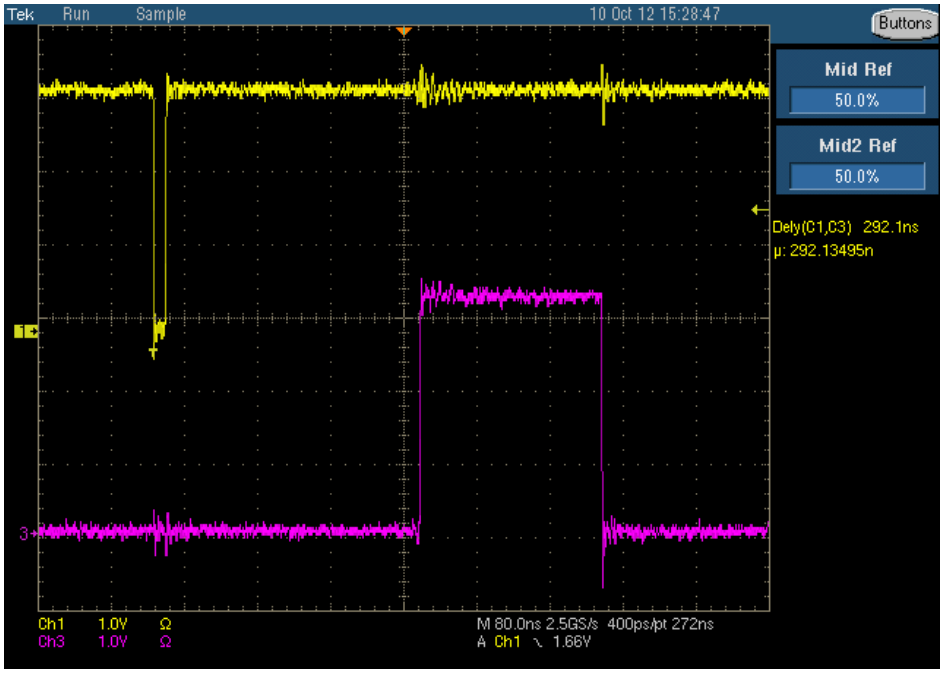

Figure 5.11: *Measurement of the trigger delay using an oscilloscope [23]. The negative data pulse is represented by the yellow (upper) waveform, the positive T1 trigger signal is shown in magenta (lower waveform). The average delay between both signals has been measured to be* $\Delta T^{scope} = (292.135 \pm 0.003)\,\text{ns}$ *for an overall number of 21,493 events.*

detailed measurement of the jitter is performed. By setting the oscilloscope's trigger threshold to the 50 %-level of the data pulse and by triggering on the falling edge, it is possible to measure the time where the rising edge of the T1 trigger signal crosses a fixed threshold of $U_{\text{thr}} = 1.65\,\text{V}$ corresponding to half of the signal amplitude. For an overall number of 66,899 events, this timing information is recorded in terms of filling a histogram (Figure 5.12). The sum of two Gaussian distributions is fitted to the data ($\chi^2/\text{NDF} = 249.7/44 = 5.676$), which is assumed to be a sufficient representation of the data when solely aiming at a conservative estimation of the systematic uncertainty. The deviation of the distribution from a single Gaussian distribution can be explained by the fact that the measurement of the jitter has been performed close to the maximum resolution of the oscilloscope, at which the internal $\sin(x)/x$-interpolation has a non-negligible effect on the measurement. From the fit, the statistical uncertainty is derived by applying a horizontal cut in such a way that the integral of the fit between the two intersections of the cut and the fit contains 68.3 % of the overall area under the fit curve (1-σ interval). With the time difference between the two intersection points calculated to be $\sigma_{\text{fit}} = 126.5\,\text{ps}$, the uncertainty due to the jitter between the two signals results in $\sigma_{\text{jitter}} \approx 0.06\,\text{ns}$.

Taking everything mentioned above into account, the measured delay is found to be

$$\Delta T^{\text{meas}} = \left(-7.87 \pm 0.003\,(\text{stat.}) \pm 0.06\,(\text{jitter}) \,^{+0}_{-0.11}\,(\text{sys.})\right)\,\text{ns} \quad . \tag{5.8}$$

When summing the given uncertainties quadratically, the deviation of the measurement from the Monte Carlo simulation ($\Delta T^{sim} = -8.03\,\text{ns}$) can be calculated as

$$\frac{\left|\Delta T^{\text{sim}}\right| - \left|\Delta T^{\text{meas}}\right|}{\sigma(\Delta T^{\text{meas}})} = 1.28 \quad . \tag{5.9}$$

The total error is dominated by the systematic uncertainty of the measurement, both results are in agreement with each other. The downsampling of input signals, as it is performed by the FPGA firmware, is well understood and the output can be reproduced with simulations. These simulations could be incorporated into a full detector simulation of the AMIGA muon counter, which, however, is beyond the scope of this thesis.

5.5 The Occupancy-N Trigger

In order to be independent of any external trigger source, such as the T1 trigger of the SD station or a pulse generator in the laboratory, an internal self-trigger algorithm has been included in the FPGA firmware, referred to as Occupancy-N trigger. This internal trigger was implemented at a very early stage of the code development and could therefore be used for debugging and testing almost all the FPGA firmware features as well as the AMIGA hardware itself. Aiming at a flexible trigger, that can be used for various testing scenarios and which is solely formed by the incoming signals of the PMT, or any other input device such as the Pattern Board (Section A), the Occupancy-N trigger evaluates the multiplicity of channels which simultaneously show a signal. To fulfill the trigger criterion of the Occupancy-N trigger, at least N front-end channels must show a signal within one 80 MHz time bin after having

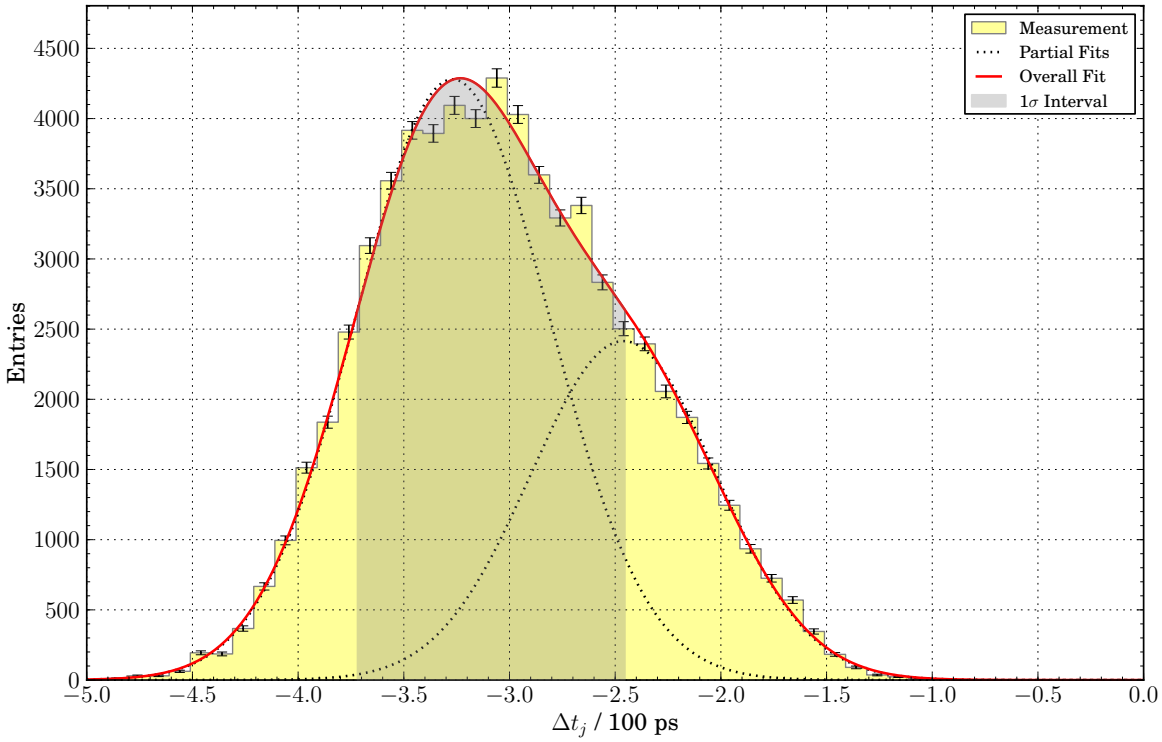

Figure 5.12: *Measurement of the jitter between data pulse and T1 trigger signal for a total number of 66,899 events represented by the yellow histogram. The systematic uncertainty due to the jitter is derived by determining the 68.3 %-interval around the maximum of the fitted distribution (gray shaded area). The black dotted curves indicate the two Gaussian fits of the left and right tail of the distribution. The red curve shows the superposition of two Gaussian distributions fitted to the data ($\chi^2/NDF = 5.676$). The absolute values given on the x-axis are of no importance for the determination of the jitter since they only depend on the adjustment of the oscilloscope during the measurement.*

passed the downsampling algorithm. By this, the internal self-trigger is also sensitive to signals which are shorter than 12.5 ns, since all signals are sampled synchronously to the 320 MHz clock. However, they do not necessarily have to fulfill the criterion of being exactly simultaneous in time (see Section 5.4).

The Occupancy-N trigger can be activated by setting the fourth bit of the control register `0x48` to a high state by e.g. executing the corresponding script of the AMIGA SBC acquisition software [S4]. The number of channels N which have to simultaneously show a signal, also referred to as active channels, is predefined by the value of the corresponding input register (the six most significant bits of register `0x4A` (Section 5.3, $N \in [0; 63]$). This value can be set by the user by e.g. using a script of the AMIGA SBC software framework. Synchronously to each rising edge of the 80 MHz clock, this number has to be compared to the present number of active channels. Therefore, the number of signals in the 64 channels is first summed in packages of six channels at a time using a look-up table, thus converting a 6-bit value into

a 3-bit number. The choice of combining six lines at once is a compromise between speed and simplicity of the code. The results of these routines are then added pair-by-pair in an iterative process which is repeated four times until the algorithm results in the calculation of the number of active channels. The FE channels 60 to 63 are not accounted for in the first step of the iterative process, but only in the second step. Finally, the number of active channels is compared to the predefined occupancy value in the input register and, in case both values agree or the multiplicity of active channels exceeds the predefined value, the trigger signal is formed. In Figure 5.13, the complete routine is represented by a flow chart. Although the whole algorithm of calculating the multiplicity of active channels is executed asynchronously in order to not affect the overall timing of the FPGA firmware, the data which are obtained after the fourth step of the calculation as well as the final trigger signal are latched to the 80 MHz clock to ensure data integrity. Therefore, the algorithm has been split into two parts, implemented into the D-bin and the E-bin routine of the FPGA firmware, and thus requires two clock cycles of the 80 MHz clock. At the same time, the actual PMT data is pipelined for two clock cycles to follow the concept of synchronicity of the FPGA firmware.

Despite the fact that the Occupancy-N trigger, as it is implemented in its current form, is realized in a well and long term proven manner (Section 5.5.1), it could be simplified by using a parallel add algorithm, which is available as a megafunction [Alt07] for the FPGA in use and that could reduce determining the multiplicity of active channels to a one-step calculation [Sza12]. However, this possible simplification of the design is beyond the scope of this thesis but could be implemented in future versions of the AMIGA FPGA firmware.

5.5.1 Test of the Occupancy-N Trigger

The Occupancy-N trigger has been used not only for performing extended tests of the AMIGA detector hardware itself, but also for data taking with the first prototype muon counters at the experimental site in Argentina. In order to assure the correct functionality of the Occupancy-N trigger, various tests of this internal self-trigger have been performed in advance, such as recording data multiplicity sensitive patterns with the internal pattern generator as well as external signal sources. In addition, all self-triggered data recorded with the prototype detectors can be used to verify the performance of the trigger in the framework of data analysis at a later stage. Here, one test of the Occupancy-N trigger will be discussed in detail, as a representative example of the measurements which have been performed.

The Pattern Board (Section A) allows for generating arbitrary patterns, which can be adapted to be used to test the Occupancy-N trigger. In Figure 5.14 two measurements of a dedicated pattern, that includes several different multiplicities of active channels, is shown. For these measurements, the Pattern Board is programmed such that it generates single events, which contain eight different signal multiplicities each, starting with one active channel and, with a given delay between the blocks of data, sequentially increasing the number of active channels up to a signal multiplicity of eight. The Occupancy-N trigger is expected to be raised as soon as the given signal multiplicity equals the adjusted occupancy level. Since each event is made up of different signal multiplicities, using this pattern in a fully automated test environment allows for a test of the functionality of the Occupancy-N trigger with high

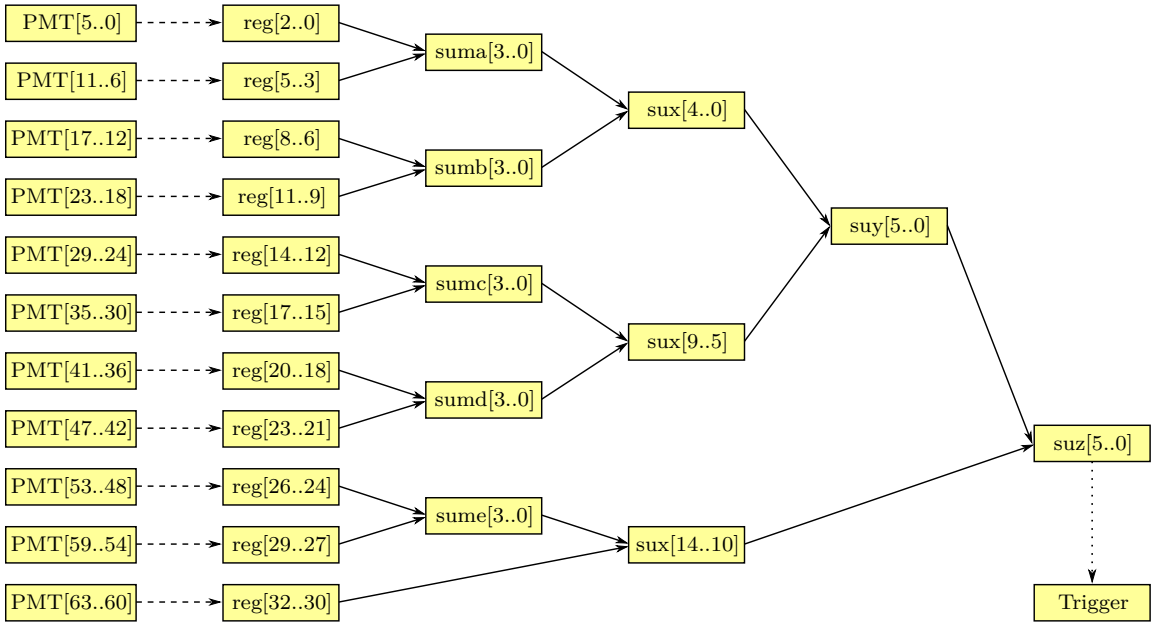

Figure 5.13: *Flowchart of the Occupancy-N trigger algorithm. In a first step, the number of active channels of the 64 channels is counted in packages of six channels at a time (dashed lines). In the following four steps, the results are summed up pair-by-pair (solid lines) in an iterative process. In a last step, dependent on the result of the comparison between the calculated number of active channels and the predefined value in the input register, the trigger signal is formed (dotted line).*

statistics. By generating the different signal multiplicities on different front-end channels, a malfunction of the Occupancy-N trigger can be easily identified as a significant shift of the pattern structure within the recorded event data.
To avoid that recorded events are modified by the copy mechanism when switching between both input buffers of the FPGA firmware (Section 5.2), the overall length of the pattern is chosen to be less than 3.2 µs, which corresponds to one half of the length of the fast buffer. Therefore, the width of each pulse inside the pattern is chosen to be $\Delta t_{\mathrm{p}}^{\mathrm{pb}} = 6.25\,\mathrm{ns}$ corresponding to two clock cycles of the Pattern Board's internal 320 MHz clock, the time between two consecutive pulses is set to 32 clock cycles and thus measuring up to $\Delta t_{\mathrm{gap}}^{\mathrm{pb}} = 100\,\mathrm{ns}$. By directly connecting the outputs of the Pattern Board to the input socket of the Mother Board, the output pulses will pass the amplifier and discriminator circuits of the Analog Boards and the pattern will be recorded by the Digital Board as soon as the signal multiplicity of the pattern fulfills the criterion of the Occupancy-N trigger. To suppress noise, which might cause multiplicities to occur independent from the generated pattern, channels which are not used within the pattern are disabled inside the FPGA by setting the values of the associated registers (`0x4C`...`0x4F`, Section 5.3), e.g. by executing the corresponding script of the AMIGA SBC software framework [S4].

The results of two measurements with the described pattern are shown in Figure 5.14 for two different occupancy levels. Overall, 184,576 events (721 runs with 256 events each) and

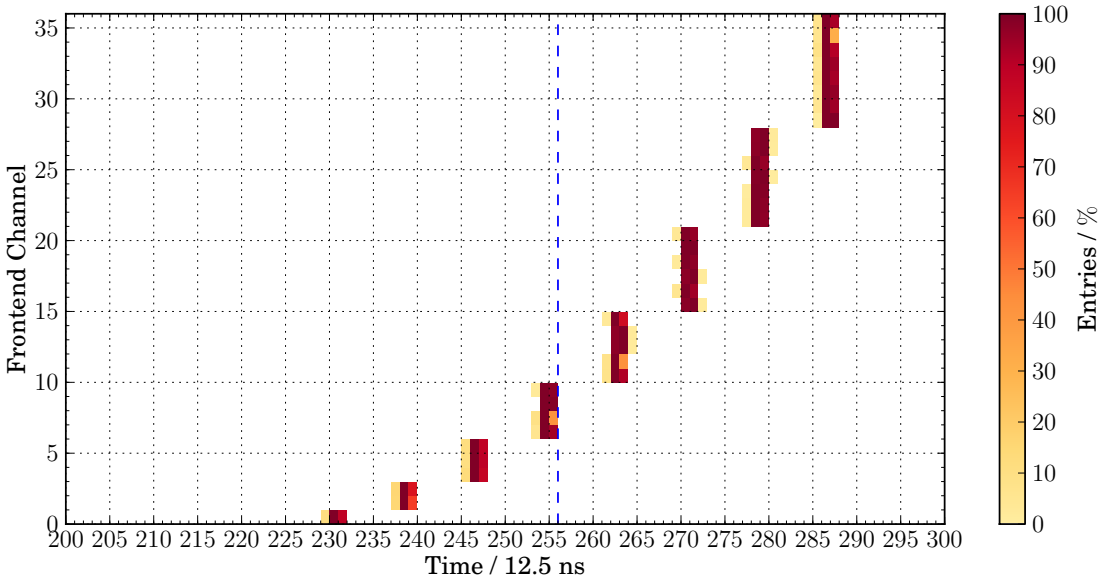

(a) *Occupancy-4*

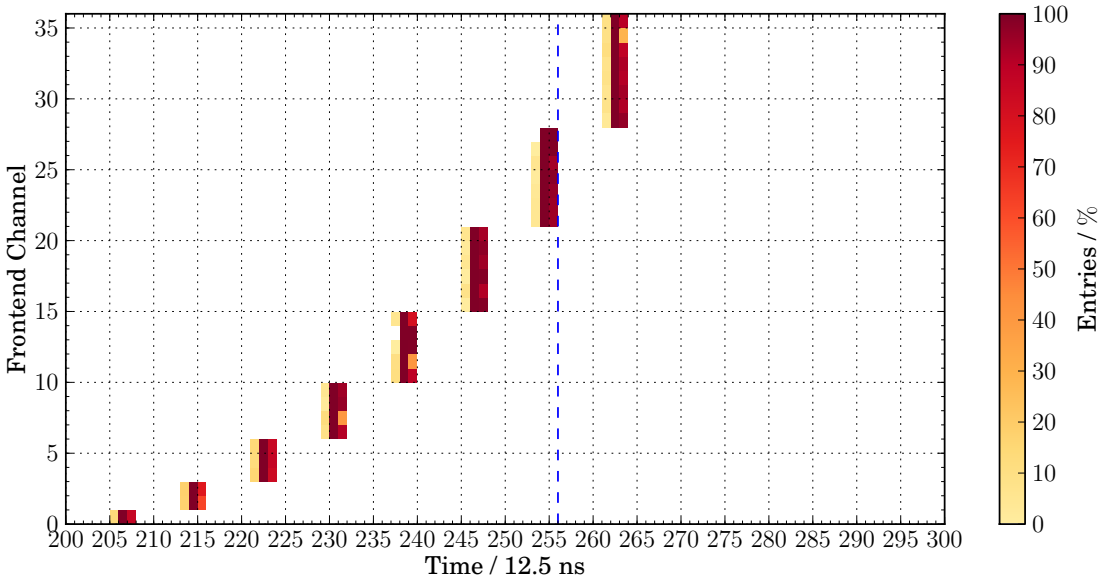

(b) *Occupancy-7*

Figure 5.14: *Laboratory test of the Occupancy-N trigger for two measurements with occupancy levels of $N = 4$ and $N = 7$, respectively. The plots show an overlay of all recorded events. The color coded markers represent the probability of having an entry in an event as a function of time and the front-end channel number. In both subfigures the trigger condition is fulfilled on time bin 254, the blue dashed line indicates the transition from one of the two ring buffers to the corresponding fast buffer. No malfunction of the Occupancy-N trigger, which could be identified as a significant shift of the pattern, has been observed. Overall, 184,576 events (Occupancy-4) and 166,656 events (Occupancy-7) have been recorded.*

166,656 events (651 runs with 256 events each) have been recorded for occupancy levels of $N = 4$ (Figure 5.14a) and $N = 7$ (Figure 5.14b), respectively. Both plots show an overlay of all signals contributing to the measured events normalized to the total number of recorded events, thus depicting the probability for the appearance of entries within an AMIGA event as a function of time and the front-end channel number. In both subfigures, the time at which the storage of incoming signals switches from one of the two ring buffers to the corresponding fast buffer is indicated by the blue dashed line between the time bins 255 and 256, where the trigger signal is raised. In all events the condition of the Occupancy-N trigger is, for the first time, fulfilled on time bin 254. The shift of the data by one time bin (trigger condition fulfilled on time bin 254 instead of 255) of all entries is an artifact of the prescaler module (Section 5.6), which prolongates the trigger signal by one clock cycle with respect to the data even if the prescaling itself is disabled. The different fragmentations of the signals into up to three time bins, even though the width of the output pulses of the Pattern Board is being set to $\Delta t_{\mathrm{p}}^{\mathrm{pb}} = 6.25\,\mathrm{ns}$, can be explained by considering two effects: first of all, the signals are modified in terms of their pulse shapes as soon as they pass the amplifying circuits of the Analog Boards. The extent of this modification is dependent on the unique characteristics of each single channel, especially when using a global threshold of the discriminators for all 64 channels (here: $U_{\mathrm{thr}} = 60\,\mathrm{mV}$). Apart from that, all amplified signals are then subject to the statistical spreading due to the input downsampling procedure (Section 5.4), which is dependent on the absolute timing of the system. Taking this fragmentation as well as the shift due to the prescaler module into account, it is found that the Occupancy-N trigger reacts on the multiplicity of the incoming data with an efficiency of 100 %. This result is also confirmed by dedicated analyses of high statistics data taken with the muon counters of the PUC, in which no malfunction of the Occupancy-N trigger has been observed.

5.6 The Prescaler Algorithm

The AMIGA detector has been designed to take data synchronously with the SD array of the Pierre Auger Observatory. This in particular effects the choice of the depth of the memory and the length of a single muon counter event, since these settings have to adapt to the average trigger rate of the assigned SD station of $f_{\mathrm{T1\,Trigger}}^{\mathrm{SD}} \approx 100\,\mathrm{Hz}$ (Section 3.1.2). In contrast to this, self-triggered data taking with low occupancy values or measurements with low threshold settings applied to the Analog Boards might lead to high trigger rates. As a consequence, dead times, which arise due to the rejection of new trigger signals during the event readout when both fast buffers are completely filled, might lead to a bias of the recorded data, since rapidly incoming sequential events will be systematically suppressed. This issue can be overcome with the implementation of a prescaler algorithm, that filters the trigger signals by only reacting on every n-th trigger signal, where the prescaler value n can be set during the runtime of the muon detector.
A second advantage of having the possibility to prescale the recorded events is due to the fact that the AMIGA PUC is composed of different types of electronics systems, which especially concerns the depth of the event memory. Whereas six muon counter stations of the PUC can handle 2,048 recorded events, two detectors (the $5\,\mathrm{m}^2$ and $10\,\mathrm{m}^2$ counters connected to the SD station 'Corrientes') are limited to a maximum number of 256 events, which can

be stored into the internal memory at a time. Since receiving an event request sent by the CDAS can be delayed by up to 10 seconds [Sat10] relative to the time when the event has been recorded, event data might be already overwritten. The delay heavily depends on the workload put on the CDAS but may not exceed the time given above, since the amount of memory of the local station electronics is limited to 1,024 events with an average trigger rate of $f^{\mathrm{SD}}_{\mathrm{T1\ Trigger}} \approx 100\,\mathrm{Hz}$. Therefore a successful readout of all events might be in general no longer possible, thus leading to a time-dependent bias of the results of the measurements. This issue can be overcome by prescaling the incoming trigger signals, which causes the recorded events to be evenly spread over time.

5.6.1 Implementation of the Prescaler Algorithm

The prescaler algorithm is implemented into the F-bin routine of the AMIGA FPGA firmware. At this stage of the code, the final trigger signal, which will initiate the acquisition of an AMIGA event, is generated from one of the possible trigger sources. In addition to the external trigger mode, which primarily uses the T1 trigger signal of the associated SD station (Section 5.7), and the internal Occupancy-N trigger (Section 5.5), two other trigger modes, which have only been used for debugging the system in laboratory measurements, can be chosen by the user by setting the intertwined bit of the control register (Section 5.3). In order to adjust the prescaler so that it fits the needs of the measurement, a 16-bit register (`0x52`) is implemented to be the interface between the user and the prescaler algorithm. This register can be controlled by e.g. executing the corresponding script of the AMIGA SBC software framework [S4]. Whereas the highest bit of this register will turn the prescaler function on (bit set to 1) or off (bit set to 0), the 15 least significant bits are used to define the prescaler value n.

In order to verify the correct functionality of the prescaler algorithm, some selected results of laboratory measurements will be discussed in the following. For these measurements, the Pattern Board (Section A) is connected to the AMIGA system and repeatedly generating an analog output pulse with a length of $\Delta t^{\mathrm{pb}}_{\mathrm{p}} \approx 15\,\mathrm{ns}$ on one of its 64 outputs. Although the pulse width is chosen to be in the order of magnitude of a real scintillator signal, the exact value is of no importance for the measurements discussed here. The time delay between two consecutive pulses is set to be $\Delta T = 32\,\mu\mathrm{s}$ corresponding to 32 clock cycles of the internal 1 MHz clock of the Pattern Board. By choosing the time between two events to be larger than the total length of an AMIGA event of $\tau_{\mathrm{event}} = 9.6\,\mu\mathrm{s}$ (see Section 5.2) it can be assured that the buffer copy mechanism of the FPGA firmware will not become active. By using the internal self-trigger of the AMIGA system and setting the occupancy value to $N = 1$, each data pulse will cause the system to form a trigger signal. Different internal signals of the FPGA firmware closely linked to the execution of the prescaler module, such as the input data, the sampled data pulses and the trigger signals at different stages of the data processing, are routed to the dedicated test outputs of the Digital Board where they can be tapped and recorded with a digital logic analyzer [03] with a timing resolution of 1 GHz operated in the half channel mode. In this way, the measurements allow to investigate the behavior of the prescaler algorithm and especially its impact on the overall timing of the system.

Figure 5.15 allows to follow the signals as they are pipelined throughout the internal signal

chain of the FPGA. The incoming data pulse (`Ext_PMT`) will be first synchronized to the internal sampling clock with a frequency of 320 MHz (`RA_PMT`). Modified by the downsampling procedure (`RB_PMT`), which in this case produces a signal with a length of two time bins defined by the 80 MHz clock (`Clk`), the data is propagated for three clock cycles to the E-bin routine (`RE_PMT`) where it is used to form a trigger signal (`RE_PMT_Trig`) since the requirements of the Occupancy-1 condition are fulfilled. In case of running the detector without the prescaler, this trigger signal will not be affected but only be delayed by one clock cycle of the 80 MHz clock (Figure 5.15a) since it has to be linked to an internal signal (`!timer_400ns`) which disables the trigger for a time window of 2.9 µs in order not to interpret the timestamp which follows a T1 trigger signal as additional incoming trigger signals (Section 5.7.1). This will cause the recorded data (`RG_PMT`) to be shifted by one time bin with respect to the final trigger signal (`RF_Fast_Trig_Sync`), i.e. the PMT signals that cause the trigger to be formed when using the internal Occupancy-N trigger will be stored on time bin 254 (compare Figure 5.14).

With the prescaling algorithm enabled, the original trigger signal is used to increment the value of a counter implemented into the prescaler routine of the FPGA firmware. Synchronously to each rising edge of the 80 MHz clock, the value of the counter is compared to the prescaler value n, which is defined by the user and which is stored in the register mentioned above. Only if both values agree with each other, the counter is reset and a trigger signal is formed, which then will initiate the recording of the event data. As can be seen from figure Figure 5.15b, enabled prescaling will add an additional delay of 3 time bins to the trigger signal which in total causes the data (`RG_PMT`) to be shifted by 4 clock cycles of the 80 MHz clock with respect to the position of the final trigger signal (`RF_Fast_Trig_Sync`). A second artifact of the prescaler algorithm modifying the outgoing trigger signal is due to the fact that the rising edge of the trigger output of the algorithm itself is used for resetting the prescaler counter. This causes the final trigger signal to be prolonged to a total length of three time bins (Figure 5.15b).

By increasing the time window of the measurement to about 500 µs, the correct functionality of the prescaler algorithm can be verified. Some results of these measurements are exemplarily shown in Figure 5.16. Whereas the data flow inside the FPGA, when running the detector with the prescaling routine being disabled, is shown in Figure 5.16a, Figure 5.16b illustrates the case for which the prescaling value is set to $n = 4$. Again, since the system is running in occupancy mode with an occupancy value of $N = 1$, each incoming signal generated by the Pattern Board (`Ext_PMT`) will cause the system to form a trigger signal (`RE_PMT_Trig`). The final trigger signal (`RF_Fast_Trig_Sync`) processed by the prescaling algorithm is now generated for every fourth incoming trigger signal (`RE_PMT_Trig`) neglecting the incoming trigger signals in between.

5.6.2 Dependence of the Prescaling on the Trigger Rate

In order to analyze the behavior of the prescaling algorithm for different trigger rates, an arbitrary waveform generator [01] is used as a trigger source. This allows to perform measurements with the AMIGA system which cover a wide range of trigger rates from several Hz to a few hundred kHz and in which the trigger rate can be adjusted with very high precision. Since the waveform generator cannot produce differential signals, it is set up in a way that it generates

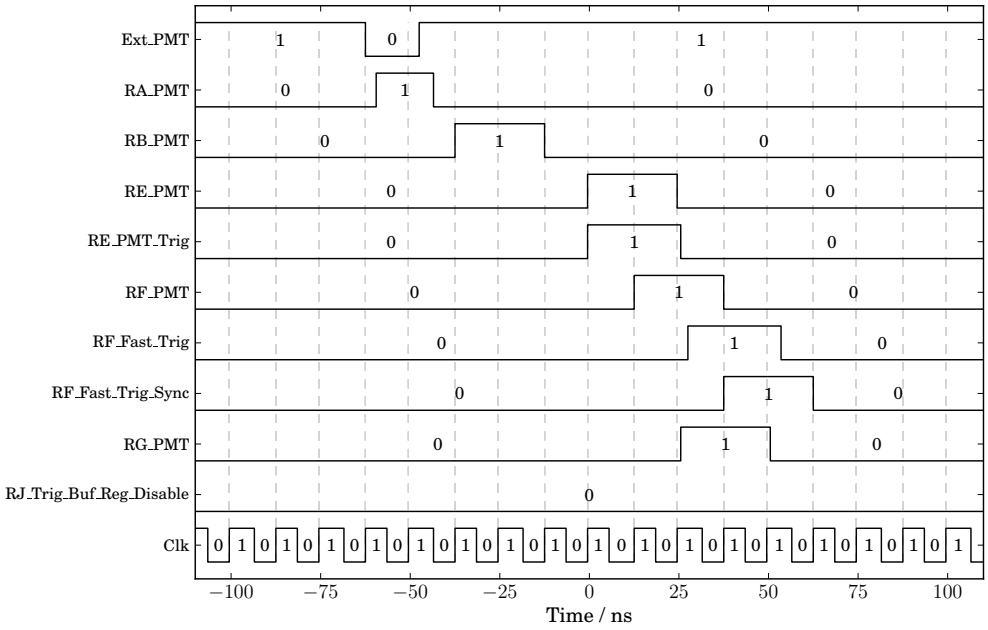

(a) *Timing measurement with the prescaler algorithm disabled.*

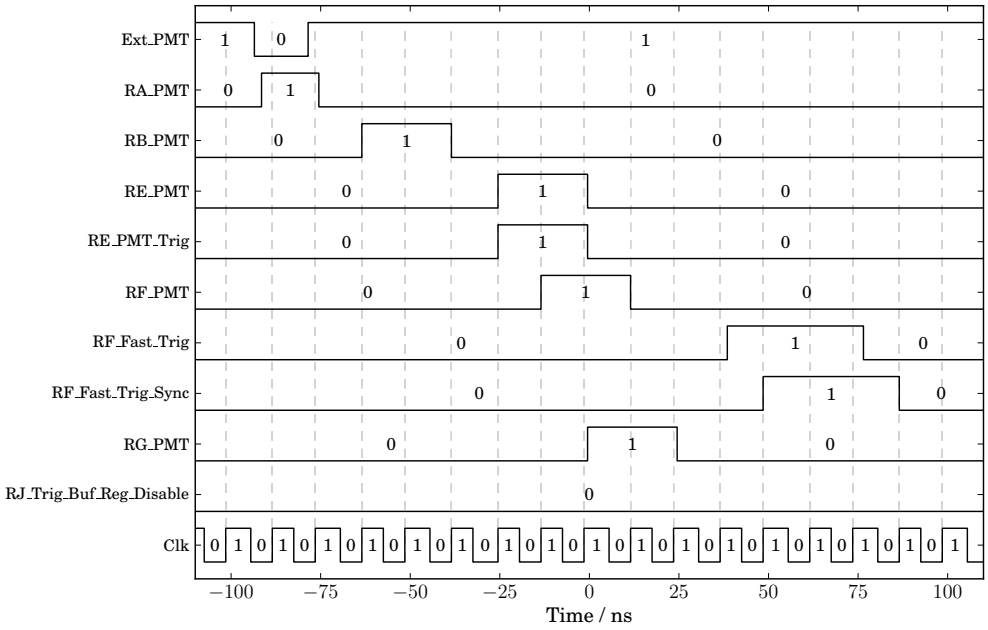

(b) *Timing measurement with the prescaler algorithm enabled.*

Figure 5.15: *Laboratory measurement of the timing of the prescaler algorithm for disabled (upper panel) and enabled prescaling (lower panel). Both pictures show the logic states of FPGA signals characteristic for the functionality of the prescaler. Here,* `R[A...J]` *denotes the routine where the individual signal is measured (e.g. A-bin routine).* `Ext_PMT` *shows the data pulse generated by the Pattern Board. In particular, the specific delay between the final trigger signal (*`RF_Fast_Trig_Sync`*) and the recorded data pulse (*`RG_PMT`*) can be clearly seen.*

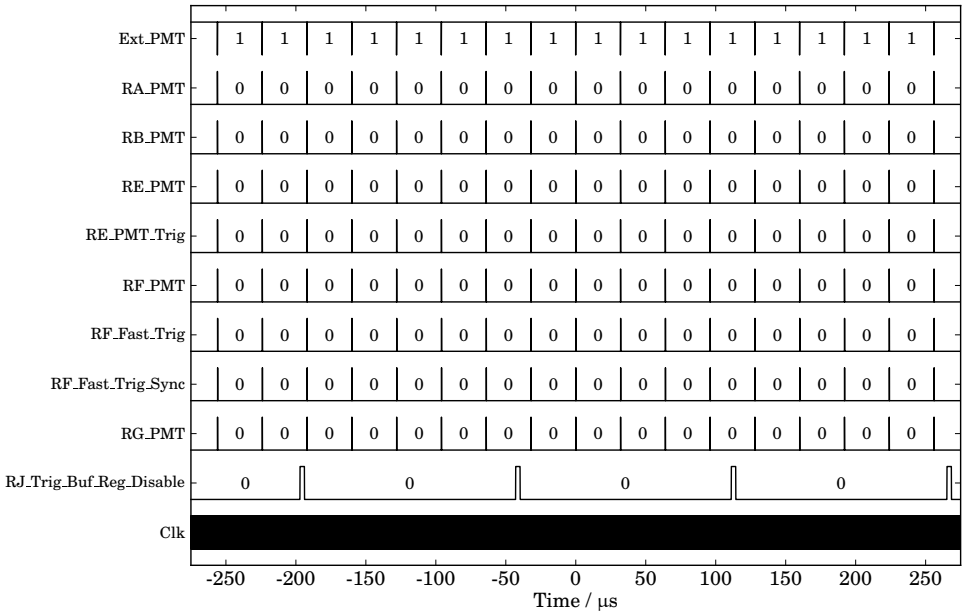

(a) *Measurement of the trigger system with disabled prescaling.*

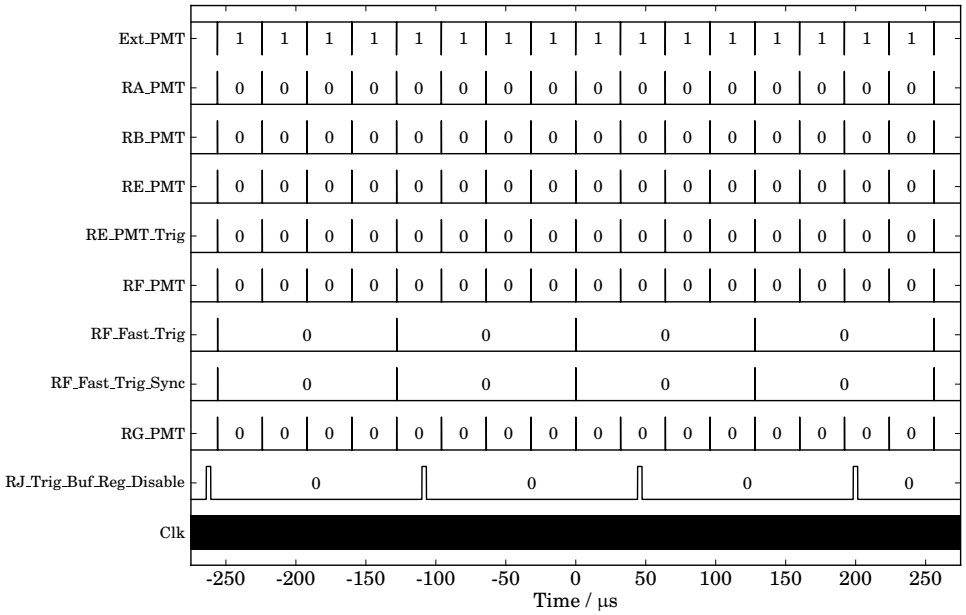

(b) *Measurement of the trigger system with the prescaler value set to* $n = 4$.

Figure 5.16: *Laboratory measurement of the trigger system with and without prescaler. The upper and lower panel show the logic states of FPGA signals characteristic for the functionality of the prescaler for disabled prescaling and a prescaler value of* $n = 4$*, respectively. Here,* `R[A...J]` *denotes the routine where the individual signal is measured (e.g. A-bin routine).* `Ext_PMT` *shows the data pulses generated by the Pattern Board, the final trigger signal is denoted as* `RF_Fast_Trig_Sync`*. Compared to Figure 5.15, a wider time window is chosen in order to cover multiple prescaling cycles.*

negative polarized trigger signals with an amplitude of $U_{\text{high}} = 3.3\,\text{V}$ (TTL standard) and a pulse width of 100 ns. These signals then first have to be converted into symmetrical LVDS signals before they can be fed into the T1 trigger chain of the AMIGA system. This conversion is done by an independent PCB (printed circuit board), that originally was intended to be used for tests of the AMIGA Power Distributor Board and which includes a converter and isolator circuit as it is realized on the Power Distributor Board itself (Section 4.5.1). After the AMIGA FPGA is set up to acquire data in the T1 trigger mode, the rate of the incoming trigger signals can be directly measured with the internal rate counter implemented into the FPGA firmware.

The standard version of the rate counter as it is used for measurements in the field, i.e. for the detector calibration with background muons [Pon12], consists of a 11-bit counter which is incremented with every incoming trigger signal after it has been processed by the prescaler algorithm. By using the most significant bit for disabling the counter, the maximum trigger rate, that can be measured, is limited to $f_{\text{trig}}^{\text{max}} = 1024\,\text{Hz}$ (corresponding to 10 bits). Synchronously to the rising edges of a clock with a frequency of 1 Hz, the latest counter value is written into an output register of the FPGA (`0x42`) and a synchronous reset of the counter is performed. The output register can be automatically read out, e.g. by executing a dedicated shell script on the AMIGA single board computer (SBC DAQ software version [S4]). A more detailed description of the rate counter as well as measurements determining its precision are discussed in [Tig11]. Since the measurements described in this section also include the determination of the performance of the prescaler algorithm at high incoming trigger rates, the rate counter procedure is extended in terms of enhancing the depth of the counter to 16 bits, thus increasing the maximum trigger rate that can be measured to $f_{\text{trig}}^{\text{max}} = 65.535\,\text{kHz}$. By reserving all 16 bits of the readout register and the counter to display the measured trigger rate without using a stop bit to prevent the counter from overflowing, rates which exceed the maximum rate $f_{\text{trig}}^{\text{max}}$ will not be measured correctly. This effect has to be accounted for in the following discussion of the measurements.

In Figure 5.17a the measured rate of trigger signals, which have been processed by the prescaling algorithm f_{meas}, is plotted as a function of the adjusted frequency of the arbitrary waveform generator f_{out} for different prescaler values n. Each data point represents the mean value of 20 successive rate measurements, the error bars indicate the uncertainty of the mean calculated from the standard deviation of the measurements. For most of the data points, the error bars can hardly be seen since the maximum scatter of the measurements is in the order of only 1 Hz. For adjusted trigger rates below $f_{\text{out}} = 10\,\text{Hz}$ for a prescaling factor of $n = 10$ and below $f_{\text{out}} = 100\,\text{Hz}$ for $n = 100$, respectively, the size of the error bars increases due to the fact, that the exact values cannot be directly gained from measurements since the rate counter will measure either 0 Hz or 1 Hz. Therefore, the values of the data points have to be calculated offline with the significance being limited by the number of measurements, which then is reflected in the size of the error bars.
The residuals $f_{\text{meas}} - f_{\text{theo}}$ of the measurements are shown in Figure 5.17b. Here, for the y-axis a symmetric logarithmic scale is used in which the range from minus one to one is plotted on a linear scale. This allows for depicting positive as well as negative values. Over a wide frequency range, the measured prescaled trigger rates follow the theoretical characteristics of

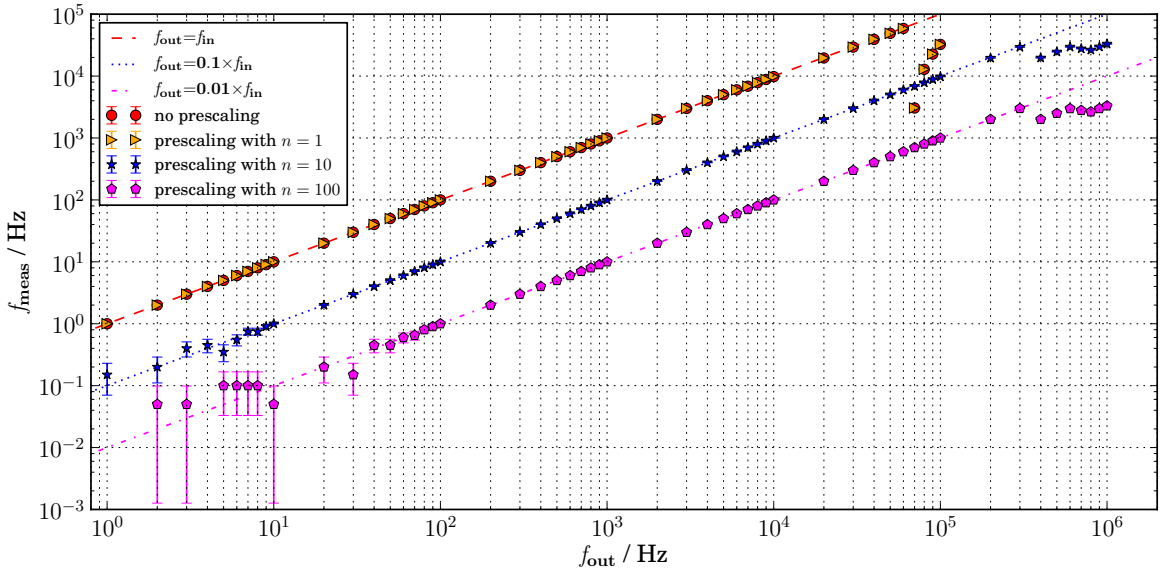

(a) *Measured trigger rate as a function of the incoming trigger rate.*

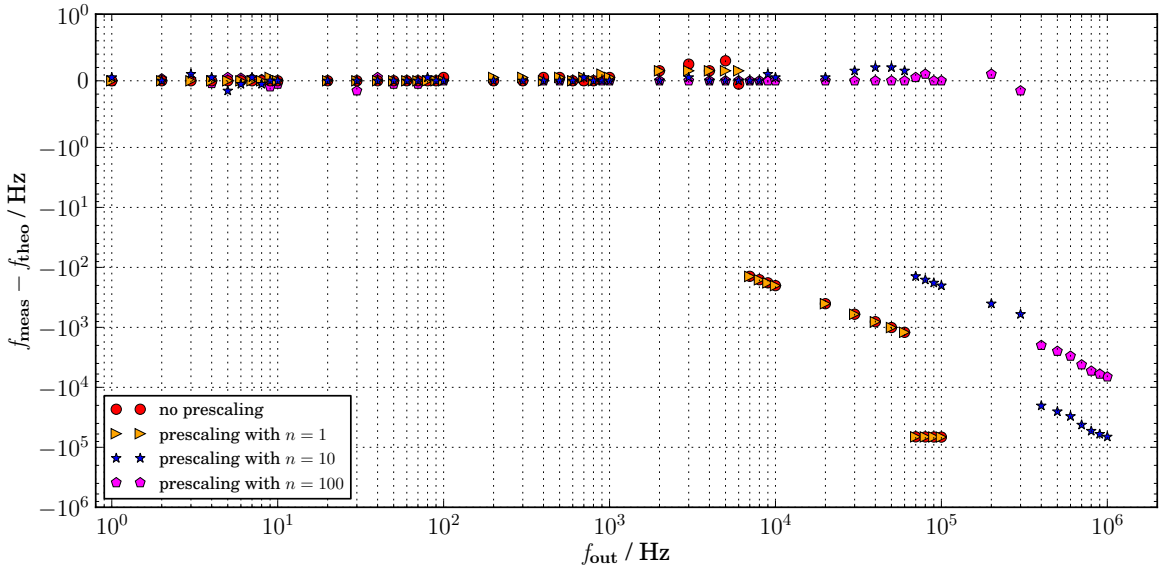

(b) *Residuals of the measured trigger rates.*

Figure 5.17: *Laboratory measurement of the prescaler algorithm. The upper panel shows the measured trigger rate for disabled prescaling (red circles) and processed by the prescaler with prescaling factors of $n = 1$ (orange triangles), $n = 10$ (blue asterisks) and $n = 100$ (magenta pentagons) as a function of the frequency of incoming trigger signals. The theoretical characteristics are illustrated by the different line plots. The lower panel depicts the residuals of this measurement. Here, to allow the logarithmic y-axis to cover positive and negative values, the range from minus one to plus one is plotted on a linear scale.*

the prescaling algorithm. Small deviations of the residuals from zero are solely due to the precision of the rate counter in combination with the limited statistics of the measurement. For example, an absolute error of 1 Hz, which translates into a relatively small mismatch at high rates, occurring for one out of the 20 measurements per data point propagates into a value of the residuum of 0.05. Since changing the resolution of the rate counter is closely connected to a non-negligible intervention in the FPGA firmware, potential future measurements could overcome this effect by increasing the statistics of each data point. Looking at the frequency range up to $f_{\text{out}} \approx 6\,\text{kHz}$ for disabled prescaling or a prescaling factor of $n = 1$ and up to $f_{\text{out}} \approx 60\,\text{kHz}$ for a prescaling factor of $n = 10$, respectively, and taking the resolution of the rate counter into consideration, the measured trigger rates are in perfect agreement with the theoretical values.

Although the AMIGA FPGA firmware uses two identical buffer structures for the data acquisition (Section 5.2), the maximum rate at which the incoming events can be recorded is limited. As a consequence of the fact that the speed of reading the data from the buffers and storing it into the external RAM modules is determined by the frequency of the RAM modules of $f_{\text{RAM}} = 10\,\text{MHz}$ and the bus width of the RAM of 32 bits, the AMIGA detector will be subject to a dead time of $\tau_{\text{rw}} = 154.1\,\mu\text{s}$ when both buffers are completely filled with event data. This behavior is reflected in Figure 5.16, in which the dead time can be found as the gap between to high states of the `RJ_Trig_Buf_Reg_Disable` signal. This signal is set to a logical one for 3.2 µs when one of the two ring buffers is filled with new data. By applying this veto signal, it is assured that all data is overwritten before a new trigger is accepted, thus preventing the acquisition of corrupted events. Not accepting new trigger signals during the dead time of the detector will cause the system to miss some of the incoming trigger signals above a characteristic frequency of $f_{\text{dead}} = 1/\tau_{\text{rw}} = 6.489\,\text{kHz}$. In Figure 5.17b, this behavior can be found in the cutoff between 6 kHz and 7 kHz for disabled prescaling and between 60 kHz and 70 kHz for a prescaling factor of $n = 10$. For higher frequencies, the constant dead time causes the residuals to drop by one decade when increasing f_{out} by a factor of ten. The large values of the residuals of the last four data points measured for disabled prescaling and a prescaler value of $n = 1$ in the order of -10^5 Hz originate from the overflow of the rate counter and therefore reflect its maximum value of $f_{\text{trig}}^{\text{max}} = 65.535\,\text{kHz}$.
In addition, a second effect, which is observable by the measurement, results from already masking the incoming trigger signals to prevent the system from interpreting the rising edges of the incoming 24-bit T1 timestamp as new trigger signals. This is achieved by disabling the trigger input for a time window of 2.9 µs after the detection of a trigger signal by using the `!Timer_400ns` signal, which as a consequence will diminish the measured trigger rates above $f_{\text{TSdis}} = 1/2.9\,\mu\text{s} = 344.828\,\text{kHz}$. Contrary to the effect discussed above, this process will affect the trigger signals before they are processed by the prescaler algorithm and thus will change the measured trigger rate independent of the choice of the prescaler value n. In Figure 5.17b this effect can be observed as the rapid drop of the calculated residuals between 300 kHz and 400 kHz in the datasets with prescaling factors of $n = 10$ and $n = 100$.

In summary, the prescaler algorithm, as it is implemented into the FPGA firmware for the use with the AMIGA PUC, enables the system to a prescaling of the received trigger signals with high precision. By choosing appropriate prescaler values n, it allows to compensate

differences between the muon counters of the PUC in terms of different memory depths. In addition, it enhances the detector to be able to take data in the occupancy mode with low occupancy numbers and/or low thresholds of the discriminators since it extends the viable frequency range of trigger signals by almost two decades.

5.7 The T1/T3 Trigger Chain

The AMIGA enhancement has been designed to measure the muon content of cosmic ray air showers synchronously to the SD of the Pierre Auger Observatory. Therefore, the muon counters have been integrated into the trigger chain of the SD array (Section 3.1.3). After a muon counter is triggered by the corresponding SD station in terms of receiving a T1 trigger signal, the data acquisition is started and the recorded event data is stored into the RAM of the AMIGA Digital Board. In case the T1 trigger of the SD station, which has been formed only based on local trigger conditions, also fulfills the T3 criteria validated by CDAS, a T3 request is sent to the muon counter. Then the corresponding muon data has to be localized in the RAM and will be sent to the SBC of the muon detector from where it will be further transmitted to CDAS. In order to identify the correct event in the RAM, a modified version of the LS FPGA firmware [S5] sends the T1 trigger signal together with a 24-bit timestamp (local timestamp, LTS), which is taken from a free running counter inside the FPGA firmware of the Front-End Board electronics of the SD station. Since the counter is driven by a clock with a frequency of 1.25 MHz [Wai11], the T1 timestamp value stays unique for around 13.42 s. This is sufficient to label all the events stored by the SD station. In the following, the decoding and the storage of the T1 timestamp inside the AMIGA FPGA firmware as well as the data readout based on the 'event request by timestamp' will be described and discussed in detail.

5.7.1 Algorithm for Decoding the T1 Timestamp

A T1 trigger signal, which is sent by the LS electronics of the SD, consists of a 200 ns wide trigger pulse, that is followed by the 24-bit timestamp after a time delay of 300 ns. Each bit of the timestamp is represented by a 100 ns long signal. Overall, the T1 trigger signal is formed of a pulse train of a total length of $\Delta T_{\mathrm{T1}} = 2.9\,\mu\mathrm{s}$. The algorithm for decoding the T1 timestamp is implemented as a subroutine of the F-bin routine and will be described in the following. The timing of the decoding algorithm is illustrated in Figure 5.18.

In order to decode the value of the timestamp, an enable signal (`Timer_Clock_En`) is generated synchronously to the rising edge of the trigger pulse. This signal stays at high level for approximately 2.9 µs, thus defining a time window containing the whole trigger signal, and is used for enabling a 8 bit wide counter running with a frequency of 80 MHz. After 35 clock cycles, and therefore being delayed by 437.5 ns with respect to the rising edge of the enable signal, a second signal (`Timer_400nS`) is formed to mask the LTS part of the T1 trigger signal. Within this time window and synchronously to the rising edges of a 10 MHz clock (`Clk_Shift`), the present bit of the timestamp is analyzed and stored into a 24 bit wide shift register. The timing of the clock is chosen to ensure that its rising edges always coincide with the center part of the single bits of the timestamp, thus avoiding the readout of unstable data. After 230 clock cycles of the 80 MHz clock, corresponding to a time delay of 2.875 µs,

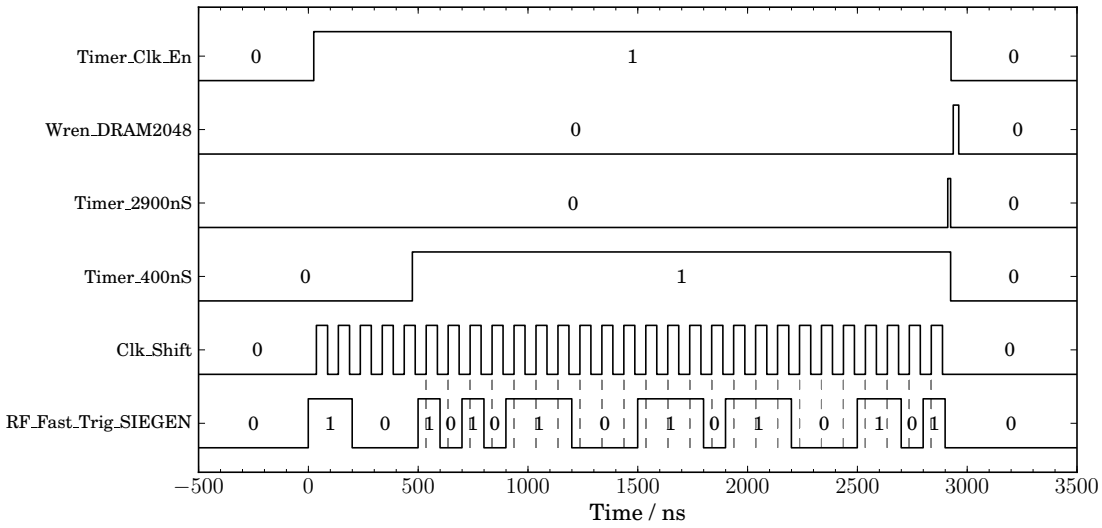

Figure 5.18: *Timing of the T1 timestamp decoding procedure measured with a logic analyzer [03]. The event (timestamp `0xAE3B8D`) has been chosen as an example. The plot shows the time development of the trigger signal (`RF_Fast_Trig_SIEGEN`), the 10 MHz clock for reading the timestamp (`Clk_Shift`) and other important control signals. The moments, at which the 24 bits of the timestamp are read out, are highlighted with the gray dashed lines.*

the timestamp is completely stored into the shift register and a stop flag (`Timer_2900nS`) is generated, which disables the `Timer_Clk_En` signal and resets the 80 MHz counter. This allows the system to accept the next incoming T1 trigger.

Since the AMIGA muon counter electronics is designed to store event data of up to 2048 events, a dual-port-RAM (DPRAM) with a depth of 2048 words and a width of 35 bits is implemented into the FPGA firmware, allowing for the storage of the associated timestamps. On the basis of the `Timer_2900nS` flag, a write enable signal (`Wren_DRAM2048`) is generated. This signal initiates the storage of the pairwise information of timestamp value (24 bit) and address of the event in the external RAM (11 bit) into the DPRAM. By this, the unambiguous allocation of the T1 timestamp to the respective event data can be assured, thus allowing for an unequivocal identification and request of the event driven by the central DAQ system.

5.7.2 Requesting Event Data by Timestamp

An event request performed in the T3 acquisition mode requires several processes to be executed by the SBC, which are included into the AMIGA DAQ software framework [S4]. In a first step, the 24 bit timestamp value of the event, which is expected to be requested, is transmitted to the AMIGA FPGA in two parts. Since all input registers of the FPGA have a fixed width of 16 bits, the eight most significant bits of the timestamp are stored into input register `0x45` of the FPGA whereas the 16 least significant bits are written into register `0x44`. In a second step, the ninth bit of control register `0x48` is set to a high state for a short time. The rising edge of this signal will cause the firmware of the FPGA to search for this timestamp value inside a look-up table. Synchronously to the internal 80 MHz clock, the stored timestamp

information inside the DPRAM will be consecutively read out and compared to the timestamp value which has been sent by the SBC. This process can take up to 25.6 µs for the frequency given. If the requested timestamp matches one entry of the look-up table inside the DPRAM, the associated address of the event inside the RAM is stored into a 35 bit wide D-flip-flop together with the timestamp value (`TS_Buffer[34..0]`=`Evt_Addr[10..0]`+`T1_TS[23..0]`). In case the event information cannot be found, this timestamp value is replaced by an error code (`0xEEFFEE`). By copying the content of the flip-flop to two output registers of the FPGA, `TS_Buffer[15..0]` to register `0x46` and `TS_Buffer[31..16]` to register `0x47`, the information is made available to the SBC. In the next step, the SBC reads the content of the second register. In case it contains the error code, an empty file is created and stored on the local storage medium. If the contents of the registers differ from the value of the error code, the SBC will request an event by sending its position in the RAM of the Digital Board. These structures have been implemented long before the implementation of the T1/T3 trigger chain to be able to read out events which have been acquired with other trigger modes, such as the Occupancy-N trigger. Since here the firmware of the FPGA is running in T3 mode, by setting the third bit of the control register (`0x48`) to one, it will ignore the RAM address, which is sent with the readout request by the SBC, but read the event information starting at the position inside the RAM which is stored inside the `TS_Buffer` register. This event information is rewritten to the output buffer of the FPGA (see Section 5.2) from where it can be accessed by the microcontroller and by this transmitted to the SBC. Here, the event information is first stored as a file on the local storage medium and in a second step sent to CDAS. In Figure 5.19, the procedure of requesting an event by timestamp is shown as a flow chart.

Since the SBC only takes the content of register `0x47` into account to check the availability of the event, there is still a small probability of $\mathcal{P}_{\text{fail}} = 2^{-16}$ that the SBC does not request the event even though it has been correctly acquired by the AMIGA system. This situation occurs when the eight least significant bits of the event address and the eight most significant bits of the LTS equal to `0x00` and `0xEE`, respectively. By including an additional check of register `0x46`, which includes the complementary information of the error code, with one of the future firmware upgrades of the SBC DAQ software, this probability could be lowered to $\mathcal{P}_{\text{fail}} = 2^{-32}$.

5.7.3 Efficiency of the T1/T3 Trigger Chain

Decoding the timestamp value and storing this information together with the associated RAM address of the event as well as finding the correct event address in the look-up table inside the DPRAM, when receiving a T3 request, is of high importance to ensure the proper operation of the muon detector. Losing event data as a result of an unsuccessful search of the LTS or even sending wrong event data to CDAS will have non-negligible consequences for the event reconstruction and offline data analysis. To exclude these effects, two different laboratory measurements have been performed. They aim at proving the proper functionality of the algorithm:

1. The efficiency of requesting an event with a known timestamp is measured. This tests

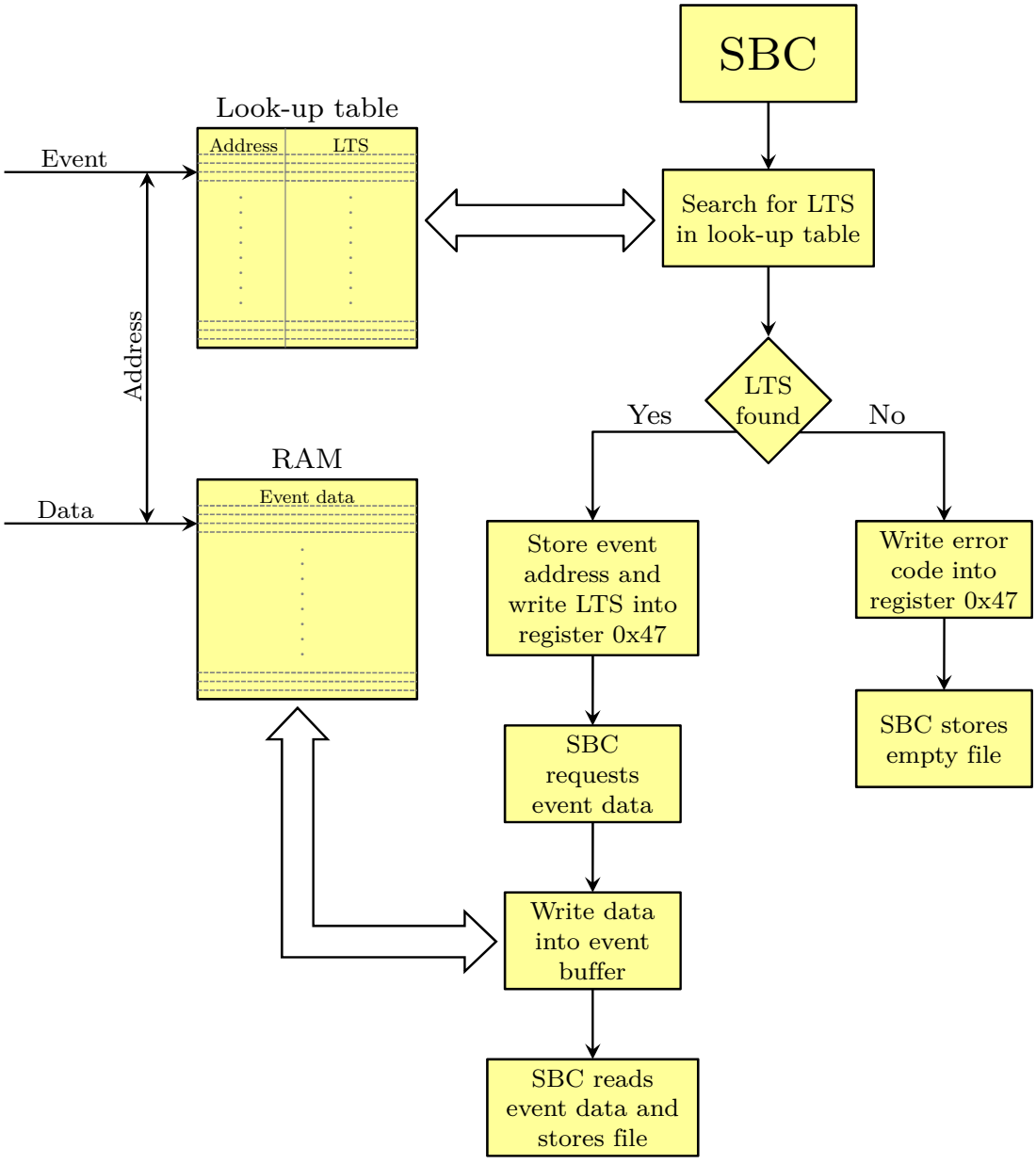

Figure 5.19: *Flow chart of the T1/T3 trigger chain as implemented into the AMIGA FPGA firmware [S2].*

the error-free operation of the decoding algorithm and of the data handling by the DPRAM as well as the performance of the event requesting itself.

2. It is assured that the event data, which is provided after a T3 request, contains the measured data of the correct event.

Whereas the measurement, which examines the second requirement for the system, will be described in Section 5.8.1, the first measurement and its results will be discussed in the following.

A schematic overview of the experimental setup, which is used to measure the efficiency of requesting events by timestamp, is shown in Figure 5.20. The measurement is started with an arbitrary waveform generator [01] sending a negative, 500 ns wide TTL signal to the Pattern Board (Section A), which initializes the firmware of the FPGA of the Pattern Board and sets it to a predefined state. With a frequency of 122.07 Hz, corresponding to 8192 (13 bit) clock cycles of the internal 1 MHz clock, the Pattern Board will now send T1 trigger signals via the dedicated trigger output to the AMIGA Digital Board. This frequency is chosen to operate the electronics with trigger rates that are comparable to the ones of the SD station. For each trigger signal sent by the Pattern Board, the timestamp value is generated by a counter with a depth of 24 bit, which is pre-loaded with a start value of `0xAAAAAA` synchronously to the signal of the waveform generator. The counter value is incremented for each trigger signal, thus generating an unique timestamp for each T1 event. Since the Digital Board is operated in the T1 acquisition mode, it will store all received and decoded timestamps into the look-up table inside the DPRAM. After a defined time ΔT_{delay}, the AMIGA SBC tries to request an event by sending a T3 request with a known timestamp value S ($S >$ `0xAAAAAA`). By repeating these steps multiple times, the efficiency of the request procedure as a function of the time ΔT_{delay} can be calculated from the fraction of

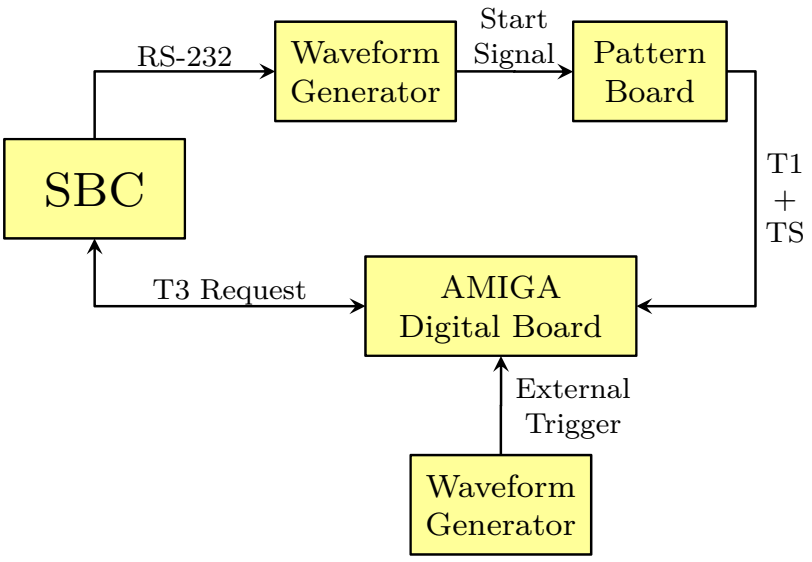

Figure 5.20: *Schematic overview of the experimental setup used to measure the efficiency of the T1/T3 trigger chain.*

successful readouts. A serial connection between the SBC and the waveform generator allows to subsequentially start new measurements by sending control signals in the SCPI (standard commands for programmable instruments) format [Ivi99]. In this process, the number of measurements, given by the number of start signals being sent from the generator to the Pattern Board, are counted with an internal counter of the Pattern Board, which can be read with a digital logic analyzer [03]. By using the SBC not only for sending the T3 request but also for starting the measurement, the delay ΔT_{delay} can be set with a high precision, that only depends on the workload of the SBC's micro processor (see below).
In this measurement, a second waveform generator [01] is connected to one pin of the test connector of the Digital Board and continuously sending positive TTL pulses with a width of 100 ns and a frequency of 5 kHz. By a remote command sent from the SBC the Digital Board can be configured to use this waveform generator as a trigger source. Therefore, switching from the T1 trigger mode to the external trigger source (and back) overwrites all events in the RAM and deletes all associated timestamp values in the look-up table of the DPRAM. This procedure assures that a T3 request will not result in a successful event readout of an event which was recorded in a previous measurement.

In the following, one measurement is discussed in more detail. Figure 5.21 shows the result of the efficiency measurement for requesting the 299th event, which is sent by the Pattern Board with a timestamp value of `0xAAABD5`. Since the analysis does not depend on the exact value, this event has been chosen randomly. The efficiencies represented by the data points are calculated from the ratio of the number of successful event readouts and the total number of start signals sent by the SBC and are plotted as a function of the time delay ΔT_{delay} between sending the individual start signal and the following T3 request.

For a correct treatment of the uncertainties of the data points, asymmetric errors have to be taken into account, since efficiencies are only defined on the interval $[0; 1]$. The plotted uncertainties of the measured efficiencies are derived from an efficiency probability density function for binomial statistics following [Ull07]. Due to the fact that the request delays depend on the workload on the SBC, ΔT_{delay} is measured by the SBC with an accuracy of 10 ms. Therefore, the position in x-direction of each data point represents the arithmetic mean of the data sample whereas the uncertainties are given by the standard deviation. In Figure 5.22, the deviations of the measured delays from the requested ones are plotted for the individual measurements. Whereas the measured delays can differ by up to 145 ms from the requested ones for single event requests, the timing uncertainties of the data points in Figure 5.21, which result from calculating the standard deviations from a multitude of the single measurements, are in the order of only 30 ms.
Since the Pattern Board generates events with a frequency of about 122 Hz, the event with the timestamp value given above will be sent with a delay of $\Delta T_{\text{event}} = 2.45\,\text{s}$. As a direct consequence, the SBC will never accomplish a successful event readout for request delays smaller than ΔT_{event}, which leads to an efficiency of the trigger chain of 0 %. With increasing the adjusted delay, the efficiency raises to a value of 100 % reaching a stable plateau, where the system runs with full efficiency, meaning that all events generated by the Pattern Board are correctly recorded, stored and read out by the AMIGA system. After a certain delay, the efficiency drops back to zero, since the continuous data taking in combination with the

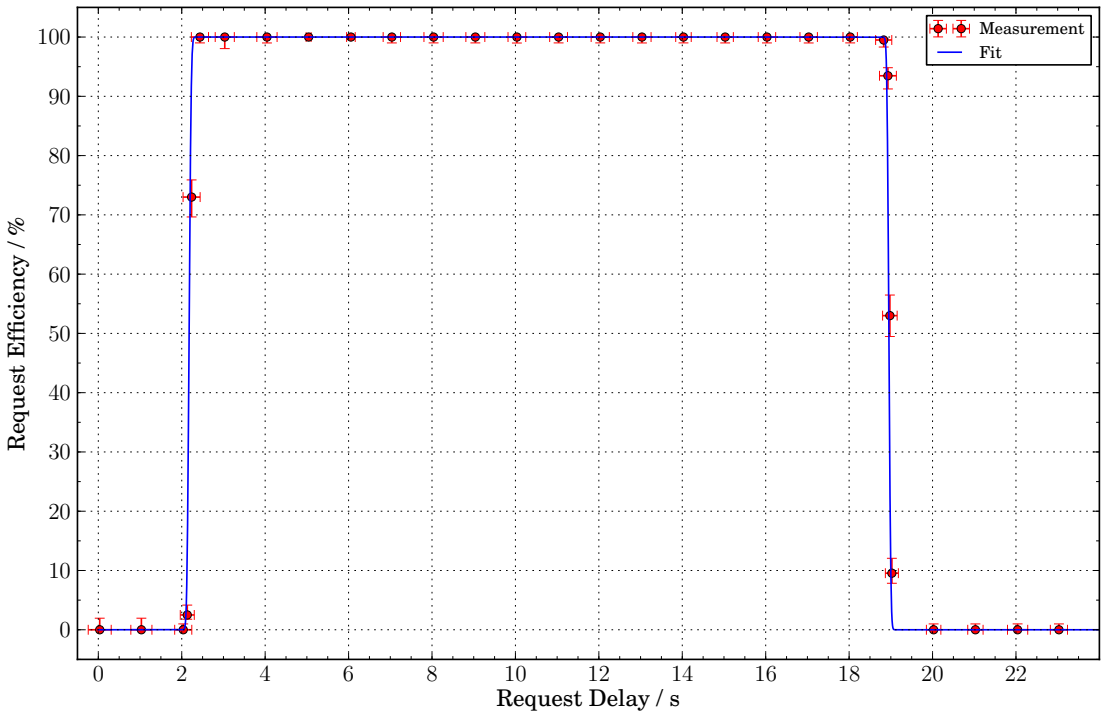

Figure 5.21: *Efficiency measurement of the T1/T3 trigger chain. The plot shows the efficiency of requesting one particular event as a function of the time delay of the request with respect to the time at which the event is generated. Overall, a total number of 11,350 requests have been performed. The uncertainties of the request efficiencies, represented by the red error bars, are calculated following [Ull07] and scaled by a factor of 100. The blue curve shows the fit of a superposition of two error functions to the data ($\chi^2/NDF = 0.22$).*

limited amount of memory will cause the recorded events to be overwritten.

The data points plotted in Figure 5.21 can be fitted with the sum of two error functions of the form

$$F(x) = \frac{p_4}{2} \times \left[\mathrm{erf}\left(\frac{x - p_0}{p_1}\right) - \mathrm{erf}\left(\frac{x - p_2}{p_3}\right) \right] \tag{5.10}$$

with the Gaussian error function being defined as

$$\mathrm{erf}(x) = \frac{2}{\sqrt{\pi}} \int_0^x e^{-t^2} dt \quad . \tag{5.11}$$

The absolute amplitude of the fit function (p_4) as well as the position (p_0 and p_2) and the steepness (p_1 and p_3) of the rising and the falling edges of the function are used as free

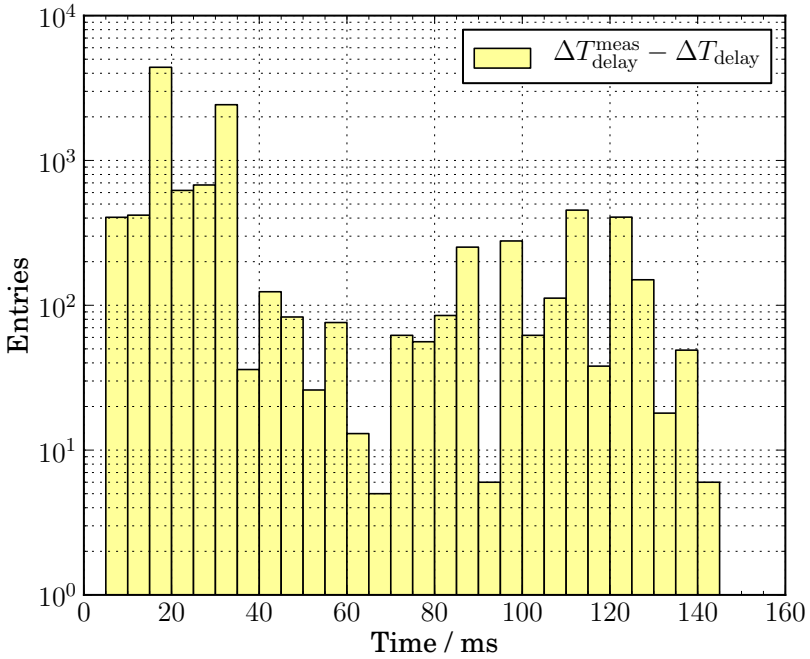

Figure 5.22: *Timing uncertainties in the measurement of the trigger efficiency. The histogram shows the deviations of the measured delays from the requested ones.*

parameters for the fit and are determined to be

$$\begin{aligned} p_0 &= (2.176 \pm 0.004)\,\text{s} \quad , \quad p_1 = (0.055 \pm 0.005)\,\text{s} \quad , \\ p_2 &= (18.953 \pm 0.002)\,\text{s} \quad , \quad p_3 = (0.050 \pm 0.003)\,\text{s} \quad , \\ p_4 &= (99.98 \pm 0.04)\,\% \end{aligned} \tag{5.12}$$

with a quality of the fit of $\chi^2/\text{NDF} = 5.447/25 = 0.22$.

Although no single malfunction of the trigger chain is observed in the plateau region of Figure 5.21, based on the statistics of this measurement, full trigger efficiency can only be guaranteed down to a level of 1.1×10^{-4}. This is also reflected by the fact, that the fit of the data points does not result in a value of 100 % for the amplitude. It is however compatible with full efficiency within an interval of 0.5σ, when taking the statistical uncertainties resulting from the limited statistics of the measurement into account.

As a cross check of the measurement, the event rate can be reconstructed from the time interval between both points at which the fit function reveals a request efficiency of 50 %: $\Delta t_\text{p} = p_2 - p_0 = (16.777 \pm 0.004)\,\text{s}$. Taking into account that within this time period the AMIGA system records 2048 events, the average reconstructed event rate can be calculated as $f_\text{rec} = 2048/\Delta t_\text{p} = (122.07 \pm 0.03)\,\text{Hz}$. This value is in perfect agreement with the true event rate (122.0703 Hz), at which the Pattern Board generates events, within an error interval of 0.01σ.

5.8 End-of-Event Information

In order to get a more detailed insight into the data taking with the detectors of the PUC, the FPGA firmware has been upgraded such, that the muon counter events contain additional information about the status of the system, in the following referred to as end-of-event (EoE) information. This upgrade has been successfully tested with the prototype version of the 320 MHz firmware [S3] (Section 5.9). It is also compatible with the standard version of the FPGA firmware [S2], which is used at the PUC.

To add the EoE information, an additional multiplexer is implemented into the code, which modifies the last three words (time bins) of the acquired event data when it is written from the input buffer to the external RAM. The EoE information includes the LTS, which was sent with the T1 trigger signal, the value of a free running counter, that is continuously driven by the 80 MHz clock of the FPGA firmware, and the address of the event inside the external RAM. In addition, two bits of the EoE structure are used as a buffer identifier, indicating which input buffer was occupied for storing the incoming data of the particular event. Here, a value of one denotes the first buffer (A) whereas a value of two identifies the second input buffer (B). The last part of the EoE information is made up of a fixed data string, that contains the expression 'EndofEvt' encoded in hexadecimal ASCII values. In total, the last three words of the event data containing the EoE information are given by

```
765  <24 bit zero> <24 bit local timestamp> <2 bit buffer identifier>
     <4 bit zero> <10 bit event address>
766  <16 bit zero> <48 bit free running counter>
767  45 6e 64 6f 66 45 76 74
```

with the time bins within an AMIGA event given by the bold printed numbers.

5.8.1 Check of T3 Requested Events

Any recorded AMIGA event, which is triggered by an incoming T1 trigger signal, is uniquely labeled through the LTS sent with the trigger signal. The particular event, that is made available by the system to be read from the external electronics (such as the SBC) on the basis of a T3 request, must consist of the data which was recorded synchronously to the T1 trigger signal that contained the appropriate LTS. In addition, and complementary to the measurement of the request efficiency of the T1/T3 trigger chain (Section 5.7.3), the evaluation of the EoE information in dedicated laboratory measurements allows for verifying whether the AMIGA muon counter electronics fulfills this requirement of sending the appropriate event data.

For the measurement described in the following, the AMIGA electronics is integrated into the experimental setup as already described in Section 5.7.3 and shown in Figure 5.20. Again, the Pattern Board (Section A) is used to trigger the AMIGA system by sending T1 trigger

signals, which include the 24-bit LTS, via its dedicated trigger output to the Digital Board. The LTS is generated by an internal 24 bit wide counter inside the Pattern Board software. This counter starts at a value of zero and is incremented for each T1 signal, thus assuring that each single event is associated with an unique timestamp. By adjusting the maximum value of another digital counter inside the firmware of the Pattern Board, the trigger rate can be set to a frequency of $f_{\mathrm{trig}} = 100\,\mathrm{Hz}$. In contrast to the efficiency measurement, the Pattern Board is not continuously triggering the AMIGA system but stops as soon as 2,048 T1 trigger signals are generated. By this, the events that are stored inside the external RAM of the Digital Board will not be overwritten. Since the SBC is again used as the master device within the experimental setup, it is possible to run a fully automated longterm measurement in which the SBC will start the individual measurement by sending the start signal to the Pattern Board. After a waiting time of $t_{\mathrm{wait}} = 25\,\mathrm{s}$, which suffices for the AMIGA system to record the 2,048 events, the SBC reads out the last timestamp value X_{last}, that has been decoded by the Digital Board. Then it successively performs 2,048 T3 requests starting with a value of the LTS of $X = X_{\mathrm{last}} - 2047$ for which the retrieved events are stored on an external storage device connected to the SBC. Following the last T3 request, the SBC starts the next measurement by sending another start signal to the Pattern Board.

For all requested events, the LTS that was send with the individual T3 request can be compared to the timestamp value that is stored inside the EoE information of the corresponding event. With a total number of 1,138,488 events being analyzed, no single mismatch between the two LTS values has been found. By this, the fraction of T3 requests, which result in erroneously provided event data, can be narrowed down to a level of 8.78×10^{-7}. This upper limit could be further decreased by significantly extending the measurement time. This could be realized with a dedicated test system permanently running for a long time period in the order of several months up to several years.

5.8.2 Verification of Correct Event Handling

The EoE information allows for a verification of the correct event handling inside the FPGA firmware. This concerns the switching between both input buffers as soon as an event is written to the external RAM as well as the correct addressing of the events inside the RAM. The functionality of these processes can be tested by analyzing the EoE information, which includes both, a buffer identifier and the address of the acquired event inside the external RAM.

The dataset already mentioned in the previous subsection is analyzed with respect to these observables. To verify the correct functionality of the buffer switching algorithm, the absolute difference of the buffer identifier values is calculated for pairwise subsequent events ($\Delta_{\mathrm{BufferID}}$). For a successful switching of the input buffers, this calculation results in $\Delta_{\mathrm{BufferID}} = 1$. For a total number of 1,137,928 events no malfunction of the algorithm has been observed (see Figure 5.23), which corresponds to an error rate below 8.79×10^{-7}. The difference in the overall number of events compared to Section 5.8.1 is due to the fact, that the dataset is subdivided into 560 runs and that the analysis described in this section can only be performed within single runs.

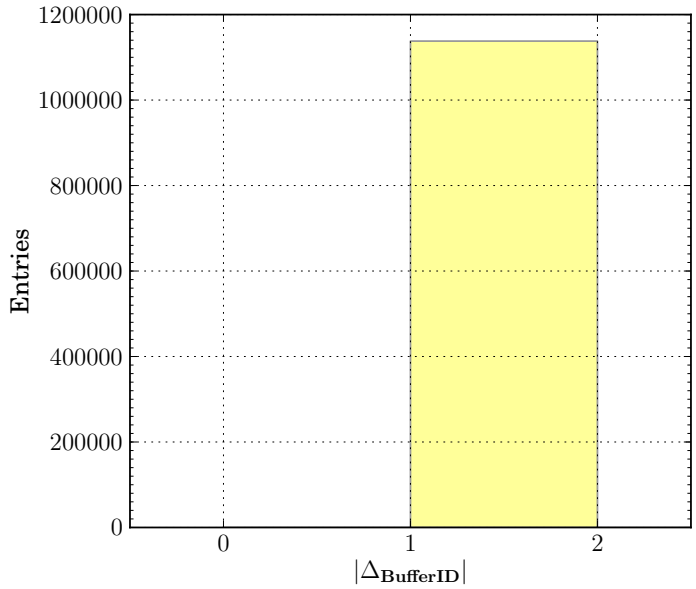

Figure 5.23: *Verification of the input buffer switching algorithm. The plot shows the absolute difference of the buffer identifier values of pairwise subsequent events. For a successful switching of the input buffers, this calculation results in* $\Delta_{BufferID} = 1$*. Overall, a total number of 1,137,928 events have been analyzed.*

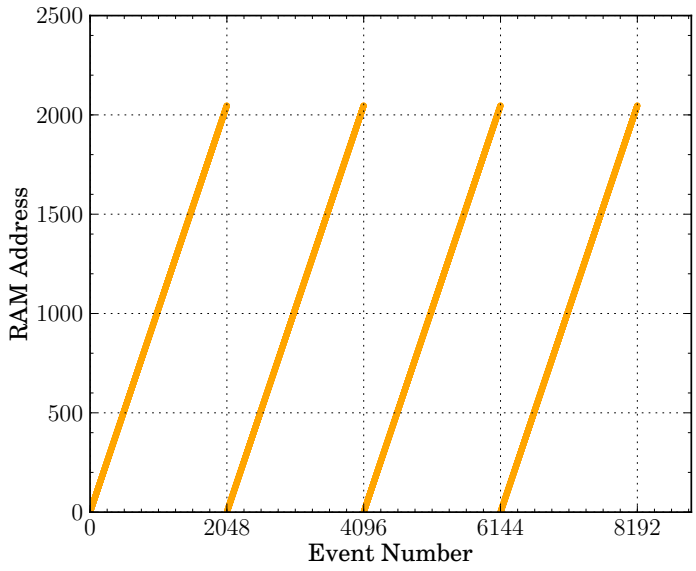

Figure 5.24: *Addressing of events inside the external RAM. The RAM addresses of recorded events are plotted versus the corresponding event numbers. The dataset contains 8,192 subsequent events, divided into 4 runs with 2,048 events each. The event numbers are shifted for the first event to start at zero.*

In a similar way, the correct addressing of all 2,048 events inside the external RAM can be verified. In Figure 5.24, the addresses of 8,192 subsequent events, which are included in 4 runs, are plotted against their event numbers. The event numbers are shifted for the first event to start at zero. As can be seen for this small data subsample, all events are correctly addressed inside the external RAM since the address is incremented for each event. Also with extending the analysis to the full dataset, no failure in the event addressing has been observed.

5.8.3 Reconstruction of the Trigger Rate

The FPGA firmware includes a 48 bit wide free running counter, driven by the internal 80 MHz clock. Synchronously to the detection of a trigger signal, the value of the counter is read out and attached to the EoE information of the triggered event. By analyzing this information, the time between two subsequent events can be calculated. Whereas a reconstruction of the average trigger rate for the data taking in the field is of limited use only, since the actual trigger rate is subject to random processes, a constant trigger rate, as it is applied to the system during the laboratory measurements, can be reconstructed from the EoE information with high precision.

For the data gained from the measurements mentioned in Section 5.8.1, the occurrence of the difference between the values of the free running counter of two subsequent events is shown in Figure 5.25 for a total number of 1,137,928 events. By calculating the mean and the standard deviation of the data, the reconstructed trigger rate is found to be

$$f_{\text{trig}}^{\text{EoE}} = (99.96969716 \pm 0.00000007)\,\text{Hz} \quad . \tag{5.13}$$

The measured values of the free running counter would be expected to be symmetrically distributed around the value that corresponds to the true trigger rate. However, the measured distribution is found to be asymmetric. This deviation could be explained to be caused by the sum of several effects, e.g. :

- The AMIGA system is not synchronized to the trigger frequency of the waveform generator. Thus, the rising edges of the free running counter will be randomly shifted with respect to the trigger signal.
- The output frequency of the waveform generator as well as the frequency of the free running counter are only stable to a certain extent and will therefore be subject to statistical variations.
- The edges of both, the free running counter and the trigger signal, are modified by jitter effects and will therefore deviate from their true periodicity.

However, the exact shape of the distribution is of no importance for the measurement discussed here and has not been analyzed in more detail.
A measurement of the trigger rate using a digital oscilloscope [04], which is operated in the segmented trigger mode, and an active probe [02] connected to the trigger output of the Pattern Board results in

$$f_{\text{trig}}^{\text{scope}} = (99.9697 \pm 0.0001)\,\text{Hz} \tag{5.14}$$

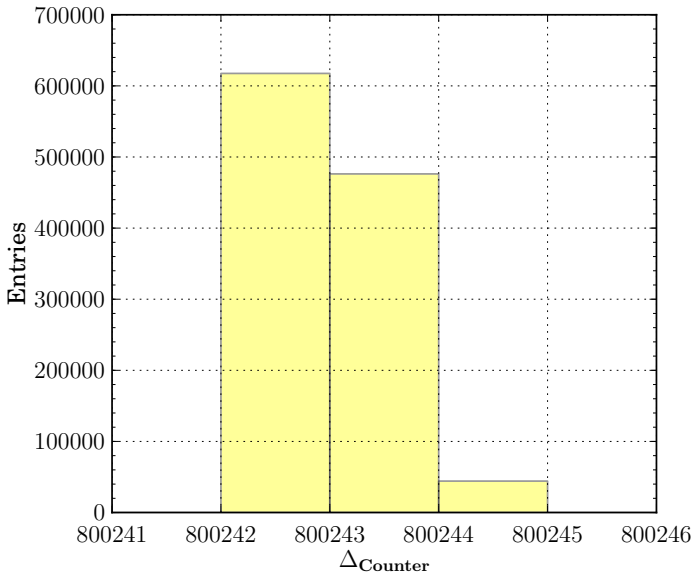

Figure 5.25: *Reconstruction of the trigger rate from EoE information. $\Delta_{Counter}$ denotes the difference between the 48-bit counter values of two consecutive events. The counter is driven by an 80 MHz clock, i.e. each increase corresponds to 12.5 ns. Overall, a total number of 1,137,928 events have been analyzed.*

for a total number of 20,480 recorded trigger signals. This value is derived by averaging ten single measurements of the time intervals which include 2,048 trigger signals. Both results are in agreement within an error interval of 0.03σ.

5.9 Upgrade to 320 MHz Data Acquisition

The first periods of data taking with the AMIGA muon counters of the PUC, until August 2012, are based on a detector operation with the FPGA firmware [S2], as described in the previous sections. Although the data is processed by the FPGA with a frequency of 80 MHz, the input data stream is sampled with a resolution of 3.125 ns, given by the frequency of the 320 MHz sampling clock. This resolution suffices to resolve individual PMT pulses with widths in the order of a few nanoseconds [San12b]. However, as a consequence of the downsampling of the input pulses, the acquired data can hardly be interpreted in terms of applying discrete muon counting strategies, which were obtained from detector simulations for a full data processing with a frequency of 320 MHz. A description of possible counting strategies is given in [Wun11].

To follow the baseline design of the AMIGA detector, in which a timing resolution of the processed data of 320 MHz is foreseen, the FPGA firmware is upgraded such that it meets this requirement, but with the aim of only applying minimal changes to the existing structures of the code. In the following, one possible realization of this upgrade, which has lead to a new FPGA firmware [S3], is described in more detail.

The upgrade to 320 MHz data processing consists of two changes inside the FPGA firmware. First, the downsampling procedure is bypassed by directly piping the input data stream to the input buffers, after it is latched to the 320 MHz sampling clock inside the A-bin routine (Section 5.1). The second change concerns the structure of the input buffers itself. The incoming data of each of the 64 input channels is now stored into a shift register with a depth of 4 bit. By reading all four bits at a time synchronously to the rising edges of the 80 MHz clock, the data of all 64 channels and of four consecutive time bins is combined to a single word of a depth of 256 bits, which can then be stored into one of the two input buffers. Hence, further processing of the data can be driven by the internal 80 MHz clock in a well proven way. Due to the limited amount of memory of the external RAM and since the experimental environment constrains the overall number of events to be stored, the increase of the data volume resulting from acquiring the data with a resolution of 3.125 ns has to be compensated by a reduction of the time window which is covered within the event. This is achieved by using an input buffer with a length of 192 words corresponding to a time window of 2.4 µs, with the position of the trigger dividing the event at the ratio of 1:2. As in the 80 MHz version of the code, the content of the input buffer is written to the external RAM with a frequency of 10 MHz. In Figure 5.26, a schematic overview of the modified buffer structure is given. Again, the implementation of a second buffer circuit and alternated switching between both buffers as soon as the content of one buffer is written to the external RAM guarantees that the detector is subject to a minimum of dead time only. This dead time is in the order of 150 µs and is therefore comparable to the one of the 80 MHz FPGA firmware (Section 5.6.2).

The performance of the new FPGA firmware was first validated in laboratory measurements. After basic measurements, such as testing the single and double pulse resolution of the system with a pulse generator used as the signal source [Tca12], the AMIGA system was operated with a muon hodoscope connected. Here, a 16 strip scintillator module is coupled to a 64-pixel photomultiplier [15] which is connected to the AMIGA electronics. The trigger is formed by an external coincidence electronics, which is sensitive to the signals produced by two smaller, movable scintillator panels and which therefore represents a position-dependent trigger system that reacts on muons traversing both, the small scintillator panels and the AMIGA scintillator. A detailed description of the hodoscope system as well as of its installation for the use with the AMIGA detector is given in [Lau12].
For a comparison of the data acquired with both versions of the FPGA firmware, Figure 5.27a and Figure 5.27b show a representation of the data around the trigger region taken with 80 MHz and 320 MHz data processing, respectively. Both plots show the time distribution of the superposition of recorded pulses as a function of time. Whereas Figure 5.27a contains all information of the pulses that were sampled on the 320 MHz grid modified by the downsampling procedure and therefore reduced in timing resolution, the underlying substructure is more resolved in Figure 5.27b. However, the shapes of both distributions are in good agreement to each other. The timing offset in both plots results from the external delay of the trigger signal, which can be calculated from the shift of the peak with respect to time bin 255 and is found to be in the order of $\Delta t_{\mathrm{trigger}} \approx 15 \times 12.5\,\mathrm{ns} = 180\,\mathrm{ns}$. In case of the 320 MHz data storage, additional shifts in the order of 50 ns have to be taken into account due to a change in the internal routing of the trigger signal within the buffer structure as well

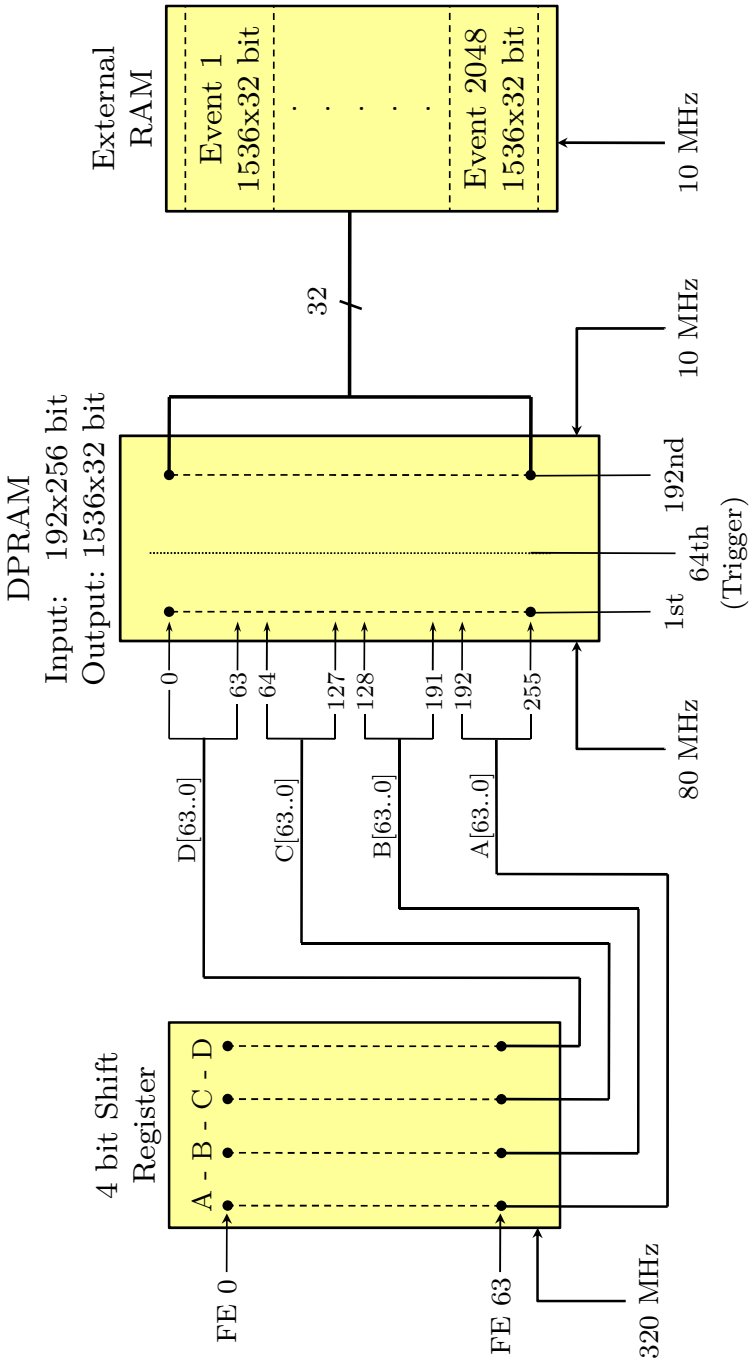

Figure 5.26: *Buffer structure for 320 MHz data recording as implemented in the FPGA firmware version [S3].*

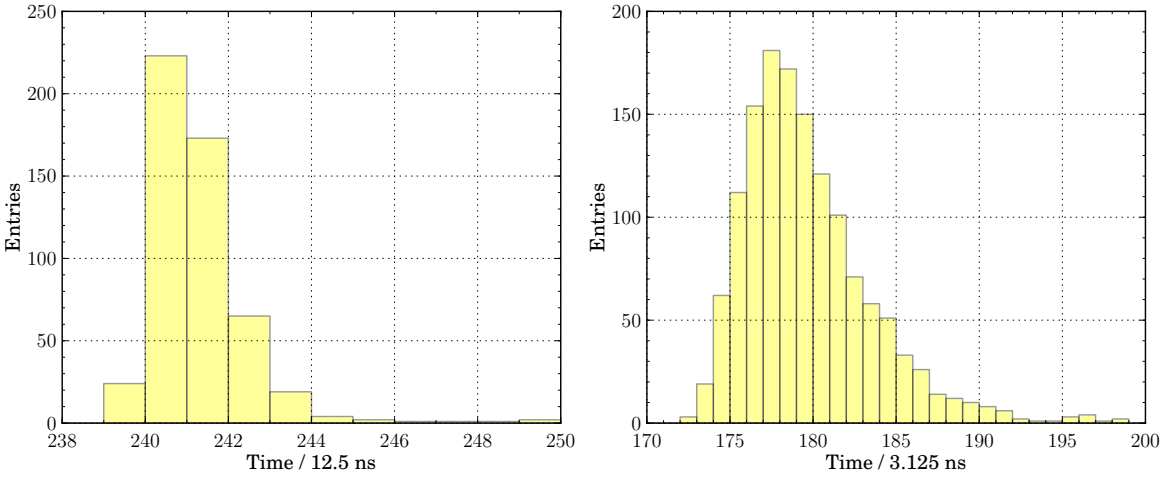

(a) *Hodoscope measurements with 80 MHz data processing.*

(b) *Hodoscope measurements with 320 MHz data processing.*

Figure 5.27: *Hodoscope measurements with 80 MHz and 320 MHz data processing. The left panel shows the superposition of 515 entries out of 281 events, recorded using the FPGA firmware [S2] (80 MHz), as a function time and independent of their channel number. The right panel depicts this information for 287 events (1,378 entries) recorded with the FPGA firmware [S3] (320 MHz). In both plots, the scale on the x-axis covers a selected time window around the trigger region.*

as due to the disabling of the downsampling procedure.

A more detailed analysis of the performance of the upgraded FPGA firmware or the analysis of 320 MHz data taken with the AMIGA PUC in Argentina is beyond the scope of this thesis and may be presented elsewhere.

6 Analysis of First Prototype Data

Contents

6.1 Event Structure of the AMIGA MD Data . . . 106
6.2 Data Taking Periods . . . 107
6.3 System Debugging Using Occupancy- and T1/T3-triggered Data . . . 111
6.3.1 Trash Events in T1/T3-triggered Data . . . 113
6.3.2 Magic Word Information in T1/T3-triggered Data . . . 116
6.3.3 Repeated Events in T1/T3-triggered Data . . . 117
6.4 Selection of Combined MD/SD Events . . . 118
6.4.1 Properties of Combined MD/SD Events . . . 119
6.5 Occupancy-based Analyses of T1/T3-triggered Data . . . 120
6.5.1 Definition of N_{Occ} and N_{Trig} . . . 122
6.5.2 Dataset for Occupancy-based Analyses . . . 122
6.6 Correlation of N_{Occ} with SD-related Shower Observables . . . 124
6.6.1 Occurrence of Signal Multiplicities in T1/T3-triggered Data . . . 127
6.6.2 Correlation of N_{Occ} with Distance to the Shower Axis or SD Energy . . . 128
6.6.3 Correlation of N_{Occ} with SD Energy for Different Distances to the Shower Axis 134

The readout electronics systems of the AMIGA (Auger Muons and Infill for the Ground Array) muon counters, that have been partially developed and tested at the University of Siegen, have been successfully installed at the experimental site in Argentina in seven prototype muon detector (MD) modules. Over an extended period of time, these MD modules have been operated with the AMIGA Digital Boards running the FPGA (field programmable gate array) firmware [S2] described in Chapter 5. Most of the time, data has been acquired by triggering the MD modules with the internal self-trigger (Occupancy-N trigger, Section 5.5), only during the last measurement periods synchronous data taking with the surface detector (SD) of the Pierre Auger Observatory became possible. Whereas occupancy-triggered data has mainly been used to debug the detector hardware and software, T1/T3-triggered data for the first time allowed for a combined analysis of MD data and SD observables, that are connected to the properties of extensive air showers.

Within the following sections a first analysis of this T1/T3-triggered prototype data will be presented. After introducing the data structure of MD events and a first selection of data taking periods (Section 6.1 and Section 6.2), the T1/T3 triggered events will be analyzed with respect to known deficiencies of the detector hardware and software (Section 6.3). A

comparison with previous analyses based on occupancy-triggered data proves a successful debugging of the system. A combined dataset including SD data as well as MD data will be presented (Section 6.4) and basic properties of this dataset will be discussed in more detail (Section 6.4.1). The following analyses will investigate the dependence of the number of time-coincident signals, recorded with the MD modules, on SD-related air shower observables like e.g. the distance of the detector to the shower axis or the reconstructed energy of the primary cosmic ray particle (Section 6.5.2 through Section 6.6.3). Based on the results of these analyses, future studies may lead to a more thorough understanding of the acquired MD data or may allow for a reinterpretation of occupancy-triggered event data.

6.1 Event Structure of the AMIGA MD Data

One event acquired with an AMIGA MD module contains the signal information of all 64 photomultiplier (PMT) pixels in a predefined time interval. Since the length of an event is limited to 768 time bins, the time window, that is covered by the data recording, depends on the version of the FPGA firmware. In the firmware version [S2], where the data is processed with a frequency of 80 MHz, this time interval amounts to 9.6 µs. For the data processing with a frequency of 320 MHz in version [S3], the time interval covered is reduced by a factor of four to 2.4 µs. In both versions, an incoming trigger signal causes the firmware to switch the data storage from a continuously overwritten ring buffer with a length of 256 time bins to a second buffer with a length of 512 time bins (Section 5.2). As a consequence, the arrival time of the trigger signal on time bin 256, which is usually referred to as trigger time bin, divides the MD event at a ratio of 1:2. Self-triggered data, i.e. data recorded on the basis of the Occupancy-N trigger with $N \geq 2$, is therefore expected to show an accumulation of signals at the position of the trigger time bin. A typical shift of this accumulation by a few time bins, as it is found in occupancy data, is due to other internal routines like e.g. the prescaler algorithm (Section 5.6). Since the AMIGA FPGA firmware is, to some extent, derived from the firmware of the SD front-end electronics [S5], the structure of an MD event is similar to the one of an SD event.
When operating the AMIGA muon counter such that it is externally triggered by the associated SD station, an additional delay of the trigger signal has to be taken into account. If the shower front of an extensive air shower (EAS) traverses the SD station and the acquired signals fulfill the T1 trigger condition (Section 3.1.3), the trigger signal is formed and sent to the readout electronics of the underground muon counter. The time needed for the trigger forming is typically in the order of 1 µs. During this time, the relevant physics data will be shifted towards smaller time bin values. The delay corresponding to the time of flight of the shower particles, when propagating through the soil, is in the order of 30 ns for particles moving at the speed of light and a distance between the SD station and the underground muon counter of approximately 10 m. However, this additional delay has not to be taken into account since it will be almost completely compensated by the time delay due to the propagation of the trigger signal.

In Figure 6.1, the time distribution of recorded signals in all MD modules of the pre-unitary cell (PUC, Section 4.3) is shown. The double-peak structure can be explained by the two

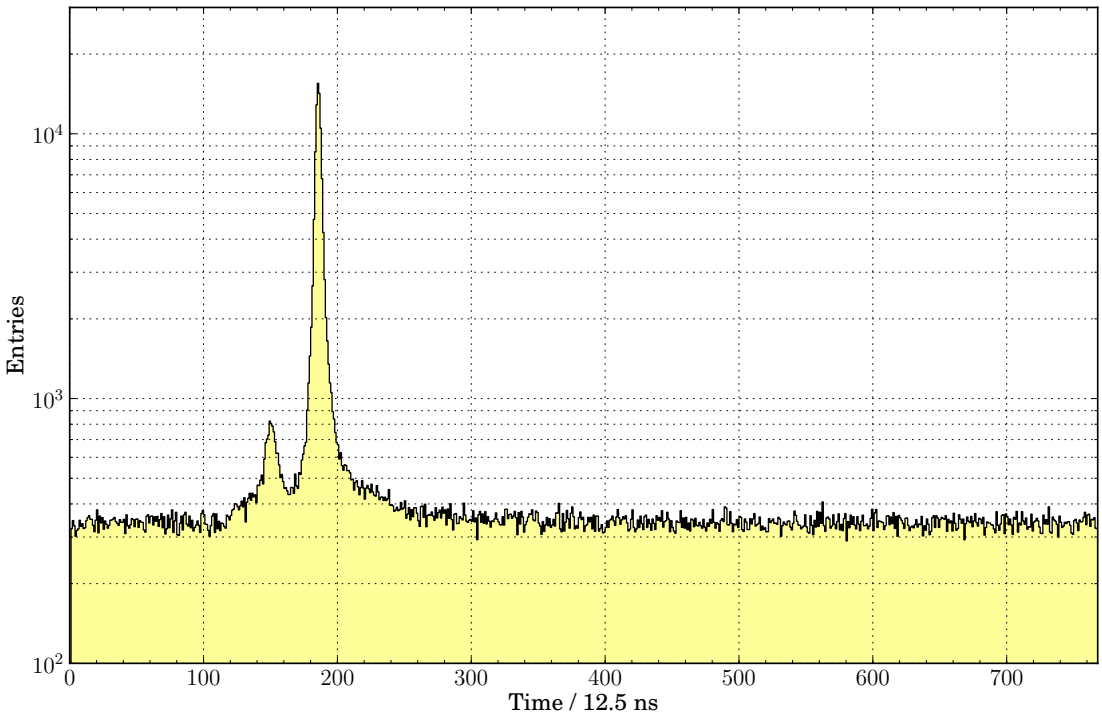

Figure 6.1: *Time distribution of T1-triggered data. The histogram shows an overlay of 107,222 non-empty events acquired with all muon counter modules of the AMIGA pre-unitary cell. The double peak structure is due to the two classes of T1 triggers, the T1-ToT (time-over-threshold) trigger (first peak) and the T1-TH (threshold) trigger (second peak). The observed shift of 26 time bins between both peaks is a consequence of the time needed to form the T1-ToT of* $T_{ToT} = 325\,ns$.

different classes of T1 triggers generated by the SD station. Whereas the first peak is due to the T1-ToT (time-over-threshold) trigger, the second peak results from events that fulfilled the condition of the T1-TH (threshold) trigger (Section 3.1.3). The generation of the former trigger requires more time since the measured signal amplitudes need to be above the given threshold for at least $T_{\mathrm{ToT}} = 325\,\mathrm{ns}$ [Abr10b]. This will cause the corresponding shower signals to be stored in earlier time bins than it is the case for the threshold trigger, i.e. the shift of 26 time bins, corresponding to the value of T_{ToT}, is found in the data. The peak-to-peak ratio of $N_{\mathrm{TH}}/N_{\mathrm{ToT}} \approx 18$ roughly agrees with the theoretical ratio of the corresponding trigger rates at the T2 level $N^{\mathrm{T2}}_{\mathrm{TH}}/N^{\mathrm{T2}}_{\mathrm{ToT}} = 10$ (Section 3.1.3). However, since T1-TH-triggered events show larger signal multiplicities in the muon counter data (Section 6.6.1) and since the widths of the peaks are not taken into account, the exact value of the theoretical ratio is not expected to be found in the data.

6.2 Data Taking Periods

The AMIGA PUC consists of seven detector stations forming a hexagonal unit of the SD array of the Pierre Auger Observatory. Each of these stations is connected to at least one

underground muon counter of the AMIGA extension. A complete list of the detector stations, that contribute to the PUC, including more detailed information about the single detectors, is given in Table 6.1.

With the installation of the first underground muon counter, connected to the SD station 'Corrientes', in November 2009, the acquisition of self-triggered data was started using the internal Occupancy-N trigger (Section 5.5). Within the following months, more occupancy data was recorded, not only with the first prototype detector, but also with newly installed muon counters. By performing several measurements with various combinations of the occupancy levels and thresholds, that were applied to the discriminator circuits of the AMIGA readout electronics, multiple datasets have been recorded. These sets allowed for an analysis of the data mainly aiming at a deeper understanding of the characteristic behaviors of the detectors by means of debugging the electronics system as well as investigating first physics results.

Starting in October 2010 with the installation of the auxiliary electronics constituting the T1/T3 trigger chain (Section 4.5.2), coincident data taking with the AMIGA muon counters and the associated SD stations became possible. From that time on, it was possible to trigger the MD modules by sending T1 trigger signals from the SD stations to the connected underground muon counters. At first, this data had to be stored locally on flash memory drives attached to the AMIGA single board computers (SBCs). The installation of all detectors of the PUC was completed in March 2012. In June 2012, after replacing the existing wireless communication system by a more powerful one (based on the Institute of Electrical and Electronics Engineers (IEEE) 802.11 standard), a stable integration of the AMIGA muon counters into the central data acquisition system (CDAS) of the Pierre Auger Observatory [Wun12] and the added capability of the counters to receive and decode T3 event requests allowed for a radio-bound transmission of the event data. At this stage, first events were recorded that contain data acquired by multiple muon counters [San12b].

Station Name	*LSID*	*UTM Position*		*Associated Muon*
		Easting	*Northing*	*Counters*
Corrientes	93	449,879.54 m	6,113,943.05 m	$5\,\mathrm{m}^2$, $10\,\mathrm{m}^2$
Heisenberg	1773	450,615.50 m	6,113,922.50 m	$10\,\mathrm{m}^2$
Kathy Turner	1764	450,992.16 m	6,114,576.09 m	$10\,\mathrm{m}^2$
Los Piojos	1574	449,497.37 m	6,114,579.39 m	$10\,\mathrm{m}^2$
Phil Collins	1622	450,246.21 m	6,114,570.33 m	$10\,\mathrm{m}^2$
Toune	688	450,624.52 m	6,115,227.18 m	$10\,\mathrm{m}^2$
Yeka	1570	449,871.66 m	6,115,222.57 m	$10\,\mathrm{m}^2$

Table 6.1: *List of SD stations contributing to the AMIGA pre-unitary cell. Inside the SD event structure, participating SD stations can be identified by using their local station identifier (LSID). The position of each detector is given in the universal transverse mercator (UTM) coordinate system (WGS84, Zone 19H, cf. [Bil01]).*

The analyses presented in the following are based on T1/T3-triggered data acquired with the AMIGA PUC in the time from July 2012 until October 2012. In Figure 6.2a, the availability of the seven muon counters that contribute to the AMIGA PUC is shown as a function of time ('Corrientes' (93), 'Heisenberg' (1773), 'Kathy Turner' (1764), 'Los Piojos' (1574), 'Phil Collins' (1622), 'Toune' (688) and 'Yeka' (1570); local station identifier (LSIDs) given in brackets). The information about the uptime of the detectors is gained from a dedicated monitoring tool [Pon12] that checks for the availability of each detector. More specifically, it checks for the reachability of the single SBCs via the radio network, which is the basis for any data acquisition (DAQ), in time intervals of 30 minutes. The exchange of the radio hardware in June 2012 significantly increased the availability of the muon detectors and thus allowed for establishing synchronous data taking with multiple muon counters. Since the AMIGA PUC was further on used for the debugging and development of the electronics hardware and the DAQ system, the detectors had to be rebooted and DAQ had to be stopped and relaunched from time to time. This process also caused interruptions in the recording of event data and the corresponding time intervals will be excluded from the following analyses.

To achieve a more thorough understanding of the detector performance, measurements with different detector calibrations were performed. Therefore, dedicated calibration routines were executed that allow for an adjustment of the discriminator thresholds of the Analog Boards in such a way that each of the 64 channels of a muon counter observes the same predefined signal rate. A more detailed description of this procedure can be found in [Kec13] and [Pon12]. As can be seen from Figure 6.2b, four different calibrations for fixed trigger rates were used. At sea level, the flux of background muons with momenta above $p_\mu \geq 1\,\mathrm{GeV/c}$ is in the order of $I_\mu^{\mathrm{bg}} \approx 1\,\mathrm{cm^{-2}\,min^{-1}}$ [Beh12]. With one strip of the AMIGA muon counter covering a horizontal area of $A_{\mathrm{strip}} = 4.1\,\mathrm{cm} \times 400\,\mathrm{cm} = 1640\,\mathrm{cm}^2$, the expected flux of background muons per strip can be calculated to

$$I_\mu^{\mathrm{strip}} = I_\mu^{\mathrm{bg}} \times A_{\mathrm{strip}} \approx 27\,\mathrm{Hz} \quad . \tag{6.1}$$

Although an increased muon flux is expected to be observable at the experimental site of the AMIGA enhancement ($\approx$ 1,400 m a.s.l.) the minimal calibration rate of $\mathcal{R} = 25\,\mathrm{Hz}$ is chosen such that it fits the value of I_μ given in Equation 6.1. However, this setting is applied under the optimistic assumption of the detector to be 100 % efficient for the detection of muons. Aiming at a detailed understanding of the detector performance, three additional measurement runs with increased calibration rates of $\mathcal{R} = 50\,\mathrm{Hz}$, $\mathcal{R} = 100\,\mathrm{Hz}$ and $\mathcal{R} = 300\,\mathrm{Hz}$, which have been chosen arbitrarily, were performed. Here, the calibrations result in smaller values of the discriminator thresholds, implying that signals with smaller amplitudes will no longer be rejected.
Since the following analyses will only concentrate on data that has been recorded with calibrated muon counters, the first data taking period with a global threshold level of 200 mV will be excluded. In addition, two time periods, in which the detectors were affected by extended maintenance work on the radio system (in Figure 6.2b marked with a '+') and the DAQ software (marked with one '$*$'), will not be taken into account. Albeit the last two data taking periods, in which the detectors were calibrated to a signal rate of $\mathcal{R} = 300\,\mathrm{Hz}$ and which are marked with two and three asterisks, were also influenced by minor ongoing

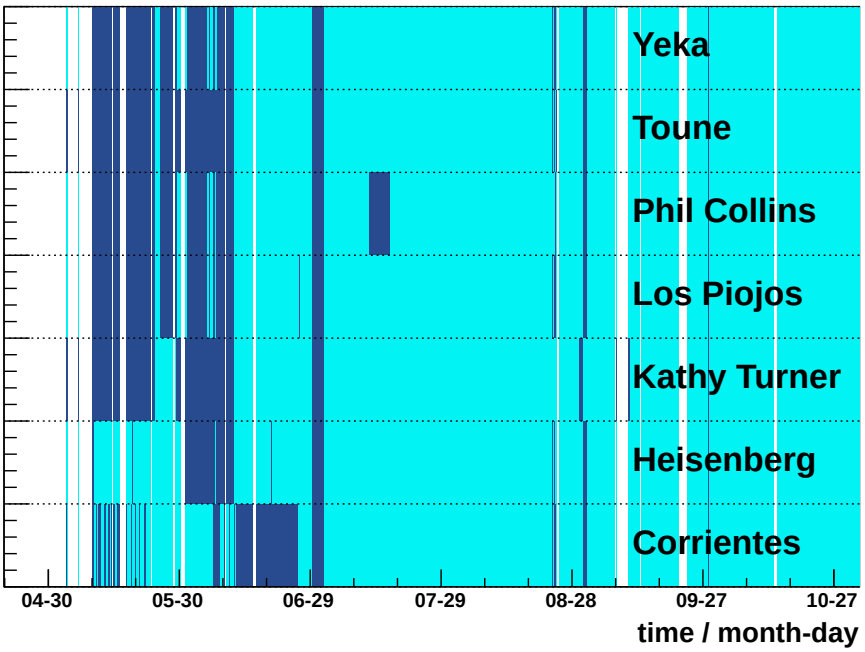

(a) Uptime of the muon counter modules.

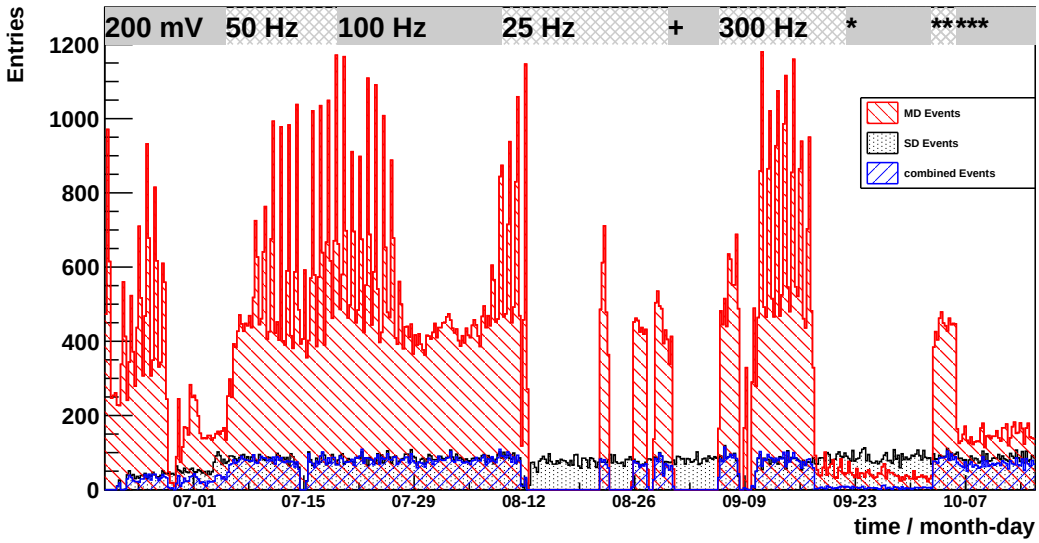

(b) The different data taking periods.

Figure 6.2: *Uptime of the muon counter modules and the different data taking periods. The upper panel shows the uptime of all seven muon counter modules that constitute the AMIGA PUC, measured with a dedicated monitoring software [Pon12]. In this plot, light blue areas indicate the availability of an SBC, whereas dark blue areas represent unavailable systems. White areas denote periods where the monitoring system itself was not operating. In the lower panel, the different data taking periods are illustrated [Pon12]. In addition, the number of MD and SD events as well as the the number of combined events is shown by the histograms. A detailed discussion of both plots is presented in [Pon12].*

Period	*Start (UTC time)*	*End (UTC time)*
50 Hz / strip	2012-07-05 05:15:00	2012-07-19 11:16:37
100 Hz / strip	2012-07-19 11:22:16	2012-08-09 07:23:40
25 Hz / strip	2012-08-09 07:43:55	2012-08-30 08:55:36
300 Hz / strip	2012-09-05 21:17:00	2012-10-15 23:59:59
Radio maintenance	2012-08-30 08:55:36	2012-09-05 20:16:59
Software maintenance	2012-09-22 00:00:00	2012-10-02 18:45:00

Table 6.2: *List of data taking periods that will be taken into account in the analyses. The two last lines specify periods of maintenance work, which are excluded from the data analyses. The exact time intervals have been determined in [Pon12].*

maintenance work, they don't have to be excluded from the analyses. Detailed information about the data taking periods that will be accounted for in the analyses presented here are given in Table 6.2.

6.3 System Debugging Using Occupancy- and T1/T3-triggered Data

From the time of the installation of the first AMIGA muon counter module until the time of the commissioning of the T1/T3 trigger for the PUC, various measurements using the Occupancy-N trigger have been performed. This data has been mainly used to debug the software of the AMIGA DAQ system and the detector hardware itself. Analyses of occupancy data led to the detection of data structures in the AMIGA events which pointed to undiscovered hardware- or software-related deficiencies of the detector electronics and the DAQ system. Most prominently, they revealed a substantial amount of signals recorded up to several microseconds after the trigger, which are not in agreement with the expected noise rate. Detailed laboratory measurements have proven that these signals can be solely attributed to effects of the PMT. However, it is found that the signal rate significantly decreases when increasing the thresholds of the discriminator circuits of the AMIGA Analog Boards. Especially for threshold values in the order of several hundreds of mV, as they result from the detector calibration to a constant signal rate per channel of about 100 - 300 Hz (Section 6.2), the impact of this effect on the recorded data is negligible. A detailed description of the laboratory measurements and a discussion of the results is given in [Son13].
Apart from that, four classes of errors, that can be attributed to the DAQ system, were detected by analyzing occupancy-triggered data. These will be discussed in the following.

Trash events

Events with a significantly increased number of active channels on time bin 0 are referred to as 'trash events'. This affects up to 32 channels, that show randomly distributed data. The distribution of the number of active channels on time bin 0 compared to the number of active channels per time bin in the noise region (time bins ranging from 1 to 119 and above 240,

Section 6.1) is shown in Figure 6.3. The average number of signals can be calculated to

$$\begin{aligned} N_{\mathrm{tb0}} &= (19.9 \pm 3.6) \quad \text{and} \\ N_{\mathrm{noise}} &= (\ 1.1 \pm 0.2) \quad . \end{aligned} \tag{6.2}$$

Both distributions differ by 5.21σ.

Corrupt magic word information

In order to reduce the probability of recording corrupted events, when transmitting event data from the Microcontroller Board to the SBC, the Microcontroller Board adds a magic word (`0x0A0B0C`) on time bin 769 to mark the end of the event structure. When operating the AMIGA detector without CDAS, the event is stored on a local flash drive connected to the SBC after the magic word is received. However, three kinds of errors have been found in analyses of occupancy-triggered data:

- The magic word appears on a different time bin than time bin 769 or the event does not include the magic word.
- Events contain more than one magic word.
- Events only consist of the magic word.

Wrong size of AMIGA events

Some of the analyzed events consist of less than 769 time bins. In this case, the magic word has been received on the last time bin of the event, but the event structure itself only covers a reduced time window of less than 768 time bins.

Repeated events

When operating the AMIGA detectors in the self-triggered mode, data taking is arranged in measurement runs of a given length in time. During this time, the detector records new events in terms of storing them in the external RAM (random access memory) of the Digital Board. Afterwards, the events are consecutively transmitted to the SBC and stored on the local flash drive. It was found that consecutive events in rare cases consist of exactly identical event structures. Even for complex event structures, the occurrence of this effect was found to be in the order of a few percent. However, the chance probability of having repeated events with only one bit differing from 0 is in the order of 2×10^{-5}. It is assumed that repeated events result from corrupted event requests, e.g. when sending erroneous event addresses.

The dataset of T1-triggered data, that is selected following Section 6.2, is analyzed with regard to these known errors. It is examined whether the system was successfully debugged since the discovery of the deficiencies mentioned above. In the following sections, recent results of these analyses will be presented.

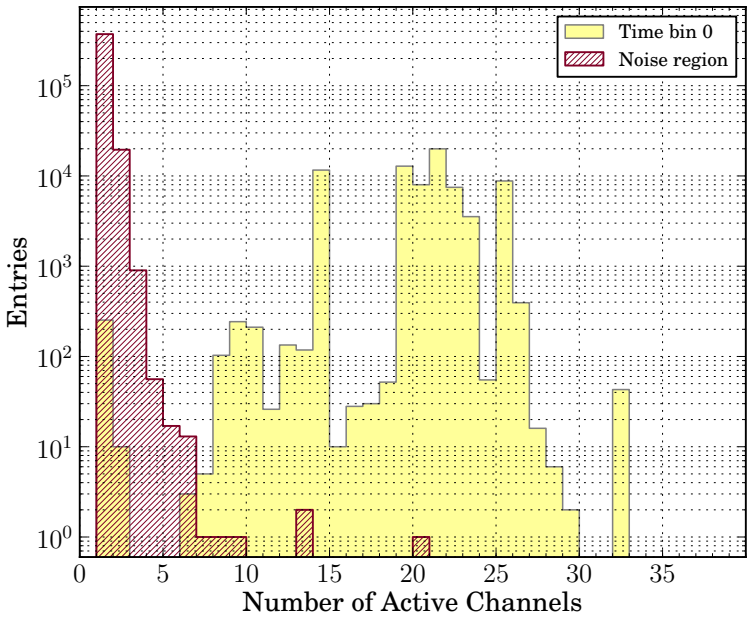

Figure 6.3: *Number of active channels on time bin 0 (yellow histogram) and in the noise region (red hatched histogram). The noise region covers time bins between 1 and 119 and above 240. Overall, 107,222 non-empty events acquired with the AMIGA pre-unitary cell have been analyzed.*

6.3.1 Trash Events in T1/T3-triggered Data

Trash events have also been found in the dataset of T1-triggered data. All events that show signals on time bin 0 and on at least one more time bin will be assigned to this category of events. Events that only show signals on time bin 0 and events without signals on time bin 0 are further on referred to as 'empty trash events' and 'normal events', respectively. By comparing both distributions shown in Figure 6.3, the probability of misidentifying a normal event as a trash event is estimated to be on the per mill level. Following the above definitions, out of the 107,222 non-empty events, that are contained in the dataset, 33,252 (31.0 %) normal events, 12,537 (11.7 %) trash events and 61,433 (57.3 %) empty trash events have been identified. The probability of recording trash events does not solely depend on the combination of the choice of the individual counter module and the detector calibration, rather, the internal routing of the signals seems to be the dominant criterion. The effect is expected to be due to the timing of the clock enable and write enable signals inside the FPGA firmware, which control the process of writing the event data from the input buffers to the external RAM. This could be proven by investigating the dependence of the jitter of the relevant signals on the individual signal routings inside the FPGA. Although the cause has not been investigated in detail for the FPGA firmware of the PUC [S2], the problem of having trash events has been eliminated for the 320 MHz version of the FPGA firmware [S3] with the implementation of a different buffer structure and by adjusting the timings of the writing processes [Kol13]. However, clarifying the origin of trash events is beyond the scope of this thesis. Instead, it will be examined in the following whether trash events have to be

excluded from any physics analysis.

To qualitatively study the differences between trash events and normal events, the time distribution of both classes of events will be compared to each other. In order not to bias the analysis with detector or calibration specific effects, like e.g. the noise levels resulting from different calibrations, only one detector and one calibration is chosen for the comparison. A statistically significant number of both classes of events is available for the MD module associated to the SD station 'Toune' and a muon counter calibration of 100 Hz per strip. For this setting, the dataset contains 3,553 trash events and 1,799 normal events.

In the upper panel of Figure 6.4, the normalized time distributions of trash events and normal events are plotted as an overlay. Time bin 0 has been removed from both distributions. The normalization factors are gained from the total number of entries in each set (trash events: 18,238 entries; normal events: 9,265 entries), the errors are calculated from Poissonian statistics. For a better comparison of both distributions, the normalized residuals are plotted as a function of the time bin in the lower left panel of Figure 6.4. The lower right panel depicts the distribution of the residuals including a Gaussian fit to the data. From this fit, the mean and the standard deviation of the distribution are determined to be $\mu = 0.02 \pm 0.03$ and $\sigma = 1.00 \pm 0.03$, respectively. By this, it is found that the deviations between the two time distributions are compatible with the assumption of resulting purely from statistical effects. This result will be further quantified in the following.

In order to test the hypothesis of homogeneity of both unweighted histograms, meaning that both histograms represent random values of the same distribution, a χ^2-test [Pea04] has been performed. With both histograms having the same number of bins of $r = 767$ and with n_i and m_i being the number of entries in the ith bin of the first and the second histogram, respectively, the total number of entries is equal to $N = \sum_{i=1}^{r} n_i$ in the first histogram and $M = \sum_{i=1}^{r} m_i$ in the second histogram. Following [Gag06], the hypothesis of homogeneity is equivalent to the existence of r constants $p_1 \dots p_r$, with $\sum_{i=1}^{r} p_i = 1$, and the probability that some measured value belongs to the ith bin in each of the both distributions is equal to p_i. The number of entries in the ith bin is a random variable with a distribution approximated by a Poissonian probability distribution $f_i^n = e^{-Np_i}(Np_i)^{n_i}/n_i!$ for the first histogram and $f_i^m = e^{-Mp_i}(Mp_i)^{m_i}/m_i!$ for the second histogram. If both histograms originate from the same underlying distribution, then the maximum likelihood estimator $\hat{p}_i$ [Boh10] of p_i $(i = 1 \dots r)$ is given by

$$\hat{p}_i = \frac{n_i + m_i}{N + M} \quad . \tag{6.3}$$

With this, the compatibility of both histograms can be examined by evaluating

$$X^2 = \sum_{i=1}^{r} \frac{(n_i - N\hat{p}_i)^2}{N\hat{p}_i} + \sum_{i=1}^{r} \frac{(m_i - M\hat{p}_i)^2}{M\hat{p}_i} = \frac{1}{MN} \sum_{i=1}^{r} \frac{(Mn_i - Nm_i)^2}{n_i + m_i} \tag{6.4}$$

which follows approximately a χ^2-distribution with $r - 1$ degrees of freedom [Cra46]. For the given dataset the calculation results in $X^2 = 811.37$, corresponding to a value of $\chi^2/\mathrm{NDF} = X^2/766 = 1.06$.

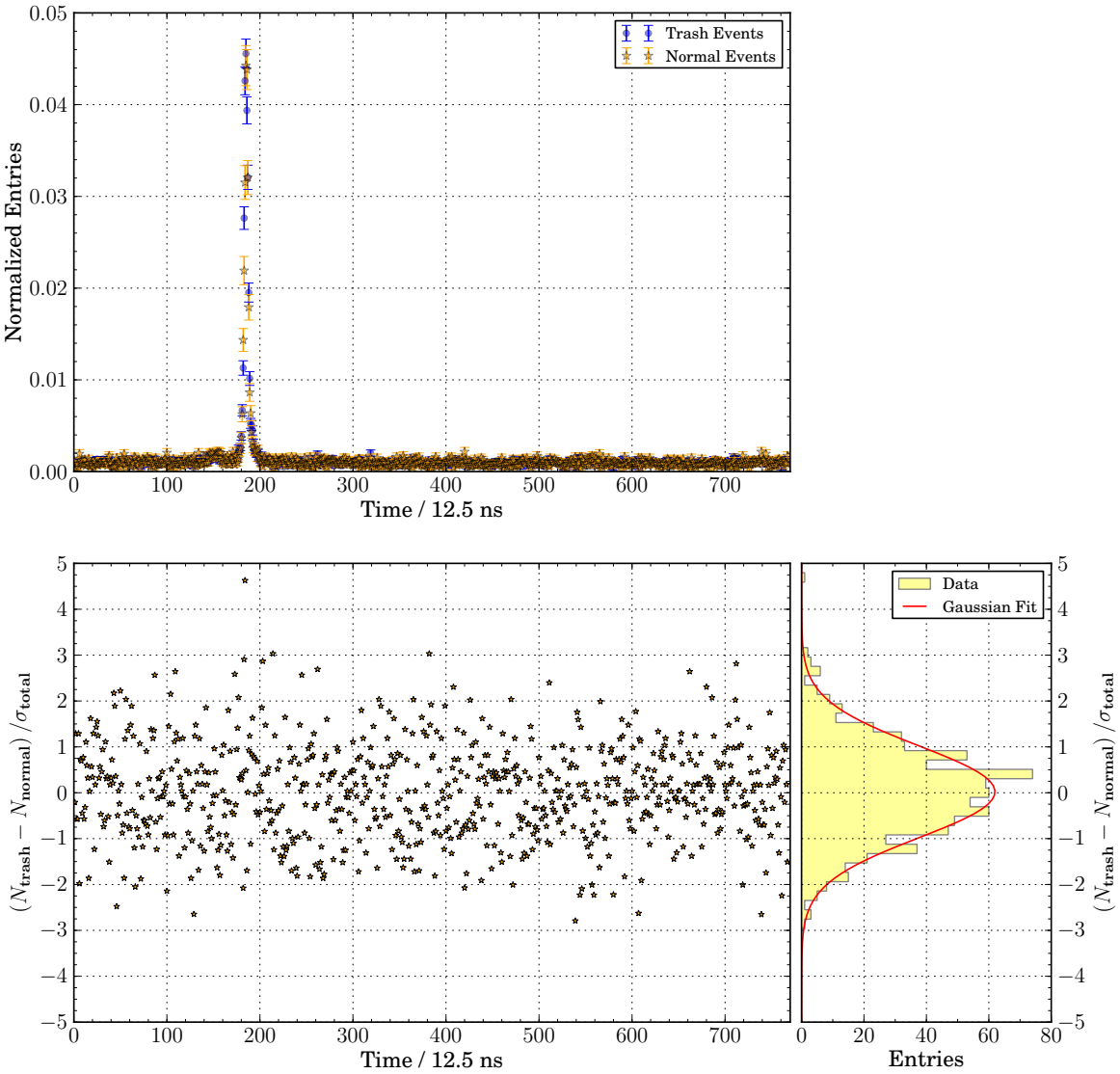

Figure 6.4: *Comparison of the time distributions of trash events and normal events. The upper panel shows the cumulative time distributions of both classes of events, measured with the muon counter associated to the SD station 'Toune' calibrated to a signal rate of* 100 Hz *per strip (trash events: blue circles; normal events: orange asterisks) as an overlay. The left panel of the lower subfigure depicts the normalized residuals of both time distributions. The right panel shows the distribution of the residuals and a Gaussian fit to the data. Overall, 3,553 trash events and 1,799 normal events have been acquired.*

This result can also be translated into a probability value $p(\chi^2, \mathrm{NDF})$, which is defined as

$$p(\chi^2, \mathrm{NDF}) = \frac{(\chi^2)^{\left(\frac{\mathrm{NDF}}{2}-1\right)} \times e^{-\frac{\chi^2}{2}}}{\Gamma\left(\frac{\mathrm{NDF}}{2}\right) \times 2^{\frac{\mathrm{NDF}}{2}}} \quad , \tag{6.5}$$

with $\Gamma(x)$ being the gamma function. Here, the calculation of the probability value results in $p = 0.124$. When testing the hypothesis of homogeneity at a confidence level of $\mathrm{CL} = 95\,\%$ ($\alpha = 1 - \mathrm{CL} = 0.05$), the difference between the two distributions can be considered to be not statistically significant since p is larger than α.

When removing time bin 0 from any AMIGA muon counter event, no significant differences between the time structures of trash events and normal events are found. This finding supports the assumption of time bin 0 not to contain relevant physics data but to be modified by internal processes of the FPGA. Due to the limited statistics of the measurements taken with the individual muon counters, the statistical test could only be performed for one combination of detector and calibration. However, since all detector modules are similar, there is no reason to assume that the result of the test would differ for the other detector stations or any other detector calibration. For the further analysis, time bin 0 will be systematically removed from any AMIGA MD event.

6.3.2 Magic Word Information in T1/T3-triggered Data

The dataset described in Section 6.2 solely consists of events that have been requested by CDAS based on a T3 trigger condition and that have been transmitted via radio link. In order to reduce the amount of data that has to be transmitted, every recorded MD event is compressed before being sent to CDAS. Instead of all 64×768 bits of an AMIGA MD event, only the front-end channel numbers and the time bin information of individual signals are transmitted. This compression is performed by the Microcontroller Board of the underground electronics. The microcontroller adds the magic word, which marks the end of the event, to the data structure before transmitting the data to the SBC. Contrary to uncompressed event data, the length of an event is no longer fixed to 768 time bins. Therefore, the position of the magic word is not confined to time bin 769 any more. In order not to lose the additional information of the length of the event that was transmitted, the number of 16-bit words contained in the event data is appended to the magic word structure. An example of the magic word structure of a compressed event is given in Listing 6.1.

The SBC checks for the presence of the magic word in each event received from the Microcontroller Board and compares the number of 16-bit words given by the magic word structure with the real event size. The event is accepted if both checks are successful, otherwise the event data will be requested again. After being transmitted via the radio link, the same checks will be repeated by CDAS. Again, the event will be requested until the correct magic word information is detected and as long as the number of requests does not exceed a maximum number of attempts [San13]. Before the event is finally stored in the data tree, the magic word information is removed from the event structure. Therefore the MD data, that is available for

```
...          ...                          ...
00000bf0   0b ee 00 27 0b f0 f0 95   0b f2 55 12 0b f3 01 00
00000c00   0b f6 00 ae 0b f8 66 45   0b fa 76 74 0b fb 01 00
00000c10   0b fc 45 6e 0b fe 64 6f   0a 0b 0c 00 03 06 00 00
```

Listing 6.1: *Realization of the magic word structure in compressed event data. The listing shows the last three lines of the hexdump output of an AMIGA MD event. The first column denotes the position of the data, event data is shown in black in the second and third column. The magic word* `0x0A0B0C` *(shown in blue) on the last line is followed by the event size in measures of 16-bit words (red). All other entries on the last line have to be* `0x00` *(orange).*

analyses, only contains events that originally included valid magic word information.

The problem of having no magic word or corrupted magic word information, as well as finding the magic word on a different time bin than 769 in uncompressed events, can be attributed to problems in the transmission of event data via the CAN (controller area network) bus between the Microcontroller Board and the SBC at the time of software development. High data rates in combination with an increased workload on the SBC could cause a loss of event data, which, as a consequence, will lead to storing corrupted event data. The number of corrupted events has been significantly reduced by introducing the compression of event data and by repeatedly requesting event data that is found to be corrupted on the basis of checking the magic word information.

In previously analyzed data, which mainly has been recorded using the Occupancy-N trigger, the appearance of a second magic word inside the event structure has been found in approximately 0.003 % of the events [Tca12]. Also this effect is suspected to be a consequence of the problems in the CAN bus communication mentioned above. Even with the magic word structure being removed in T1/T3-triggered events, the occurrence of the magic word within the event data can be searched for. By analyzing the 107,222 non-empty events, which are contained in the dataset described in Section 6.2, no magic word inside the event data has been found. The chance probability of finding the magic word structure (4 bytes `0x0A0B0C00` + 2 bytes of random data + 2 bytes zero) in uncompressed events can be calculated to $\mathcal{P}_{\mathrm{mw}} = 2^{16}/2^{64} \approx 3.55 \times 10^{-15}$. For compressed events, this probability is reduced by several orders of magnitude since the event has to fulfill more criteria: at position `0x0A0B`, the event has to have a data content of `0x0C00` and, in addition, this entry has to be the last one inside the data structure with an overall odd number of entries (only then, the event is filled up with zeros). For the given statistics, the result of not finding the magic word structure within the data content of T1/T3-triggered events is therefore in agreement with the theoretical expectations.

6.3.3 Repeated Events in T1/T3-triggered Data

In contrast to operating the muon counters in the self-triggered mode, the acquisition of T1/T3-triggered data is not organized in measurement runs of a given length in time. Whereas the former acquisition mode is based on requesting and storing blocks of up to 2,048 subsequent

events, in the latter case, the detector is continuously recording data. Here, all events are uniquely labeled by the local timestamp of the corresponding T1 trigger signal (Section 5.7). The event data is transmitted to CDAS on the basis of T3 requests, for which the event identification is solely based on the timestamp information. In general, there is no direct link between the timestamp and the position of the event inside the external RAM of the Digital Board, i.e. consecutive event requests will result in events originating from randomly distributed RAM addresses. Therefore, a direct comparison of the detection of subsequent repeated events in self-triggered and T1/T3-triggered data appears to be pointless, when aiming at the understanding of the problems found in occupancy-triggered data.

However, the search for identical events in the dataset remains interesting in itself. After removing time bin 0 from any muon counter event, the available data tree contains 45,789 non-empty MD events. This subsample is analyzed for the occurrence of pairwise identical events.
If an air shower is observed by the SD as well as by the fluorescence detector (FD), both detectors will generate a trigger signal on the T3 level. Each T3 trigger will cause CDAS to send an event request to the AMIGA muon counters. Therefore, one muon counter event might be stored twice in the data tree. Since both event requests are performed independently of each other, i.e. both requests will take a different amount of time to be accomplished, both events will not necessarily be stored on subsequent positions in the data tree. However, these pairwise identical events will include the same T3 timestamp. The occurrence of the doubling of the event data is time dependent and dominated by the uptime of the FD. The finding of an increased number of MD events recorded during the operation times of the FD has already been discussed in [Pon12].
In the available dataset, 567 subsequent event repetitions (6,559 overall repetitions) with identical T3 timestamps are identified. In addition, 29 subsequent events with identical data content but with different T3 timestamps are found. For these events, the differences between the timestamps of pairwise identical events are in the order of 10 s. The origin of this effect is not yet understood. However, the cause is suspected to be related to processes inside the CDAS software framework [Sat13].

6.4 Selection of Combined MD/SD Events

For the physics analyses discussed in this chapter, only air shower events will be taken into account, that contain the measured information of the SD array as well as recorded muon counter data.
The data related to SD observables is available in the advanced data summary tree (ADST, version v2r9p3, [Mar06]) files provided by [Dem13]. Since the ADST files are available for single days, only files are selected which cover the time periods mentioned in Table 6.2 and which include the infill array of the SD. An overall number of 147,246 reconstructed SD events is stored inside the corresponding data trees. The event data, that have been recorded with the AMIGA MD and that have been received by CDAS after successful T3 requests, are stored in SD-independent data trees on more irregular time intervals. The files, that cover the relevant time periods, contain 133,086 MD events.

Both, the data trees of the SD as well as of the MD, contain detailed information about the time when the individual events were triggered. To all SD events, a timestamp, consisting of the GPS (Global Positioning System) second and the GPS microsecond of the trigger, is attached. Whereas for the MD events, the information about the GPS second of the trigger time is always available, the storage of the GPS microsecond was only implemented around July 20th, 2012 [San12a]. In order to match the muon counter information to the corresponding SD events, the GPS second between individual events of the two data trees is compared and, whenever possible, the GPS microsecond is included into this comparison. From the two datasets, 59,825 event matches could be identified, for which the muon counter information of at least one AMIGA counter of the PUC and the reconstructed shower information of the SD is available. Events, that have been measured with both detectors, the SD and the FD, will be contained twice inside the MD tree. These duplicates are identified based on the timestamp of the event and are removed from the final dataset.
In a second step, this dataset is modified in two ways. Events, which have not been recorded in one of the four calibration runs and which do not fulfill the criteria of the T5 trigger (Section 3.1.3), are excluded from the dataset. In addition, two additional cuts are applied: Only events with a reconstructed zenith angle of $\theta \leq 60\,^\circ$ and with a reconstruction level of $L = 4$ are accepted. The latter condition is fulfilled, if the shower axis and the curvature of the shower front have been successfully reconstructed. Additionally, the reconstruction has to result in a successful determination of the lateral distribution function (LDF, Section 2.3). These conditions assure that only high-quality events with a larger number of participating SD stations are selected. After all, the final dataset contains 55,014 events, which will be taken into account for further analyses.

6.4.1 Properties of Combined MD/SD Events

The PUC of AMIGA stations is part of the infill array of the SD. Therefore, the primary energy spectrum of measured air showers is expected to show a maximum at an energy in the order of $10^{17}\,\mathrm{eV}$, where the trigger system of the infill array reaches full trigger efficiency, almost independent of the mass of the primary particle and for zenith angles smaller than $60\,^\circ$ [Set11a]. The energy spectrum of events included in the combined dataset is shown in Figure 6.5a. Towards lower energies, the number of recorded events decreases due to the fact that the trigger algorithms of the infill become more and more inefficient. The continuing decline at the right tail of the distribution is consistent with a decreasing flux of primary cosmic rays with increasing energy. The expected maximum is found in the data, although its position is shifted towards lower energies. This can be explained by the fact that the spectrum is affected by the convolution of the energy dependent trigger efficiency and the rapidly increasing flux of primary cosmic ray particles towards lower energies.

For the combined dataset, the reconstructed zenith angles θ of the arrival directions of the primary cosmic rays are shown in Figure 6.5b. The shape of the distribution is in agreement with the expectation of being approximately proportional to $\sin\theta\cos\theta$. In case of full detector efficiency, this proportionality is due to two different contributions: for larger zenith angles, the number of events increases due to geometrical considerations, since the surface element on the sphere from where the primary cosmic ray comes from grows proportional to $\sin\theta$.

Contrary, the effective area of the detector array decreases proportional to $\cos\theta$. The deficit of events on the right tail of the zenith angle distribution results from the effective acceptance of the experiment, which acts as a suppression at large zenith angles. Here, a larger depth of the atmosphere, which particles of an inclined air shower must traverse compared to vertical showers, corresponds to an increased number of interaction lengths. Therefore, less particles reaching ground level might lead to a non-fulfillment of the trigger criteria and, as a consequence, to a suppression of recorded events towards larger zenith angles. The cutoff at $\theta = 60\,^\circ$ is due to the geometry cut mentioned in Section 6.4.

The reconstructed core positions at ground level of the events contained in the combined dataset are shown in Figure 6.6. The area of the infill array is clearly visible with its borders being well defined. This effect can be attributed to the T5 quality cut applied to the dataset, since the T5 trigger condition (Section 3.1.3) is only fulfilled if the SD station which measures the largest signal is surrounded by six active stations. A triangular structure of all core positions inside the detector area is expected to occur since all recorded events have to fulfill one of the T3 trigger conditions at an earlier stage of the data acquisition. Due to geometrical considerations, the probability of fulfilling any of the T3 criteria, for which the most rigorous one requires to have three triggered SD stations in a compact spatial configuration, is reduced on the connection lines between two detector stations. This structure can clearly be seen in Figure 6.6.
During the commissioning phase of AMIGA, the infill array is operated using a parallel CDAS. This version of the software will request data of all the infill stations as soon as a T3 trigger condition is fulfilled for any stations within the infill array. The combined dataset only contains events for which at least one SD station of the PUC, and by this also the associated MD, has been triggered on the T1 trigger level, even if no MD event data has been acquired. Therefore, the reconstructed position of the shower core may fall outside the area of the PUC. In these cases, the stations of the PUC may not even participate in the SD shower reconstruction. However, an increase of the density of reconstructed core positions for smaller distances between the PUC and the shower core is found in the data. This results from the increased probability of fulfilling the T1 trigger condition and therefore from the increased probability to include the recorded event into the combined dataset.
The reconstruction of shower core positions on the left side of the infill is due to stations of the HEATLet enhancement (Section 3.3.2), which expand the instrumented area of the infill to the west.

6.5 Occupancy-based Analyses of T1/T3-triggered Data

The Occupancy-N trigger (Section 5.5) has mainly been used for data taking to debug the hardware and the software of the AMIGA underground muon counters. Since the MD modules could only be triggered by the associated SD stations at a later stage of the AMIGA prototype phase, the Occupancy-N trigger was, over a long time, the only possible trigger, that could be used for data taking. Given the possibility of setting the multiplicity level of this self-trigger to any desired value and the implementation of the prescaler algorithm (Section 5.6) in the FPGA firmware, the detector was operated in various configurations. However, the results

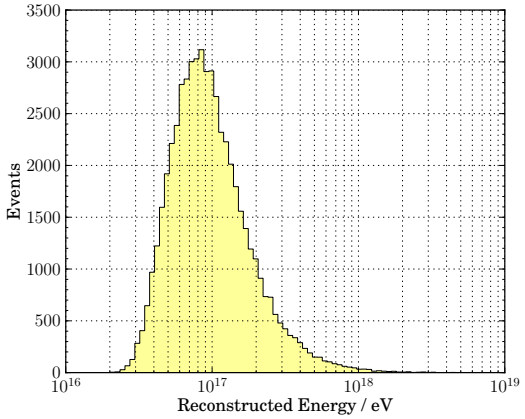

(a) *Energy distribution of combined SD/MD events.*

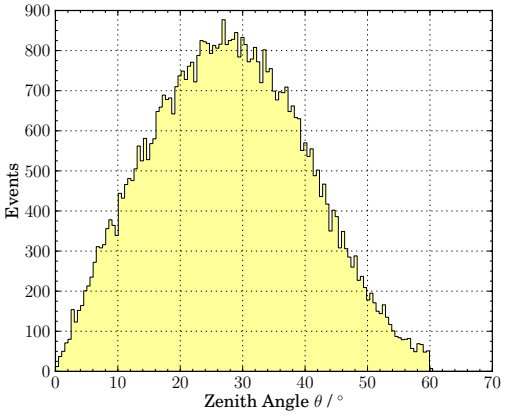

(b) *Zenith angle distribution of combined SD/MD events.*

Figure 6.5: *Energy and zenith angle distributions of combined SD/MD events. The shape of the energy distribution (left panel) results from a convolution of the energy dependent trigger efficiency of the detector array and the decreasing flux of primary particles. The right panel depicts the dependence of the number of measured events on the zenith angle of the primary particle, which is approximately* $\propto \sin\theta\cos\theta$*. The geometry cut at* $\theta = 60°$ *is clearly visible. The analyzed dataset contains 55,014 events.*

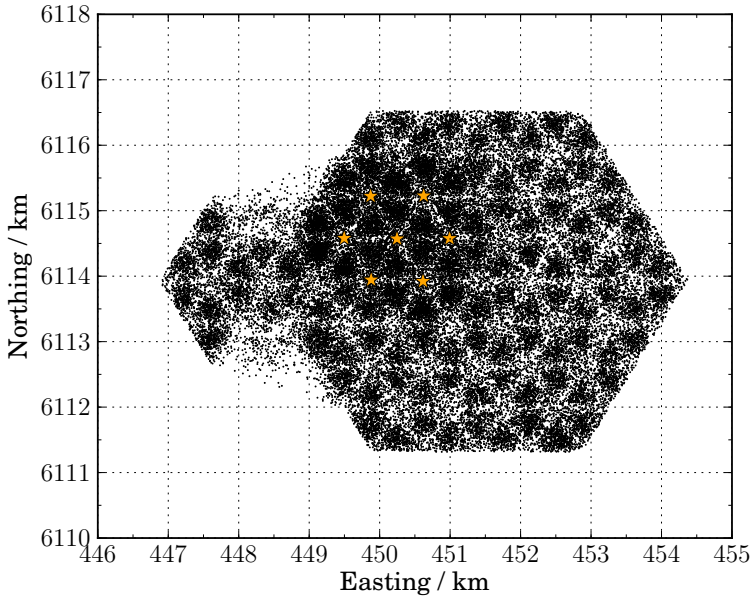

Figure 6.6: *Reconstructed shower core positions of combined SD/MD events (black dots). The infill area and the triangular structure of the array are clearly visible. The increased density of events around the PUC (orange asterisks) is an intrinsic property of the dataset, which only includes events for which recorded SD and MD data is available. Stations of the HEATLet enhancement expand the instrumented area to the west. Overall, 55,014 events have been analyzed.*

of analyses, that are based on self-triggered data, could not yet been compared to any air shower related observables. In the following sections, the available dataset of T1/T3-triggered (Section 6.4) data will now be analyzed with regard to the signal multiplicities contained in the event data.

6.5.1 Definition of N_{Occ} and N_{Trig}

An overlay of the time distributions of all T1/T3-triggered events, recorded with the AMIGA PUC in the data taking periods listed in Table 6.2, is shown in Figure 6.1. As already indicated in Section 6.1, the air shower related data will be recorded in a time interval that is characterized by the double peak structure resulting from the two different types of T1 triggers, namely T1-TH and T1-ToT. A region around the two peaks is defined as the trigger region, which includes the time bins in the range from time bin 120 up to time bin 239 [Pon12], thus covering a recording time of 1.5 µs. The merger of all other time bins will, in the following, be referred to as the noise region. N_{Trig} is defined as the number of digital entries within the trigger region. This corresponds to the number of digitized sample points of the signals with amplitudes above the thresholds adjusted on the Analog Boards. More detailed information on N_{Trig} as well as first analysis results based on this observable can be found in [Pon12].

Whereas N_{Trig} is given by the sum of all entries in the given time interval, the analysis aiming for a deeper understanding of the occupancy level of the recorded events only concentrates on the number of time-coincident signals. N_{Occ} is defined as the maximum multiplicity of entries that is detected on any of the 767 time bins of an MD event. Therefore, the defined observable corresponds to the maximum occupancy level N for which the detector would have been triggered by the event in case of being operated in self-triggered mode. N_{Occ} can cover values in the range $0 \ldots 64$, e.g. a value of $N_{\mathrm{Occ}} = 64$ implies, that time-coincident signals were recorded on all 64 channels of the MD on at least one time bin. Since N_{Occ} is not restricted to time bins of the trigger region, $N_{\mathrm{Occ}} = 0$ will only be found for empty events.

As shown in Figure 6.7, both observables N_{Occ} and N_{Trig} are significantly correlated. Therefore it can be concluded that the number of signals in the trigger region of an AMIGA MD event does not result from multiple signals being isolated in time, but rather from the appearance of time-coincident signals. This finding shows that the MD modules are sensitive to muons in air showers. Thus it confirms the analysis results derived in [Pon12], where a correlation between N_{Trig} and the signal strength S_{LDF} measured with the associated SD station has been found.

6.5.2 Dataset for Occupancy-based Analyses

The maximum number of time-coincident signals N_{Occ} found in an AMIGA MD event strongly depends on the calibration of the underground muon counter. Calibrations with low trigger rates per strip lead to rather high threshold voltages of the discriminator electronics of the Analog Boards, in the order of several 100 mV. Low-amplitude signals, which result from air shower particles traversing the MD, are therefore no longer recorded by the detector and N_{Occ}

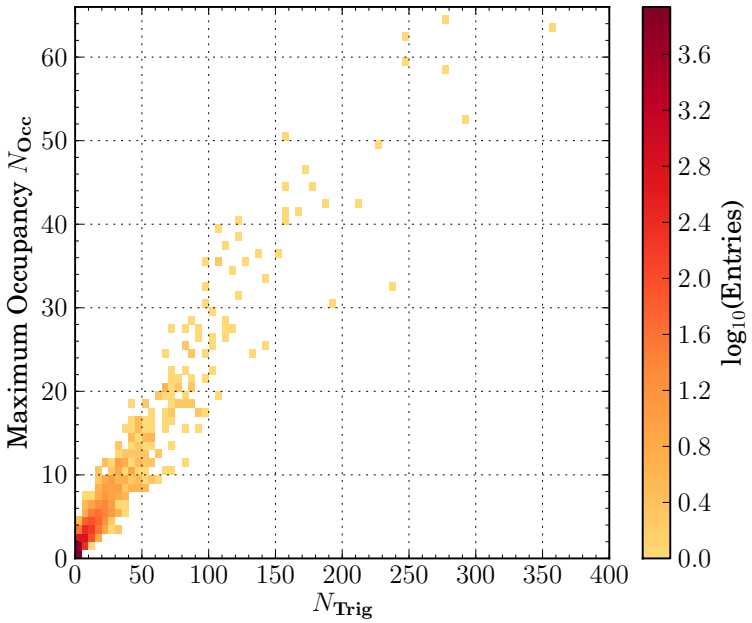

Figure 6.7: *Correlation between N_{Occ} and N_{Trig}. Overall, 16,889 MD events acquired with the PUC stations 'Los Piojos', 'Phil Collins' and 'Heisenberg' are taken into account. Detailed information about the selection of the dataset is given in Section 6.5.2.*

will cover smaller values. Since the opposite is true for calibrating the detector to high signal rates, mixing up data taking periods with different calibrations, which in addition contain an individual number of recorded events each, might bias the results of any analysis. Therefore, N_{Occ}-related analyses will always be restricted to one data taking period (Table 6.2) only. In the following, the calibration with a signal rate of $\mathcal{R} = 300\,\mathrm{Hz/strip}$ will be chosen since the recorded events are the ones for which the data content is less affected by the discriminators of the analog electronics.

Aiming for a clean dataset, additional constraints on the data have to be taken into account. Although all muon counter modules have been calibrated to a predefined signal rate for each data taking period, problems during these calibration processes might lead to differences in the trigger rates of individual channels of single detectors. These problems mainly result from bad fits to the measured calibration data. Noisy channels will bias the determination of signal multiplicities in such a way that larger values for N_{Occ} will be preferred. The affected MDs will be rejected from further analyses. This behavior was found for the muon counter modules associated to the SD stations 'Kathy Turner', 'Toune' and 'Yeka'. An overlay of all events measured with the MD at 'Toune' is shown in Figure 6.8, which illustrates this effect. The noisy channels are clearly visible. Since the problematic channels occur in groups of eight, the cause of the bad fit results of the calibration is expected to be found in the electronics of the Analog Boards, which each provide the discriminator circuits for eight channels (Section 4.5.1).

The two MD modules associated to the SD station 'Corrientes' both appear to be not suited

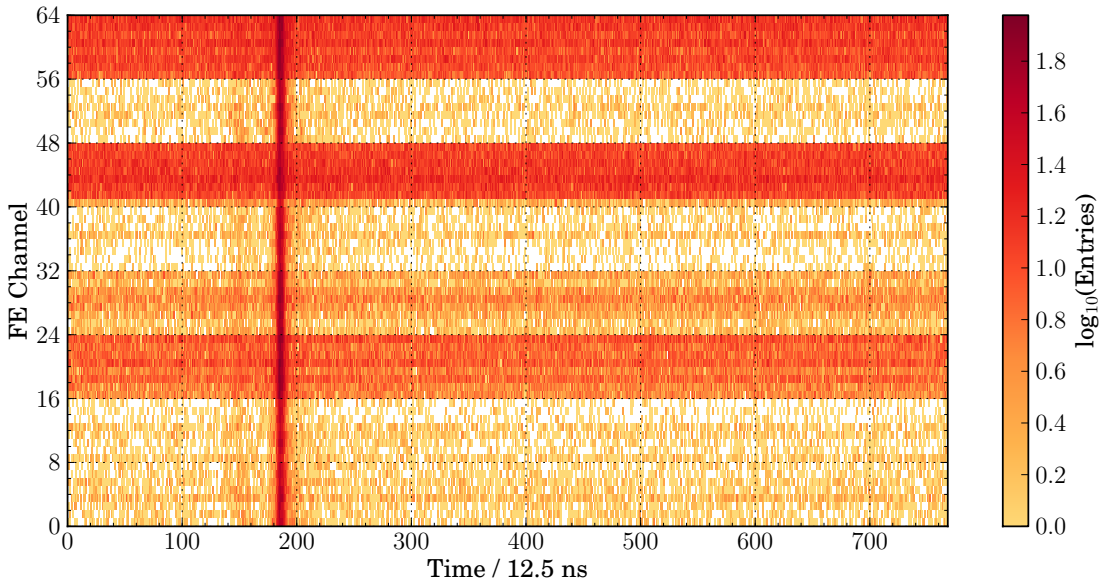

Figure 6.8: *Overlay of events acquired with the MD module at 'Toune'. The noisy front-end (FE) channels resulting from bad fits in the calibration runs are clearly visible. Overall, the plot contains information from 6,605 non-empty events.*

for occupancy analyses for two reasons. The $10\,\mathrm{m}^2$ module differs from the one of all other detectors by having five fibers which are not connected to the PMT. Being one of the first muon counter prototypes installed at the experimental site, this module has been modified in that way to allow for studies of the optical crosstalk inside the module. The $5\,\mathrm{m}^2$ module differs from the other ones because of its smaller size and, in addition, has been excluded from data taking over extended periods of time. Apart from that, 'Corrientes' has permanently been used to debug and test the electronics. Therefore, it had to be restarted more frequently and could only be used for data taking for a limited period of time only. For these reasons, also this MD will be excluded from further analyses.

Taking everything mentioned so far into account, the combined dataset, that can be used for analyses based on any occupancy-related observable like e.g. N_{Occ}, contains an overall number of 16,889 events. These events contain the data recorded with the SD as well as MD data that has been acquired with the PUC stations 'Los Piojos' (5,650 events), 'Phil Collins' (5,462 events) and 'Heisenberg' (5,777 events).

6.6 Correlation of N_{Occ} with SD-related Shower Observables

In the following sections the physics interpretation of occupancy-triggered data will be discussed analyzing the combined dataset. As already shown in Figure 6.7, a linear relation between both MD observables N_{Trig} and N_{Occ} was found in the data. The number of signals in the trigger region N_{trig} measured by an MD module significantly correlates with the signal strength of the associated SD station S_{LDF} [Pon12]. Here, S_{LDF} is calculated by evaluating

the reconstructed LDF for the measured distance between the SD station and the shower axis. As a direct consequence of this and of Figure 6.7, also N_{Occ} is expected to correlate with S_{LDF}.

The scatter plots of N_{Trig} and N_{Occ} versus S_{LDF} for the dataset selected following Section 6.4 and Section 6.5.2 and for a signal strength of $S_{\mathrm{LDF}} \geq 20\,\mathrm{VEM}$ are shown in Figure 6.9. The cut on S_{LDF} has been introduced to exclude data points with small signal strength, that do not show any dependence on one of the two MD observables, i.e. N_{Trig} and N_{Occ} are both flat distributed for events with $S_{\mathrm{LDF}} \leq 20\,\mathrm{VEM}$. The reconstructed signal S_{LDF} represents the strength of the signal that a hypothetic station would have measured at the given distance from the shower axis based on the LDF fit of the air shower event. The uncertainty of S_{LDF} should account for the signal fluctuations as they arise from shower fluctuations on an event-by-event basis. Since multiple SD stations are taken into account for the determination of the LDF, the uncertainty of S_{LDF} resulting from the uncertainties of the fit parameters will not sufficiently account for these fluctuations. Therefore, the uncertainty on the reconstructed signal strength, as shown in Figure 6.9, is estimated following

$$\sigma\left(S_{\mathrm{LDF}}\right) = \left(0.32 + 0.42\sec\theta\right) \times \sqrt{S_{\mathrm{LDF}}} \quad . \tag{6.6}$$

Equation 6.6 has been derived from measurements with pair tanks [Ave07b]. It analytically models the signal accuracy including a dependence on the zenith angle of the air shower for non-inclined showers up to $\theta = 68\,^{\circ}$.

In order to quantify the strength of the correlation in both plots the correlation coefficient r defined through [Bro00]

$$r = \frac{Cov(X,Y)}{\sqrt{Var(X)\,Var(Y)}} = \frac{\sum_i \left(x_i - \bar{x}\right)\left(y_i - \bar{y}\right)}{\sqrt{\sum_j \left(x_j - \bar{x}\right)^2 \sum_k \left(y_k - \bar{y}\right)^2}} \tag{6.7}$$

is determined. Here, $Cov(X,Y)$ and $Var(X)$ ($Var(Y)$) denote the covariance and the variances of the observables X and Y, x_i (y_i) and $\bar{x}$ ($\bar{y}$) represent the individual measurements and the arithmetic mean of the data, respectively. This definition of r implicates $r \in [-1;+1]$, in particular this means $r = -1$ for totally anti-correlated observables, $r = 0$ in case of uncorrelated observables and $r = +1$ for observables that are 100 % correlated. The uncertainty of r is given through [Cow98]

$$\sigma_r = \frac{1 - r^2}{\sqrt{N}} \tag{6.8}$$

with N being the total number of measurements taken into account.

The calculations result in $r = 0.45 \pm 0.02$ for N_{Occ} and in $r = 0.48 \pm 0.02$ for N_{Trig}. Both correlation coefficients are in agreement within an error interval of 1.06σ. Therefore, both observables, N_{Trig} and N_{Occ}, are appropriate for further analyses. In the following, N_{Occ} will be chosen as the MD observable.

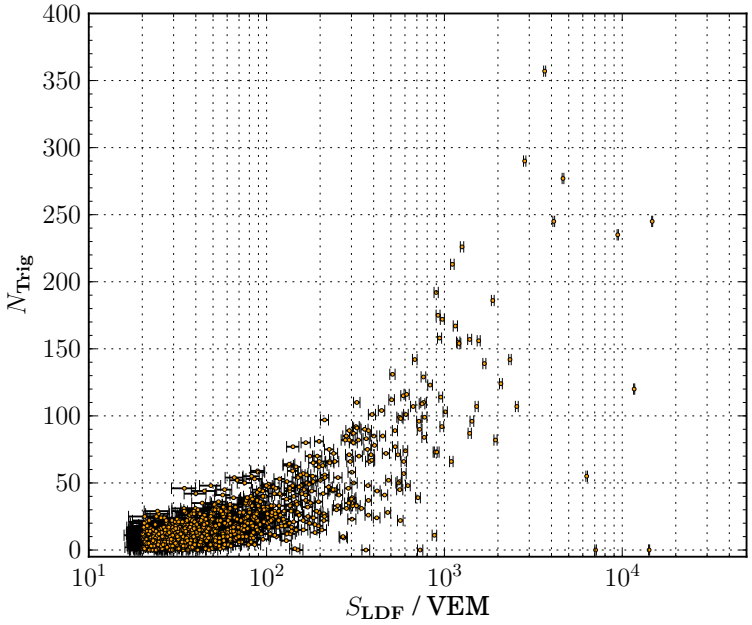

(a) *Correlation between S_{LDF} and N_{Trig}.*

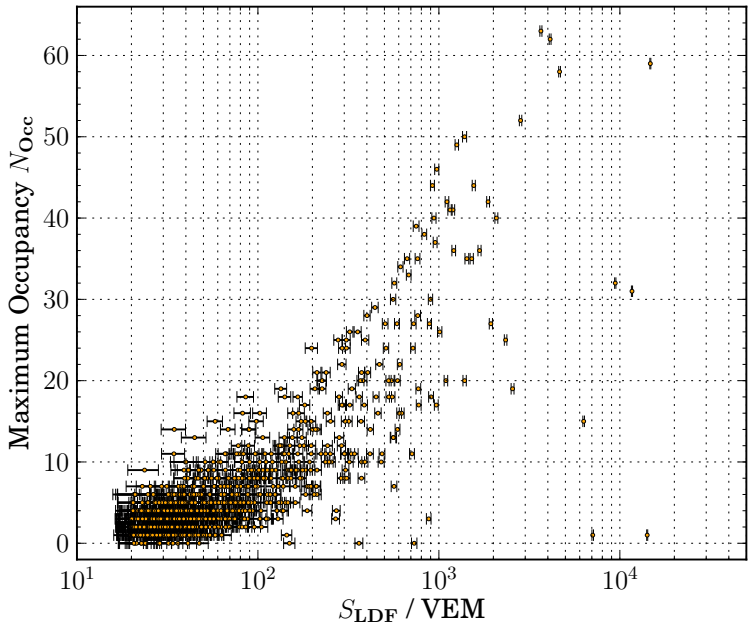

(b) *Correlation between S_{LDF} and N_{Occ}.*

Figure 6.9: *Correlations between MD observables and S_{LDF}. The upper panel shows the dependence of N_{Trig} on the reconstructed SD signal S_{LDF}. The lower panel depicts this relation for N_{Occ}. For SD signals below 20 VEM no dependence is found in the data, the corresponding region is excluded from both plots. Overall, 1,100 combined events from the selected dataset with muon counter calibrations of $\mathcal{R} = 300$ Hz/strip and $S_{LDF} > 20$ VEM are taken into account.*

The time averaged correlation factor of N_{Trig} and S_{LDF} was already calculated in [Pon12], revealing a value of $\langle r_{\mathrm{S}} \rangle = 0.8 \pm 0.2$ for a calibration of $\mathcal{R} = 300\,\mathrm{Hz/strip}$ with the given uncertainty including the temporal fluctuations of the correlation factor. Therefore, both observables r and $\langle r_{\mathrm{S}} \rangle$ emphasize different aspects of the data.
Further, both analyses are based on different event selections. The dataset of the analyses presented here contains all combined events measured with three detector pairs of the AMIGA PUC (Section 6.4 and Section 6.5.2). Contrary, the analysis presented in [Pon12] includes the information of all seven detector pairs of the PUC but is based on events in which at least one detector of the PUC has participated in the SD event reconstruction. Therefore, it favors air shower events with the shower core falling close to the PUC, i.e. it favors showers with larger values of S_{LDF}. In addition, in [Pon12] the determination of N_{Trig} includes a correction accounting for badly calibrated channels of the muon counter modules, which can lead to reduced values of N_{Trig}. However, since noisy front-end channels have only been found in muon counter modules that are excluded from the dataset discussed here (Section 6.5.2), this correction will not be applied for the following analyses. Thus, for all three muon counter modules included in the dataset, N_{Occ} can cover values in the interval $[0; 64]$.
For the given reasons, a direct comparison of r and $\langle r_{\mathrm{S}} \rangle$ is misleading.

The signal strength S_{LDF} measured by the SD as well as any MD observable depend on properties of the individual air showers such as zenith angle, primary energy and the type of the primary particle. Based on the event selection described in the previous sections, correlations between the maximum number of time coincident signals N_{Occ} and SD-related observables, especially the reconstructed energy of the primary cosmic ray particle, will be investigated in more detail.

6.6.1 Occurrence of Signal Multiplicities in T1/T3-triggered Data

In each event the maximum occupancy N_{Occ} is determined. The distribution of N_{Occ} is shown in Figure 6.10a. The maximum of the distribution at $N_{\mathrm{Occ}} = 0$ implies, that approximately half of the recorded events do not contain any acquired MD data. Although the probability for the occurrence of individual occupancy levels rapidly decreases for higher values of N_{Occ}, events with large values of N_{Occ} are still found in the data. The number of random coincidences with a coincidence level p within a time window τ of a system of q independent detectors, each having a counting rate of N, is given by [Gru08]

$$R_p(q) = \binom{q}{p} p N^p \tau^{p-1} \quad . \tag{6.9}$$

For an AMIGA muon counter with $q = 64$, a coincidence window of $\tau = 12.5\,\mathrm{ns}$, due to the $80\,\mathrm{MHz}$ signal processing, and the selected calibration with $N = 300\,\mathrm{Hz/strip}$, the rate of two-fold chance coincidences amounts to $R_2(64) = 4.54\,\mathrm{Hz}$. Therefore, the probability $\mathcal{P}_{\mathrm{c}}$ of having a twofold coincidence within the time window that is covered by the MD data acquisition ($\tau_{\mathrm{event}} = 9.6\,\mu\mathrm{s}$) can be calculated to

$$\mathcal{P}_{\mathrm{c}} = R_2(64) \times \tau_{\mathrm{event}} = 4.35 \times 10^{-5} \quad . \tag{6.10}$$

The dataset consists of 2,481 events (approx. 14.7 % of the dataset) that contain a maximum number of time coincident signals of $N_{\mathrm{Occ}} \geq 2$. These occupancies are, due to the given probability $\mathcal{P}_{\mathrm{c}}$ and the overall number of events, not expected to arise from chance coincidences but may result from physics processes.

For the events taken into consideration the maximum occupancy N_{Occ} is shown as a function of time in Figure 6.10b. The position of the data points on the time axis represent the time of the first occurrence of the maximum signal multiplicity within an individual AMIGA event. The entries can be interpreted as the time at which the event would also have been triggered with the internal self trigger of the AMIGA electronics with an occupancy level of $N = N_{\mathrm{Occ}}$. Low values of N_{Occ}, especially $N_{\mathrm{Occ}} = 1$ and $N_{\mathrm{Occ}} = 2$, are uniformly distributed over all time bins. These entries are expected to originate from processes that are not necessarily connected to the observation of an air shower by the SD, like e.g. single background muons traversing the scintillator module of the AMIGA underground muon counter. This may include processes in which a single muon produces a local electromagnetic shower in the soil above the muon counter (punch-through) [Med09], thus leading to a cluster of signals within the recorded MD event [Nie11]. Contrary, higher signal multiplicities of $N_{\mathrm{Occ}} > 2$ are mainly contained in the trigger region of AMIGA events between time bins 120 and 239 (Section 6.5.1), thus indicating that these signals may originate from time coincident muons in EASs. The most distinct signal multiplicities are found at the position of the T1-TH trigger around time bin 180. This confirms the idea of the T1-TH trigger to be most sensitive to dominantly muonic showers [Abr10b] whereas the T1-ToT trigger is optimized for the detection of near-by, low-energy showers, that are dominated by the electromagnetic component.

6.6.2 Correlation of N_{Occ} with Distance to the Shower Axis or SD Energy

The density of muons in an air shower strongly depends on the distance between the observation point and the shower axis. Based on phenomenological considerations this dependence can be described with the lateral distribution function of muons (MLDF) [Gre60]:

$$\rho_{\mu}(r,N_{\mu}) = k_G N_{\mu} \left(\frac{r}{r_G}\right)^{-a} \left(1+\frac{r}{r_G}\right)^{-b} \quad [\mathrm{m}^{-2}] \quad . \tag{6.11}$$

Here, N_{μ} is the muon size of the shower at a given distance along the shower axis, k_G is a constant, r is the distance to the shower axis, $a = 0.75$, $b = 2.5$ and $r_G = 320\,\mathrm{m}$ is the Greisen radius. This empirical function, often referred to as Greisen formula for muons, is valid for muons with energies $E_{\mu} \geq 1\,\mathrm{GeV}$ but has also been adapted to different muon energies. During the last decades many astroparticle physics experiments developed their own empirical MLDF by modifying Equation 6.11. Improved versions of the Greisen formula include other normalization factors that e.g. account for a dependence of the muon density on the zenith angle of the air shower.

Independent of the exact shape of the MLDF the density of muons is found to decrease for increasing distances to the shower axis. Assuming the shower front to have a thickness in the order of a few meters and to move approximately with the speed of light c, the muons, that

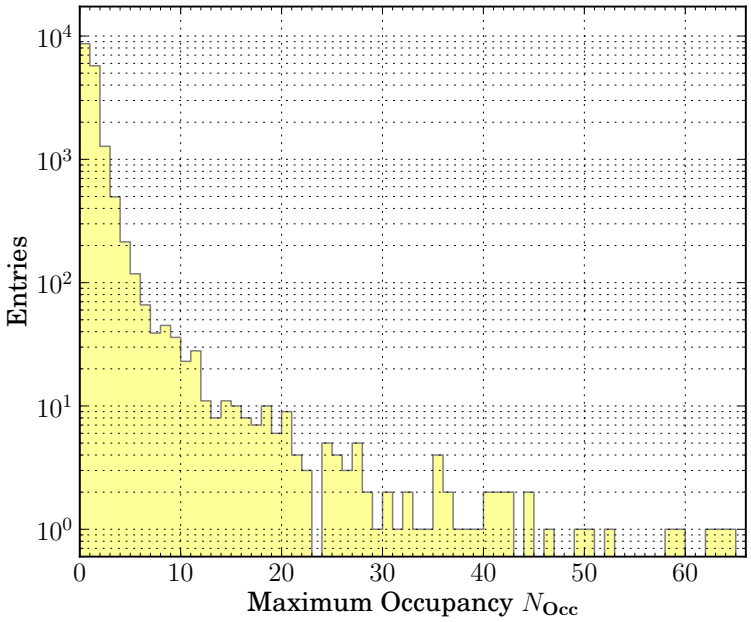

(a) *Occurrence of N_{Occ}.*

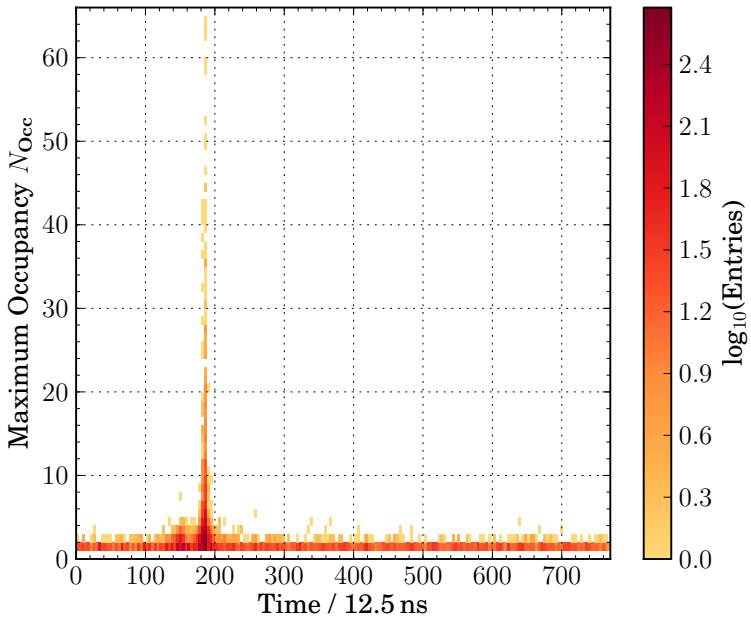

(b) *Time distribution of N_{Occ}.*

Figure 6.10: *Maximum signal multiplicities in T1/T3-triggered data. In the upper panel the distribution of the maximum occupancy in single events N_{Occ} is plotted. The lower panel depicts N_{Occ} as a function of the time of its first occurrence inside an AMIGA event. A correlation between the position of T1-ToT-triggered signals around time bin 180 and the highest occupancies is found. Both plots contain the information of 16,889 events, empty events are not taken into account in panel (b).*

are traversing the underground muon counter, are in first order expected to be coincident in time. Therefore, a dependence of the maximum number of coincident signals N_{Occ} on the distance of the detector station to the reconstructed shower axis is expected to be found in the data.

If the impact point of the reconstructed shower axis on ground as well as the zenith and azimuth angles of the shower axis are known, the distance in the plane of the shower front between any SD station and the shower axis can be calculated by geometrical considerations. The position of the shower core on ground is determined by the barycenter of all triggered tank positions, weighted with the square root of their signals [Pri03]. The accuracy of this calculation depends on the geometry of the individual shower but is typically in the order of a few tens of meters for the infill array [Set13]. The orientation of the shower axis is derived from fitting a shower front model to the measured arrival time of the earliest particle in each SD station. The precision in the determination of the direction of the shower axis depends on the precision of the FADC clock (flash analog-to-digital converter) of the station, on the model of the shower front as well as on the fluctuations in the arrival time of the first particle. A detailed study of the angular resolution achieved with the SD is presented in [Ave07c].

In Figure 6.11, the timing information of an exemplarily chosen air shower event, that was acquired with the SD as well as with the MD, is shown. SD stations of the infill array and of the HEATLet (Section 3.3.2) extension are plotted as black open circles. Filled circles represent stations that participated in the event, with the size of the markers being proportional to the measured signal strength. The color code illustrates the trigger times of the individual detectors on a scale ranging from yellow to red for early and late triggered stations. Gray filled circles represent SD stations which fulfilled the T2 trigger condition but that were excluded from the event reconstruction. This mainly concerns 'off-grid stations', which are not included in the standard SD reconstruction routine, 'lonely stations' which are spatially completely isolated from other triggered stations, and stations that were out of time, i.e. that their trigger times do not fit the timing of the shower front within a given tolerance (Section 3.1.3). The black line indicates the reconstructed direction of the shower axis ending at the calculated impact point on ground.

Figure 6.12 depicts the maximum multiplicity of signals N_{Occ} as a function of the distance in the plane of the shower front between the detector station and the reconstructed shower axis. The plot contains all combined SD/MD events from the selected dataset (Section 6.5.2). For distances $\lesssim 1{,}000\,\mathrm{m}$ the expected dependence of N_{Occ} on the station distance is found in the data. The highest signal multiplicities arise if the impact point of the reconstructed shower axis falls close to the position of the individual muon counter module. The increased density of entries at a distance around 450 m results from the fact, that most of the non-empty events result from air showers with reconstructed shower cores falling inside the hexagon that surrounds the triggered MD station. For distances above 1,000 m the data becomes flat distributed and the maximum multiplicity mainly covers values up to $N_{\mathrm{Occ}} = 3$.

As discussed in Section 2.3.2 the number of muons in an air shower, that reach ground level, is expected to increase with the energy of the incoming primary cosmic ray particle. Whereas

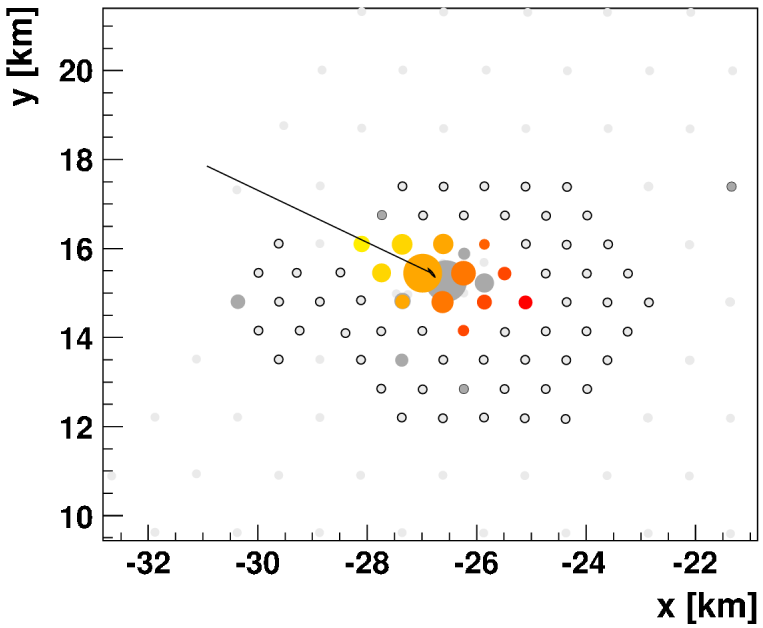

Figure 6.11: *Footprint of a measured SD event included in the combined dataset (event ID 15853071, recorded on 2012-07-26 16:41:20 UTC) [Mar06]. SD stations of the infill array are plotted as black open circles. Filled color circles represent stations that were triggered on T2 level and that contribute to the event reconstruction. The size of the markers is proportional to the measured signal strength, the color code illustrates the trigger time on a scale ranging from yellow (early) to red (late). Gray filled circles represent SD stations which fulfilled the T2 trigger condition but that were excluded from the event reconstruction. The black line indicates the reconstructed orientation of the shower axis ending at the calculated impact point on ground. The axes are scaled in site coordinates.*

the FD is capable of performing a calorimetric measurement of the shower development in the atmosphere, the SD only allows for a determination of the primary energy of an air shower by fitting an LDF to the lateral profile of the time-integrated signals $S_{\mathrm{LDF}}(r)$, which have been measured with the individual detector stations of the SD (Figure 6.13). The LDF is given through

$$S_{\mathrm{LDF}}(r) = S(r_{\mathrm{opt}}) \times f_{\mathrm{NKG}}(r) \tag{6.12}$$

including a modified NKG (Nishimura-Kamata-Greisen) function [Kam58, Gre56] of the form:

$$f_{\mathrm{NKG}}(r) = \left(\frac{r}{r_{\mathrm{opt}}}\right)^{\beta} \times \left(\frac{r + r_{\mathrm{scale}}}{r_{\mathrm{opt}} + r_{\mathrm{scale}}}\right)^{\beta+\gamma} \quad . \tag{6.13}$$

Here r denotes the distance in the shower plane of the SD station to the reconstructed shower axis. A minimum likelihood method is used to determine the free fit parameters $S(r_{\mathrm{opt}})$ and β. The LDF parameter γ is usually set to 0, as a simultaneous fit of β and γ is difficult on an event-by-event basis, i.e. it sets out rigorous requirements on the individual events, especially concerning the number of triggered stations [Sch12]. The optimal distance r_{opt} is

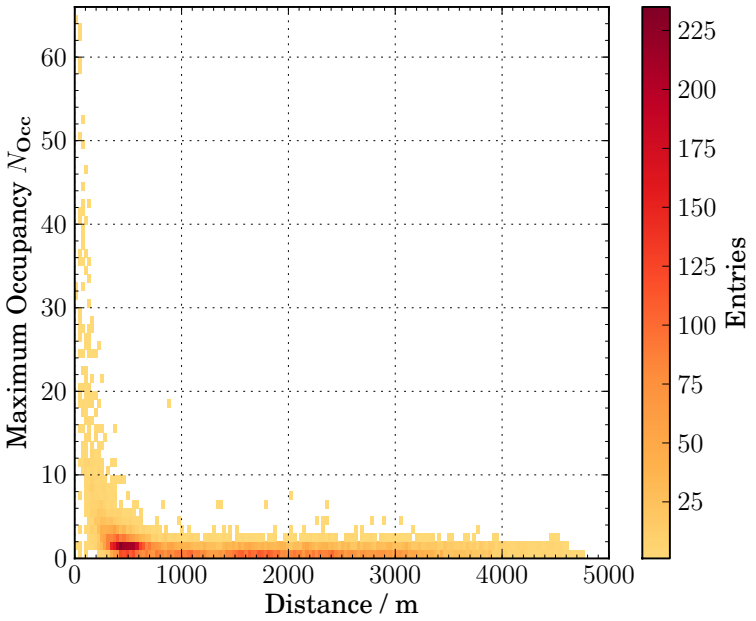

Figure 6.12: *Dependence of the maximum signal multiplicity N_{Occ} on the distance in the shower plane between the detector station and the reconstructed shower axis. For distances $\lesssim$ 1,000 m a negative correlation is found. The plot includes information of 16,889 events contained in the combined dataset.*

primarily determined by the array geometry and is chosen in a way that the signal variation with respect to the slope parameter β is smallest [New07]. For the standard array the optimal distance is found to be $r_{\text{opt}} = 1{,}000\,\text{m}$, whereas for the infill array it is taken as $r_{\text{opt}} = 450\,\text{m}$ [Mar11].

The measured $S(r_{\text{opt}})$, which corresponds to the time-integrated signal that would be measured by an SD station at a distance r_{opt} from the shower axis, does not only depend on the energy of the primary particle but in addition on the zenith angle θ of the air shower. The slant depth of the SD array varies from $870\,\text{g}\,\text{cm}^{-2}$ for vertical showers to $1{,}740\,\text{g}\,\text{cm}^{-2}$ for showers with $\theta = 60\,^\circ$ [Som05]. The attenuation of the signal $S(r_{\text{opt}})$ at large slant depths is corrected for by using a constant intensity cut (CIC) method [Her61], that results in a zenith angle dependent correction function $CIC(\theta)$. By applying this correction, the zenith angle independent energy parameter $S_{38} = S(1000)/CIC(\theta)$ is calculated for the standard array. This parameter is interpreted as the signal $S(1000)$ if the shower would have arrived $38\,^\circ$ from the zenith, which is the value of the median zenith angle. In hybrid measurements, that include the reconstructed shower information derived from both the FD and the SD, a relation between S_{38} and the measured calorimetric energy E_{FD} is determined. Applying a linear fit of the form $\lg E_{\text{FD}} = A + B \lg S_{38}$ to this data [Pes11] allows for the conversion of S_{38} into the primary energy of the air shower on an event-by-event basis. For the energy reconstruction of the infill array the zenith angle independent energy estimator is found to be S_{35} [Mar11].

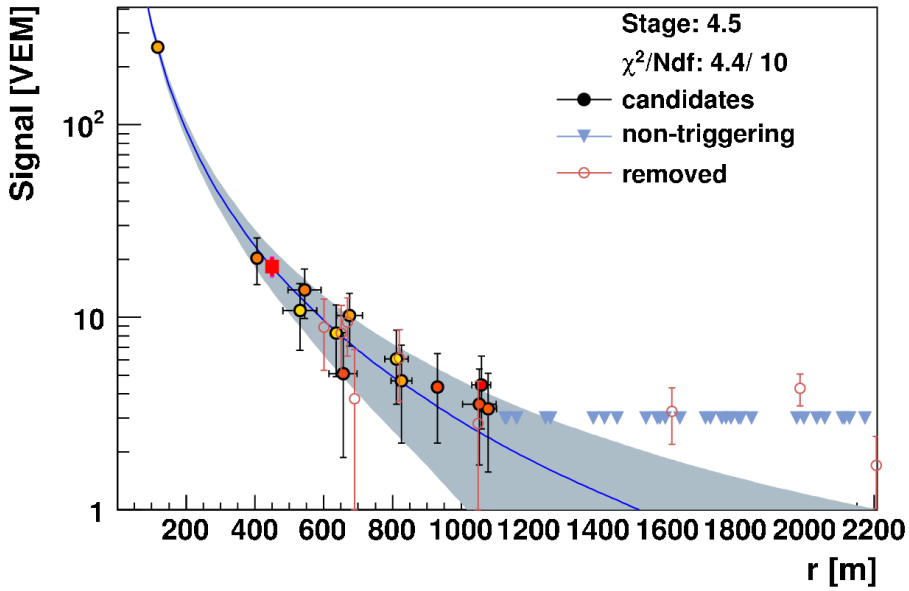

Figure 6.13: *LDF fit of a measured SD event included in the combined dataset (event ID 15853071, recorded on 2012-07-26 16:41:20 UTC) [Mar06]. The plot shows the time-integrated signals measured with multiple SD stations as a function of the distance to the shower axis. The color code illustrates the trigger time on a scale ranging from yellow (early) to red (late) (compare Figure 6.11). Blue triangles represent non-triggered stations of the infill array, red open circles indicate stations that were excluded from the event reconstruction. The blue line shows the fitted LDF with its uncertainty given by the blue shaded area. The reconstructed S(450) is represented by the red square marker.*

In case of constant initial and boundary conditions, like e.g. shower geometry, detector efficiency and especially the type of the primary particle, also the measured signal multiplicity N_{Occ} is supposed to be positively correlated with the primary energy of the shower. In Figure 6.14, the relation between the reconstructed primary energy and the measured N_{Occ} is plotted for all events included in the combined dataset. The correlation between both observables is smeared out due to several reasons: First, the dataset includes events that arrive from different zenith angles and that have been measured at different distances from the shower axis. For larger zenith angles $\theta \gtrsim 40\,^\circ$ an additional dependence on the azimuth angle of the shower axis may be considered, since the density of particles in the shower plane is higher on the side before the shower core impact point ('early region') than on the opposite side ('late region') [Dov03]. However, this effect is expected to mainly concern the electromagnetic shower component and will affect the measured density of muons on ground only on a small scale. In addition, no information about the type of the primary cosmic ray particle can be gained from the available SD data.

The smearing may be overcome by eliminating at least one of these dependencies. In the following, the relation between N_{Occ} and the reconstructed SD energy will be studied in more detail.

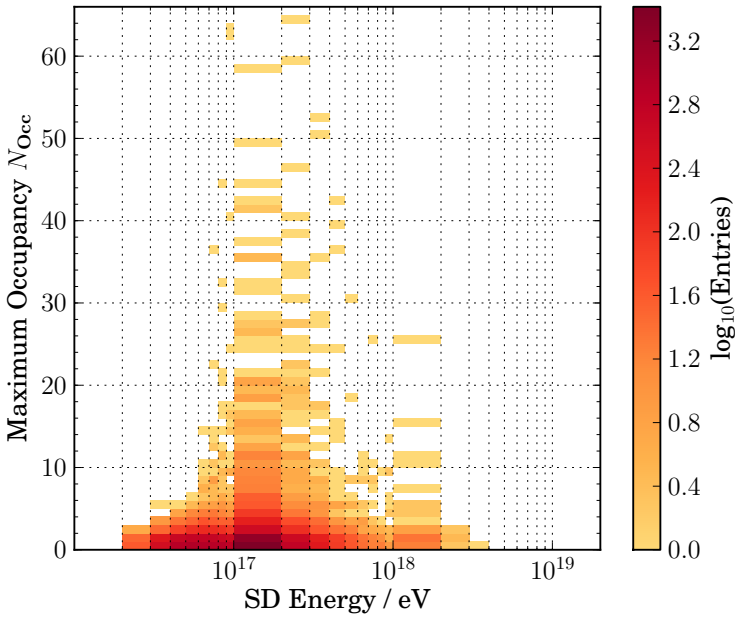

Figure 6.14: *Dependence of N_{Occ} on the primary energy reconstructed with the SD. No significant correlation between both observables is found in the data. The plot includes information of 16,889 events contained in the combined dataset.*

6.6.3 Correlation of N_{Occ} with SD Energy for Different Distances to the Shower Axis

In order to study the correlation between the maximum multiplicity of time-coincident signals and the primary energy of the individual air showers, the smearing, which is caused by the different effects mentioned above and which affects the distribution, has to be reduced. In an ideal case the available statistics of the experiment would be sufficient to allow for applying strict cuts on the data that would remove dependencies on all other variables but the one under investigation. In consequence of the limited statistics of the dataset, the simultaneous determination of all dependencies is not possible. As discussed in the previous section, significant values of N_{Occ} are only found for distances between the detector station and the shower axis below $\approx 1{,}000\,\mathrm{m}$. In the following, the dependence of the correlation on the distance will be reduced by subdividing the dataset into bins of the distance. Motivated by the uncertainty of the reconstruction of the station distance in the order of a few tens of meters on the one hand and by the limited statistics of the dataset on the other hand, a graduation in 5 bins with a width of 200 m in the interval $[0\,\mathrm{m}; 1{,}000\,\mathrm{m}]$ has been chosen.

Figure 6.15a exemplarily shows the scatter plot of the reconstructed SD energy versus the maximum occupancy value N_{Occ} for all events of the combined dataset for the second bin covering distances in the interval $[200\,\mathrm{m}; 400\,\mathrm{m})$. Each data point represents one event from the combined dataset that was selected following Section 6.5.2. The errors on the SD energy result from the uncertainty of the SD event reconstruction. The corresponding plots representing the data of the other four bins are given in Figure 6.16a through Figure 6.16d. The additional information given in the figures is explained in the following.

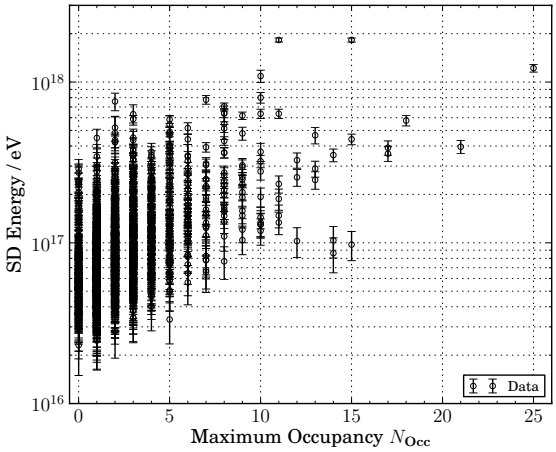

(a) Scatter plot.

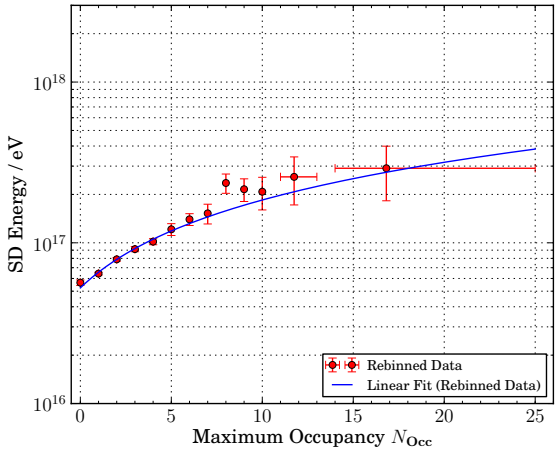

(b) Linear fit of the re-binned data.

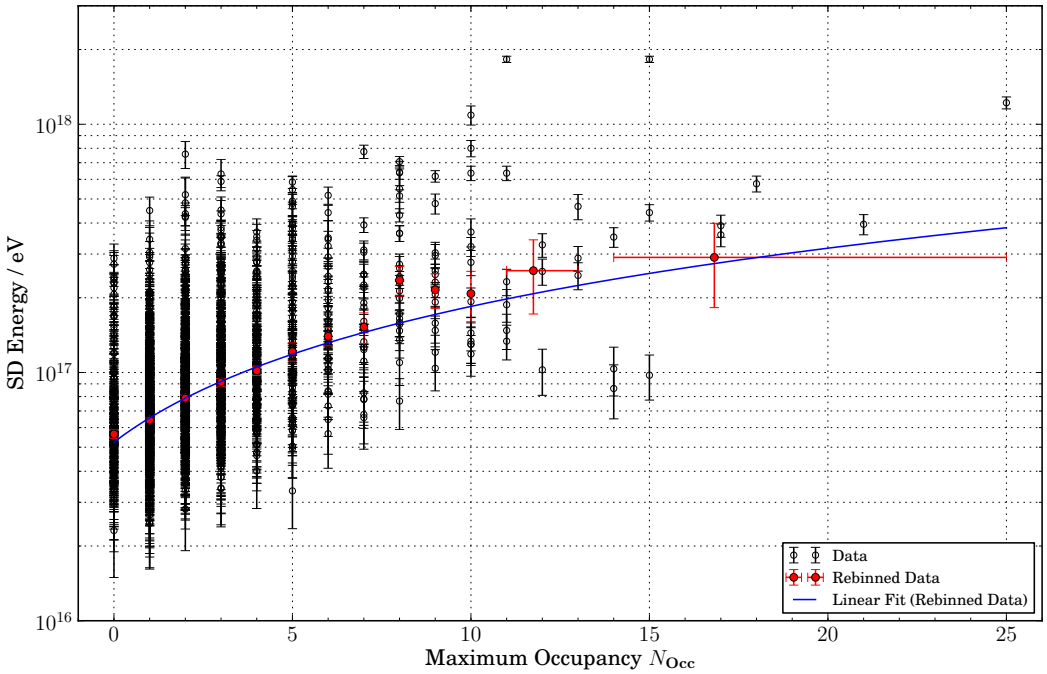

(c) Scatter plot and linear fit to the re-binned data.

Figure 6.15: *Scatter plot of N_{Occ} and reconstructed SD energy for shower distances between 200 m and 400 m. The raw data is shown in the upper left panel, each data point represents one event from the combined dataset with the given error resulting from the SD event reconstruction. The upper right panel depicts the linear fit (blue curve) to the re-binned data with a minimum number of ten events in each bin, which is represented by the red circles. The size of the vertical error bars is given by the uncertainty of the weighted mean, whereas the horizontal error bars indicate the width of the individual bins. The combination of both plots is given in the lower figure.*

As can be seen from Equation 2.20, the dependence of the number of muons in an air shower on the primary energy is found to be approximately linear. A positive correlation between the reconstructed SD energy and the maximum occupancy N_{Occ} would be equivalent to a slope of the linear function significantly deviating from zero. For each occupancy bin the weighted mean of the energy $\langle E \rangle$ of the data points contained within this bin is calculated following

$$\langle E \rangle = \frac{\sum_i g_i E_i}{\sum_i g_i} \quad , \tag{6.14}$$

with E_i being the reconstructed energy of the individual events and $g_i = 1/\sigma^2(E_i)$ being the weighting factors, depending on the energy uncertainty $\sigma(E_i)$ of each event. For low statistics, and especially for bins which contain only one event, this quantity is less reliable or not reliable at all, since it does not contain any information about the possible spread of the data points. In order to mitigate this effect the dataset is re-binned such that each of the new bins contains at least ten events (Figure 6.15b). The re-binned data is represented by the red circles. The size of the vertical error bars is given through the statistical uncertainty of the weighted mean [Bro00]

$$\sigma(\langle E \rangle) = \sqrt{\frac{\sum_i g_i \left(E_i - \langle E \rangle\right)}{(n-1)\sum_i g_i}} \quad , \tag{6.15}$$

taking the statistical spread of the data points in each bin into account. Here, n denotes the number of events contained in the considered bin. The horizontal error bars of the re-binned data, as shown in the figures, indicate the widths of the individual bins, the horizontal position of the data points is given by the mean of all events that are included into these bins. A linear fit to the re-binned data, performed using a χ^2-minimization method, is shown by the blue curve (Figure 6.15b). Figure 6.15c shows the combination of Figure 6.15a and Figure 6.15b.

In Table 6.3, the correlation coefficients r (Equation 6.7), the slope values s resulting from the linear fits and their magnitude of deviation from zero s/σ_s are given for the five cases discussed above. In addition, the table includes the corresponding values for all events with distances between the detector station and the shower axis above 1,000 m. A linear relation between r and s/σ_s is found in the data, supporting the expectation that both quantities are suitable for measuring the correlation between the two observables.

For all five bins correlations between the maximum number of time-coincident signals N_{Occ} and the reconstructed SD energy significantly deviating from zero are found in the data. The most prominent correlation of $r = 0.52 \pm 0.02$ is observed for the second bin with distances ranging from 200 m to 400 m (Figure 6.15). As expected from the MLDF (Equation 6.11), for larger distances to the shower axis it becomes more likely to record only small values of N_{Occ}. This results in a decrease of the correlation between both observables and in an increase of the relative uncertainty of the slope parameter s. In the first bin, covering distances below 200 m, the correlation is reduced although the data covers the complete spectrum of possible signal multiplicities (Figure 6.16a). Here, the uncertainty in the calculation of the distance between

Distance / m	***# Events***	***Slope* s / 10^{16} *eV***	$\mathbf{s}/\sigma_{\mathbf{s}}$	χ^2***/NDF***	***Corr. Coeff.* r**
0 - 200	305	0.24 ± 0.04	6.0	$23.39/18 = 1.30$	0.25 ± 0.05
200 - 400	1,745	1.32 ± 0.08	16.5	$13.77/11 = 1.25$	0.52 ± 0.02
400 - 600	2,877	1.2 ± 0.1	12.0	$15.61/\ 6 = 2.60$	0.40 ± 0.02
600 - 800	1,321	2.9 ± 0.3	9.7	$5.61/\ 3 = 1.85$	0.26 ± 0.03
800 - 1,000	916	2.0 ± 0.6	3.3	$2.44/\ 2 = 1.22$	0.21 ± 0.03
> 1,000	9,725	0.1 ± 0.1	1.0	$2.30/\ 3 = 0.77$	0.04 ± 0.01

Table 6.3: *Results of the correlation analyses. The table contains information about the number of events, the slope of the linear fit, its deviation from $s = 0$, the quality of the fit and the correlation coefficient of the correlation between the primary energy and N_{Occ} for five different distances between the SD station and the reconstructed shower axis as well as for distances above 1,000 m.*

the SD station and the reconstructed shower axis, in the order of a few tens of meters, leads to a non-negligible smearing of the data points and thus to a disguise of the correlation. For distances above 1,000 m, the calculations result in a very small value of the correlation coefficient of $r = 0.04 \pm 0.01$ and in a slope parameter of $s = 0.1 \pm 0.1$, which is compatible with $s = 0$ within the given uncertainty. This supports the expectation of the data to be not correlated for the given bin size or of the muon densities to be too small in order to reveal a significant correlation.

Based on the linear fits applied to the data, an analytical description of the relation between the maximum number of time-coincident MD signals N_{Occ} and the reconstructed SD energy E_{SD} can be obtained. Even though this parameterization does not allow for the calculation of the primary energy as a function of N_{Occ} and the distance to the shower axis on an event-by-event basis, it can nevertheless be understood as a criterion that future measurements have to be consistent with. In the case of significantly increasing the amount of recorded MD data, especially for high N_{Occ} and for distances between the detector stations and the shower axis above 400 m, this parameterization could be further refined. In an ideal case, it could be extended to include a dependence of E_{SD} on the distance d as well as on the zenith angle θ of the air shower or on the mass A of the primary particle. The analysis could be supported by air shower simulations including a super-dense array of SD stations. These simulations would allow for a fine binning in all SD observables without being limited by the experimental statistics, thus enabling an analytical parameterization of N_{Occ} as a function of the shower properties mentioned above. In case N_{Occ} turns out to be suitable for determining the number of muons with segmented detectors it could preferentially be used as an observable in future experiments. It comes along with the advantage that the determination of the multiplicity of time-coincident signals can be easily implemented into any FPGA-based readout electronics.

The data analyses, as presented in the previous sections, lead to the conclusion that the number of signals recorded with the AMIGA muon counter modules, and especially the maximum number of time-coincident signals N_{Occ}, shows clear correlations with air shower-

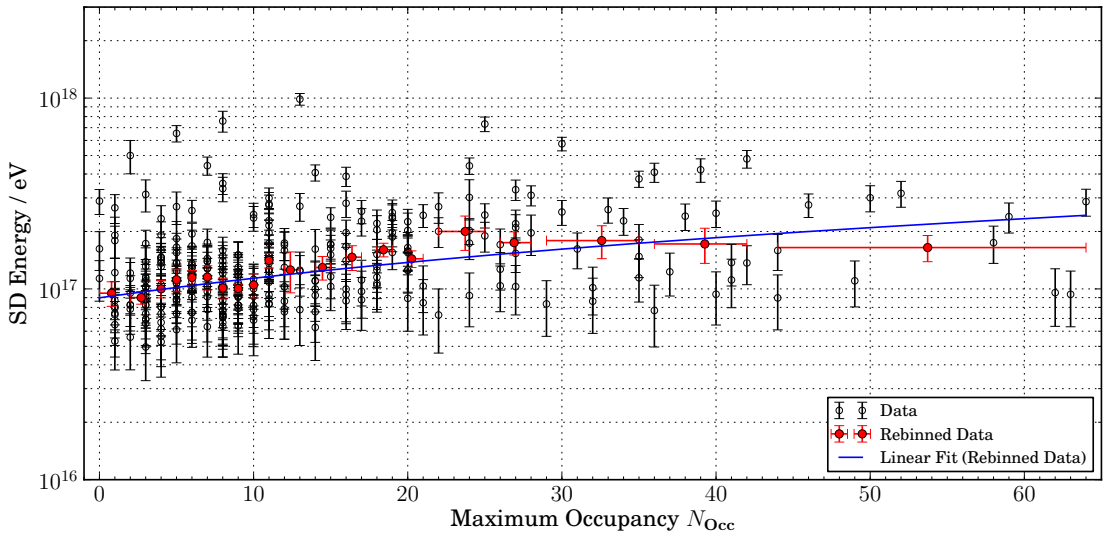

(a) *Shower distances between 0 m and 200 m.*

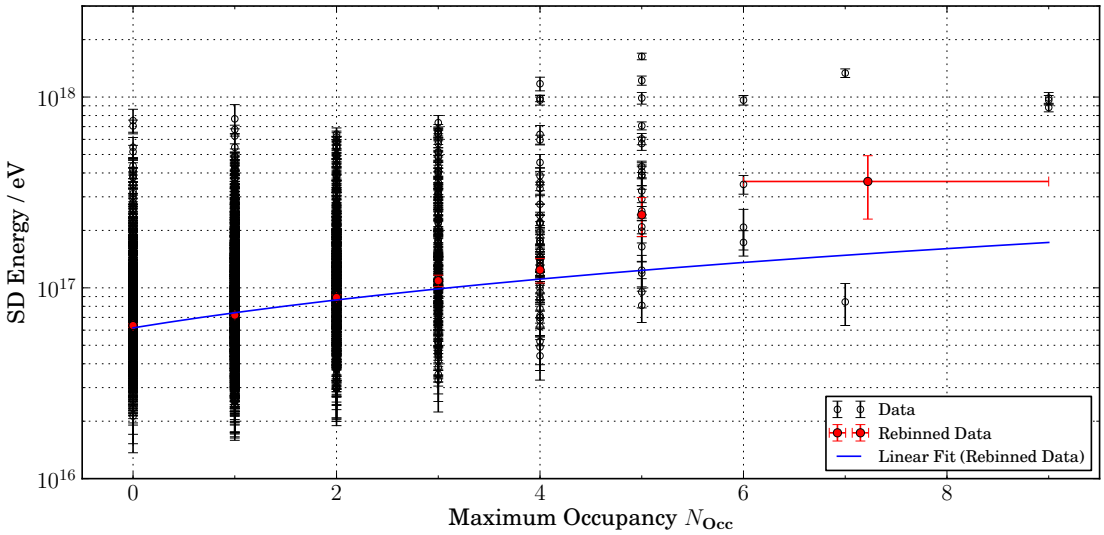

(b) *Shower distances between 400 m and 600 m.*

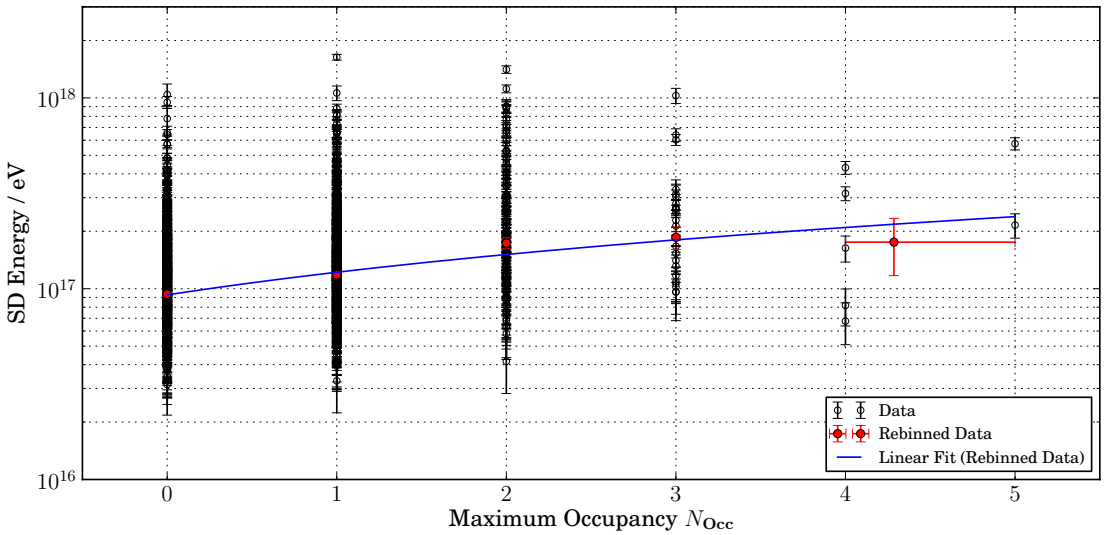

(c) *Shower distances between 600 m and 800 m.*

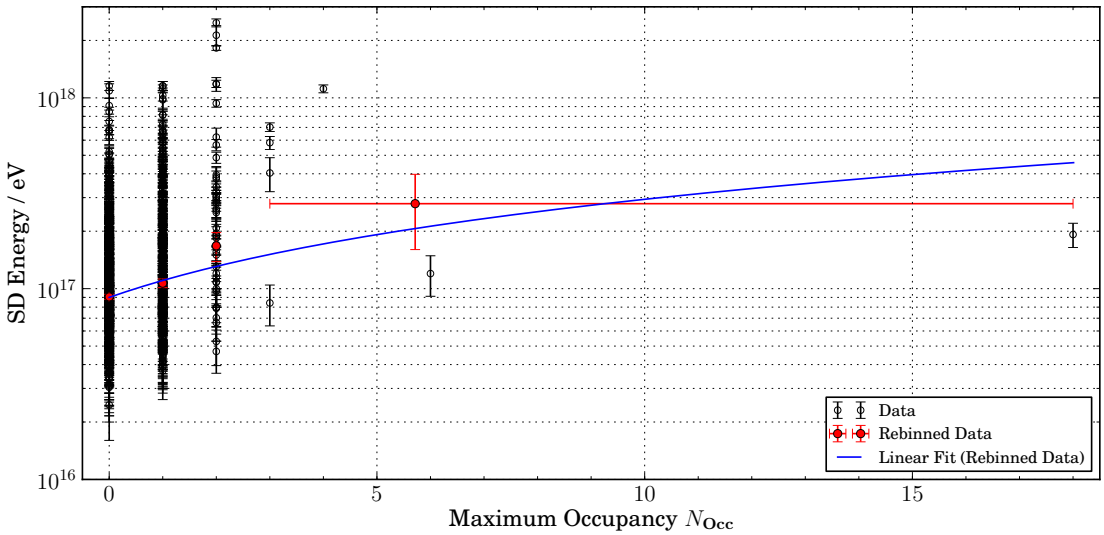

(d) *Shower distances between 800 m and 1,000 m.*

Figure 6.16: *Scatter plot of N_{Occ} and reconstructed SD energy for four different bins of shower distances. Each data point represents one event from the combined dataset with the given error resulting from the SD event reconstruction. The red circles represent a re-binning of the data with a minimum number of ten events in each bin. The size of the vertical error bars is given by the statistical uncertainty of the weighted mean, whereas the horizontal error bars indicate the width of the individual bins. The blue lines show linear fits to the re-binned data.*

related observables like e.g. the distance between the SD station and the reconstructed shower axis or the reconstructed energy of the primary cosmic ray particle. It has been proven that the MD modules are capable of recording signals of muons in air showers, even by using the internal self-trigger algorithm. This finding may encourage future studies, which will benefit from an increase in the amount of recorded data. The recording of a significant number of super hybrid events, which contain the reconstructed information of SD, FD and MD, could even enable analyses of data including selections on the type of the primary particle.

7 Summary and Outlook

Between 2009 and 2012 seven underground muon counters were successfully installed at the experimental site of the AMIGA enhancement (Auger Muons and Infill for the Ground Array) of the Pierre Auger Observatory. They constitute the first hexagon of the muon detector (MD), referred to as the pre-unitary cell (PUC). Prior to this, the readout electronics of these systems were built and tested at laboratories of the University of Siegen [Pon12].

The subject of this thesis is the development and commissioning of firmware [S2] for the FPGA (field programmable gate array) of the AMIGA Digital Board, which allows for the commissioning of the muon counters as well as for first data taking. Based on existing firmware [S5], that has been used with the data acquisition (DAQ) electronics of the surface detector (SD) stations of the Pierre Auger Observatory for many years, a first prototype version of the AMIGA FPGA firmware was developed. This firmware was successfully refined and adopted to the needs of the AMIGA muon counter. Additional features were added and characterized.

The AMIGA FPGA firmware, as it is used for the PUC, is capable of a sampling of the incoming photomultiplier (PMT) signals at a frequency of 320 MHz, whereas the following data processing is performed at a frequency of 80 MHz. The downsampling of the digitized PMT signals represents one of the most crucial steps of the data processing performed by the AMIGA FPGA firmware, since it changes the raw data already at a very early stage of the signal chain. The output of the downsampling procedure depends on several external factors, such as the delay between the input signals and the corresponding trigger signal or the relative timing between these signals with respect to the FPGA's internal 320 MHz and 80 MHz clocks. Detailed laboratory measurements were carried out in order to achieve a thorough understanding of the downsampling procedure (Section 5.4). Within the timing uncertainties given by the experimental setup the results of the measurements are in good agreement with theoretical predictions, that were derived from Monte Carlo simulations. In future, these simulations may be incorporated into a full detector simulation of the AMIGA muon counter.
The Occupancy-N trigger was implemented into the FPGA firmware (Section 5.5). This internal self-trigger, for which the multiplicity of time-coincident signals is evaluated, already allowed for a data taking with the very first prototype detector system installed at the experimental site. This data was mainly used to debug the full DAQ system, including the detector hardware and software. Laboratory measurements were performed to proof the functionality of the Occupancy-N trigger. It was found that the Occupancy-N trigger reacts on the multiplicity of the incoming PMT signals with an efficiency of 100 %. This result could also be confirmed by dedicated analyses of high statistics data taken with the muon counters of the PUC, in which no malfunction of the Occupancy-N trigger has been observed.
A prescaler algorithm was implemented into the firmware. The performance of this algorithm

and in particular the dependence of the prescaling on the trigger rate was determined in laboratory measurements (Section 5.6). It enables the detector system to a prescaling of the received trigger signals with high precision. By choosing appropriate prescaler values n, it allows to compensate differences between the muon counters of the PUC in terms of different memory depths. In addition, the prescaler enables the detector to take data at high trigger rates, e.g. as they occur in the occupancy mode with low occupancy numbers and/or low thresholds of the discriminators, since it extends the viable frequency range of trigger signals by almost two decades.
The AMIGA enhancement has been designed to measure the muon content of cosmic ray air showers synchronously to the SD of the Pierre Auger Observatory. Therefore, the muon counters were integrated into the trigger chain of the SD array. The FPGA firmware was enhanced such that it is capable of extracting the 24-bit timestamp from the T1 trigger signal sent by the SD station. An advanced algorithm for the internal event handling allows for the extraction of recorded data based on T3 event requests. Measurements were presented which test the error-free operation of the decoding algorithm and of the data handling (Section 5.7). Using additional end-of-event information, which was implemented into the event structure generated by the FPGA firmware (Section 5.8), the efficiency of the trigger chain was evaluated. As a result of these measurements, the fraction of erroneously provided event data was determined to be smaller than 8.78×10^{-7}.
Finally, a proposal for a possible upgrade of the FPGA firmware was presented (Section 5.9). This upgrade allows for the recording of 320 MHz sampled data without the need of any downsampling of the digitized input signals. The performance of this new FPGA firmware was validated in laboratory measurements. The upgrade would allow for applying discrete muon counting strategies, which were obtained from detector simulations for a full data processing with a frequency of 320 MHz [Wun11].
The firmware developed within the framework of this thesis contributed to the successful commissioning of the PUC at the experimental site in Argentina.

Over an extended period of time, the MD modules of the PUC were operated with the AMIGA Digital Boards running the FPGA firmware discussed here. Most of the time, data has been acquired by triggering the muon counters with the Occupancy-N trigger. During the last measurement periods synchronous data taking with the SD of the Pierre Auger Observatory became possible. Whereas occupancy-triggered data has mainly been used to debug the detector hardware and software, T1/T3-triggered data for the first time allowed for a combined analysis of MD data and SD observables, that are connected to the properties of extensive air showers.
Analyses of self-triggered data have led to the detection of data structures in the AMIGA events which pointed to undiscovered hardware- or software-related deficiencies of the detector electronics and the DAQ system. With regard to these known errors the dataset of T1-triggered data recorded with the PUC was analyzed and it was shown that the system has been successfully debugged (Section 6.3).
A combined dataset, which contains only events with MD and SD information available, was selected (Section 6.4). Analyses presented in this thesis have proven that the MD modules are capable of recording signals of muons in air showers, even by using the internal self-trigger algorithm. Further it was shown that the number of signals recorded with the AMIGA muon

counter modules, and especially the maximum number of time-coincident signals N_{Occ}, clearly depend on air shower-related observables like e.g. the distance between the SD station and the reconstructed shower axis or the reconstructed energy of the primary cosmic ray particle (Section 6.6.2). In particular, significant values of N_{Occ} were found for distances between the detector station and the shower axis below $\approx 1{,}000\,\mathrm{m}$. For five different bins of the distance, significant correlations between N_{Occ} and the reconstructed SD energy were found in the data. The most prominent correlation of $r = 0.52 \pm 0.02$ was observed for distances ranging from 200 m to 400 m (Section 6.6.3).

In summary, the PUC, as the first step towards the installation of the AMIGA MD array, has been successfully commissioned and synchronous data taking with the SD has been established. The data recorded so far shows the expected correlations with air shower related observables measured by the SD. In the meantime, several new proposals for the direct measurement of the number of muons in air showers have been worked out. Research and development, including studies with the PUC, will continue before the final layout of the muon detector system for the upgrade program beyond 2015 will be decided.

A The Pattern Board

The Pattern Board (PaB, Figure A.1) is designed to facilitate testing and debugging of the AMIGA (Auger Muons and Infill for the Ground Array) muon detector (MD) readout systems. Testing procedures using the PaB are described in [Buc12] and [Pon12].
The PaB is intended to be used in combination with a commercial FPGA (field programmable gate array) development board [06]. By this, in analogy to the operation of an AMIGA detector pair consisting of a muon counter module and the surface detector (SD) station, the PaB allows to generate 64-bit pattern words synchronized with a trigger signal plus a 24-bit timestamp. Connected to the AMIGA readout electronics, the pattern words generated by the PaB simulate digital input signals emulating the pulses, which for the real detector operation would be derived from the multi-anode photomultiplier (PMT). The number of data words as well as their timing, i.e. the pulse widths and the distances between the pulses, can be freely chosen by configuring the FPGA firmware. The timestamp data is also programmable. The PaB can be connected to the AMIGA electronics by either directly attaching it to the PMT socket of the Mother Board (Section 4.5.1) or by using a specially designed 64 connector output panel. In this way, the PaB can also be used as an external programmable 64-bit pattern generator.

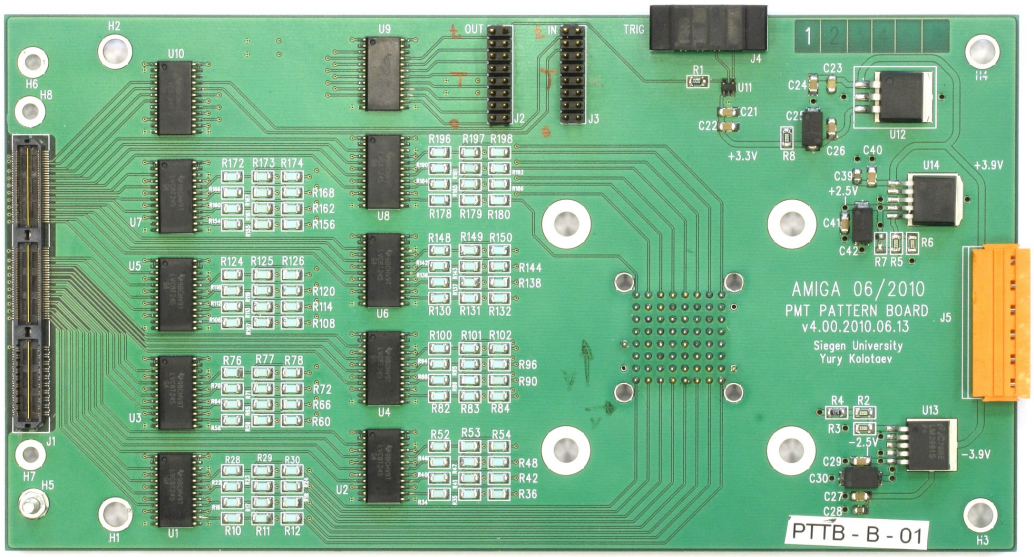

Figure A.1: *The Pattern Board.*

List of Figures

2.1 Elemental composition of cosmic radiation 5
2.2 Upper limits on the photon flux 7
2.3 Hillas diagram 9
2.4 Arrival directions of the highest-energy cosmic rays 12
2.5 The all-particle spectrum of cosmic rays 13
2.6 Schematic view of an extensive air shower 19
2.7 Lateral and longitudinal shower profiles 20

3.1 Schematic view of the Pierre Auger Observatory 26
3.2 One station of the surface detector 28
3.3 Charge and pulse height histograms from an SD station 29
3.4 Schematic view of the hierarchy of the SD trigger system 31
3.5 T3 trigger configurations 33
3.6 Schematic view of a fluorescence telescope 35
3.7 Layout of the infill array 37
3.8 Properties of the infill array 37
3.9 Air shower measurement with the HEAT telescopes 39
3.10 Layout of the AERA array 40

4.1 Schematic view of an AMIGA detector pair 44
4.2 Mass discrimination power of different air shower observables 47
4.3 Schematic view of a scintillator strip and a scintillator module 49
4.4 A completely assembled system of the underground muon counter electronics 51
4.5 The AMIGA Digital Board 54

5.1 Schematic overview of the buffer structure 61
5.2 Examples of 320 MHz sampling and downsampling to 80 MHz 65
5.3 Simulated output pulse length distribution for the downsampling algorithm 65
5.4 Examples of the processing of T1 triggered data 67
5.5 Comparison of a measured pulse length distribution with Monte Carlo simulations 68
5.6 Measurement of the input pulse width. 70
5.7 Measurement of the input pulse width for the comparison with Monte Carlo simulations. 70
5.8 Detection of the logic states of digital input signals 71
5.9 Possible timing scenarios of pulse and trigger detection 72

5.10 Comparison of the measured time distribution with Monte Carlo simulations for externally triggered data . . . 73
5.11 Measurement of the trigger delay. . . . 74
5.12 Measurement of the jitter between data pulse and T1 trigger signal . . . 76
5.13 Flowchart of the Occupancy-N trigger algorithm . . . 78
5.14 Laboratory test of the Occupancy-N trigger . . . 79
5.15 Laboratory measurement of the timing of the prescaler algorithm . . . 83
5.16 Laboratory measurement of the trigger system with and without prescaler . . . 84
5.17 Laboratory measurement of the prescaler algorithm . . . 86
5.18 Timing of the T1 timestamp decoding procedure . . . 89
5.19 Flow chart of the T1/T3 trigger chain . . . 91
5.20 Schematic overview of the experimental setup used to measure the efficiency of the T1/T3 trigger chain . . . 92
5.21 Efficiency measurement of the T1/T3 trigger chain . . . 94
5.22 Timing uncertainties in the measurement of the trigger efficiency . . . 95
5.23 Verification of the input buffer switching algorithm . . . 98
5.24 Addressing of events inside the external RAM . . . 98
5.25 Reconstruction of the trigger rate from EoE information . . . 100
5.26 Buffer structure for 320 MHz data recording . . . 102
5.27 Hodoscope measurements with 80 MHz and 320 MHz data processing . . . 103

6.1 Time distribution of T1-triggered data . . . 107
6.2 Uptime of the muon counter modules and the different data taking periods . . . 110
6.3 Number of active channels on time bin 0 and in the noise region . . . 113
6.4 Comparison of the time distributions of trash events and normal events . . . 115
6.5 Energy and zenith angle distributions of combined SD/MD events . . . 121
6.6 Reconstructed shower core positions of combined SD/MD events . . . 121
6.7 Correlation between N_{Occ} and N_{Trig} . . . 123
6.8 Overlay of events acquired with the MD module at 'Toune' . . . 124
6.9 Correlations between MD observables and S_{LDF} . . . 126
6.10 Maximum signal multiplicities in T1/T3-triggered data . . . 129
6.11 Footprint of a measured SD event . . . 131
6.12 Dependence of N_{Occ} on the distance to the reconstructed shower axis . . . 132
6.13 LDF fit of a measured SD event . . . 133
6.14 Dependence of N_{Occ} on the reconstructed primary energy . . . 134
6.15 Scatter plot of N_{Occ} and reconstructed SD energy for shower distances between 200 m and 400 m . . . 135
6.16 Scatter plot of N_{Occ} and reconstructed SD energy for four different bins of shower distances . . . 139

A.1 The Pattern Board . . . 145

List of Tables

5.1 Important input and output registers of the FPGA firmware 62
5.2 Structure of the control register of the FPGA firmware 63
5.3 Comparison of a measured pulse length distribution with Monte Carlo simulations 68
5.4 Comparison of the measured time distribution with Monte Carlo simulations for externally triggered data 73

6.1 List of SD stations contributing to the AMIGA pre-unitary cell 108
6.2 List of data taking periods 111
6.3 Results of the correlation analyses 137

List of Abbreviations and Acronyms

AC	alternating current
ADC	analog-to-digital converter
ADST	Advanced Data Summary Tree
AERA	Auger Engineering Radio Array
AGASA	Akeno Giant Air Shower Array
AGN	active galactic nucleus
AHDL	Altera Hardware Description Language
AMBER	Air-shower Microwave Bremsstrahlung Experimental Radiometer
AMIGA	Auger Muons and Infill for the Ground Array
ASCII	American Standard Code for Information Interchange
ASIC	application specified integrated circuits
AuxLS	local station auxiliary board
AuxSBC	SBC auxiliary board
CAN	controller area network
CDAS	Central Data Acquisition System
CIC	constant intensity cut
CMB	cosmic microwave background
CORSIKA	Cosmic Ray Simulations for KASCADE
CPLD	complex programmable logic device
CRS	Central Radio Station
DAC	digital-to-analog converter
DAQ	data acquisition
DC	direct current
DPRAM	dual-port RAM
DSAM	diffusive shock acceleration mechanism
EAS	extensive air shower
EASIER	Extensive Air Shower Identification using Electron Radiometer
EG	event generator
EIA	Electronic Industries Alliance
EoE	end-of-event
FADC	flash analog-to-digital converter
FD	fluorescence detector
FE	front-end
FEB	front-end board
FLT	first level trigger
FM	frequency modulation

FPGA	field programmable gate array
FR-II	Fanaroff-Riley class II radio-galaxy
GND	ground
GPS	Global Positioning System
GRB	gamma-ray burst
GTS	GPS timestamp
GUT	grand unified theory
GZK	Greisen-Zatzepin-Kuz'min
HEAT	High Elevation Auger Telescopes
HEGRA	High Energy Gamma Ray Astronomy
HSTL	high-speed transistor logic
I/O	input/output
ID	identifier
IEEE	Institute of Electrical and Electronics Engineers
ISA	industry standard architecture
JACEE	Japanese-American Collaborative Emulsion Experiment
JEDEC	Joint Electron Device Engineering Council
JTAG	Joint Test Action Group
KASCADE	Karlsruhe Shower Core and Array Detector
LDF	lateral distribution function
LHC	Large Hadron Collider
LPDA	logarithmic periodic dipole antenna
LPM	Landau–Pomeranchuk–Migdal
LS	local station
LSID	local station identifier
LTS	local timestamp
LVDS	low voltage differential signaling
MCU	microcontroller unit
MD	muon detector
MIDAS	Microwave Detection of Air Showers
MINOS	Main Injector Neutrino Oscillation Search
MLDF	muon lateral density function
MSU	Moscow State University
MUX	multiplexer
NDF	number of degrees of freedom
NKG	Nishimura-Kamata-Greisen
OPERA	Oscillation Project with Emulsion-Tracking Apparatus
PaB	Pattern Board
PCB	printed circuit board
PMT	photomultiplier (tube)
PS	passive serial
PUC	pre-unitary cell

PVC	polyvinyl chloride
RAM	random access memory
RDS	radio detection station
RS	recommended standard (formerly: radio sector)
SBC	single board computer
SCPI	standard commands for programmable instruments
SD	surface detector
SLT	second level trigger
SNR	supernova remnant
SPE	single photo-electron
SPI	serial peripheral interface
TLT	third level trigger
ToT	time-over-threshold
TTL	transistor–transistor logic
UB	unified board
UC	unitary cell
UHECR	ultra-high-energy cosmic ray
UTC	coordinated universal time
UTM	universal transverse mercator
UV	ultraviolet
VCC	voltage at the common collector
VEM	vertical equivalent muon
WLS	wavelength shifting

List of Components and Devices

[01] *Agilent Technologies Inc.*
Arbitrary pulse generator: 33250A.

[02] *Agilent Technologies Inc.*
Active probe: 1152A.

[03] *Agilent Technologies Inc.*
Logic analyzer: 16823A.

[04] *Agilent Technologies Inc.*
Oscilloscope: Infiniium DSA90804A.

[05] *Altera Corporation*
CPLD: Altera MAX II, TMS570G100C5N.

[06] *Altera Corporation*
Cyclone III FPGA starter kit: DK-START-3C25N.

[07] *Altera Corporation*
FPGA: Cyclone III EP3C25F324I7N.

[08] *Analog Devices Inc.*
DAC: AD5620.

[09] *Analog Devices Inc.*
Operational amplifier: AD8012ARMZ.

[10] *Caddock Electronics, Inc.*
Ultra-precision voltage divider: HVD5-A50M-050-05.

[11] *Cypress Semiconductor Corporation*
Static RAM: CY62177DV30LL-55BAXI.

[12] *Fermilab*
Scintillator material: Dow Styron 663W polystyrene, doped with 1 % PPO and 0.03 % POPOP [Pla11].

[13] *Hamamatsu Photonics K.K.*
High voltage supply: C4900-01.

[14] *Hamamatsu Photonics K.K.*
Photomultiplier: H7546B-200.

[15] *Hamamatsu Photonics K.K.*
Photomultiplier: H8804-200 MOD.

[16] *Jauch Quartz GmbH*
Oscillator: O-40.0-VX3MH-T1.

[17] *Photonis*
Photomultiplier: XP3062.

[18] *Saint-Gobain Ceramics & Plastics Inc.*
Detector assembly materials: Optical Grease.

[19] *Saint-Gobain Ceramics & Plastics Inc.*
Optical cement: BC-600.

[20] *Saint-Gobain Ceramics & Plastics Inc.*
Wavelength shifting fiber: BFC-99-29AMC.

[21] *Technologic Systems Inc.*
Single Board Computer with CAN module: TS-7260 with TS-CAN1.

[22] *Tektronix Inc.*
Active probe: P7225.

[23] *Tektronix Inc.*
Oscilloscope: TDS7254.

[24] *Texas Instruments Inc.*
16/32-Bit RISC Flash Microcontroller (Rev. A): TMS470R1B1M.

[25] *Texas Instruments Inc.*
Comparator: TLV3502-AIDCNT.

[26] *Texas Instruments Inc.*
DAC: TLV-5630-IPW.

[27] *Texas Instruments Inc.*
LVDS receiver: DS90LT012A.

List of Software

[S1] *AMIGA DAQ firmware for the FPGA of the underground readout electronics (2009)*
version: AMIGA_21a900
by: Szadkowski, Z.

[S2] *AMIGA DAQ firmware for the FPGA of the underground readout electronics (2009)*
version: AMIGA_21a900_21ab_TS4_v0.1a_2048
in cooperation with: Kolotaev, Y.; Pontz, M.; Szadkowski, Z. and Wainberg, O.

[S3] *AMIGA DAQ firmware for the FPGA of the underground readout electronics (2011)*
version: AMIGA_21a900_21ab_TS4_v0.1e_EoE_320MHz_2048x64
in cooperation with: Kolotaev, Y. and Pontz, M.

[S4] *AMIGA DAQ firmware for the SBC of the underground readout electronics (2009)*
in cooperation with: Keckert, S.; Pontz, M. and Sanchez, F.

[S5] *Modified DAQ firmware of the SD local station electronics (2010)*
by: Wainberg, O.

Bibliography

[Abb08a] Abbasi, R. U. et al. (HiRes Collaboration): First Observation of the Greisen-Zatsepin-Kuzmin Suppression. *Phys. Rev. Lett.* (2008), vol. 100(10):101101.

[Abb08b] Abbasi, R. U. et al. (HiRes Collaboration): Search for correlations between HiRes stereo events and active galactic nuclei. *Astropart. Phys.* (2008), vol. 30(4): pp. 175–179.

[Abr08a] Abraham, J. et al. (Pierre Auger Collaboration): Correlation of the highest-energy cosmic rays with the positions of nearby active galactic nuclei. *Astropart. Phys.* (2008), vol. 29: pp. 188–204.

[Abr08b] Abraham, J. et al. (Pierre Auger Collaboration): Observation of the Suppression of the Flux of Cosmic Rays above 4×10^{19} eV. *Phys. Rev. Lett.* (2008), vol. 101(6):061101.

[Abr10a] Abraham, J. et al. (Pierre Auger Collaboration): The fluorescence detector of the Pierre Auger Observatory. *Nucl. Instrum. Meth. A* (2010), vol. 620(2-3): pp. 227–251.

[Abr10b] Abraham, J. et al. (Pierre Auger Collaboration): Trigger and aperture of the surface detector array of the Pierre Auger Observatory. *Nucl. Instrum. Meth. A* (2010), vol. 613(1): pp. 29–39.

[Ada98] Adamson, P. et al. (MINOS Collaboration): The MINOS Detectors Technical Design Report (1998).

[Ada07] Adam, T. et al.: The OPERA experiment Target Tracker. *Nucl. Instrum. Meth. A* (2007), vol. 577: pp. 523–539.

[Agl96] Aglietta, M. et al. (EAS-TOP Collaboration): A Measurement of the Solar and Sidereal Cosmic-Ray Anisotropy at $E_0 \sim 10^{14}$ eV. *Astrophys. J.* (1996), vol. 470: p. 501.

[Alk75] Alkhofer, O. C.: *Introduction to Cosmic Radiation*, Verlag Carl Thiemig (1975).

[All07] *see e.g.* Allard, D.; Parizot, E. and Olinto, A. V.: On the transition from galactic to extragalactic cosmic-rays: Spectral and composition features from two opposite scenarios. *Astropart. Phys.* (2007), vol. 27: pp. 61–75, *and references therein.*

[All08] Allekotte, I. et al. (Pierre Auger Collaboration): The surface detector system of the Pierre Auger Observatory. *Nucl. Instrum. Meth. A* (2008), vol. 586(3): pp. 409–420.

[All11] Allison, P. S. et al. (Pierre Auger Collaboration): Microwave detection of cosmic ray showers at the Pierre Auger Observatory. *Proc. 32nd Int. Cosmic Ray Conf. (Beijing)* (2011).

[Alo12] *see e.g.* Aloisio, R.; Berezinsky, V. and Gazizov, A.: Transition from galactic to extragalactic cosmic rays. *Astropart. Phys.* (2012), vol. 39: pp. 129–143, *and references therein.*

[Alt07] Altera: parallel_add Megafunction User Guide (March 2007), document version 2.2.

[Alt12] Altera: Cyclone III Device Handbook (July 2012), vol. 2.

[Ame96] Amenomori, M. et al. (Tibet ASγ Collaboration): The Cosmic-Ray Energy Spectrum between $10^{14.5}$ and $10^{16.3}$ eV Covering the "Knee" Region. *Astrophys. J.* (1996), vol. 461: pp. 408–414.

[Ant04] Antoni, T. et al. (KASCADE Collaboration): Large-Scale Cosmic-Ray Anisotropy KASCADE. *Astrophys. J.* (2004), vol. 604: pp. 687–692.

[Ant05] Antoni, T. et al. (KASCADE Collaboration): KASCADE measurements of energy spectra for elemental groups of cosmic rays: Results and open problems. *Astropart. Phys.* (2005), vol. 24: pp. 1–25.

[Ape11] Apel, W. D. et al. (KASCADE-Grande Collaboration): Kneelike Structure in the Spectrum of the Heavy Component of Cosmic Rays Observed with KASCADE-Grande. *Phys. Rev. Lett.* (2011), vol. 107(17):171104.

[Ape13] Apel, W. D. et al. (KASCADE-Grande Collaboration): KASCADE-Grande measurements of energy spectra for elemental groups of cosmic rays. *Astropart. Phys.* (2013).

[Arq00] Arqueros, F. et al. (HEGRA Collaboration): Energy Spectrum and Chemical Composition of Cosmic Rays between 0.3 and 10 PeV determined from the Cherenkov-Light and Charged-Particle distributions in Air Showers. *Astron. Astrophys.* (2000), vol. 359: p. 682.

[Asa93] Asakimori, K. et al.: *Proc. 23rd Int. Cosmic Ray Conf. (Calgary)* (1993), vol. 2: p. 25.

[Ask65] Askaryan, G. A.: Coherent Radio Emission from Cosmic Showers in Air and in Dense Media. *Sov. JETP* (1965), vol. 21: p. 658.

[Aub11] Aublin, J. et al.: Evidence for a GHz emission from air-showers. *Auger Internal Note* (2011), (GAP-2011-082).

[Aug39] Auger, P.; Ehrenfest, P.; Maze, R.; Daudin, J. and Fréon, R. A.: Extensive Cosmic-Ray Showers. *Rev. Mod. Phys.* (1939), vol. 11(3-4): pp. 288–291.

[Ave07a] Ave, M. et al. (AIRFLY Collaboration): Measurement of the pressure dependence of air fluorescence emission induced by electrons. *Astropart. Phys.* (2007), vol. 28: pp. 41–57.

[Ave07b] Ave, M. et al. (Pierre Auger Collaboration): The accuracy of signal measurement with the water Cherenkov detectors of the Pierre Auger Observatory. *Nucl. Instrum. Meth. A* (2007), vol. 578(1): pp. 180–184.

[Ave07c] Ave, M. et al. (Pierre Auger Collaboration): Reconstruction accuracy of the surface detector array of the Pierre Auger Observatory. *Proc. 30th Int. Cosmic Ray Conf. (Mérida)* (2007), vol. 4: pp. 307–310.

[Ave08] Ave, M. et al. (AIRFLY Collaboration): Temperature and humidity dependence of air fluorescence yield measured by AIRFLY. *Nucl. Instrum. Meth. A* (2008), vol. 597: pp. 50–54.

[Bau09] Bauleo, P. M. and Martino, J. R.: The dawn of the particle astronomy era on ultra-high-energy cosmic rays. *Nature* (2009), vol. 458: p. 847.

[Beh12] Behringer, J. et al. (Particle Data Group): The Review of Particle Physics. *Phys. Rev. D* (2012), vol. 86(010001).

[Ber99] Berezhko, E. G. and Ksenofontov, L. T.: Composition of cosmic rays accelerated in supernova remnants. *J. Exp. Theor. Phys.* (1999), vol. 89: pp. 391–403.

[Ber03] Bertou, X. et al. (Pierre Auger Collaboration): Calibration and Monitoring of the Pierre Auger Surface Detectors. *Proc. 28th Int. Cosmic Ray Conf. (Tsukuba)* (2003): pp. 813–816.

[Ber06a] Berezinsky, V.: On transiton from galactic to extragalactic cosmic rays. *J. Phys. Conference Series* (2006), vol. 47: pp. 142–153.

[Ber06b] Bertou, X. et al. (Pierre Auger Collaboration): Calibration of the surface array of the Pierre Auger Observatory. *Nucl. Instrum. Meth. A* (2006), vol. 568(2): pp. 839–846.

[Ber09] Berg, A. van den et al. (Pierre Auger Collaboration): Radio detection of cosmic rays at the southern Auger Observatory. *Proc. 31st Int. Cosmic Ray Conf. (Lodz)* (2009).

[Bha37] Bhabha, H. J. and Heitler, W.: The Passage of Fast Electrons and the Theory of Cosmic Showers. *Proc. R. Soc. Lond. A* (1937), vol. 159(898): pp. 432–458.

[Bha00] *see e.g.* Bhattacharjee, P. and Sigl, G.: Origin and Propagation of Extremely High Energy Cosmic Rays. *Phys. Rept.* (2000), vol. 327: p. 109, *and references therein.*

[Bie87] Biermann, P. L. and Strittmatter, P. A.: Synchrotron emission from shock waves in active galactic nuclei. *Astrophys. J.* (1987), vol. 322: p. 643.

[Bil01] Billoir, P. and Revenu, B.: Notions of geodesy and the UTM coordinate system. Proposition of a local cartesian coordinate system for the southern Auger site. *Auger Internal Note* (2001), (GAP-2001-038).

[Bir94] Bird, D. J. et al. (HiRes Collaboration): The cosmic-ray energy spectrum observed by the Fly's Eye. *Astrophys. J.* (1994), vol. 424: pp. 491–502.

[Blü09] *see e.g.* Blümer, J.; Engel, R. and Hörandel, J. R.: Cosmic Rays from the Knee to the Highest Energies. *Prog. Part. Nucl. Phys.* (2009), vol. 63: pp. 293–338, *and references therein.*

[Blü10] Blümer, J.: The northern site of the Pierre Auger Observatory. *New J. Phys.* (2010), vol. 12(3): p. 035001.

[Boh10] *see e.g.* Bohm, G. and Zech, G.: *Introduction to statistics and data analysis for physicists*, DESY (2010), *and references therein.*

[Bor04] Borer, K. and Wälchli, T.: Hamamatsu H8804MOD-1 multianode PMT tests for OPERA (2004).

[Bro00] *see e.g.* Bronstein, I. N.; Semendjajew, K. A.; Musiol, G. and Mühlig, H.: *Taschenbuch der Mathematik*, Verlag Harri Deutsch, 5 edn. (2000), *and references therein.*

[Brü04] Brüning, O. S.; Collier, P.; Lebrun, P.; Myers, S.; Ostojic, R.; Poole, J. and Proudlock, P.: *LHC Design Report Vol. 1 - The LHC Main Ring*, CERN, Geneva (2004).

[Buc03] Buchvarova, M.; Ruder, H.; Velinov, P. I. Y. and Tonev, P.: Ionization by galactic cosmic rays in the ionosphere and atmopshere depending on the solar activity. *Proc. ISCS 2003 Symposium (Tatransá Lomnica)* (2003): pp. 351–354.

[Buc12] Buchholz, P.; Fröhlich, U.; Kolotaev, Y.; Pontz, M. and Tcaciuc, R.: Brief Description of the Production and Test Procedures of the Muon Counter Electronics for the AMIGA Pre-Unitary Cell. *Auger Internal Note* (2012), (GAP-2012-062).

[Bur05] Buren, J. van et al. (KASCADE-Grande Collaboration): Muon Size Spectrum measured by KASCADE-Grande. *Proc. 29th Int. Cosmic Ray Conf. (Pune)* (2005).

[Can03] Candia, J.; Mollerach, S. and Roulet, E.: Cosmic ray spectrum and anisotropies from the knee to the second knee. *J. Cosmol. Astropatt. Phys.* (2003), vol. 5: p. 3.

[Che34] Cherenkov, J. A.: Visible emission of clean liquids by action of gamma radiation. *Doklady Akad. Nauk S.S.S.R.* (1934), vol. 2: p. 451.

[Che86] Cheng, K. S.; Ho, C. and Ruderman, M.: Energetic radiation from rapidly spinning pulsars. I - Outer magnetosphere gaps. II - VELA and Crab. *Astrophys. J.* (1986), vol. 300: pp. 500–539.

[Com35] Compton, A. H. and Getting, I. A.: An Apparent Effect of Galactic Rotation on the Intensity of Cosmic Rays. *Phys. Rev.* (1935), vol. 47: pp. 817–821.

[Cow98] *see e.g.* Cowan, G.: *Statistical Data Analysis*, Oxford University Press (1998), *and references therein.*

[Cra46] *see e.g.* Cramér, H.: *Mathematical Methods of Statistics*, Princeton University Press (1946), *and references therein.*

[Cut86] Cutler, D. J. and Groom, D. E.: Observation of terrestrial orbital motion using the cosmic-ray Compton-Getting effect. *Nature* (1986), vol. 322: pp. 434–436.

[Dan77] Danilova, T. V. et al.: *Proc. 15th Int. Cosmic Ray Conf. (Plovdiv)* (1977), vol. 8: p. 129.

[Dem09] Dembinski, H. P.: *Measurement of the flux of ultra high energy cosmic rays using data from very inclined air showers at the Pierre Auger Observatory*, Ph.D. thesis, RWTH Aachen University (2009).

[Dem13] Dembinski, H. P. et al.: The Auger Observer (2013), URL `http://augerobserver.fzk.de`.

[Dic65] Dicke, R. H.; Peebles, P. J. E.; Roll, P. G. and Wilkinson, D. T.: Cosmic Black-Body Radiation. *Astrophys. J.* (1965), vol. 142: pp. 414–419.

[Don09] *see e.g.* Donato, C. de and Medina-Tanco, G. A.: Experimental constraints on the astrophysical interpretation of the cosmic ray Galactic-extragalactic transition region. *Astropart. Phys.* (2009), vol. 32: pp. 253–268, *and references therein.*

[Dov03] Dova, M. T. et al. (Pierre Auger Collaboration): Asymmetries Observed in Giant Air Showers Using Water Cherenkov Detectors. *Proc. 28th Int. Cosmic Ray Conf. (Tsukuba)* (2003): pp. 369–372.

[Dru83] *see e.g.* Drury, L. O'C.: An introduction to the theory of diffusive shock acceleration of energetic particles in tenuous plasmas. *Rep. Prog. Phys.* (1983), vol. 46(8): p. 973, *and references therein.*

[Eic11] Eichler, D. and Pohl, M.: Can Ultrahigh-Energy Cosmic Rays Come from Gamma-Ray Bursts? Cosmic Rays Below the Ankle and Galactic Gamma-Ray Bursts. *Astrophys. J. Lett.* (2011), vol. 738: p. L21.

[Elb95] Elbert, J. W. and Sommers, P.: In Search of a Source for the 320 EeV Fly's Eye Cosmic Ray. *Astrophys. J.* (1995), vol. 441: pp. 151–161.

[Eng11] Engel, R.; Heck, D. and Pierog, T.: Extensive Air Showers and Hadronic Interactions at High Energy. *Annu. Rev. Nucl. Part. Sci.* (2011), vol. 61: pp. 467–489.

[Erl97] Erlykin, A. D. and Wolfendale, A. W.: A single source of cosmic rays in the range 10^{15} - 10^{16} eV. *J. Phys. G* (1997), vol. 23: pp. 979–989.

[Erl98] Erlykin, A. D.; Lipski, M. and Wolfendale, A. W.: High energy cosmic ray spectroscopy. IV. The evidence from direct observations at lower energies and directional anisotropies. *Astropart. Phys.* (1998), vol. 8: pp. 283–292.

[Etc10] Etchegoyen, A.; Fröhlich, U.; Lucero, A.; Sidelnik, I. and Wundheiler, B. (Pierre Auger Collaboration): *The Pierre Auger Project and Enhancements*, American Institute of Physics (2010), pp. 129–138.

[Fac11] Facal San Luis, P. et al. (Pierre Auger Collaboration): The distribution of shower maxima of UHECR air showers. *Proc. 32nd Int. Cosmic Ray Conf. (Beijing)* (2011): p. 0725.

[Fal03] *see e.g.* Falcke, H. and Gorham, P.: Detecting radio emission from cosmic ray air showers and neutrinos with a digital radio telescope. *Astropart. Phys.* (2003), vol. 19: pp. 477–494, *and references therein.*

[Fan74] Fanaroff, B. L. and Riley, J. M.: The morphology of extragalactic radio sources of high and low luminosity. *Mon. Not. R. astr. Soc.* (1974), vol. 167: p. 31P.

[Fer49] Fermi, E.: On the Origin of the Cosmic Radiation. *Phys. Rev.* (1949), vol. 75(8): p. 1169.

[Fom91] Fomin, Yu. A. et al.: *Proc. 22nd Int. Cosmic Ray Conf. (Dublin)* (1991), vol. 2: p. 85.

[Fra01] Frail, D. A. et al.: Beaming in Gamma-Ray Bursts: Evidence for a Standard Energy Reservoir. *Astrophys. J. Lett.* (2001), vol. 562: p. L55.

[Frö09] Fröhlich, U.: *Charakterisierung der Szintillatoren und der Ausleseelektronik des AMIGA-Myonsystems*, Master's thesis, Universität Siegen (2009).

[Fuc12] Fuchs, B. et al. (Pierre Auger Collaboration): The Auger Engineering Radio Array. *Nucl. Instrum. Meth. A* (2012), vol. 692: pp. 93–97.

[Gag06] Gagunashvili, N. D.: Comparison of weighted and unweighted histograms. *ArXiv Physics e-prints* (2006).

[Gai91] *see e.g.* Gaisser, T. K.: *Cosmic Rays and Particle Physics*, Cambridge University Press (1991), *and references therein.*

[Gel08] Gelmini, G. B.; Kalashev, O. E. and Semikoz, D. V.: GZK photons as ultra-high-energy cosmic rays. *J. Exp. Theor. Phys.* (2008), vol. 106(6): pp. 1061–1082.

[Ghi05] Ghia, P. L. et al. (Pierre Auger Collaboration): Statistical and systematic uncertainties in the event reconstruction and $S(1000)$ determination by the Pierre Auger surface detector. *Proc. 29th Int. Cosmic Ray Conf. (Pune)* (2005).

[Gla99] Glasmacher, M. A. K. et al.: The cosmic ray energy spectrum between 10^{14} and 10^{16} eV. *Astropart. Phys.* (1999), vol. 10: pp. 291–302.

[Glu10] Glushkov, A. V. et al.: Constraints on the flux of primary cosmic-ray photons at energies $E > 10^{18}$ eV from Yakutsk muon data. *Phys. Rev. D* (2010), vol. 82(4).

[Gor08] Gorham, P. W. et al.: Observations of microwave continuum emission from air shower plasmas. *Phys. Rev. D* (2008), vol. 78(3):032007.

[Gre56] Greisen, K.: *Progress in Cosmic Ray Physics*, North Holland Amsterdam (1956).

[Gre60] Greisen, K.: Cosmic Ray Showers. *Annu. Rev. Nucl. Sci.* (1960), vol. 10(1): pp. 63–108.

[Gre66] Greisen, K.: End to the Cosmic-Ray Spectrum? *Phys. Rev. Lett.* (1966), vol. 16: pp. 748–750.

[Gri70] Grigorov, N. L.; Nesterov, V. E.; Rapoport, I. D.; Savenko, I. A. and Skuridin, G. A: Investigation of energy spectrum of primary cosmic particles with high and superhigh energies of space stations *proton*. *Yad. Fiz.* (1970), vol. 11: pp. 1058–1069.

[Gri10] *see e.g.* Grieder, P. K. F.: *Extensive Air Showers*, vol. 2, Springer-Verlag Berlin Heidelberg (2010), *and references therein.*

[Gru05] *see e.g.* Grupen, C.: *Astroparticle Physics*, Springer-Verlag Berlin Heidelberg (2005), *and references therein.*

[Gru08] *see e.g.* Grupen, C. and Shwartz, A.: *Particle Detectors*, Cambridge University Press, 2nd edn. (2008), *and references therein.*

[Gru12] *see e.g.* Grupen, C. and Buvat, I.: *Handbook of Particle Detection and Imaging*, Springer-Verlag Berlin Heidelberg (2012), *and references therein.*

[Hal97] Halzen, F. and Zas, E.: Neutrino Fluxes from Active Galaxies: a Model-Independent Estimate. *Astrophys. J.* (1997), vol. 488: p. 669.

[Ham03] Hamamatsu: *Multianode Photomultiplier Tube Assembly H7546B Datasheet* (2003).

[Ham11] Hamamatsu: *Multianode Photomultiplier Tube Assembly H8804-200 MOD Datasheet* (2011).

[Hea06] *see e.g.* Healy, M.; Barnhill, D.; Arisaka, K.; Lee, J. and Boghrat, P.: A study of composition trends using rise time and curvature data. *Auger Internal Note* (2006), (GAP-2006-092), *and references therein.*

[Her61] Hersil, J.; Escobar, I.; Scott, D.; Clark, G. and Olbert, S.: Observations of Extensive Air Showers near the Maximum of Their Longitudinal Development. *Phys. Rev. Lett.* (1961), vol. 6(1): pp. 22–23.

[Hes12] Hess, V. F.: Über Beobachtungen der durchdringenden Strahlung bei sieben Freiballonfahrten. *Phys. Z.* (1912), vol. 13: pp. 1084–1091.

[Hil84] Hillas, A. M.: The origin of ultra-high-energy cosmic rays. *Ann. Rev. Astron. Astrophys.* (1984), vol. 22: p. 425.

[Hör03] *see e.g.* Hörandel, J. R.: On the knee in the energy spectrum of cosmic rays. *Astropart. Phys.* (2003), vol. 19: pp. 193–220, *and references therein.*

[Hör04] *see e.g.* Hörandel, J. R.: Models of the knee in the energy spectrum of cosmic rays. *Astropart. Phys.* (2004), vol. 21: pp. 241–265, *and references therein.*

[Hör06] Hörandel, J. R.; Kalmykov, N. N. and Timokhin, A. V.: The end of the galactic cosmic-ray energy spectrum - a phenomenological view. *J. Phys. Conference Series* (2006), vol. 47: pp. 132–141.

[Hör07] *see e.g.* Hörandel, J. R.: Cosmic rays from the knee to the second knee: 10^{14} to 10^{18} eV. *Mod. Phys. Lett. A* (2007), vol. 22(21): pp. 1533–1551, *and references therein.*

[Hue05] Huege, T. and Falcke, H.: Radio emission from cosmic ray air showers: Simulation results and parametrization. *Astropart. Phys.* (2005), vol. 24: pp. 116–136.

[Ivi99] Ivi Foundation: Standard Commands for Programmable Instruments (SCPI) (1999), vol. 1.

[Jed07] JEDEC and EIA: Interface Standard for Nominal 3 V/3.3 V Supply Digital Integrated Circuits (September 2007), (JESD8C.01).

[Kam58] Kamata, K. and Nishimura, J.: The Lateral and the Angular Structure Functions of Electron Showers. *Prog. Theor. Phys. Suppl.* (1958), vol. 6: pp. 93–155.

[Kaz01] Kazanas, D. and Nicolaidis, A.: Cosmic ray "knee": A herald of new physics? *Proc. 27th Int. Cosmic Ray Conf. (Hamburg)* (2001), vol. 5: pp. 1760–1763.

[Kec13] Keckert, S.: *Entwicklung einer Kalibrationsmethode für die AMIGA-Myonzähler des Pierre-Auger-Observatoriums*, Bachelor's thesis, Universität Siegen (2013).

[Kel11] Kelley, J. L. et al. (Pierre Auger Collaboration): AERA: the Auger Engineering Radio Array. *Proc. 32nd Int. Cosmic Ray Conf. (Beijing)* (2011).

[Ken77] *see e.g.* Kendall, M. G. and Stuart, A.: *The advanced theory of statistics - distribution theory*, vol. 1, J. B. Lippincott Company, Philadelphia, 4 edn. (1977), *and references therein.*

[Kif86] Kifune, T. et al. (Akeno Collaboration): Anisotropy of the arrival direction of extensive air showers observed at Akeno. *J. Phys. G* (1986), vol. 12: pp. 129–142.

[Kle09] Kleifges, M. et al. (Pierre Auger Collaboration): Extension of the Pierre Auger Observatory using high-elevation fluorescence telescopes (HEAT). *Proc. 31st Int. Cosmic Ray Conf. (Lodz)* (2009).

[Kol13] Kolotaev, Y.: Private Communication (2013).

[Lan53] Landau, L. and Pomeranchuk, I.: *Doklady Akad. Nauk S.S.S.R.* (1953), vol. 92: pp. 535, 735.

[Lau12] Lauber, F. H.: *Aufbau eines Myon-Hodoskops für den AMIGA-Teststand*, Bachelor's thesis, Universität Siegen (2012).

[Lin62] Linsley, J. and Scarsi, L.: Arrival Times of Air Shower Particles at Large Distances from the Axis. *Phys. Rev.* (1962), vol. 128(5): pp. 2384–2392.

[Lod03] Lodders, K.: Solar System Abundances and Condensation Temperatures of the Elements. *Astrophys. J.* (2003), vol. 591(2): pp. 1220–1247.

[Lon11] *see e.g.* Longair, M. S.: *High Energy Astrophysics*, Cambridge University Press, 3 edn. (2011), *and references therein.*

[Mar06] Mariş, I. C. et al.: Data Summary Trees and Shower Visualization for Reconstructed Auger Events. *Auger Internal Note* (2006), (GAP-2006-081).

[Mar11] Mariş, I. C. et al. (Pierre Auger Collaboration): The AMIGA infill detector of the Pierre Auger Observatory: performance and first data. *Proc. 32nd Int. Cosmic Ray Conf. (Beijing)* (2011).

[Mat05] Matthews, J.: A Heitler model of extensive air showers. *Astropart. Phys.* (2005), vol. 22(5-6): pp. 387–397.

[Mau03] Maurin, G.; Cohen, F.; Lamblin, J.; Brunet, J. M. and Lachaud, C.: Discrimination between Photon, Proton and Iron in Atmospherics Showers. *Auger Internal Note* (2003), (GAP-2006-086).

[Med09] Medina-Tanco, G. A.: BATATA: A device to characterize the punch-through observed in underground muon detectors and to operate as a prototype for AMIGA. *Proc. 31st Int. Cosmic Ray Conf. (Lodz)* (2009).

[Meu11] Meurer, C. and Scharf, N. et al. (Pierre Auger Collaboration): HEAT - a low energy enhancement of the Pierre Auger Observatory. *Astrophys. Space Sci.* (2011), vol. 7: pp. 183–186.

[Mig56] Migdal, A. B.: Bremsstrahlung and Pair Production in Condensed Media at High Energies. *Phys. Rev.* (1956), vol. 103(6): pp. 1811–1820.

[Mil95] Milgrom, M. and Usov, V.: Possible Association of Ultra-High-Energy Cosmic-Ray Events with Strong Gamma-Ray Bursts. *Astrophys. J. Lett.* (1995), vol. 449: p. L37.

[Nag84] Nagano, M.; Hara, T.; Hatano, Y.; Hayashida, N.; Kawaguchi, S.; Kamata, K.; Kifune, T. and Mizumoto, Y.: Energy spectrum of primary cosmic rays between $10^{14.5}$ and 10^{18} eV. *J. Phys. G* (1984), vol. 10: pp. 1295–1310.

[Nag04] Nagano, M.; Kobayakawa, K.; Sakaki, N. and Ando, K.: New measurement on photon yields from air and the application to the energy estimation of primary cosmic rays. *Astropart. Phys.* (2004), vol. 22: pp. 235–248.

[New07] Newton, D.; Knapp, J. and Watson, A.: The optimum distance at which to determine the size of a giant air shower. *Astropart. Phys.* (2007), vol. 26(6): pp. 414–419.

[Nie11] Niechciol, M.: *Muon counter simulation studies for the AMIGA enhancement of the Pierre Auger Observatory*, Master's thesis, Universität Siegen (2011).

[Nor95] Norman, C. A.; Melrose, D. B. and Achterberg, A.: The Origin of Cosmic Rays above $10^{18.5}$ eV. *Astrophys. J.* (1995), vol. 454: p. 60.

[Oeh13] Oehlschläger, J.: Private Communication (2013).

[Pac97] Pierre Auger Collaboration: The Pierre Auger Project Design Report (1997), 2nd edition.

[Pac06] Pierre Auger Collaboration: AMIGA Design Report (2006).

[Pea04] Pearson, K.: *On the theory of contingency and its relation to association and normal correlation*, Dulau and Co. London (1904).

[Pea85] Peacock, J. A.: The high-redshift evolution of radio galaxies and quasars. *Mon. Not. R. astr. Soc.* (1985), vol. 217: p. 601.

[Pen65] Penzias, A. A. and Wilson, R. W.: A Measurement of Excess Antenna Temperature at 4080 Mc/s. *Astrophys. J.* (1965), vol. 142: pp. 419–421.

[Pes11] Pesce, R. et al. (Pierre Auger Collaboration): Energy calibration of data recorded with the surface detectors of the Pierre Auger Observatory: an update. *Proc. 32nd Int. Cosmic Ray Conf. (Beijing)* (2011).

[Pla09] *see e.g.* Platino, M. et al. (Pierre Auger Collaboration): AMIGA - Auger Muons and Infill for the Ground Array of the Pierre Auger Observatory. *Proc. 31st Int. Cosmic Ray Conf. (Lodz)* (2009), *and references therein.*

[Pla11] Platino, M. et al.: AMIGA at the Auger Observatory: the scintillator module testing system. *JINST* (2011), vol. 6: p. 06006.

[Pod04] Podsiadlowski, P.; Mazzali, P. A.; Nomoto, K.; Lazzati, D. and Cappellaro, E.: The Rates of Hypernovae and Gamma-Ray Bursts: Implications for Their Progenitors. *Astrophys. J. Lett.* (2004), vol. 607: pp. L17–L20.

[Pon12] Pontz, M.: *System Tests, Initial Operation and First Data of the AMIGA Muon Detector for the Pierre Auger Observatory*, Ph.D. thesis, Universität Siegen (2012), and Erratum.

[Pri03] Privitera, P. et al. (Pierre Auger Collaboration): The Angular Reconstruction and Angular Resolution of Air Showers Detected at the Auger Observatory. *Proc. 28th Int. Cosmic Ray Conf. (Tsukuba)* (2003): pp. 357–360.

[Pro92] Protheroe, R. J. and Szabo, A. P.: High energy cosmic rays from active galactic nuclei. *Phys. Rev. Lett.* (1992), vol. 69(20): p. 2885.

[Pro96] Protheroe, R. J. and Johnson, P. A.: Propagation of ultra high energy protons and gamma rays over cosmological distances and implications for topological defect models. *Astropart. Phys.* (1996), vol. 4: pp. 253–269.

[Ptu93] Ptuskin, V. S.; Rogovaya, S. I.; Zirakashvili, V. N.; Chuvilgin, L. G.; Khristiansen, G. B.; Klepach, E. G. and Kulikov, G. V.: Diffusion and drift of very high energy cosmic rays in galactic magnetic fields. *Astron. Astrophys.* (1993), vol. 268: pp. 726–735.

[Ptu10] Ptuskin, V. S.; Zirakashvili, V. N. and Seo, E. S.: Spectrum of Galactic Cosmic Rays Accelerated in Supernova Remnants. *Astrophys. J.* (2010), vol. 718(1): p. 31.

[Rac93] Rachen, J. P. and Biermann, P. L.: Extragalactic Ultra-High Energy Cosmic-Rays - Part One - Contribution from Hot Spots in Fr-II Radio Galaxies. *Astron. Astrophys.* (1993), vol. 272: p. 161.

[Rav13] Ravignani, D. et al. (Pierre Auger Collaboration): Measurement of the energy spectrum of cosmic rays above 3×10^{17} eV using the AMIGA 750 m surface detector array of the Pierre Auger Observatory. *Proc. 33rd Int. Cosmic Ray Conf. (Rio de Janeiro)* (2013).

[Ros41] Rossi, B. and Greisen, K.: Cosmic-Ray Theory. *Rev. Mod. Phys.* (1941), vol. 13(4): pp. 240–309.

[San12a] Sanchez, F.: Private Communication (2012).

[San12b] Sanchez, F. et al.: First showers seen by the AMIGA Muon Detector. *Auger Internal Note* (2012), (GAP-2012-120).

[San13] Sanchez, F.: Private Communication (2013).

[Sat10] Sato, R.: Private Communication (2010).

[Sat13] Sato, R.: Private Communication (2013).

[Sch38] Schmidt, B.: Ein lichtstarkes komafreies Spiegelsystem. *Mitteilungen der Hamburger Sternwarte in Bergedorf* (1938), vol. 7: pp. 15–17.

[Sch09] Schmidt, A.; Asch, T.; Gemmeke, H.; Kleifges, M.; Mathes, H.-J.; Menchikov, A.; Schüssler, F. and Tcherniakhovski, D.: Third level trigger for the fluorescence telescopes of the Pierre Auger Observatory. *Nucl. Instrum. Meth. A* (2009), vol. 601: pp. 347–353.

[Sch12] Schulz, A.: *Measurement of the Energy Spectrum of Cosmic Rays between 0.1 EeV and 30 EeV with the Infill Extension of the Surface Detector of the Pierre Auger Observatory*, Diploma thesis, Karlsruhe Institute of Technology - IEKP (2012).

[Set11a] Settimo, M. and Perrone, L.: Trigger efficiency of the infill detector for photon and hadron primaries. *Auger Internal Note* (2011), (GAP-2011-107).

[Set11b] Settimo, M. et al. (Pierre Auger Collaboration): An update on a search for ultra-high energy photons using the Pierre Auger Observatory. *Proc. 32nd Int. Cosmic Ray Conf. (Bejing)* (2011).

[Set13] Settimo, M.: Private Communication (2013).

[She95] Shemi, A.: Cosmic rays from accreting isolated neutron stars. *Mon. Not. R. astr. Soc.* (1995), vol. 275: p. 115.

[Shi02] Shinozaki, K. et al.: Upper Limit on Gamma-Ray Flux above 10^{19} eV Estimated by the Akeno Giant Air Shower Array Experiment. *Astrophys. J.* (2002), vol. 571(2): pp. L117–L120.

[Sig03] *see e.g.* Sigl, G.: The Enigma of the Highest Energy Particles of Nature. *Ann. Phys.* (2003), vol. 303(1): p. 117, *and references therein.*

[Sim83] Simpson, J. A.: Elemental and Isotopic Composition of the Galactic Cosmic Rays. *Annu. Rev. Nucl. Part. Sci.* (1983), vol. 33: pp. 323–382.

[Som05] Sommers, P. et al. (Pierre Auger Collaboration): First Estimate of the Primary Cosmic Ray Energy Spectrum above 3 EeV from the Pierre Auger Observatory. *Proc. 29th Int. Cosmic Ray Conf. (Pune)* (2005).

[Son13] Sonntag, S.: *Analyse der Signale eines Multianoden-Photomultipliers auf Mikrosekunden-Zeitskala*, Bachelor's thesis, Universität Siegen (2013).

[Sua08] Suarez, F. et al.: Multi-pixel PMTs for the AMIGA project: Proposal for the testing facility and first measurements. *Auger Internal Note* (2008), (GAP-2008-164).

[Sua13] Suarez, F. et al. (Pierre Auger Collaboration): The AMIGA muon detectors of the Pierre Auger Observatory: overview and status. *Proc. 33rd Int. Cosmic Ray Conf. (Rio de Janeiro)* (2013).

[Sup08] Supanitsky, A. D.; Etchegoyen, A.; Medina-Tanco, G.; Allekotte, I.; Gómez Berisso, M. and Medina, M. C.: Underground muon counters as a tool for composition analyses. *Astropart. Phys.* (2008), vol. 29: pp. 461–470.

[Sza05] Szadkowski, Z.; Becker, K.-H. and Kampert, K.-H.: Development of a new first level trigger for the surface array in the Pierre Auger Observatory based on the Cyclone™ Altera® FPGA. *Nucl. Instrum. Meth. A* (2005), vol. 545(3): pp. 793–802.

[Sza09] Szadkowski, Z. et al.: The 3rd generation Front-End cards of the Pierre Auger surface detectors: Test results and performance in the field. *Nucl. Instrum. Meth. A* (2009), vol. 606: pp. 439–445.

[Sza11] Szadkowski, Z.: Triggers, Data Flow and the Synchronization Between the Auger Surface Detector and the AMIGA Underground Muon Counters. *IEEE Trans. Nucl. Sci.* (2011), vol. 58(4): pp. 1771–1777.

[Sza12] Szadkowski, Z.: Private Communication (2012).

[Tak03] Takeda, M. et al. (AGASA Collaboration): Energy determination in the Akeno Giant Air Shower Array experiment. *Astropart. Phys.* (2003), vol. 19: pp. 447–462.

[Tay08] Taylor, F. E.: Comparison of cosmic ray flux at $\sqrt{s} > 14\,\mathrm{TeV}$ with LHC luminosity. *ArXiv Physics e-prints* (2008).

[Tca12] Tcaciuc, R.: Private Communication (2012).

[Tig11] Tigges, M.: *Systemtests der Ausleseelektronik der AMIGA-Erweiterung des Pierre-Auger-Observatoriums*, Master's thesis, Universität Siegen (2011).

[Tsu11] Tsunesada, Y. et al. (Telescope Array Collaboration): Highlights from Telescope Array. *Proc. 32nd Int. Cosmic Ray Conf. (Bejing)* (2011).

[Ull07] Ullrich, T. and Xu, Z.: Treatment of Errors in Efficiency Calculations. *ArXiv Physics e-prints* (2007).

[Vcv06] Véron-Cetty, M.-P. and Véron, P.: A catalogue of quasars and active nuclei: 12th edition. *Astron. Astrophys.* (2006), vol. 455: pp. 773–777.

[Ven97] Venkatesan, A.; Miller, M. C. and Olinto, A. V.: Constraints on the Production of Ultra-High-Energy Cosmic Rays by Isolated Neutron Stars. *Astrophys. J.* (1997), vol. 484(1): p. 323.

[Vid12] Videla, M. et al.: The interface board between AMIGA moun counter surface and underground electronics: Hardware. *Auger Internal Note* (2012), (GAP-2012-103).

[Wai11] Wainberg, O.: Private Communication (2011).

[Wig00] Wigmans, R.: On Big Bang Relics, the Neutrino Mass and the Spectrum of Cosmic Rays. *Nucl. Phys. B (Proc. Suppl.)* (2000), vol. 85: pp. 305–310.

[Wil10] Williams, C. et al.: The MIDAS Experiment: A New Technique for the Detection of Extensive Air Showers. *XVI International Symposium on Very High Energy Cosmic Ray Interactions (Batavia)* (2010).

[Wul10] Wulf, Theodor: Observations on the radiation of high penetration power on the Eiffel tower. *Phys. Z.* (1910), vol. 11: p. 811.

[Wun11] Wundheiler, B. et al. (Pierre Auger Collaboration): The AMIGA muon counters of the Pierre Auger Observatory: Performance and first data. *Proc. 32nd Int. Cosmic Ray Conf. (Bejing)* (2011).

[Wun12] Wundheiler, B. et al.: AMIGA muon data structure inside CDAS. *Auger Internal Note* (2012), (GAP-2012-086).

[Zat66] Zatsepin, G. T. and Kuz'min, V. A.: Upper Limit of the Spectrum of Cosmic Rays. *Sov. JETP Lett.* (1966), vol. 4: p. 78.

Acknowledgements

I would like to express my gratitude to all the people who supported me over the last years, without their help this thesis would not have been possible.

In the first place, I would like to thank my supervisor Prof. Dr. Peter Buchholz for his overall support, guidance and encouragement, and the chance to participate in the research in his group. I am grateful for the opportunity to work on the exciting field of astroparticle physics at the Pierre Auger Observatory. He always showed me that there are still open questions to be answered and new things to learn.

Further, I would like to offer my special thanks to Prof. Dr. Markus Risse for agreeing to be the co-reviewer of this thesis, for his continued assistance and for the numerous discussions, which proved to be very helpful.

I also owe a debt of gratitude to Dr. Michael Pontz for his close collaboration within the AMIGA project. I really enjoyed his company, especially during our stays at the Pierre Auger Observatory.

I am particularly grateful for the assistance given by Marcus Niechciol and Dirk Fröhlich, who spent a lot of time proofreading this thesis. It is due to their great efforts that many mistakes could be sought out and removed.

Many thanks to all the members of the working groups of particle and astroparticle physics, not only for feedback, criticism and teamwork but also for the pleasant working atmosphere. In this context, a very special thanks is due to Hendrik Czirr and Dr. Marcus Rammes for all the serious and the funny discussions, which we had, and especially for the numerous leisure-time activities we shared. I would like to particularly thank Dr. Rodica Tcaciuc and Nadine Foerster with whom I had the pleasure to share my office.

I am particularly grateful to Yury Kolotaev, who always offered help in answering my questions concerning electronics, and to Prof. Dr. Zbigniew Szadkowski for collaborating on large parts of the FPGA firmware. I would also like to extend my thanks to the technicians of the electronics and the mechanical workshop of the Physics Department of the University of Siegen, who supported my work whenever a helping hand was needed.

Special thanks is due to Dr. Wolfgang Walkowiak for providing the computing environment and for the many fruitful discussions related to the mathematical treatment of statistics. I also wish to acknowledge the help provided by Dr. Thomas Bäcker, who solved many programming issues occurring in the course of this work.

Thanks to my colleagues from Buenos Aires, Malargüe and Mendoza, and in particular to Fernando Contreras, Dr. Alberto Etchegoyen, Dr. Beatrice García, Dr. Manuel Platino, Dr. Federico Sánchez, Dr. Ricardo Sato, Gonzalo A. de la Vega, Mariela Videla and Oscar Wainberg.

I would like to thank Christian Dehn, Frederik Lauber, Sebastian Keckert and Sebastian Sonntag, who contributed to the AMIGA project with their Bachelor's theses.

Last but not least, I am proud to express my gratefulness to my family:

Meiner Familie, die zu jeder Zeit zu mir gestanden hat und ohne deren Rückhalt und Unterstützung diese Promotion nicht möglich gewesen wäre, schulde ich großen Dank. Besonders meinen Eltern Dagmar und Detlev, die fortwährend und selbstlos alles getan haben, um mir und meinen Geschwistern ein erfülltes Leben zu ermöglichen, kann ich nicht genug danken. Uneingeschränkter Dank gilt auch meinen Geschwistern Anna und Dirk, auf die ich mich immer verlassen kann. Auch ohne die Unterstützung, die ich bei Patricia Kreps und ihrer Familie finden konnte, hätte ich diese Arbeit nicht abschließen können. Danke!